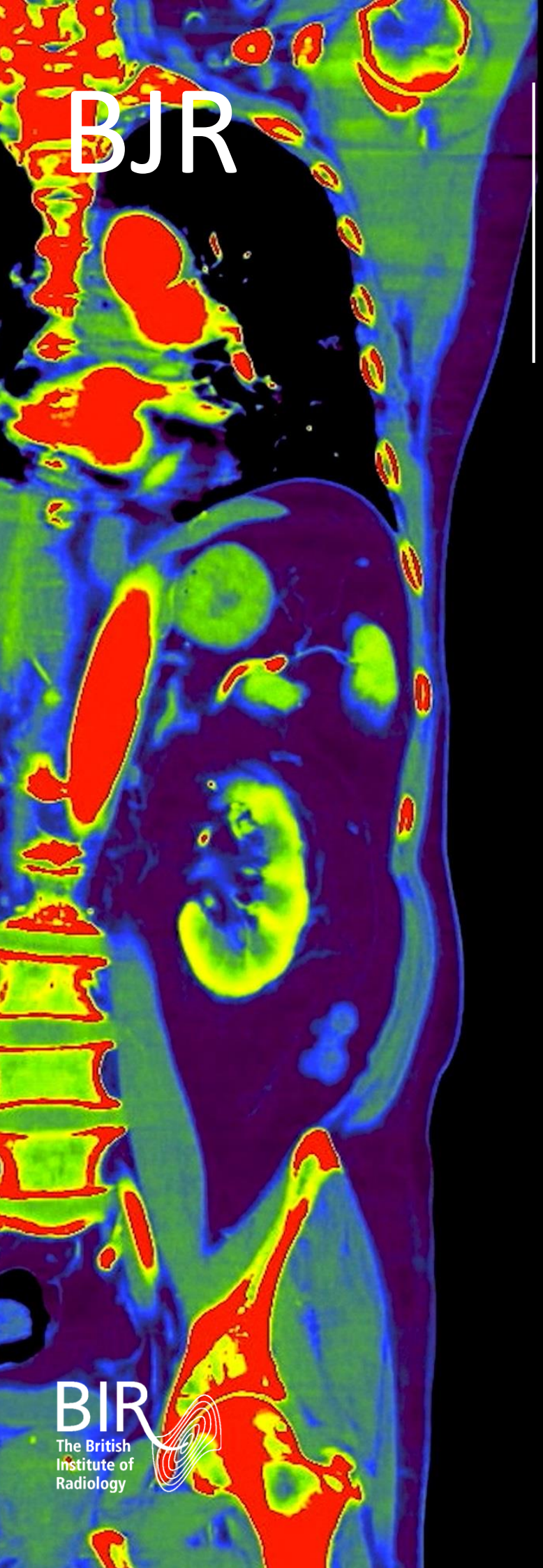

BJR

Image Optimisation

Research papers from *BJR*

BIR
The British Institute of Radiology

BAYER

Contents

Bayer plc has sponsored the production and distribution of this curated collection of independently produced articles originally published in *BJR*. Bayer plc had no involvement in the selection of these articles prior to their inclusion in this collection.

BJR

BJR is the international research journal of the British Institute of Radiology and is the oldest scientific journal in the field of radiology and related sciences.

An international, multi-disciplinary, research journal, *BJR* covers the clinical and technical aspects of medical imaging, radiotherapy, radiation oncology, medical physics, radiobiology and the underpinning sciences. *BJR* is essential reading for anyone with a professional interest in radiology and radiation oncology and specifically radiologists, medical physicists, radiation oncologists, radiotherapists, radiographers and radiobiologists.

BJR https://doi.org/10.1259/bjr.20220544

Received: 26 May 2022 | Accepted: 30 January 2023 | Published online: 10 February 2023

Cite this article as:
Sartoretti T, Wildberger JE, Flohr T, Alkadhi H. Photon-counting detector CT: early clinical experience review. *Br J Radiol* (2023) 10.1259/bjr.20220544.

REVIEW ARTICLE

Photon-counting detector CT: early clinical experience review

[1,2,3]THOMAS SARTORETTI, BMed, [2,3]JOACHIM E WILDBERGER, MD, PhD, [4]THOMAS FLOHR, PhD and [1]HATEM ALKADHI, MD, MPH, EBCR, FESER

[1]Diagnostic and Interventional Radiology, University Hospital Zürich, University of Zürich, Zürich, Switzerland
[2]Department of Radiology and Nuclear Medicine, Maastricht University Medical Center, Maastricht, The Netherlands
[3]Cardiovascular Research Institute Maastricht (CARIM), Maastricht University, Maastricht, The Netherlands
[4]Siemens Healthcare GmbH, Computed Tomography, Forchheim, Germany

Address correspondence to: Dr Hatem Alkadhi
E-mail: *hatem.alkadhi@usz.ch*

ABSTRACT

Since its development in the 1970s, X-ray CT has emerged as a landmark diagnostic imaging modality of modern medicine. Technological advances have been crucial to the success of CT imaging, as they have increasingly enabled improvements in image quality and diagnostic value at increasing radiation dose efficiency. With recent advances in engineering and physics, a novel technology has emerged with the potential to surpass several shortcomings and limitations of current CT systems. Photon-counting detector (PCD)-CT might substantially improve and expand the applicability of CT imaging by offering intrinsic spectral capabilities, increased spatial resolution, reduced electronic noise and improved image contrast. In this review we sought to summarize the first clinical experience of PCD-CT. We focused on most recent prototype and first clinically approved PCD-CT systems thereby reviewing initial publications and presenting corresponding clinical cases.

INTRODUCTION

X-ray CT has emerged as a landmark diagnostic imaging modality of modern medicine since its development in the 1970's. The benefits and clinical demand for CT imaging continue to rise due to continued technical advancements facilitating improvements in image quality and diagnostic value at constantly higher radiation dose efficiency, together with broadening of the clinical indications.[1–4]

The X-ray detector constitutes a decisive component of a CT system that critically influences image quality and dose efficiency. Accordingly, the detector design has undergone radical transformations and improvements. Currently, most available CT systems use solid-state energy-integrating detectors (EIDs) with third-generation rotate–rotate designs to convert X-rays to electrical signals. The indirect conversion technology of EIDs is based on a scintillator layer converting X-ray photons to visible light, which is then detected by a photodiode layer and converted into an electric output signal that is proportional to the total energy deposited during a measurement interval.[4–8] As the detector element integrates the energy from all photons, the output electrical signal does not convey any information on the energy of individual photons. Ultimately, in a substrate layer the generated signal is transmitted to analog electronics for amplification.[6,9]

Despite its continuous merits, EIDs exhibit some inherent limitations. First, the detector design and more importantly the detector element size of current CT systems limits its maximum achievable spatial resolution. The maximum achievable spatial resolution of a CT system depends on both the size of the focal spot of the X-ray tube and the size of the detector elements—both must be matched and approximately equal. The spatial resolution as a function of the spatial frequency (in line pairs per cm) is described by the so-called modulation transfer function (MTF) and shows the relative contrast with which small periodic structures are represented in the image. The MTF can be modified by choosing different convolution kernels, but in doing so, the resolution limit of the measurement system cannot be exceeded. The ultimate resolution limit is reached at a spatial frequency equal to 1/(2*pixel size) (Nyquist theorem)—so detectors must be made smaller to improve spatial resolution. This is a problem for EID detectors, because the individual elements have to be separated by thin septa to avoid

optical cross-talk. With smaller detector elements, more area is occupied by the optically isolating septa, which absorb X-rays without contributing to the detector signal, resulting in lower dose efficiency.[5,7,10] Second, electronic readout noise stemming from the analog electronic circuits remains a problem of EIDs. In case of high photon flux on the detector, the effect of electronic readout noise on image quality is negligible. At low to very low radiation doses, however, the number of detectable photons is low and electronic readout noise may become apparent thus degrading image quality.[6] Third, each photon contributes to the total input detector signal with an amount that is proportional to its own energy. Thus, the relative contribution of high-energy photons to the total signal is higher than that of low-energy photons. This underweighting of low-energy photons can be suboptimal as low contrast differences are most prominent at low X-ray energies. Contrast-enhanced CT scans in particular show suboptimal iodine contrast.[5,6] Fourth, most current high-end CT systems offer dual-energy (DE) applications. DECT enables functional imaging by exploiting material-specific differences in X-ray attenuation at different X-ray energies.[11,12] DECT data can be generated by means of various technologies including dual-source (DS), rapid kV switching, and dual-layer (DL) detector technology. However, each of these technologies has its specific set of inherent limitations such as imperfect spatial or temporal registration of data sets, field of view (FOV) restrictions and limitations in terms of tube voltage selection and the use of tube current modulation. Furthermore, for most of these technologies, DECT data are only available if a specific workflow has been selected prior to image acquisition.[13]

With recent advances in engineering and physics, a novel technology has emerged with the potential to surpass many of the shortcomings and limitations of current CT systems. Photon-counting detector (PCD-) CT is a promising technology that might substantially improve and expand the applicability of CT imaging.

In this review, we want to summarize the basic technical features and the initial experience with PCD-CT by reviewing first publications with prototype and clinical systems and try to illustrate with case examples how this emerging technology may translate into improved clinical diagnostics.

PHOTON-COUNTING DETECTOR CT

Detailed reviews about the technical principles of PCD-CT systems have been published elsewhere.[5–7,10] Therefore, we will not provide too much detail on these aspects but will rather focus on basic specifications and the first experience with the new technology.

Basic physical principles of the detector

PCDs differ considerably from EIDs. In contrast to EIDs, which require a separate scintillator layer to convert X-rays to light, PCDs use a single layer of a semi-conductor made of cadmium telluride (CdTe), cadmium zinc telluride (CZT), or silicon. A large bias voltage is applied between a cathode on top of and pixelated anodes at the bottom of the semi-conductor. Each incident X-ray photon produces a cloud of positive and negative charges which are separated in the strong electric field and pulled away from each other rapidly. The electrons move towards the anodes to generate an electric signal that is registered by an attached electronic readout circuit. Thus, with PCDs X-ray photons are directly converted into an electrical signal and each photon leads to an electrical pulse whose amplitude is directly proportional to the energy of the photon. The PCD then counts the number of pulses to quantify the number of incident X-ray photons and compares the amplitude of each pulse to several pre-set threshold levels that are set by means of multiple electronic comparators and counters. Specifically, an initial threshold is set at a level that is higher than the electronic noise level but lower than the pulses of incident photons (*e.g.* at 25 keV). Furthermore, as all pulses are additionally compared to further threshold levels, photons can be assigned to energy bins depending on their energy.[5–7,10]

The detector design of PCDs relying on a direct conversion technology overcomes the above-mentioned issues of EIDs. First, by eliminating the scintillator material and consequently the optically isolating septa, the detector elements of PCDs can be made much smaller, thus offering improved spatial resolution. Second, by thresholding incoming photons according to their energies, electronic noise can be eliminated and spectral (*i.e.* dual- or multienergy) imaging becomes inherently available. Third, as the detective quantum efficiency (DQE) of a photon counting detector is approximately constant as a function of X-ray energy,[5] there is no underweighting of low-energy X-ray photons as with EIDs, and image contrasts can be improved.[5,6] In a practical detector design, the thickness of the semi-conductor layer of a PCD has to be chosen large enough to provide a total DQE similar to EIDs. Thin layers of about 1.4–2 mm are sufficient for CdTe or CZT because of their high atomic number. Si with its low atomic number and low absorption efficiency in the X-ray energy range relevant to medical CT requires thick layers >30 mm.[5,6] Still, the exact total DQE strongly depends on the detector design.

Temporal evolution

Computational power

Until recently, the use of PCDs has mainly been limited to nuclear imaging as the X-ray photon-count rate in CT imaging is much higher than in nuclear medicine.[14] Specifically, the PCD has to register each incoming X-ray photon before the next one arrives. If the PCD does not manage this, a pile-up occurs where the photons can no longer be separately registered and the count rate is no longer proportional to the X-ray flux, leading to image quality degradation. A further challenge concerns the cross-talk between detector elements. X-ray photons hitting the detector close to the border of a detector element produce charge clouds that spread out and may be wrongfully registered by more than one detector element. This results in a loss of spatial resolution and spectral separation. By implementing faster readout electronics, smaller pixel sizes, subdivided detector elements, and optimized electronic circuits that can detect coincidental registration of photons, these hurdles were recently overcome, making industrial production of PCD-CT possible.[5,6,10]

Figure 1. 63-year-old male patient (body weight 77 kg) with multifocal hepatocellular carcinoma. Contrast-enhanced abdominal portal venous phase scans were acquired on a clinical PCD-CT system (NAEOTOM Alpha, Siemens Healthineers) in the spectral imaging mode at 120 kV with a tube current of 86 mAs. The $CTDI_{vol}$ was 6.7 mGy. Virtual monoenergetic images at 60 keV were reconstructed with a 2 mm slice thickness without Quantum Iterative Reconstruction and with all strength levels of QIR (QIR 1–4). $CTDI_{vol}$, volume of CT dose index; PCD, Photon-counting detector; QIR, Quantum Iterative Reconstruction

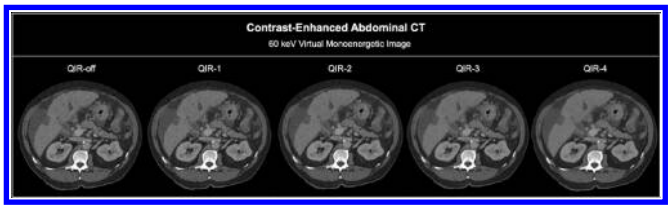

PCD-CT systems

A series of prototype PCD-CT systems enabled pre-clinical research but were all limited in one way or another. One prototype system was a whole-body research PCD-CT system built (SOMATOM Count, Siemens Healthineers, Forchheim, Germany) using a modified DS CT platform (SOMATOM Definition Flash, Siemens Healthineers), with the B-subsystem equipped with a CdTe PCD array. 2 × 2 subpixels of the photon counting detector can be binned to a "sharp pixel" or "ultra-high resolution (UHR) pixel" with a pixel size of 0.45 × 0.45 mm^2 (0.25 × 0.25 mm^2 at the isocenter), 4 × 4 subpixels can be binned to a "MACRO pixel" with a size of 0.9 × 0.9 mm^2 (0.5 × 0.2 mm^2 at the isocenter) comparable to today's medical CT systems. A detailed description of this system can be found elsewhere.[5,15–20] The main limitations of this scanner included a detector z-coverage of 8–16 mm depending on the acquisition mode, an in-plane FOV of the PCD array of 27.5 cm at the isocenter, and a lack of angular tube current modulation (for comparison: a conventional SOMATOM Definition Flash scanner has a detector z-coverage of 38.4 mm and a maximum in-plane FOV of 50 cm[21]). In addition, due to the hybrid design, DS PCD scanning at high temporal resolution was not possible. Later, a further investigational whole-body full FOV single-source PCD-CT system (SOMATOM Count Plus, Siemens Healthineers, Forchheim, Germany) was developed thereby overcoming most of the key limitations of the hybrid DS scanner by offering a 50 cm scan FOV, 57.6 mm longitudinal detector coverage as well as automatic exposure control in both angular and longitudinal directions.[22] Recently, another prototype single-source CT scanner with a full FOV silicon-based PCD (modification of a commercial Lightspeed VCT scanner, GE Healthcare, Chicago, Illinois, USA) was presented with a phantom study.[23] Another, further advanced PCD-CT prototype system based on a CZT detector (modified Brilliance iCT scanner, Philips Healthcare) and capable of human imaging was recently developed.[24,25] This system enables cardiac imaging on a level and beyond the technical performance of a comparable EID-CT system.[24,26] This prototype relies on a single-layer of energy-sensitive PCDs of 2 mm thick CZT with five adaptable energy thresholds set at 30, 51, 62, 72 and 81 keV and a detector element size of 0.27 × 0.27 mm^2 at the isocenter. An in-plane FOV of 50 cm and a z-coverage of 1.76 cm (64 × 0.275 mm at the isocenter) is offered. Tube voltage can be set at 80, 100, 120 or 140 kV, and tube current can be modulated between 10 and 500 mAs. The system has a focal spot of 0.6 × 0.7 mm and a gantry rotation time of 0.33–1 s for 2400 projections per rotation.

Importantly, however, a PCD-CT system has recently been cleared for clinical use (NAEOTOM Alpha; Siemens Healthineers/ FDA approval September 30, 2021). A detailed description of this CT system has been published recently.[8] In brief, this scanner exhibits a DS geometry with a minimum gantry rotation time of 0.25 s offering a temporal resolution of 66 ms. The system uses two dedicated PCDs with 1.6 mm thick CdTe. Each detector element has a size of 0.151 × 0.176 mm^2 projected to the isocenter. The detector pixels can be read out either independently, thus allowing for UHR imaging with a z-coverage of 24 mm (120 × 0.2 mm at the isocenter) or can be binned into 2 × 2 groups (resulting pixel size 0.302 × 0.352 mm^2 at the isocenter) for standard imaging with a z-coverage of 57.6 mm (144 × 0.4 mm at the isocenter). Scans acquired in the spectral mode use fixed energy bin thresholds of 20/35/55/70 keV and offer full spectral image information. The system is equipped with two Vectron tubes each with 120 kW power output. To match the spatial resolution of the detector, the Vectron tubes offer several focal spots with dimensions down to 0.4 mm x 0.4 mm^2 (0.181 × 0.181 mm^2 at the isocenter) for UHR scanning.

Images can be reconstructed with a range of slice thicknesses as low as 0.2 mm depending on the protocol and with various matrix sizes (512 × 512, 768 × 768, 1024 × 1024).[8,22,27] A novel iterative reconstruction (IR) algorithm named Quantum Iterative Reconstruction (QIR) that is suitable for the reconstruction of spectral imaging data[28] has been introduced. As with previous IR algorithms, higher strength levels lead to greater noise reductions.[27,28] A representative image example illustrating the performance of the novel IR algorithm is provided in Figure 1.

TRANSLATING THE BENEFITS OF PCD-CT INTO CLINICAL ROUTINE

Improved spatial resolution without dose penalty

The lack of a scintillator layer and the use of subdivided detectors in a PCD enables dose-efficient UHR imaging. A range of technological approaches have previously enabled UHR imaging for EID-CT including the use of very small detector element sizes or the implementation of comb filters to reduce detector aperture in the z-axis and/or in-plane. All these approaches, however, were associated with manufacturing difficulties or reduced dose efficiency of up to 50%.[27,29,30]

The detector design of the current PCD-CT systems bypass these difficulties, by exhibiting a 125 µm limiting (4.00 lp/mm) (NAEOTOM Alpha, Siemens Healthineers)[8] to 178 µm limiting (2.81 lp/mm) (Philips Healthcare prototype) in-plane spatial resolution.[24,25] The limiting spatial resolution is defined as the spatial frequency at 0% MTF for the sharpest convolution kernel available at the CT system. For comparison, the limiting spatial

Figure 2. 65-year-old male patient (body weight 94 kg) with calcified coronary plaques in the left main and left anterior descending coronary artery with an Agatston Score of 245. Coronary CTA images were acquired in the UHR mode (z-coverage of 24 mm) on a clinical dual source PCD-CT system (NAEOTOM Alpha, Siemens Healthineers) at 120 kV with a tube current of 61 mAs. The gantry rotation time was 0.25 s, with a temporal resolution of 66 ms. The $CTDI_{vol}$ was 46.3 mGy. Images at different slice thicknesses and kernels were reconstructed. Note the improved sharpness of anatomical structures, vessels, and calcified coronary plaques on UHR images reconstructed with the Bv64 kernel and 0.2 mm section thickness. CTA, CT angiography; $CTDI_{vol}$, volume of CT dose index; PCD, Photon-counting detector; UHR, ultra-high resolution.

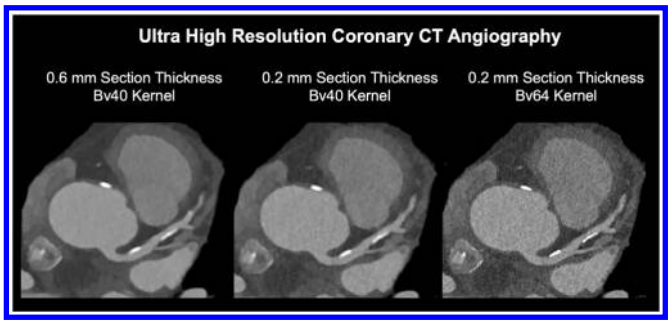

resolution of a comparable EID system (SOMATOM Force, Siemens Healthineers) is 240 µm (2.08 lp/mm).

Based on the UHR mode of a prototype PCD-CT system with 150 µm limiting spatial resolution (3.33 lp/mm) (SOMATOM Count) , Leng et al were able to show that the UHR mode with a pixel size of 0.25 × 0.25 mm^2 at the isocenter exhibited a 87% improvement in spatial resolution (10% MTF) using the sharpest available convolution kernel as compared to the so-called MACRO scan mode of the same system with 0.5 × 0.5 mm^2 pixel size (*i.e.* standard-resolution PCD-CT) comparable to today's medical CT systems. Alternatively, a 15% reduction in image noise could be achieved at the same in-plane spatial resolution (sharpest kernel available in the MACRO mode) for scans acquired with the UHR scan mode as compared to the MACRO scan mode.[6,15] Klein et al and Pourmorteza et al confirmed that the UHR mode achieves lower noise levels than the standard MACRO mode at comparable spatial resolution because detector cell binning is avoided. This further highlights the high dose efficiency of the PCD-CT UHR mode.[18,31]

Importantly, using dedicated phantom experiments, cadaveric and patient scans, both Leng et al[15,32] and Zhou et al[33] provided evidence that the UHR PCD-CT mode outperforms the comb-filter UHR EID-CT mode when using comparable imaging and reconstruction parameters. The latter study even demonstrated 40% less noise for PCD-CT UHR-based temporal bone imaging as compared to comb-filter UHR EID-CT imaging at matching radiation doses and reconstruction settings.[33]

A variety of further studies have been published on HR and UHR PCD-CT imaging highlighting its value for lung assessment,[15,25,27,34–39] cardiac imaging[20,24,40–44] and musculoskeletal applications.[19,33,45–48]

UHR imaging is of particular interest for these anatomical areas because the clear depiction of fine details may effectively enhance diagnostic accuracy. In case of lung imaging, fine parenchymal changes may be better detected, delineated and characterized.[15,36–38] Inoue et al scanned 30 patients with suspicion of interstitial lung disease on a research PCD-CT system in the UHR mode with optimized reconstruction settings and on standard-of-care EID-CT systems. PCD-CT improved reader's confidence for the presence of imaging findings of reticulation, ground-glass opacities, and mosaic pattern as determined by three thoracic radiologists. Furthermore, reader confidence in the probability of usual interstitial pneumonia increased for one of the three thoracic radiologists. Lastly, overall image quality and sharpness of PCD-CT images was deemed improved despite the slightly lower radiation dose (median CTDIvol of 6.49 mGy for PCD-CT *vs* 7.88 mGy for EID-CT).[38] A further clinical study with 80 systemic sclerosis patients showed that the UHR mode of the first clinical PCD-CT system maintains image quality and diagnostic accuracy for the assessment of interstitial lung disease at only 33% of the dose of comparable EID-CT scans performed on a third generation (*i.e.* latest generation) DS EID-CT scanner.[39]

In regard to coronary artery imaging, plaque visualization and stent imaging can be improved.[24,40] Two recent studies assessing the UHR scan mode of clinical PCD-CT in patients referred for coronary CT angiography have shown that coronary arteries can be visualized in excellent quality with improved visualization of non-calcified plaque components and with reduced blooming of calcified plaques.[43,44] For bone imaging, fine bone details and previously occult hairline fractures may become apparent.[33,46,49,50]

In a clinical feasibility study including 32 patients who underwent both UHR PCD-CT imaging on a prototype CT system with optimized reconstruction settings and standard-of-care EID-CT imaging, Baffour et al reported improved visualization of osseous structures of the pelvis and shoulder for UHR PCD-CT imaging at a 31–47% lower radiation dose. A further study on 29 multiple myeloma patients showed that the visualization of lytic bone lesions, medullary lesions and fat attenuation in myeloma lesions could significantly be improved with a clinical PCD-CT in the UHR mode as compared to standard-of-care EID-CT systems with matching reconstruction parameters and radiation dose.[51] Further clinical studies will demonstrate whether or not the improvements in anatomic display will also impact on therapeutic management and ultimately, on patient outcome.[52]

Representative PCD-CT cases scanned with the UHR mode illustrating the benefits for coronary CT angiography and upper ankle joint imaging can be found in Figures 2–3.

Improved CNR and noise properties

Improved contrast-to-noise ratio (CNR) and noise performance stemming from factors such as lack of electronic noise or equal

Figure 3. 32-year-old male patient (body weight 64 kg) presenting with a depression fracture of the talus. The fracture gap extends to the lateral part of the talus. Images were acquired in the UHR mode (z-coverage of 24 mm) on a clinical PCD-CT system (NAEOTOM Alpha, Siemens Healthineers) at 120 kV and with a tube current of 40 mAs. Radiation dose was 3.23 mGy $CTDI_{vol}$. Images were reconstructed with a Br56 kernel, 2 mm section thickness and a 512 × 512 matrix size, with a Qr68 kernel, 1 mm section thickness and a 512 × 512 matrix size and with a sharp Qr72 kernel, 0.2 mm section thickness (UHR image) and 1024 × 1024 matrix size. The left image represents the default setting for bone imaging, while the right image leverages the potential of PCD-CT UHR imaging. Note the excellent visualization of bone features and trabeculae and the exquisite delineation of the small fracture gap. $CTDI_{vol}$, volume of CT dose index; PCD, Photon-counting detector; UHR, ultra-high resolution.

weighting of all X-ray photons (no underweighting of low energy photons) are a key feature of PCD-CT systems enabling radiation and contrast media dose reduction for routine clinical imaging.[53]

Using the first clinical PCD-CT system, Liu et al quantified the ability of PCD-CT to eliminate electronic background noise, with it achieving mean percent noise reductions of up to 74% at a radiation dose level of 0.4 mGy $CTDI_{vol}$ compared to a third generation (*i.e.* latest generation) DS EID-CT system.[54] Rajagopal et al investigated the technical performance of a prototype PCD-CT system for low dose abdominal CT imaging in a phantom[55] and found that both for PCD-CT and EID-CT spatial resolution as a function of noise and contrast remained unaffected by dose while PCD-CT achieved a 22–24% improvement in noise across four radiation dose levels ranging from 1.7 to 6 mGy $CTDI_{vol}$. Consequently, this improved noise performance could be translated to a 29–41% improvement in CNR and a 20–36% improvement in detectability index. Using the first clinical PCD-CT, Racine et al confirmed that PCD-CT outperforms third generation (*i.e.* latest generation) DS EID-CT for the detection of hypo- and hyperattenuating focal liver lesions across a wide range of radiation dose levels.[56] Gutjahr et al showed that iodine CNR was improved by 11–38% for a prototype PCD-CT system relative to EID-CT at matching scan and tube voltage settings of 80–140 kV.[21] This was further confirmed by Sawall et al who showed that with a prototype PCD-CT, dose-normalized iodine CNR could be improved by up to 37% relative to EID-CT, thus potentially enabling a radiation dose reduction of up to 46%.[57] More recently, Booij et al investigated the iodine CNR benefits of the first clinical PCD-CT on VMI relative to a third generation (*i.e.* latest generation) DS EID-CT system run in DE mode with largely matching imaging and reconstruction settings. The authors confirmed that the CNR benefits of PCD-CT were also applicable for VMI, with low keV images below 60 keV exhibiting a 55–75% higher CNR than their EID-CT based counterparts depending on the tube voltage settings.[58]

Further experiments on sinus and temporal bone imaging with a prototype PCD-CT have shown significant radiation dose reductions between 56 and 85% relative to EID-CT depending on the exact imaging protocol without compromising image contrast and image noise.[19] Specifically, experiments were performed using an UHR PCD-CT mode with an additional tin (Sn) filter at 100 kV tube voltage. Besides the use of the tin filter, the authors also cite the advantages of the UHR PCD-CT mode with better intrinsic detector resolution and the detector design of PC detectors that eliminates the need for comb/grid filters for UHR imaging as reasons for the improved performance of the PCD-CT system. More recent studies performed on the first clinical PCD-CT system support these previous results, with two experimental studies showing that the clinical PCD-CT outperforms third generation (*i.e.* latest generation) DS EID-CT systems across a variety of widely matching protocol parameters, reconstruction settings and radiation dose levels in terms of objective and subjective image quality.[59,60]

The improved performance of PCD-CT was also confirmed *in-vivo* in a variety of clinical studies. Exemplarily, Symons et al showed that a prototype PCD-CT exhibited between 15 and 17% lower noise than EID-CT for 120 kV and 100 kV dose-matched chest CT scans.[61] Importantly, low dose PCD-CT imaging of the lungs was also associated with improved HU stability relative to EID-CT.[62] Specifically, across tube voltage settings of 80, 100 and 120 kV, attenuation values of lung equivalent foams of a dedicated phantom as measured on PCD-CT remained stable while the attenuation values of EID-CT decreased by up to approximately 5 HU when decreasing the dose level from 3 to 0.75 mGy $CTDI_{vol}$.

Pourmorteza et al demonstrated improved image quality of a prototype PCD-CT for brain imaging relative to EID-CT exhibiting 12.8–20.6% less image noise and 15.7–33.3% improved soft-tissue CNR.[63] Lastly, in a combined phantom and *in-vivo* study Symons et al demonstrated improved coronary artery calcium scoring (CACS) accuracy at low radiation doses for PCD-CT relative to EID-CT owing to the improved noise and CNR properties of PCD-CT.[64] The improved detection and quantification accuracy of CACS at low radiation doses was later confirmed by van der Werf et al using a different PCD-CT concept.[65]

Recently, two patient studies have been published on the performance of clinical PCD-CT operated at 120 kV compared to EID-CT scans performed on a third generation (*i.e.* latest generation) DS EID-CT scanner with automated tube voltage selection. These were intraindividual comparison studies in whom the

Figure 4. 47-year-old male patient (body weight 85 kg) with COVID-19-associated pneumonia presenting with ground-glass opacities and mild reticular abnormalities. Non-enhanced chest CT was acquired on a clinical PCD-CT system (NAEOTOM Alpha, Siemens Healthineers) in the UHR mode at 120 kV; the $CTDI_{vol}$ was 0.55 mGy. $CTDI_{vol}$, volume of CT dose index; PCD, Photon-counting detector; UHR, ultra-high resolution.

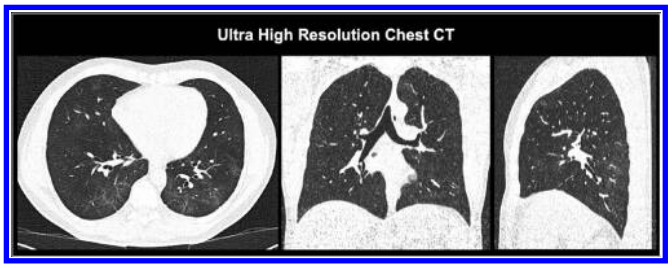

same patients underwent scans both with PCD-CT and EID-CT within a relatively short time period. For abdominal CT, 50 keV VMI reconstructions of PCD-CT exhibited higher vascular and parenchymal CNR than polychromatic EID-CT reconstructions at similar subjective image quality.[66] For high-pitch CT angiography of the aorta, 45 keV VMI reconstructions of PCD-CT showed improved vascular CNR and similar subjective image quality as compared to polychromatic EID-CT reconstructions.[67]

In a recent study, Higashigaito et al could show that CT angiography of the aorta using PCD-CT and administering 20% reduced contrast media volume provides non-inferior image

Figure 5. 82-year-old male patient (body weight 81 kg) undergoing CTA for follow-up after endovascular treatment of an abdominal aortic aneurysm. Images were acquired on a third generation dual-source EID-CT system (SOMATOM Force, Siemens Healthineers) with automated tube voltage selection (80 kV) and CTA with a clinical dual-source PCD-CT system (NAEOTOM Alpha, Siemens Healthineers) (120 kV) at matched radiation dose ($CTDI_{vol}$ 6.1 mGy) and using the same contrast media protocol. Note the reduced noise and improved contrast on PCD-CT images. CTA, CT angiography; $CTDI_{vol}$, volume of CT dose index; PCD, Photon-counting detector; EID, energy-integrating detector; PCD, Photon-counting detector.

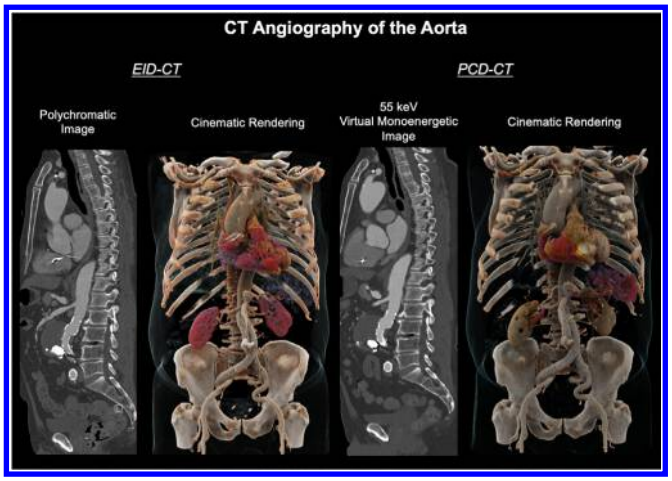

Figure 6. 71-year-old female patient (body weight 75 kg) with a cyst in liver segment VII. Contrast-enhanced abdominal portal venous phase images were acquired on a third generation dual-source EID-CT system (SOMATOM Force, Siemens Healthineers) with automatic tube voltage selection (120 kV) and with a clinical PCD-CT system (NAEOTOM Alpha, Siemens Healthineers) in the spectral imaging mode at 120 kV at matched radiation dose ($CTDI_{vol}$ 7.24 mGy) and using the same contrast media protocol. Note the improved iodine contrast and lesion conspicuity on PCD-CT images. $CTDI_{vol}$, volume of CT dose index; EID, energy-integrating detector; PCD, Photon-counting detector.

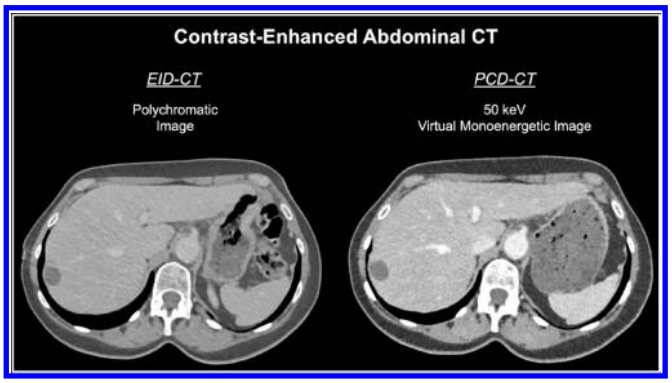

quality compared to CT angiography of the aorta using EID-CT in the same patients and at matched radiation dose.[53]

Representative images of patient studies illustrating the improved noise and CNR characteristics of PCD-CT are shown in Figures 4–6.

Intrinsic spectral capabilities

A key feature of PCD-CT is its ability to provide spectral information from every scan due to the detector being able to count

Figure 7. 67-year-old male patient (body weight 71 kg) with atypical chest pain. Coronary CTA was performed on a clinical dual source PCD-CT system (NAEOTOM Alpha, Siemens Healthineers) at 120 kV ($CTDI_{vol}$ 10.1 mGy). Virtual monoenergetic images at 55 keV and VNCa images using a novel vascular calcium removal algorithm (PureLumen) were generated. A calcified plaque can be seen in the distal right coronary artery, which is subtracted on a dual-energy basis in the VNCa (PureLumen) images. CTA, CT angiography; $CTDI_{vol}$, volume of CT dose index; PCD, Photon-counting detector; VNCa, virtual non-calcium.

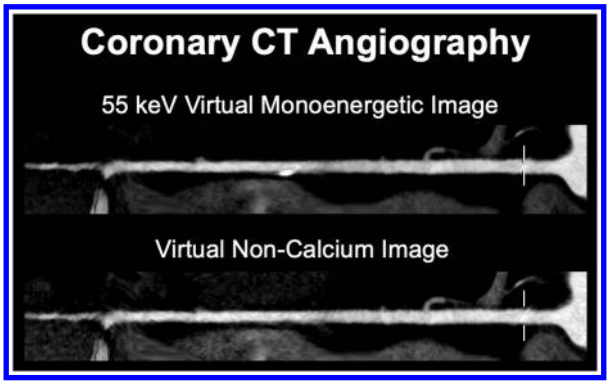

Figure 8. 54-year-old male patient (body weight 76 kg) with hepatocellular carcinoma and vascular invasion. Late arterial scans were performed with a clinical PCD-CT (NAEOTOM Alpha, Siemens Healthineers) in the spectral mode with reconstruction of virtual monoenergetic images at 70 keV, virtual non-contrast images, and iodine maps from a single acquisition ($CTDI_{vol}$3.6 mGy). Although tumor enhancement is seen also on the monoenergetic images, the iodine maps allow for a better appreciation of the carcinoma along with the possibility of quantification of iodine uptake. $CTDI_{vol}$, volume of CT dose index; PCD, Photon-counting detector.

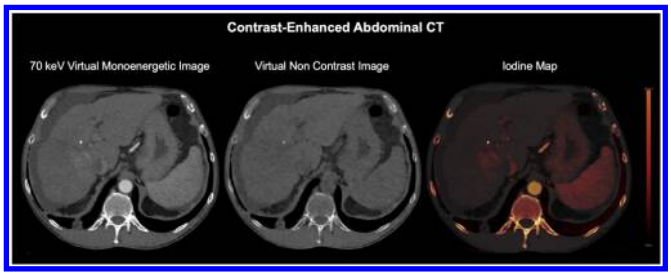

and characterize individual photons according to their energy. In contrast, most EID-CT systems require the user to choose between single-energy or DE scan modes prior to image acquisition. The intrinsic spectral capabilities of the first clinical DS PCD-CT system with 0.25 s rotation time allows for multienergy imaging at 66 ms temporal resolution and high pitch multienergy imaging with helical pitch values up to 3.2. When implemented as an ECG-triggered high-pitch scan mode for cardiac imaging, the latter may enable radiation dose reductions of up to a factor of 2 as compared to other DSCT scan techniques such as ECG-triggered sequential step-and-shoot and ECG-gated spiral with X-ray pulsing.[8,67,68]

Currently, ECG-gated UHR imaging represents an exception to this rule: due to the vast amount of image information that has to be processed, spectral image information is not yet available for this imaging mode on the first clinical DS PCD-CT system. However, additional updates to the scanner's soft- and hardware should be able to fix the problem in the near future.

The spectral capabilities of PCD-CT allow the user to reconstruct iodine maps, virtual non-contrast (VNC) and virtual monoenergetic images (VMIs) from every acquisition. The use of VMI for routine clinical PCD-CT imaging has exemplarily been shown for abdominal imaging,[28,66] cardiac CT[69–71] and coronary calcium quantification,[72] high-pitch CT angiography of the aorta,[67] lung[35,73] and brain imaging.[74] The benefits of low keV VMI include better visualization of small low-contrast structures and increased iodine signal. For CT angiography examinations, the latter may be particularly promising as high pitch CTA together with low keV VMI may set new standards in terms of radiation and contrast media dose reductions.[8,53]

Concerning VNC images and iodine maps, Rajendran et al[8] and Sartoretti et al[75] have demonstrated the feasibility of reconstructing these images from routine clinical PCD-CT scans. Quantitative accuracy of reconstructions was high with VNC showing mean absolute errors of 4 HU[75] and iodine maps exhibiting a root mean squared error of 0.5 mg/cm^3 for iodine concentration.[8] For VNC imaging, the high quantitative accuracy was later further confirmed in a larger clinical study encompassing 100 patients who underwent a triphasic examination on the first clinical PCD-CT system. Attenuation errors of VNC images were less than 5 HU in 76% and less than 10 HU in 95% of measurements compared with true non-contrast images across a variety of abdominal organs and regions. Furthermore, diagnostic image quality of VNC images as determined by two independent readers was achieved in 99 and 100% of cases, respectively.[76]

The clinical benefits of the routine availability of VNC images and iodine maps from PCD-CT include, among others, emphysema quantification from VNC images,[77] assessment of adrenal adenomas from VNC images,[78] anemia detection and quantification from VNC images[79] and myocardial extracellular volume quantification based on iodine maps from a single cardiac late enhancement scan.[70]

Beyond the opportunities discussed above, PCD-CT harbors further potential in terms of improved and novel spectral imaging applications. The spectral data allow for the reconstruction of further spectral images such as calcium-only or virtual non-calcium (VNCa) images. In this regard, a novel vascular calcium removal algorithm has been recently introduced that aims to surpass the performance of previous similar algorithms designed for DECT capable EID-CT systems.[80] With this novel algorithm, high quality VNCa images can be reconstructed thus counteracting the problem of blooming artifacts from heavily calcified plaques on standard monoenergetic or polychromatic images.[81] A representative image example illustrating the performance of the novel algorithm for high quality VNCa imaging is provided in Figure 7.

With PCD-CT, improved material decomposition can potentially be achieved, as the selection of energy thresholds can be tailored towards the spectral behavior of the materials that are to be separated. For example, by selecting optimized energy

Figure 9. 59-year-old male patient (body weight 81 kg) with chronic occlusion of the right pulmonary artery and partial occlusion of left pulmonary artery branches resulting in severely reduced perfusion of the right and, to a lesser extent, of the left lung. Axial and coronal thick maximum intensity projection images and coronal PBV map computed from a routine contrast-enhanced chest CT scan acquired on a clinical PCD-CT (NAEOTOM Alpha, Siemens Healthineers) at 120 kV ($CTDI_{vol}$ 2.37 mGy) illustrate both the anatomical and functional situation in the lungs. $CTDI_{vol}$, volume of CT dose index; PBV, perfused blood volume; PCD, Photon-counting detector.

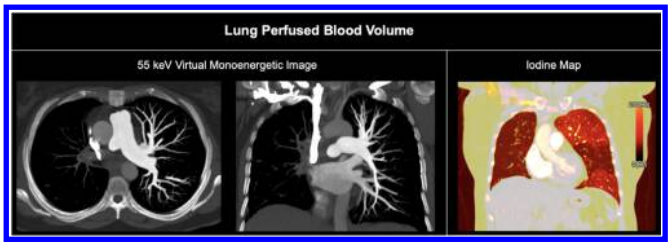

thresholds high quality VNCa and contrast media maps could be computed from coronary and carotid CTA images acquired with a range of contrast media including iodine and experimental contrast media such as bismuth, tungsten, holmium or hafnium.[82,83] Furthermore, the energy threshold capabilities of PCDs can theoretically also be leveraged for improved simultaneous dual-contrast agent imaging as shown in experimental studies[84–87] or to further reduce metal artifact burden.[88,89]

Although the latter applications are still in the preclinical phase of testing, PCD-CT opens up a range of new opportunities that may inspire a new momentum for clinical CT imaging.

Representative image examples highlighting the applications discussed above are provided in Figures 8–9.

CONCLUSION

In this review, we aimed to summarize basic technical principles and potential advantages of PCD-CT. Potential clinical benefits as evidenced by recent publications with this technology are outlined and representative clinical cases from our experience were added to illustrate the added value of the technique.

While the current possibilities of PCD-CT already considerably enhance our diagnostic capabilities, we foresee developments with spectrally optimized contrast media in combination with adaptable energy threshold imaging to enter clinical CT imaging in the near future.

AUTHOR CONTRIBUTIONS

T. S. and H. A. reviewed the literature. T. S., J. W., T. F. and H. A. wrote the paper. All coauthors contributed constructively to the manuscript.

FUNDING

JW: Institutional grants via Clinical Trial Center Maastricht: Bard, Bayer, Boston, Brainlab, GE, Philips, Siemens; Speaker's bureau via Maastricht UMC+: Bayer, Siemens HA: Institutional grants: Bayer, Guerbet, Siemens, Canon; Speaker´s bureau: Siemens TF: Employee of Siemens Healthineers, Forchheim, Germany. Open access funding provided by Universitat Zurich.

REFERENCES

1. Smith-Bindman R, Kwan ML, Marlow EC, Theis MK, Bolch W, Cheng SY, et al. Trends in use of medical imaging in US health care systems and in Ontario, Canada, 2000-2016. *JAMA* 2019; **322**: 843–56. https://doi.org/10.1001/jama.2019.11456
2. Alkadhi H, Euler A. The future of computed tomography: personalized, functional, and precise. *Invest Radiol* 2020; **55**: 545–55. https://doi.org/10.1097/RLI.0000000000000668
3. Wildberger JE, Prokop M. Hounsfield's legacy. *Invest Radiol* 2020; **55**: 556–58. https://doi.org/10.1097/RLI.0000000000000680
4. Lell MM, Wildberger JE, Alkadhi H, Damilakis J, Kachelriess M. Evolution in computed tomography: the battle for speed and dose. *Invest Radiol* 2015; **50**: 629–44. https://doi.org/10.1097/RLI.0000000000000172
5. Flohr T, Petersilka M, Henning A, Ulzheimer S, Ferda J, Schmidt B. Photon-Counting CT review. *Phys Med* 2020; **79**: S1120-1797(20)30273-8: 126–36: . https://doi.org/10.1016/j.ejmp.2020.10.030
6. Leng S, Bruesewitz M, Tao S, Rajendran K, Halaweish AF, Campeau NG, et al. Photon-Counting detector CT: system design and clinical applications of an emerging technology. *Radiographics* 2019; **39**: 729–43. https://doi.org/10.1148/rg.2019180115
7. Willemink MJ, Persson M, Pourmorteza A, Pelc NJ, Fleischmann D. Photon-Counting CT: technical principles and clinical prospects. *Radiology* 2018; **289**: 293–312. https://doi.org/10.1148/radiol.2018172656
8. Rajendran K, Petersilka M, Henning A, Shanblatt ER, Schmidt B, Flohr TG, et al. First clinical photon-counting detector CT system: technical evaluation. *Radiology* 2022; **303**: 130–38. https://doi.org/10.1148/radiol.212579
9. Shefer E, Altman A, Behling R, Goshen R, Gregorian L, Roterman Y, et al. State of the art of CT detectors and sources: a literature review. *Curr Radiol Rep* 2013; **1**: 76–91. https://doi.org/10.1007/s40134-012-0006-4
10. Sandfort V, Persson M, Pourmorteza A, Noël PB, Fleischmann D, Willemink MJ. Spectral photon-counting CT in cardiovascular imaging. *J Cardiovasc Comput Tomogr* 2021; **15**: S1934-5925(20)30503-7: 218–25: . https://doi.org/10.1016/j.jcct.2020.12.005
11. Postma AA, Das M, Stadler AAR, Wildberger JE. Dual-Energy CT: what the neuroradiologist should know. *Curr Radiol Rep* 2015; **3**: 16: 16: . https://doi.org/10.1007/s40134-015-0097-9
12. Roele ED, Timmer VCML, Vaassen LAA, van Kroonenburgh AMJL, Postma AA. Dual-Energy CT in head and neck imaging. *Curr Radiol Rep* 2017; **5**: 19: 19: . https://doi.org/10.1007/s40134-017-0213-0
13. Rajiah P, Parakh A, Kay F, Baruah D, Kambadakone AR, Leng S. Update on multienergy CT: physics, principles, and applications. *Radiographics* 2020; **40**: 1284–1308. https://doi.org/10.1148/rg.2020200038
14. Taguchi K, Iwanczyk JS. Vision 20/20: Single photon counting x-ray detectors in medical imaging: Vision 20/20: Photon counting detectors. Med Phys 2013;40:100901. https://doi.org/10.1118/1.4820371
15. Leng S, Rajendran K, Gong H, Zhou W, Halaweish AF, Henning A, et al. 150-µm spatial resolution using photon-counting detector computed tomography technology: technical performance and first patient images. *Invest Radiol* 2018; **53**: 655–62. https://doi.org/10.1097/RLI.0000000000000488
16. Yu Z, Leng S, Jorgensen SM, Li Z, Gutjahr R, Chen B, et al. Evaluation of conventional imaging performance in a research whole-body CT system with a photon-counting detector array. *Phys Med Biol* 2016; **61**: 1572–95. https://doi.org/10.1088/0031-9155/61/4/1572
17. Pourmorteza A, Symons R, Sandfort V, Mallek M, Fuld MK, Henderson G, et al. Abdominal imaging with contrast-enhanced photon-counting CT: first human experience. *Radiology* 2016; **279**: 239–45. https://doi.org/10.1148/radiol.2016152601
18. Klein L, Dorn S, Amato C, Heinze S, Uhrig M, Schlemmer H-P, et al. Effects of detector sampling on noise reduction in clinical photon-counting whole-body computed tomography. *Invest Radiol* 2020;

55: 111–19. https://doi.org/10.1097/RLI.0000000000000616

19. Rajendran K, Voss BA, Zhou W, Tao S, DeLone DR, Lane JI, et al. Dose reduction for sinus and temporal bone imaging using photon-counting detector CT with an additional tin filter. *Invest Radiol* 2020; **55**: 91–100. https://doi.org/10.1097/RLI.0000000000000614
20. Mannil M, Hickethier T, von Spiczak J, Baer M, Henning A, Hertel M, et al. Photon-Counting CT: high-resolution imaging of coronary stents. *Invest Radiol* 2018; **53**: 143–49. https://doi.org/10.1097/RLI.0000000000000420
21. Gutjahr R, Halaweish AF, Yu Z, et al. Human Imaging With Photon Counting–Based Computed Tomography at Clinical Dose Levels: Contrast-to-Noise Ratio and Cadaver Studies. Invest Radiol 2016;51:421–9. https://doi.org/10.1097/RLI.0000000000000251
22. Rajendran K, Petersilka M, Henning A, et al. Full field-of-view, high-resolution, photon-counting detector CT: technical assessment and initial patient experience. Phys Med Biol 2021;66:205019. https://doi.org/10.1088/1361-6560/ac155e
23. SilvaJGrönberg F, Cederström B, et al. Resolution characterization of a silicon-based, photon-counting computed tomography prototype capable of patient scanning. *J Med Imag* 2019; **6**: 1. https://doi.org/10.1117/1.JMI.6.4.043502
24. Si-Mohamed SA, Boccalini S. Lacombe H, et al.coronary CT angiography with photon-counting CT: first-in-human results. *Radiology* 2022. https://doi.org/10.1148/radiol.211780
25. Si-Mohamed S, Boccalini S, Rodesch P-A, et al. Feasibility of lung imaging with a large field-of-view spectral photon-counting CT system. Diagnostic and Interventional Imaging 2021;102:305–12. https://doi.org/10.1016/j.diii.2021.01.001
26. Boccalini S, Si-Mohamed SA, Lacombe H, Diaw A, Varasteh M, Rodesch P-A, et al. First in-human results of computed tomography angiography for coronary stent assessment with a spectral photon counting computed tomography. *Invest Radiol* 2022; **57**: 212–21. https://doi.org/10.1097/RLI.0000000000000835
27. Sartoretti T, Racine D, Mergen V, Jungblut L, Monnin P, Flohr TG, et al. Quantum iterative reconstruction for low-dose ultra-high-resolution photon-counting detector CT of the lung. *Diagnostics (Basel)* 2022; **12**(2): 522. https://doi.org/10.3390/diagnostics12020522
28. Sartoretti T, Landsmann A, Nakhostin D, Eberhard M, Roeren C, Mergen V, et al. Quantum iterative reconstruction for abdominal photon-counting detector CT improves image quality. *Radiology* 2022; **303**: 339–48. https://doi.org/10.1148/radiol.211931
29. Meyer M, Haubenreisser H, Raupach R, Schmidt B, Lietzmann F, Leidecker C, et al. Initial results of a new generation dual source CT system using only an in-plane comb filter for ultra-high resolution temporal bone imaging. *Eur Radiol* 2015; **25**: 178–85. https://doi.org/10.1007/s00330-014-3406-4
30. Oostveen LJ, Boedeker KL, Brink M, Prokop M, de Lange F, Sechopoulos I. Physical evaluation of an ultra-high-resolution CT scanner. *Eur Radiol* 2020; **30**: 2552–60. https://doi.org/10.1007/s00330-019-06635-5
31. Pourmorteza A, Symons R, Henning A, Ulzheimer S, Bluemke DA. Dose efficiency of quarter-millimeter photon-counting computed tomography: first-in-human results. *Invest Radiol* 2018; **53**: 365–72. https://doi.org/10.1097/RLI.0000000000000463
32. Leng S, Yu Z, Halaweish A, Kappler S, Hahn K, Henning A, et al. Dose-efficient ultrahigh-resolution scan mode using a photon counting detector computed tomography system. *J Med Imaging (Bellingham)* 2016; **3**: 043504: 043504: . https://doi.org/10.1117/1.JMI.3.4.043504
33. Zhou W, Lane JI, Carlson ML, Bruesewitz MR, Witte RJ, Koeller KK, et al. Comparison of a photon-counting-detector CT with an energy-integrating-detector CT for temporal bone imaging: a cadaveric study. *AJNR Am J Neuroradiol* 2018; **39**: 1733–38. https://doi.org/10.3174/ajnr.A5768
34. Bartlett DJ, Koo CW, Bartholmai BJ, Rajendran K, Weaver JM, Halaweish AF, et al. High-Resolution chest computed tomography imaging of the lungs: impact of 1024 matrix reconstruction and photon-counting detector computed tomography. *Invest Radiol* 2019; **54**: 129–37. https://doi.org/10.1097/RLI.0000000000000524
35. Jungblut L, Blüthgen C, Polacin M, Messerli M, Schmidt B, Euler A, et al. First performance evaluation of an artificial intelligence-based computer-aided detection system for pulmonary nodule evaluation in dual-source photon-counting detector CT at different low-dose levels. *Invest Radiol* 2022; **57**: 108–14. https://doi.org/10.1097/RLI.0000000000000814
36. Ferda J, Vendiš T, Flohr T, Schmidt B, Henning A, Ulzheimer S, et al. Computed tomography with a full FOV photon-counting detector in a clinical setting, the first experience. *Eur J Radiol* 2021; **137**: S0720-048X(21)00094-2: 109614: . https://doi.org/10.1016/j.ejrad.2021.109614
37. Zhou W, Montoya J, Gutjahr R, Ferrero A, Halaweish A, Kappler S, et al. Lung nodule volume quantification and shape differentiation with an ultra-high resolution technique on a photon counting detector CT system. *Proc SPIE Int Soc Opt Eng* 2017; **10132**: 101323Q. https://doi.org/10.1117/12.2255736
38. Inoue A, Johnson TF, White D, Cox CW, Hartman TE, Thorne JE, et al. Estimating the clinical impact of photon-counting-detector CT in diagnosing usual interstitial pneumonia. *Invest Radiol* 2022; **57**: 734–41. https://doi.org/10.1097/RLI.0000000000000888
39. Jungblut L, Euler A, von Spiczak J, Sartoretti T, Mergen V, Englmaier V, et al. Potential of photon-counting detector CT for radiation dose reduction for the assessment of interstitial lung disease in patients with systemic sclerosis. *Invest Radiol* 2022; **57**: 773–79. https://doi.org/10.1097/RLI.0000000000000895
40. Rajagopal JR, Farhadi F, Richards T, Nikpanah M, Sahbaee P, Shanbhag SM, et al. Evaluation of coronary plaques and stents with conventional and photon-counting CT: benefits of high-resolution photon-counting CT. *Radiol Cardiothorac Imaging* 2021; **3**(5): e210102. https://doi.org/10.1148/ryct.2021210102
41. Petritsch B, Petri N, Weng AM, Petersilka M, Allmendinger T, Bley TA, et al. Photon-Counting computed tomography for coronary stent imaging: in vitro evaluation of 28 coronary stents. *Invest Radiol* 2021; **56**: 653–60. https://doi.org/10.1097/RLI.0000000000000787
42. Symons R, De Bruecker Y, Roosen J, Van Camp L, Cork TE, Kappler S, et al. Quarter-millimeter spectral coronary stent imaging with photon-counting CT: initial experience. *J Cardiovasc Comput Tomogr* 2018; **12**: S1934-5925(18)30426-X: 509–15: . https://doi.org/10.1016/j.jcct.2018.10.008
43. Mergen V, Eberhard M, Manka R, Euler A, Alkadhi H. First in-human quantitative plaque characterization with ultra-high resolution coronary photon-counting CT angiography. *Front Cardiovasc Med* 2022; **9**: 981012: 981012: . https://doi.org/10.3389/fcvm.2022.981012
44. Mergen V, Sartoretti T, Baer-Beck M, Schmidt B, Petersilka M, Wildberger JE, et al. Ultra-high-resolution coronary CT angiography with photon-counting detector CT: feasibility and image characterization. *Invest Radiol* 2022; **57**: 780–88. https://doi.org/10.1097/RLI.0000000000000897
45. Wehrse E, Sawall S, Klein L, Glemser P, Delorme S, Schlemmer H-P, et al. Potential

of ultra-high-resolution photon-counting CT of bone metastases: initial experiences in breast cancer patients. *NPJ Breast Cancer* 2021; **7**: 3: 3: . https://doi.org/10.1038/s41523-020-00207-3

46. Grunz J-P, Huflage H, Heidenreich JF, Ergün S, Petersilka M, Allmendinger T, et al. Image quality assessment for clinical cadmium telluride-based photon-counting computed tomography detector in cadaveric wrist imaging. *Invest Radiol* 2021; **56**: 785–90. https://doi.org/10.1097/RLI.0000000000000789
47. Bette SJ, Braun FM, Haerting M, Decker JA, Luitjens JH, Scheurig-Muenkler C, et al. Visualization of bone details in a novel photon-counting dual-source CT scanner-comparison with energy-integrating CT. *Eur Radiol* 2022; **32**: 2930–36. https://doi.org/10.1007/s00330-021-08441-4
48. Baffour FI, Rajendran K, Glazebrook KN, Thorne JE, Larson NB, Leng S, et al. Ultra-High-Resolution imaging of the shoulder and pelvis using photon-counting-detector CT: a feasibility study in patients. *Eur Radiol* 2022; **32**: 7079–86. https://doi.org/10.1007/s00330-022-08925-x
49. Rajendran K, Baffour F, Powell G, Glazebrook K, Thorne J, Larson N, et al. Improved visualization of the wrist at lower radiation dose with photon-counting-detector CT. *Skeletal Radiol* 2023; **52**: 23–29. https://doi.org/10.1007/s00256-022-04117-2
50. Kämmerling N, Sandstedt M, Farnebo S, Persson A, Tesselaar E. Assessment of image quality in photon-counting detector computed tomography of the wrist-an ex vivo study. *Eur J Radiol* 2022; **154**: S0720-048X(22)00292-3: 110442: . https://doi.org/10.1016/j.ejrad.2022.110442
51. Baffour FI, Huber NR, Ferrero A, Rajendran K, Glazebrook KN, Larson NB, et al. Photon-Counting detector CT with deep learning noise reduction to detect multiple myeloma. *Radiology* 2023; **306**: 229–36. https://doi.org/10.1148/radiol.220311
52. Fryback DG, Thornbury JR. The efficacy of diagnostic imaging. *Med Decis Making* 1991; **11**: 88–94. https://doi.org/10.1177/0272989X9101100203
53. Higashigaito K, Mergen V, Eberhard M, Jungblut L, Hebeisen M, Rätzer S, et al. CT angiography of the aorta using photon-counting detector CT with reduced contrast media volume. *Radiology: Cardiothoracic Imaging* 2023; **5**(1). https://doi.org/10.1148/ryct.220140
54. Liu LP, Shapira N, Chen AA, Shinohara RT, Sahbaee P, Schnall M, et al. First-Generation clinical dual-source photon-counting CT: ultra-low-dose quantitative spectral imaging. *Eur Radiol* 2022; **32**: 8579–87. https://doi.org/10.1007/s00330-022-08933-x
55. Rajagopal JR, Farhadi F, Solomon J, Sahbaee P, Saboury B, Pritchard WF, et al. Comparison of low dose performance of photon-counting and energy integrating CT. *Acad Radiol* 2021; **28**: S1076-6332(20)30456-6: 1754–60: . https://doi.org/10.1016/j.acra.2020.07.033
56. Racine D, Mergen V, Viry A, Eberhard M, Becce F, Rotzinger DC, et al. Photon-counting detector CT with quantum iterative reconstruction: impact on liver lesion detection and radiation dose reduction. *Invest Radiol* 2022. https://doi.org/10.1097/RLI.0000000000000925
57. Sawall S, Klein L, Amato C, Wehrse E, Dorn S, Maier J, et al. Iodine contrast-to-noise ratio improvement at unit dose and contrast media volume reduction in whole-body photon-counting CT. *Eur J Radiol* 2020; **126**: S0720-048X(20)30098-X: 108909: . https://doi.org/10.1016/j.ejrad.2020.108909
58. Booij R, van der Werf NR, Dijkshoorn ML, van der Lugt A, van Straten M. Assessment of iodine contrast-to-noise ratio in virtual monoenergetic images reconstructed from dual-source energy-integrating CT and photon-counting CT data. *Diagnostics (Basel)* 2022; **12**(6): 1467. https://doi.org/10.3390/diagnostics12061467
59. Grunz J-P, Petritsch B, Luetkens KS, Kunz AS, Lennartz S, Ergün S, et al. Ultra-low-dose photon-counting CT imaging of the paranasal sinus with tin prefiltration: how low can we go? *Invest Radiol* 2022; **57**: 728–33. https://doi.org/10.1097/RLI.0000000000000887
60. Grunz J-P, Heidenreich JF, Lennartz S, Weighardt JP, Bley TA, Ergün S, et al. Spectral shaping via tin prefiltration in ultra-high-resolution photon-counting and energy-integrating detector CT of the temporal bone. *Invest Radiol* 2022; **57**: 819–25. https://doi.org/10.1097/RLI.0000000000000901
61. Symons R, Pourmorteza A, Sandfort V, Ahlman MA, Cropper T, Mallek M, et al. Feasibility of dose-reduced chest CT with photon-counting detectors: initial results in humans. *Radiology* 2017; **285**: 980–89. https://doi.org/10.1148/radiol.2017162587
62. Symons R, Cork TE, Sahbaee P, Fuld MK, Kappler S, Folio LR, et al. Low-Dose lung cancer screening with photon-counting CT: a feasibility study. *Phys Med Biol* 2017; **62**: 202–13. https://doi.org/10.1088/1361-6560/62/1/202
63. Pourmorteza A, Symons R, Reich DS, Bagheri M, Cork TE, Kappler S, et al. Photon-Counting CT of the brain: in vivo human results and image-quality assessment. *AJNR Am J Neuroradiol* 2017; **38**: 2257–63. https://doi.org/10.3174/ajnr.A5402
64. Symons R, Sandfort V, Mallek M, Ulzheimer S, Pourmorteza A. Coronary artery calcium scoring with photon-counting CT: first in vivo human experience. *Int J Cardiovasc Imaging* 2019; **35**: 733–39. https://doi.org/10.1007/s10554-018-1499-6
65. van der Werf NR, Rodesch PA, Si-Mohamed S, van Hamersvelt RW, Greuter MJW, Leiner T, et al. Improved coronary calcium detection and quantification with low-dose full field-of-view photon-counting CT: a phantom study. *Eur Radiol* 2022; **32**: 3447–57. https://doi.org/10.1007/s00330-021-08421-8
66. Higashigaito K, Euler A, Eberhard M, Flohr TG, Schmidt B, Alkadhi H. Contrast-enhanced abdominal CT with clinical photon-counting detector CT: assessment of image quality and comparison with energy-integrating detector CT. *Acad Radiol* 2022; **29**: 689–97. https://doi.org/10.1016/j.acra.2021.06.018
67. Euler A, Higashigaito K, Mergen V, Sartoretti T, Zanini B, Schmidt B, et al. High-pitch photon-counting detector computed tomography angiography of the aorta: Intraindividual comparison to energy-integrating detector computed tomography at equal radiation dose. *Invest Radiol* 2022; **57**: 115–21. https://doi.org/10.1097/RLI.0000000000000816
68. Flohr TG, Leng S, Yu L, Aiimendinger T, Bruder H, Petersilka M, et al. Dual-source spiral CT with pitch up to 3.2 and 75 MS temporal resolution: image reconstruction and assessment of image quality. *Med Phys* 2009; **36**: 5641–53. https://doi.org/10.1118/1.3259739
69. Mergen V, Ried E, Allmendinger T, Sartoretti T, Higashigaito K, Manka R, et al. Epicardial adipose tissue attenuation and fat attenuation index: phantom study and in vivo measurements with photon-counting detector CT. *AJR Am J Roentgenol* 2022; **218**: 822–29. https://doi.org/10.2214/AJR.21.26930
70. Mergen V, Sartoretti T, Klotz E, Schmidt B, Jungblut L, Higashigaito K, et al. Extracellular volume quantification with cardiac late enhancement scanning using dual-source photon-counting detector CT. *Invest Radiol* 2022; **57**: 406–11. https://doi.org/10.1097/RLI.0000000000000851
71. Sartoretti T, McDermott M, Mergen V, Euler A, Schmidt B, Jost G, et al. Photon-Counting detector coronary CT angiography: impact of virtual monoenergetic imaging and iterative reconstruction on image quality. *Br J Radiol*

2023: 20220466. https://doi.org/10.1259/bjr.20220466

72. Eberhard M, Mergen V, Higashigaito K, Allmendinger T, Manka R, Flohr T, et al. Coronary calcium scoring with first generation dual-source photon-counting CT-first evidence from phantom and in-vivo scans. *Diagnostics (Basel)* 2021; **11**(9): 1708. https://doi.org/10.3390/diagnostics11091708
73. Jungblut L, Kronenberg D, Mergen V, Higashigaito K, Schmidt B, Euler A, et al. Impact of contrast enhancement and virtual monoenergetic image energy levels on emphysema quantification: experience with photon-counting detector computed tomography. *Invest Radiol* 2022; **57**: 359–65. https://doi.org/10.1097/RLI.0000000000000848
74. Michael AE, Boriesosdick J, Schoenbeck D, Woeltjen MM, Saeed S, Kroeger JR, et al. Image-quality assessment of polyenergetic and virtual monoenergetic reconstructions of unenhanced CT scans of the head: initial experiences with the first photon-counting CT Approved for clinical use. *Diagnostics (Basel)* 2022; **12**(2): 265. https://doi.org/10.3390/diagnostics12020265
75. Sartoretti T, Mergen V, Higashigaito K, Eberhard M, Alkadhi H, Euler A. Virtual noncontrast imaging of the liver using photon-counting detector computed tomography: A systematic phantom and patient study. *Invest Radiol* 2022; **57**: 488–93. https://doi.org/10.1097/RLI.0000000000000860
76. Mergen V, Racine D, Jungblut L, Sartoretti T, Bickel S, Monnin P, et al. Virtual noncontrast abdominal imaging with photon-counting detector CT. *Radiology* 2022; **305**: 107–15. https://doi.org/10.1148/radiol.213260
77. Jungblut L, Sartoretti T, Kronenberg D, Mergen V, Euler A, Schmidt B, et al. Performance of virtual non-contrast images generated on clinical photon-counting detector CT for emphysema quantification: proof of concept. *Br J Radiol* 2022; **95**(1135): 20211367. https://doi.org/10.1259/bjr.20211367
78. Lennartz S, Schoenbeck D, Kröger JR, Borggrefe J, Henning Niehoff J. Photon-Counting CT material decomposition: initial experience in assessing adrenal adenoma. *Radiology* 2023; **306**: 202–4. https://doi.org/10.1148/radiol.220919
79. Decker JA, Huber A, Senel F, Bette S, Braun F, Risch F, et al. Anemia detection by hemoglobin quantification on contrast-enhanced photon-counting CT data sets. *Radiology* 2022; **305**: 650–52. https://doi.org/10.1148/radiol.220063
80. Mannil M, Ramachandran J, Vittoria de Martini I, Wegener S, Schmidt B, Flohr T, et al. Modified dual-energy algorithm for calcified plaque removal: evaluation in carotid computed tomography angiography and comparison with digital subtraction angiography. *Invest Radiol* 2017; **52**: 680–85. https://doi.org/10.1097/RLI.0000000000000391
81. Allmendinger T, Nowak T, Flohr T, Klotz E, Hagenauer J, Alkadhi H, et al. Photon-Counting detector CT-based vascular calcium removal algorithm: assessment using a cardiac motion phantom. *Invest Radiol* 2022; **57**: 399–405. https://doi.org/10.1097/RLI.0000000000000853
82. Sartoretti T, Eberhard M, Nowak T, Gutjahr R, Jost G, Pietsch H, et al. Photon-Counting multienergy computed tomography with spectrally optimized contrast media for plaque removal and stenosis assessment. *Invest Radiol* 2021; **56**: 563–70. https://doi.org/10.1097/RLI.0000000000000773
83. Sartoretti T, Eberhard M, Rüschoff JH, Pietsch H, Jost G, Nowak T, et al. Photon-Counting CT with tungsten as contrast medium: experimental evidence of vessel lumen and plaque visualization. *Atherosclerosis* 2020; **310**: S0021-9150(20)30405-6: 11–16: . https://doi.org/10.1016/j.atherosclerosis.2020.07.023
84. Ren L, Rajendran K, Fletcher JG, McCollough CH, Yu L. Simultaneous dual-contrast imaging of small bowel with iodine and bismuth using photon-counting-detector computed tomography: a feasibility animal study. *Invest Radiol* 2020; **55**: 688–94. https://doi.org/10.1097/RLI.0000000000000687
85. Ren L, Huber N, Rajendran K, Fletcher JG, McCollough CH, Yu L. Dual-Contrast biphasic liver imaging with iodine and gadolinium using photon-counting detector computed tomography: an exploratory animal study. *Invest Radiol* 2022; **57**: 122–29. https://doi.org/10.1097/RLI.0000000000000815
86. Muenzel D, Bar-Ness D, Roessl E, Blevis I, Bartels M, Fingerle AA, et al. Spectral photon-counting CT: initial experience with dual-contrast agent K-edge colonography. *Radiology* 2017; **283**: 723–28. https://doi.org/10.1148/radiol.2016160890
87. Symons R, Cork TE, Lakshmanan MN, Evers R, Davies-Venn C, Rice KA, et al. Dual-Contrast agent photon-counting computed tomography of the heart: initial experience. *Int J Cardiovasc Imaging* 2017; **33**: 1253–61. https://doi.org/10.1007/s10554-017-1104-4
88. Do TD, Sawall S, Heinze S, Reiner T, Ziener CH, Stiller W, et al. A semi-automated quantitative comparison of metal artifact reduction in photon-counting computed tomography by energy-selective thresholding. *Sci Rep* 2020; **10**: 21099: 21099: . https://doi.org/10.1038/s41598-020-77904-3
89. Zhou W, Bartlett DJ, Diehn FE, Glazebrook KN, Kotsenas AL, Carter RE, et al. Reduction of metal artifacts and improvement in dose efficiency using photon-counting detector computed tomography and tin filtration. *Invest Radiol* 2019; **54**: 204–11. https://doi.org/10.1097/RLI.0000000000000535

BJR https://doi.org/10.1259/bjr.20211232

Received: 08 November 2021 | Accepted: 25 August 2022 | Published online: 11 October 2022

Cite this article as:
Henssen D, Meijer F, Verburg FA, Smits M. Challenges and opportunities for advanced neuroimaging of glioblastoma. *Br J Radiol* (2023) 10.1259/bjr.20211232.

REVIEW ARTICLE

Challenges and opportunities for advanced neuroimaging of glioblastoma

[1]DYLAN HENSSEN, [1]FREDERICK MEIJER, [2,3]FREDERIK A. VERBURG and [2,3]MARION SMITS

[1]Department of Medical Imaging, Radboud university medical center, Nijmegen, The Netherlands
[2]Department of Radiology & Nuclear Medicine, Erasmus MC, University Medical Centre Rotterdam, Rotterdam, The Netherlands
[3]Brain Tumour Centre, Erasmus MC Cancer Institute, Rotterdam, The Netherlands

Address correspondence to: Dr Dylan Henssen
E-mail: *dylan.henssen@radboudumc.nl*

ABSTRACT

Glioblastoma is the most aggressive of glial tumours in adults. On conventional magnetic resonance (MR) imaging, these tumours are observed as irregular enhancing lesions with areas of infiltrating tumour and cortical expansion. More advanced imaging techniques including diffusion-weighted MRI, perfusion-weighted MRI, MR spectroscopy and positron emission tomography (PET) imaging have found widespread application to diagnostic challenges in the setting of first diagnosis, treatment planning and follow-up. This review aims to educate readers with regard to the strengths and weaknesses of the clinical application of these imaging techniques. For example, this review shows that the (semi) quantitative analysis of the mentioned advanced imaging tools was found useful for assessing tumour aggressiveness and tumour extent, and aids in the differentiation of tumour progression from treatment-related effects. Although these techniques may aid in the diagnostic work-up and (post-)treatment phase of glioblastoma, so far no unequivocal imaging strategy is available. Furthermore, the use and further development of artificial intelligence (AI)-based tools could greatly enhance neuroradiological practice by automating labour-intensive tasks such as tumour measurements, and by providing additional diagnostic information such as prediction of tumour genotype. Nevertheless, due to the fact that advanced imaging and AI-diagnostics is not part of response assessment criteria, there is no harmonised guidance on their use, while at the same time the lack of standardisation severely hampers the definition of uniform guidelines.

INTRODUCTION

Glioblastoma (GBM) is the most common adult-type diffuse glioma, which arises from glial cells and concerns the most aggressive and malignant primary brain tumour with astrocyte-precursors, classified as Grade 4 by the World Health Organization (WHO) grading system. In spite of advances in treatment, the prognosis remains poor with a median survival of 14–16 months.[1,2] Following the recently published 2021 WHO Classification of Central Nervous System Tumours v. 5, GBM comprises only isocitrate dehydrogenase (*IDH*) wild-type tumours. All *IDH*-mutant diffuse astrocytic tumours are considered a single type called astrocytoma, *IDH*-mutant with WHO grades ranging from 2 to 4.[3] While the separation of astrocytomas into *IDH* wild-type and -mutated tumours is an important advance in GBM classification, all of the literature which is covered within this review is based on the 2016 WHO classification of central nervous system tumours[4] (or previous versions). Therefore, when the term GBM is utilised, this will not only include *IDH*-wildtype GBM; this will also comprise the new astrocytoma Grade 4 *IDH*-mutant entity.

Due to the continuous optimisation and development of imaging protocols, the role and value of neuroimaging in the diagnostic work-up and treatment evaluation of GBMs has increased over the last years. Advanced neuroimaging aids to non-invasively provide more certainty about the prognosis and response to therapy, which is beneficial for treatment decision-making and counselling of the patient. Therefore, the omnipresent role of advanced imaging in GBM is undisputed and further consolidation is driven by various major clinical and scientific societies (*e.g.* the European Society of Radiology, the Radiological Society of North America, the European Association of Nuclear Medicine, and the Society of Nuclear Medicine and Molecular Imaging).

The purpose of this review is to provide an educational overview of advanced neuroimaging techniques in GBM.

More specifically, advanced MRI techniques, including diffusion-weighted imaging (DWI), diffusion tensor imaging (DTI), perfusion-weighted imaging (PWI) techniques (both with and without the use of contrast-agents), and magnetic resonance spectroscopy (MRS), will be discussed. In addition, Fluorine-18 fludeoxyglucose (^{18}F-FDG-) and amino-acid tracer positron emission tomography (AA-PET) are discussed. We focus on the challenges and opportunities of applying these techniques in clinical practice. Also, some new developments within the field and the potential use of new radiotracers will be addressed. Furthermore, we discuss the potential added value of artificial intelligence (AI)-based tools. To conclude, we discuss possible solutions to avoid pitfalls in the study design, data acquisition, and data analyses for future clinical studies.

CONVENTIONAL MRI OF GLIOBLASTOMA

Brain MRI with conventional imaging sequences plays a pivotal role in the diagnosis and follow-up of glioblastoma. Traditionally, the conventional sequences used in neuro-oncology include T_1weighted (T_1W, T_2W, T_2W fluid attenuation inversion recovery (FLAIR), and post-contrast T_1W (T_1W + c) sequences.[5] Anatomical details of the brain and the neoplasm within can be accurately evaluated as well as peritumoral oedema and disruptions of the blood–brain barrier (BBB). Glioblastoma is characterised by a heterogeneous appearance on T_1W and T_2W, which can be explained by necrosis, haemorrhage, soft-tissue mass, and tumoural vasculature. The combination of an irregular enhancing lesion with areas of infiltrating tumour and cortical expansion is highly suggestive of GBM (Figure 1). However, the use of conventional MRI sequences alone limits the differentiation of GBM from other intracerebral mass lesions with cystic or necrotic components (*e.g.* other neuroglial tumours, brain metastasis, or brain abscess). In addition, conventional MRI is limited with regard to differentiating high from low-grade glioma.

In GBM, conventional MRI sequences provide some hallmark features which can aid to predict molecular markers. For example, small regions of enhancement, a larger non-enhancing tumour portion, well-defined tumour margins, and T_1W hypointense areas with suppressed FLAIR signal within its necrotic components are predictive of *IDH*1-mutation (Figure 2A).[6,7] In addition, a large volume of T_2W abnormality and a higher ratio of T_2W to T_1W + c tumour components were also found to be correlated with *IDH*-1 mutation (Figure 2B).[8] Tumour location of *IDH-1* mutation GBM in the frontal lobe has been reported most frequently by various groups.[9,10]

Next to *IDH*, the second most-reviewed gene is O^6-Methylguanine-DNA methyltransferase (*MGMT*). *MGMT* methylation status is another important biomarker because high activity of *MGMT* (*i.e.* unmethylated *MGMT*) is known to result in a reduced efficacy of alkylating chemotherapeutic agents (*e.g.* temozolomide). In high-grade gliomas such as GBM, *MGMT* methylation is less common as compared to low-grade gliomas.[11,12] On conventional MRI, hypermethylated *MGMT* tumours tend to have mixed-nodular enhancement in lesions which are non-temporally located (Figure 3A).[13] Unmethylated

Figure 1. Conventional imaging of glioblastoma. Exemplary axial (a) T_1 weighted images (with motion artefacts), (b) post-contrast T_1 weighted images (with motion artefacts), (c) T_2 weighted images and (d), FLAIR images. Contrast-enhancing lesion with non-enhancing components suggesting necrosis. The lesion is surrounded by T_2W/FLAIR hyperintense signal representing tumour infiltration and oedema. The lesion itself is observed to exert mass effect. FLAIR, fluid attenuated inversion recovery.

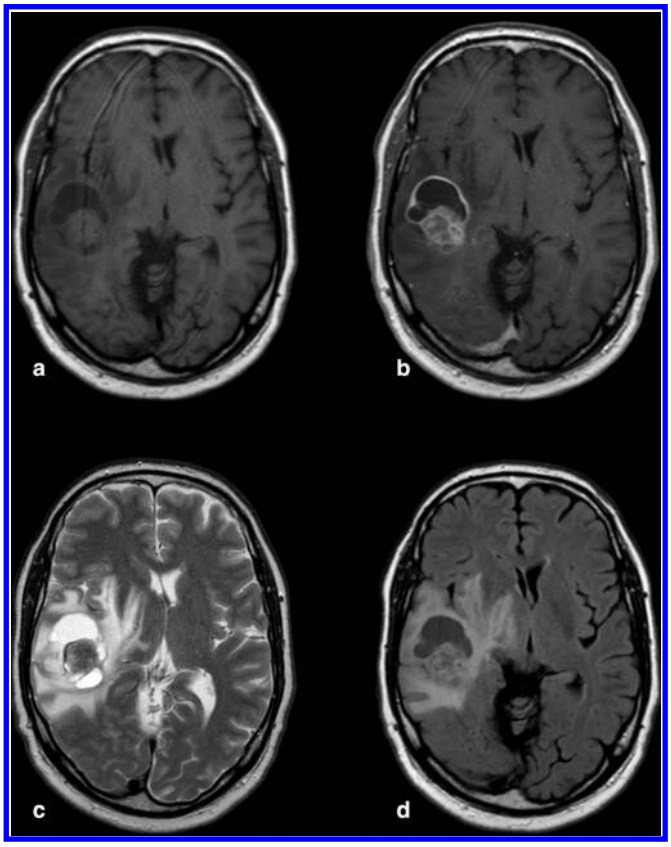

MGMT gliomas, on the other hand, show a ring-pattern enhancement (Figure 3B).[14]

In non-GBM, two radiological signs on conventional MRI sequences have been described in literature, which can provide insights in the mutational status. First, the T2-FLAIR mismatch sign describes that areas with T_2W-high signal intensity of the tumour are relatively hypointense in signal on T2-FLAIR images due to incomplete free water suppression. In addition, a rim of hyperintensity can be seen on FLAIR. These MRI features are considered a specific radiogenomic-signature of diffuse astrocytoma (*IDH*-mutant, 1p/19q intact) with a high positive predictive power.[15,16] The second radiogenomic-signature in non-GBM concerns the aspect of the T_2W-hyperintense signal and its delineation from the normal brain parenchyma. When this hyperintense area has smooth borders and has a homogeneous signal intensity, the tumour is more likely to be an astrocytoma without 1p/19q co-deletion.[17–19]

In the post-therapeutic setting, it has been advised to perform MRI within 2 days after surgical intervention to assess the extent

Figure 2. Conventional MRI of two patients, one with astrocytoma *IDH* mutant WHO Grade 4 and one with glioblastoma *IDH* wildtype. First row (a–d) shows an astrocytoma *IDH* mutant WHO Grade 4 located in the right frontal lobe with involvement of the rostrum corpus callosum. It is observed that only small regions of enhancing tumour are present on post-contrast T_1 weighted images (b; see arrow head in the enlarged section). On T_1 weighted images (a), very small hypointense areas which are also hypointense on FLAIR images (d) can be observed. Exemplary focus is encircled in the enlarged sections. These regions reflect necrotising/cystic regions. In addition, extensive T_2W hyperintense regions can be observed on T_2 weighted (c) and FLAIR images (d) surrounding the limited area of contrast-enhancing tumour. Second row (e–h) shows a glioblastoma *IDH* wildtype located in the left temporal lobe. It can be observed that a classical appearance is present with a relatively large ring-enhancing region on post-contrast T_1 weighted images (f). This contrast-enhancing tumour is surrounded by a similar amount of T_1W hyperintensity; see T_2 weighted images (g) and FLAIR images (h). FLAIR, fluid attenuated inversion recovery; IDH, isocitrate dehydrogenase.

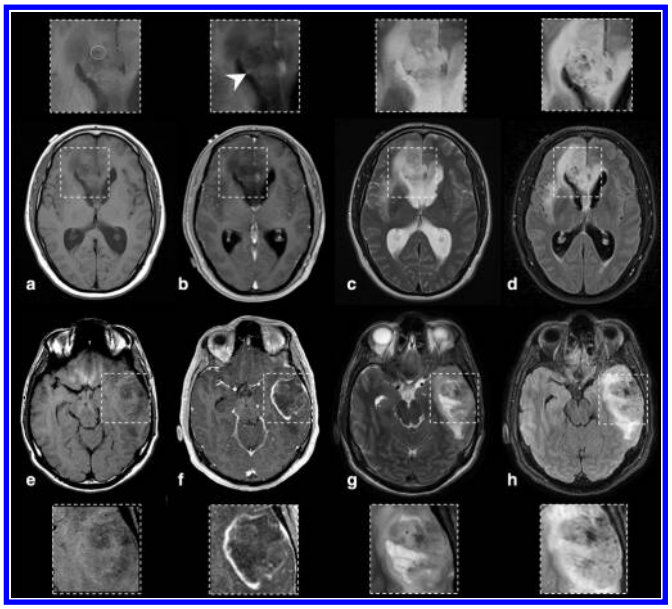

Figure 3. Axial post-contrast T_1 weighted images of patients suffering from glioblastoma with and without MGMT promoter methylation. (a) Axial post-contrast T_1 weighted images of three patients suffering from glioblastoma with MGMT promoter methylation showing a predominantly mixed-nodular pattern of enhancement. (b) Axial post-contrast T_1 weighted images of three patients suffering from glioblastoma without MGMT promoter methylation showing a predominantly ring-enhancement pattern. MGMT, O^6-Methylguanine-DNA methyltransferase.

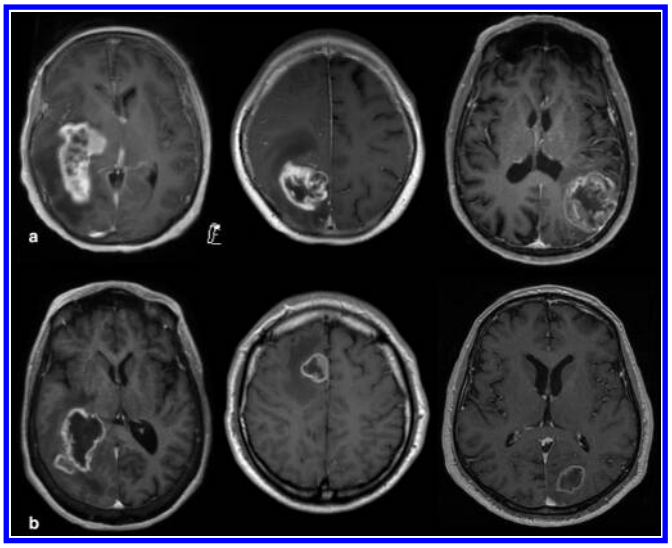

of the resection, the presence of residual tumour, and the occurrence of post-surgical complications.[20] In the post-operative setting, blood products in the resection cavity may be mistaken for residual enhancing lesion due to its intrinsic T1 shortening effects. Therefore, pre- and post-contrast T_1 weighted images must be evaluated with care. Nevertheless, enhancing lesions with a nodular aspect indicate residual neoplasm. Although these characteristics are generally reliable to assess residual or recurring neoplasm, some exceptions exist. Different treatment methods (*i.e.* chemotherapy and radiation) affect the permeability of the vascular walls which may lead to new enhancing lesions. If this contrast-enhancement is the result of treatment-induced vascular leakage, this is called pseudoprogression (PsP), whereas contrast-enhancement reflecting tumour recurrence is tumour progression (TP). Differentiation between PsP and TP is poor with conventional MR images alone (Figure 4). A 2011 study investigated the diagnostic accuracy of 11 signs as visible on conventional MRI to distinguish TP from PsP: 1) new enhancement; 2) marginal enhancement around the surgical cavity; 3) nodular enhancement; 4) callosal enhancement; 5) subependymal enhancement; 6) spreading wave front of enhancement; 7) cystic or necrotic change; 8) increased peritumoural T2 abnormality; 9) diffusion restriction; 10) decreasing enhancement intensity; and 11) increasing cystic or necrotic change. Only subependymal enhancement was found to have a limited predictive power with a sensitivity/specificity of 38/93% and with a negative-predictive value of 42%. The other 10 signs had no predictive power.[21]

DIFFUSION-WEIGHTED AND DIFFUSION-TENSOR MRI OF GLIOBLASTOMA

DWI is based on the random Brownian motion of water molecules and the magnitude of this Brownian motion is estimated as the apparent diffusion coefficient (ADC; mm^2/s). In turn, ADC is dependent on the cellular density and the presence of macromolecules or organelles/cell membranes in tissue compartments.[22] In gliomas, an inverse correlation between ADC values and tumour grade has been described.[23–25] DWI can also help to detect early tumour recurrence in enhancing and non-enhancing lesions seen as reduced diffusion[26] and to predict overall survival and progression-free survival in patients with glioblastoma.[27–30] DWI has been proposed to distinguish *MGMT* methylation status as a median ADC_{min} value of 800×10^{-6} mm^2/s or higher was found to represent methylated *MGMT* status.[31] DWI is, however, most commonly used to distinguish a brain abscess

Figure 4. Conventional MRI of two patients with glioblastoma in the post-treatment setting. Axial post-contrast T_1 weighted images of two patients with glioblastoma *IDH* wildtype. The upper images (a) show a region of contrast enhancement adjacent to the resection cavity in the right parietal lobe (white arrowheads). Radiological and clinical follow-up showed that this lesion represented pseudoprogression. The lower images (b) show nodular enhancement adjacent to the resection cavity in the left temporal lobe (white arrowheads). Radiological and clinical follow-up showed that this lesion represented tumour progression. IDH, isocitrate dehydrogenase.

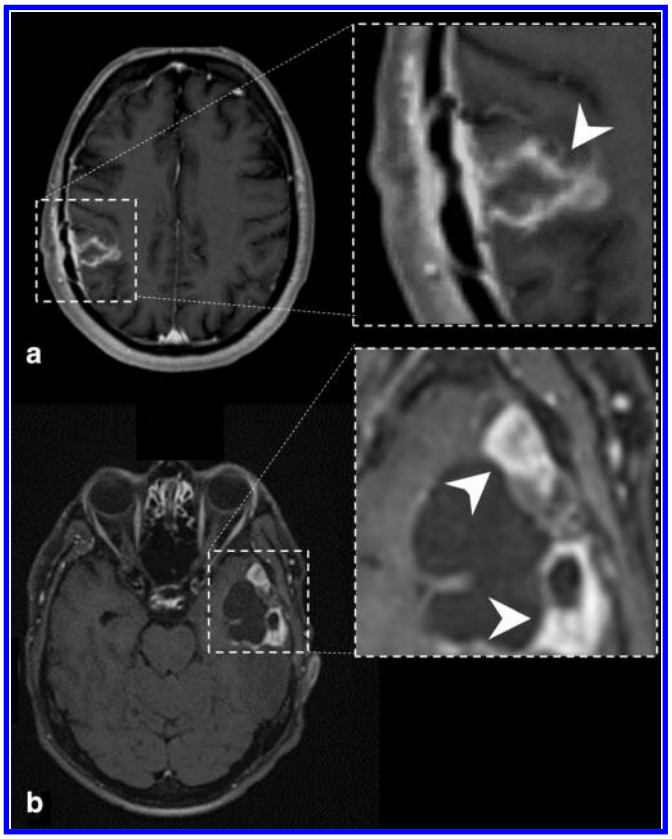

Figure 5. Diffusion-weighted imaging in tumour recurrence in a patient with glioblastoma. Axial post-contrast T_1 weighted images (a) show a new contrast-enhancing lesion cranial to the resection cavity in the right frontal lobe (white arrowheads). Restricted diffusion in this region is observed (white arrowheads) (b shows the corresponding ADC images; c shows the corresponding DWI images using a *b*-value of 1000 s/mm^2). This was highly suggestive for tumour progression, which was confirmed by radiological and clinical follow-up. ADC, apparent diffusion coefficient; DWI, diffusion-weighted imaging.

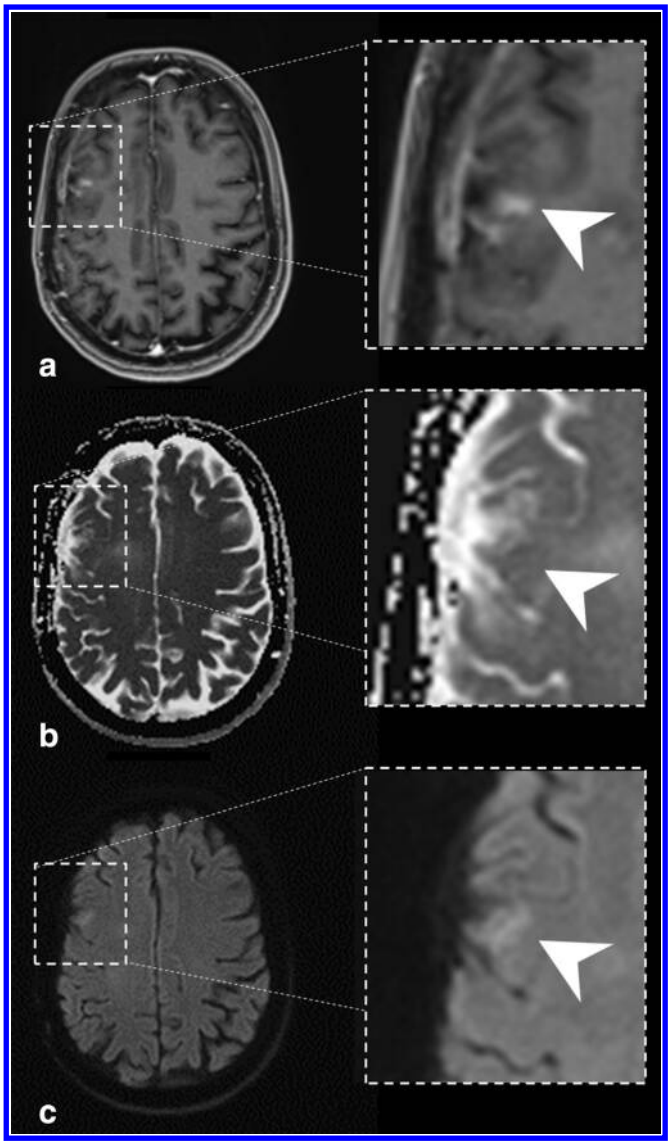

from glioma, and in the post-operative phase to identify areas of ischaemia.

In the post-therapeutic setting, differentiation between PsP and TP based on ADC values has been investigated by various groups (*e.g.*[32–42]). In general, it can be concluded that PsP lesions show a higher mean ADC-value as compared to the mean ADC-values in the TP group[26] (Figure 5). Although most studies on the use of ADC in the post-operative setting were conducted following a decent methodology, meta-analysis of ADC is hampered as different publications report different ADC metrics (*e.g.* mean, median, maximum, minimum). , When a quantitative assessment of ADC is carried out, it is recommended to use the mean ADC value of a region of interest (ROI), where necrotic areas should be excluded from the ROI-measurements. Reported cut-off values of mean ADC values to distinguish TP from PsP ranged between 1000 × 10^{-6} and 1412 × 10^{-6} mm^2/s corresponding with a range in sensitivity and specificity of 78–98.3% and 63.6–100% respectively.[43–46] The highest accuracy reported in literature (sensitivity/specificity rate of 98.3/100%) was reported by using a cut-off value of mean ADC of 1313 × 10^{-6} mm^2/s to differentiate between PsP and TP with higher values reflecting TP.[44] It must be emphasised that ADC values in post-treatment gliomas depend on a variety of factors, including post-operative artefacts (*e.g.* pneumocranium) and MRI system-related specifications such as magnetic field strength and *b*-values.[37] Therefore, it is recommended to perform ROI-analysis on fixed locations at different time points, as this allows one to assess the longitudinal changes in ADC values.

DTI models complex tissue diffusivity, based on which the microstructural organisation of tissue can be evaluated. In DTI, additional gradient pulses are introduced which cause a random phase shift for diffusing molecules and cancel out stationary molecules.[47,48] In general, diffusion of water molecules in biological tissues tends to be anisotropic. The diffusion tensor can thus be represented by a diffusion ellipsoid with its main axis parallel to the principal diffusion direction within a voxel.[47,48] Different metrics can be derived from the DTI model (most used are mean diffusivity, MD and fractional anisotropy, FA). MD is comparable with ADC. FA serves as an index for the amount of diffusion anisotropy within the tissue; a value of 0 indicates isotropic water diffusion, whereas an FA value of 1 describes a maximally anisotropic voxel.[49] Some studies found that DTI metrics can be used to assess occult neoplastic invasion of white matter tracts[50,51] and the direction of tumour growth.[52] In clinical practice, DTI is mainly used for tractography to guide neurosurgical procedures.

In the post-therapeutic setting, FA-values were found useful to differentiate PsP from TP in various papers with low or moderate risk of bias; these papers showed higher FA-values in TP as compared to PsP.[42,53–55] However, no prospective studies on this topic were found. Reported cut-off values of mean FA values to distinguish TP from PsP ranged between 0.13 and 0.18 and corresponded with sensitivity and specificity values of 68–81% and 73–79% respectively.[46,54,56] The highest reported sensitivity/specificity (81/79%) was found with a cut-off FA-value of 0.18, with lower values reflecting TP.[54] However, interpreting the FA-values suffers from similar limitations as ADC value interpretation.

PERFUSION MRI OF GLIOBLASTOMA

The role of PWI of glioblastoma is mainly based on the presence of neovascularisation. Tumour neovascularisation concerns an extensive network of suboptimal, poorly organised vessels with slow flow and leakage.[57] On T_1W + c images, areas of contrast-enhancement are seen. Slow flow and other dynamic capacities of the neo-angiogenic network can be assessed by PWI. The most commonly used PWI techniques are dynamic susceptibility contrast (DSC) perfusion, dynamic contrast enhancement (DCE) perfusion, and arterial spin labelling (ASL).

DSC PWI relies on the susceptibility induced signal loss on T_2* weighted sequences, resulting from the passage of a bolus of gadolinium-based contrast agent. The most commonly used DSC perfusion parameter is cerebral blood volume (CBV) which can be estimated[58,59] and computed[60] based on the negative enhancement integral. Other parameters include cerebral blood flow (CBF), mean transit time (MTT) and time-to-peak (TTP). The estimated value of the area under the attenuation curve is proportional to the CBV but does not yield an absolute measurement. Therefore, the measurement is expressed relative to a standard reference, usually the contralateral white matter (relative CBV ratio: rCBV ratio).[61] Overall, the rCBV ratio is an indicator of hypervascular regions and serves as the most robust parameter in DSC imaging.[62]

DCE PWI relies on the evaluation of T1 shortening induced by a gadolinium-based contrast agent bolus leaking from the blood vessels in tissue. Pharmacokinetic modelling is used to derive various perfusion metrics including K^{trans}, V_e and V_p. K^{trans} represents the capillary permeability; V_e represents the fractional volume of the gadolinium-based contrast agent in the extravascular–extracellular space; V_p represents the fractional volume of the of the gadolinium-based contrast agent in the plasma space.[58]

Figure 6. Pre-operative MRI, including DSC perfusion weighted MRI, of glioblastoma. The upper row shows axial (a) T_2 weighted, (b) T_1 weighted and (c) post-contrast T_1 weighted images of a patient with *IDH* wildtype glioblastoma. The lower row shows two axial perfusion maps derived from DSC perfusion-weighted MRI, namely (d) CBV and (f) CBF. The area of T_1W-hyperintensity (presumably haemorrhage) shows low perfusion (white arrow heads), while the enhancing portion anterior to it shows increased perfusion (white arrows). CBF, cerebral blood flow; CBV, cerebral blood volume; DSC, dynamic susceptibility contrast; IDH, isocitrate dehydrogenase.

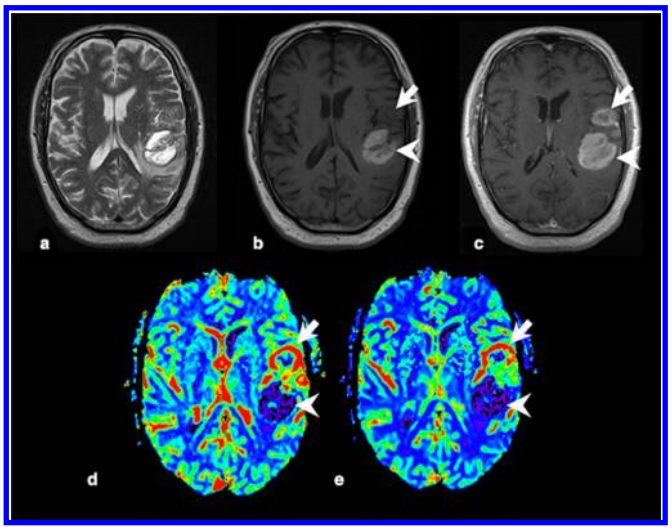

ASL is a perfusion technique without the need for contrast administration, where water molecules in blood vessels are tagged magnetically prior to entering the studied ROI (*i.e.* at the cervical level of the carotid artery). After a limited time interval (1.5–2.0 s), the labelled water molecules are imaged in the region of interest (*i.e.* the brain tissue). CBF values can be calculated from the differences in signal between the labelled images and the non-labelled images.[63,64] The major advantage of ASL is the fact that it does not suffer from contrast leakage effects.[65]

In the diagnostic work-up, PWI is used for characterisation of glioma genotype, as it is known that genetic differences in glioma subtypes correlate with the glioma vasculature. An exemplary image of DSC PWI in the pre-operative setting is provided in Figure 6. A recent review and meta-analysis reported that DSC-derived CBV values were fairly accurate when predicting *IDH* genotype, with an area under the receiver operator curve (AUROC) of 0.83.[66] When reviewing DCE parameters an AUROC of 0.81, 0.84 and 0.78 were observed for K^{trans}, V_e and V_p, respectively. Insufficient data were available with regard to the non-invasive genotype prediction of GBM based on ASL

Figure 7. Tumour progression of glioblastoma in the left temporal lobe as appreciated on post-contrast T_1 weighted images and DSC perfusion-weighted MRI. Enhancing lesion in the left temporal lobe in a patient post-treatment which shows increased cerebral blood volume on DSC perfusion-weighted MRI (white arrowhead). These features are highly suggestive for tumour progression, which was confirmed by radiological and clinical follow-up. DSC, dynamic susceptibility contrast.

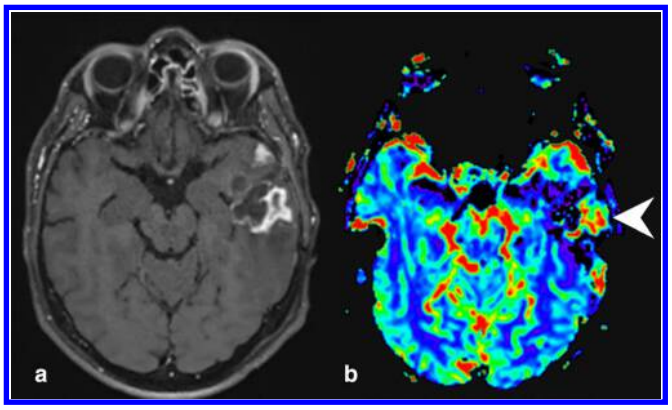

Figure 8. Post-contrast T_1 weighted images and ASL perfusion-weighted MRI overlay of glioblastoma after surgery. Panel a shows an axial post-contrast T_1 weighted image illustrating contrast-enhancement of the resection cavity borders. Panel b shows the colour-coded ASL-derived cerebral blood flow overlay image, illustrating hyperperfusion in the contrast-enhancing parts. This indicated residual tumour/tumour progression. ASL, arterial spin labelling.

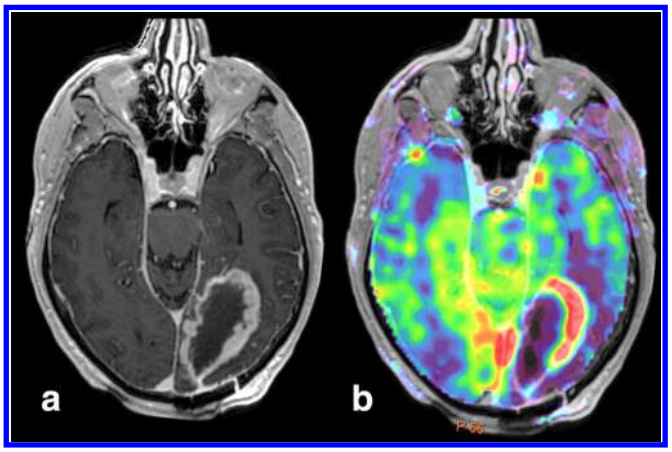

perfusion metrics. However, ASL could be used to differentiate between tumour grade (Grade 2, 3, 4) according to one meta-analysis.[67] Furthermore, some studies suggested that pre-treatment $rCBV_{max}$ values can be used as a prognostic marker for overall survival, or response to antiangiogenic treatment.[68–71]

Most commonly, PWI is used in the post-therapeutic setting to aid in the differentiation between TP and PsP. A recent meta-analysis on this topic reported the diagnostic accuracy of two DSC parameters: mean rCBV and maximum rCBV. Pooled sensitivity and specificity for detecting TP were both 88% for a $rCBV_{mean}$ ratio threshold ranging from 0.9 to 2.15. When using $rCBV_{max}$ ratios, pooled sensitivity and specificity for detecting TP were 93 and 76%, with thresholds derived from literature ranging from 1.5 to 3.1.[72] However, only the minority of papers included in these meta-analysis concerned prospective studies. An exemplary image of TP as assessed by DSC is shown in Figure 7.

Regarding the use of DCE-PWI to differentiate TP from PsP, two recent meta-analyses reported a pooled sensitivity ranging from 89 to 92%. In both meta-analyses, the specificity was found to be 85%,.[72,73] However, only the minority of papers included in these meta-analyses concerned prospective studies. Additionally, pooled diagnostic accuracies were not based on one DCE parameter but considered overall reported diagnostic accuracy of DCE. Contrary to specific meta-analyses on DSC parameters, no meta-analysis has been performed on the diagnostic accuracy of either K^{trans}, V_e or V_p in DCE PWI post-therapeutic glioblastoma. Therefore, no range of thresholds can be provided.

The use of ASL to differentiate PsP from TP has been suggested to be less accurate in comparison to other PWI techniques according to a recent meta-analysis.[73] This meta-analysis reported a sensitivity ranging between 52 and 79% and a specificity ranging between 64 and 82% when ALS was used to differentiate PsP from TP. However, too few studies are available to perform a proper meta-analysis with pooled sensitivities and specificities and further investigation is warranted. However, a recent paper from our group reports that ASL and DSC have similar diagnostic accuracies suggesting that ASL could be an alternative for DSC-PWI. An example of ASL PWI in post-operative glioma is provided as Figure 8.

It has been reported that implementation of either DSC or DCE in routine follow-up MRI of GBM can aid the detection of tumour recurrence.[74] However, as stated above a wide range of cut-off values for each technique has been reported, which complicates further clinical implementation (*e.g.*[75–77]). Also, a variety of PWI metrics has been used in imaging trials using either PWI technique. A standardised perfusion scanning protocol and standardised methods data processing with validated criteria for the diagnostic work-up and follow-up of gliomas would contribute to more robust scientific and clinical data.[60] Efforts for standardisation of PWI acquisition have been made by various organisations (*e.g.* the American Society of Functional Neuroradiology)[78] and scientific papers.[60,79] Based on extensive simulations combined with expert knowledge, recommendations have been formulated with regard to DSC PWI (*e.g.* full-dose preload, full-dose bolus dosing using an intermediate (60°) flip-angle and choosing a field strength-dependent echo time (40–50 ms at 1.5 T, 20–35 ms at 3.0 T) in order to obtain overall best signal and precision for CBV estimates.[60] No consensus recommendations with regard to the use of DCE in neuro-oncological imaging are available. Although recommendations have been published for the use of ASL, it must be emphasised that these were not specifically designed for perfusion of neuro-oncological disease {[79] #232}. In summary, this paper recommended the use of pseudocontinuous labelling and background suppression. Also, a segmented three-dimensional readout without the use of vascular crushing gradients has been recommended {[79] #232}.

Figure 9. Single voxel MRS of glioblastoma at 1.5T. Brain MRI with axial post-contrast T_1 weighted (panel a) and T2 (panel b) images of a patient with a small T2 hyperintense space occupying cortical/subcortical lesion in the right frontal lobe with some contrast enhancement. Panel c shows the MRS spectrum of the lesion. The corresponding spectrum (acquired with TE = 20 ms) can be indicative of glioblastoma tissue. The viable tumour tissue within the region of interest is recognised by high Cho signal and decreased NAA, the spectral peaks coming from lipid signal (lactate/lipid peaks are seen around 1 ppm on the spectrum) indicate the presence of necrotic tissue, even though this is not visible on structural MRI. The most prominent signals are labelled in the spectral pattern corresponding to voxel a. Cho, Choline; Cr1/Cr2, Creatine; Ins dd1, Myo-inositol; NAA, N-acetylaspartate; TE, echo time.

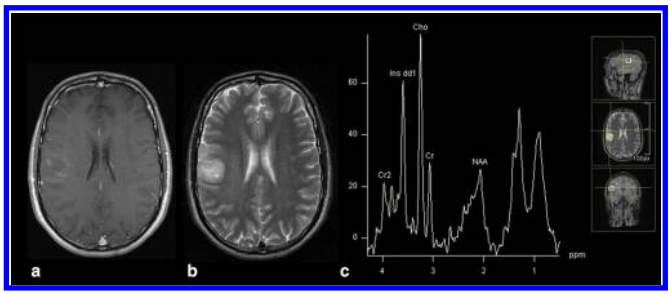

Finally, it has been shown that a well-established image-review process needs to be applied upfront to assess perfusion metrics because repeatability and reproducibility were found to be below 50 and 10% respectively in one multicentre study using DSC PWI.[80] Therefore, it has been recommended to measure rCBV in the context of clinical trials by two experienced readers. In case of disagreement, an adjudicator could be involved to provide the final perfusion measurement.[80] This is clearly time-consuming and thus impractical for clinical practice. Therefore, we recommend that PWI should be evaluated by an experienced reader and should always be interpreted together with other MRI sequences. Furthermore, radiological evolution of the area of interest over time and the clinical context of the patient should be taken into consideration when assessing PWI data.

MR SPECTROSCOPY OF GLIOBLASTOMA

The chemical composition of the tissue can be evaluated by MRS. MRS can therefore detect specific metabolites in defined regions of interest/voxels.[81,82] For GBM imaging, the most important metabolites include choline (Cho) and N-acetylaspartate (NAA) (Figure 9). In the clinical setting, MRS is often performed as a single voxel technique or as a slab comprising several voxels (*i.e.* multivoxel spectroscopy, chemical shift imaging). However, as not the entire lesion can be assessed in three dimensions at once, single voxel and multivoxel spectroscopy are known to suffer from sampling errors and outcomes can be confounded by the heterogeneous content of glioblastoma. Relatively new ^{1}H MRS sequences including 3D-echo planar spectroscopic imaging (3D EPSI) allow acquisition metabolic maps with an excellent coverage and spatial resolution. The images acquired from 3D EPSI protocols can be co-registered with anatomical images (T_1 weighted images). MRS and 3D EPSI have been described as useful imaging protocols to assess GBM metabolism and differentiation of TP from PsP.[83–87] Tumour tissue has an MRS signature of increased Cho due to the increased cell density and total cell membrane. Reduced NAA is seen due to decreased neuronal content and decreased neuronal viability. Thus, elevation of Cho and decrease of NAA is suggestive for TP, although Cho can also be elevated in patients who receive immunotherapy.[88,89] In a meta-analysis of 55 studies, MRS showed to be superior to other parametric MRI sequences (conventional, ADC, DSC PWI, DCE PWI) when differentiating PsP from TP with a pooled sensitivity/specificity of 91/95%.[73] However, this meta-analysis included a heterogeneous collection of included papers. For example, studies on MRS with single voxel and multivoxel protocols were included and compared. Furthermore, this meta-analysis made no distinction between the diagnostic capacity of the different metabolite-ratios (included were MRS studies focusing on Cho/Cre, Lac/Cho, NAA/Cho and Cho/NAA). Reported cut-off values for Cho/Cre ranged between 1.07–2.50.[90–92] The cut-off values reported for Lac/Cho and Cho/NAA were 1.05 (34) and 1.71 respectively (48). Therefore, further research is needed, preferably with well-established study reading protocols and cut-off values.

With regard to prognosis prediction, a recent MRS study showed higher Cho/NAA ratios in the post-operative peritumoral oedema zone in patients with early tumour recurrence in those areas. A higher Cho/NAA ratio in the peritumoral oedema zone was considered to be associated with poor prognosis.[93] However, this conclusion still needs to be corroborated by other research groups. 2-Hydroxyglutarate is an oncometabolite of *IDH* mutant glioma and it has recently been reported that MRS could be useful for the determination of *IDH* mutation status based on the detection of elevated levels of 2-hydroxyglutarate.[94–96] A meta-analysis on this topic found a pooled sensitivity of 84% and a pooled specificity of 97% with regard to predicting *IDH* mutation status in GBM.[97] Although promising, MRS is best carried out at 3T (or higher), requires expert knowledge and/or specific semi-automated computer-aided diagnosis software[98] and is not as widely available as other advanced MRI techniques.

^{18}F-FDG-PET IMAGING OF GLIOBLASTOMA

The use of ^{18}F-FDG-PET imaging in neuro-oncological diseases is limited by the poor tumour-to-background ratio as normal, healthy brain tissue also shows a very high physiological uptake of this tracer. Nevertheless, ^{18}F-FDG-PET can provide some useful information in GBM in research settings. For example, the maximum standardised uptake value (SUV_{max}) of ^{18}F-FDG-PET imaging could help to accurately determine the genotype of the GBM[99–102] and could help to predict patient prognosis.[100] In addition, differentiation between GBM and its main differential diagnoses (*e.g.* brain metastasis and primary central nervous system lymphoma (PCNSL)) by use of ^{18}F-FDG-PET imaging showed encouraging results.[103–106] When using cut-off values of $SUV_{max} \geq 15$, $SUV_{max} \geq 12$, and SUV_{max} of ≥9.35, a sensitivity/specificity of 88/100%, 100/71.4%, and 100/78.3%, respectively, was reported with regard to discriminating PCNSL from GBM.[107–109]

In the post-operative setting, GBM imaging by use of ^{18}F-FDG PET has been investigated by various authors to distinguish

PsP from TP.[110–118] From these studies, ^{18}F-FDG PET showed a sensitivity ranging from 68 to 100% and a specificity ranging from 33 to 100%. Reported cut-off values of SUV tumour-to-brain ratios (TBR) vary from 0.75 to 2.64 with higher values reflecting TP.[111–119] However, a more recent meta-analysis also found a statistically significantly lower pooled specificity when imaging high-grade glioma as compared to low-grade glioma (82 *vs* 90%).[119] Therefore, we conclude that FDG-PET imaging plays a limited role in post-treatment GBM imaging. Although mostly retrospective studies were carried out on this topic,[113–115] some well-performed prospective studies are also available.[117,118]

AA-PET IMAGING OF GLIOBLASTOMA

In contrast to FDG-PET imaging, radio-labelled amino-acids have a high TBR due to the increased amino-acid metabolism in GBM cells due to cell proliferation and extracellular matrix production. Therefore, AA-PET can be helpful in the imaging of GBM in the pre-operative as well as post-therapeutic setting. S-11C-methyl)-L-methionine (11C-MET), O-(2-18Ffluoroethyl)-L-tyrosine (^{18}F-FET), and 3,4-dihydroxy-6–18F-fluoro-L-phenyla lanine (^{18}F-FDOPA) are the most widely studied tracers. In the pre-operative setting, AA-PET imaging serves three main goals: primary diagnosis/differential diagnosis, glioma delineation, and treatment planning.

For ^{18}F-FET PET imaging, it has been shown that abnormal focal ^{18}F-FET uptake leads to a high sensitivity of high- grade glioma detection.[120–122] More specifically, a TBR_{max}<2.5 in ^{18}F-FET excludes a high-grade tumour with high probability.[120] It has furthermore been found that dynamic ^{18}F-FET data could be very useful for glioma grading.[123–125] Dunet et al reported that a negative slope of tumour FET time–activity was the best predictor of high-grade glioma.[125] Although several studies have been carried out with ^{11}C-MET and ^{18}F-FDOPA, these radiotracers were less accurate as compared to ^{18}F-FET.[126–128] In terms of glioma delineation, biopsy studies showed that ^{18}F-FET PET-imaging detected the extent of gliomas, including GBM, most accurately.[129,130] With regard to glioma delineation, it is known from histological validation studies that conventional MRI is limited with regard to visualising glioma extent.[129,130] TBR_{max} values of ^{18}F-FET PET imaging, on the other hand, were found to result in larger tumour volumes.[131] Similar results have been obtained with ^{18}F-FDOPA PET in progressive or recurrent GBM where a larger tumour extent was identified when compared with MRI-derived rCBV maps.[132] Accordingly, ^{18}F-FDOPA PET-based tumour volumes have been shown to extend beyond the contrast-enhancing volume on conventional MRI.[133,134]. ^{11}C-MET has only been used in the delineation of recurrent GBM indicating contrast-enhanced MRI alone resulted in an underestimation of the tumour volume.[135]

In the pre-operative setting, research showed that AA-PET imaging could be of predictive value as ^{18}F-FDOPA was found capable to predict overall survival[136] and could identify bevacizumab-responders as early as 2 weeks after treatment initiation.[137] Concerning brain biopsy planning, the use of PET imaging to identify focal hot spots has also been found relevant for GBM imaging[133,138] (Figure 10), *e.g.* for detecting

Figure 10. ^{18}F-FET PET) images of glioma in the pre-operative setting^{18}F-FET PET images show diffuse uptake of FET in the left frontoparietal lesion with focal areas of relative more uptake. These regions are thought to represent the localisations with the most high-grade tumour tissue. Biopsy was carried out and after histopathological examination, including molecular diagnostics, the diagnosis of an astrocytoma Grade III was made (according to the 2021 WHO Glioma Classification). ^{18}F-FET, O-(2-18Ffluoroethyl)-L-tyrosine; PET, positron emission tomography.

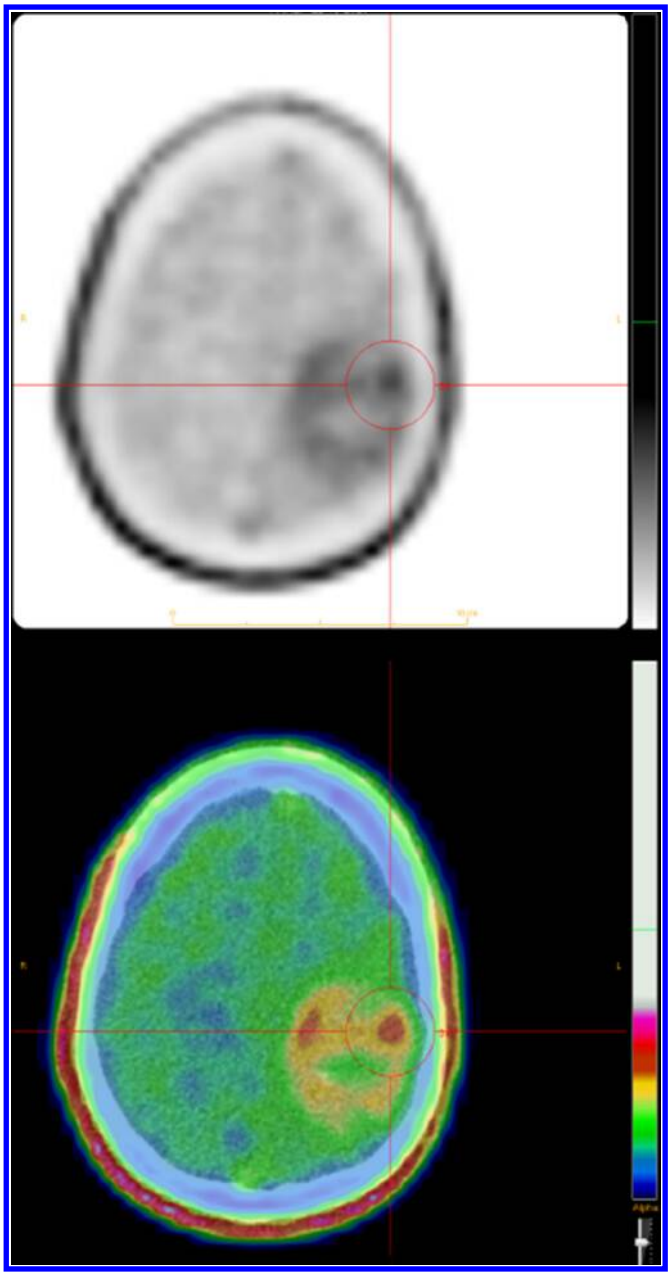

regions with abnormal activation of the *EGFR* gene due to a deletion of exons 2–7 of *EGFR*.[139] Also, AA-PET-CT was found to provide more accurate stereotactic biopsies compared to ^{18}F-FDG-PET-CT guided biopsies.[140] Studies on the use of ^{18}F-FET and ^{18}F-FDOPA to guide stereotactic biopsies showed superior results compared to ^{11}C-MET and FDG-PET guided

biopsies.[133,141,142] For instance, a recent cost-effectiveness analysis showed that the combined use of ^{18}F-FET PET and MRI resulted in a 19% higher likelihood to obtain a representative biopsy.[142] With regard to radiotherapy planning, the use of ^{11}C-MET PET imaging[143–145] and ^{18}F-FET PET imaging effectively helped to delineate areas of glioma microspread resulting in a larger target volume.[131,146,147] Nevertheless, tumour recurrence after radiotherapy was reported to occur most often within the AA-PET defined target volume.[148,149]

Additionally, the aforementioned AA-based radiotracers are widely used in the post-treatment assessment, especially with regard to differentiation of PsP from TP. Several reports presented a sensitivity/specificity ranging from 66/60 to 78/100% when distinguishing PsP from TP by use of ^{11}C-MET PET imaging.[90,119,150–159] When assessing the diagnostic accuracy of ^{18}F-FET PET imaging (see, *e.g.*[160–166]), meta-analyses reported a pooled sensitivity and specificity of 88–91% and 78–95%, respectively.[119,167] The use of ^{18}F-DOPA PET was to distinguish PsP from TP showed sensitivity and specificity ranges of 85–100% and 70–86%, respectively.[119,168–171]

With regard to research on the use of AA-PET in imaging in post-operative glioblastoma, the field is limited by the large body of retrospective studies and the unblended assessment of radiologists/nuclear medicine physicians with regard to other clinical, histopathological and imaging information.[90,113,157,158,164–166]

NOVEL MRI TECHNIQUES FOR USE IN GLIOBLASTOMA

During the last decades, tremendous developments of MRI hardware and image analysis methods allowed for micro- to macroscale imaging of GBM. These novel imaging approaches target a variety of molecular pathophysiological mechanisms occurring in GBM. To facilitate sharing of knowledge and to accelerate the clinical implementations of novel MRI techniques, the European, multidisciplinary network Glioma MR Imaging 2.0 (GliMR) was founded in 2019.[172] Although the continuous development of novel MRI techniques prevents the authors from providing a complete overview of the literature on this topic, some promising techniques are highlighted.

Diffusion kurtosis imaging (DKI) has been proposed as a sensitive method to visualise the otherwise invisible, infiltrating component of GBM. DKI is an extension of DTI methods as it provides quantitative information about how tissue water diffusion deviates from a Gaussian distributed diffusion.[173] Previous research found that DKI variables can be used to assess microstructural alterations in perilesional white matter, suggestive of tumour infiltration which is not visible on conventional MRI sequences.[174,175]

Another innovative imaging technique concerns amide proton transfer-chemical exchange saturation transfer (APT-CEST), which is aimed at assessing tumour metabolism and cell proliferation. Like other malignancies, GBM cells rewire their metabolism to grow excessively and to ensure prolonged cell-life. APT-CEST imaging indirectly visualises these mechanisms by detecting the presence of amide protons. Amide-protons accumulate in regions with an increased amount of proteins and peptides. APT-CEST imaging uses a specific radiofrequency pulse at the resonant frequency of protons inside amides (-NH). Thereby, only the protons within the amides will be saturated. In turn, the magnetic saturation of the amides will spontaneously be transferred to water due to the chemical exchange of the excited amide protons with non-excited protons within water molecules. The proton of the amides will thus be replaced with an unsaturated proton from water, causing an accumulation of saturation in water. Saturation of water will cause a decrease in water signal and is thereby an indirect reflection of amides in a target area. It has been reported that the use of APT-CEST is promising with regard to predicting *IDH* mutation status[176] and distinguishing TP from pseudoprogression.[177,178]

Deuterium metabolic imaging (DMI) is novel, non-invasive approach which combines deuterium MRS with oral intake (or intravenous injection) of non-radioactive ^{2}H-labelled substrates to generate three-dimensional metabolic maps. DMI can reveal glucose metabolism beyond uptake and thereby provides much more detailed information with regard to tissue metabolism as compared to ^{18}F-FDG-PET imaging.[179] Preliminary data showed pronounced metabolic differences between normal brain and GBM.[179]

Vessel architectural imaging (VAI) provides further insights into vessel size and type. VAI exploits the differences in observed proton relaxation from simultaneously acquired contrast-enhanced gradient recalled-echo and spin-echo MR imaging for vessel-size estimation. The temporal shift between the two relaxation curves can be used to estimate vessel type and size.[180–182] Because VAI can estimate these vessel features, it has been suggested that this technique might provide further insight into the mechanisms of pseudoprogression and the early detection of TP.[183,184]

NOVEL RADIOTRACERS FOR USE IN GLIOBLASTOMA

In recent years, several new classes of tracers have emerged that may also prove interesting for use in GBM not just from a diagnostic, but also from a therapeutic point of view as these tracers can potentially also be labelled with beta- and alpha-emitting radioisotopes. The first of these substance classes concern tracers aimed at the prostate-specific membrane antigen (PSMA). Primarily developed for use in diagnosis and therapy of metastatic prostate cancer, the inaptly named PSMA, which less colloquially is also known as glutamate carboxypeptidase two and in the brain serves as a modulator of excitatory neurotransmission, is also expressed in GBMs and their neovasculature *in vitro* as well as *in vivo*.[185–187] Although initial studies show promising results as to the diagnostic potential of PSMA in GBM,[188] no prospective data on the diagnostic value of this tracer are available as yet. However, in contrast to AA-PET, given sufficiently high uptake PSMA-PET as stated above also may indicate to possibility of radionuclide therapy with PSMA targeted substances.

The second class of interest in GBM are tracers aimed at the fibroblast activating protein (FAP). Recently introduced as a novel tracer of interest for diagnosis and possibly also therapy in a broad variety of oncological diseases,[189] this class of tracer in first, preliminary results also was shown to produce promising results in *IDH*-wildtype GBM as well as *IDH*-mutant astrocytoma, but not in low-grade *IDH*-mutant gliomas. This indicates that this class of substance may in the future play a role in non-invasively identifying high-grade *IDH*-mutant gliomas and GBMs, as well as may provide another radionuclide therapy option for these diseases.

ARTIFICIAL INTELLIGENCE AND IMAGING OF GLIOBLASTOMA

A growing number of AI-based applications is finding its way to clinical practice. Commercially available AI-based software in the field of radiology holds at least 100 CE-marked products, although the majority of these packages have not been based on peer-reviewed scientific evidence and only a minority of such software applications have demonstrated (potential) clinical impact.[190] Although AI holds the potential to perform image analyses which matches and potentially surpasses the experienced neuroradiologist's abilities,[191] important challenges for AI need to be recognised (for a review see[192]). For example, most studies on AI in GBM imaging were performed on limited sample sizes. Additionally, in most studies there was no external validation of obtained results, which limits generalisation of the study results and bears the risk of overfitting. It is therefore essential to educate the end-users on this topic, who should be familiar with the strengths and limitations for applying AI-tools in clinical practice. Also, data sharing is an important factor which will contribute to further development and implementation of AI-tools. For that reason, the open-access imaging databases of the MICCAI[193] and the Erasmus Glioma Database[194] are much needed advances in this field. Creating and maintaining such large databases are essential, though time-intensive tasks. AI could also play a role in data curation in order to preserve its integrity and ensure reusability.[195]

The potential of AI tools in glioma image analysis is also immense. First, AI-based glioma segmentation was found to be highly accurate,[196] which would relieve radiologists of the labour-intensive task of image segmentation or even tumour measurement. This explains why fully automated segmentation tools have gained interest over the years and highlights the importance of the annual multimodal Brain Tumour Segmentation (BraTS) challenge (http://braintumorsegmentation.org/). A recent report showed that the implementation of an AI- based segmentation tool in our clinical practice resulted in reasonable (77%) rates of successful segmentation.[197]

In one study, researchers used an AI application as an add-on feature in radiological readings to predict *IDH* mutation status in gliomas.[198] In this study, neuroradiologists' predictive capacity of WHO grade was improved when coupled with the predictive capacities of a random forest algorithm. In addition, the same input variables could be used to accurately predicting *IDH* mutation status.[198] Two recent meta-analysis on this subject provided an overview of the accuracy of AI with regard to predicting glioma genomics, which showed high accuracy of machine learning algorithms for the prediction of *IDH* mutation status, 1p/19q codeletion status, *MGMT* promoter mutation and *TERT* promoter mutation with AUROCs of 0.909, 0.748, 0.866 and 0.842, respectively.[199] However, again these studies mainly used internal validation and external validation was largely lacking. In a recent review, similar predictive capacities were found with pooled sensitivities and specificities of 0.88, 0.76 and 0.76 for predicting *IDH* mutation status, 1p/19q codeletion status and *MGMT* promoter mutation, respectively.[200] Pooled specificity for predicting *IDH* mutation status, 1p/19q codeletion status and *MGMT* promoter mutation showed to 0.86, 0.83 and 0.83, respectively. However, these meta-data represent the predictive capacities of the investigated artificial intelligence approaches in their training phase. With regard to the *IDH* mutation status, a meta-analysis was provided on the diagnostic accuracy parameters in the (mostly internal) validation sets. The pooled sensitivity and specificity for predicting *IDH* mutation status were 0.83 and 0.85 in validation sets, respectively.[200]

RECOMMENDATIONS AND CONCLUSIONS

From the published literature, it is evident that advanced neuroimaging techniques have the potential to add value to the diagnostic work-up, treatment planning and surveillance of patients with suspected GBM. It is, however, also clear that there is wide variability in their application and interpretation, while patient access to these techniques also varies widely.[201] With the exception of the newly defined response assessment criteria for paediatric low-grade glioma—which include DWI—advanced imaging techniques are not part of international and widely accepted response assessment criteria such as those defined by the Response Assessment for Neuro Oncology (RANO) working groups. This can at least in part be attributed to the lack of standardisation and high-level evidence. Most published work concerns retrospective, selected and often small patient populations, while prospective studies—in particular using external validation cohorts—are rare and randomised controlled trials non-existent. Here, we find ourselves somewhat in a Catch-22: due to the fact that advanced imaging is not part of response assessment criteria, there is no harmonised guidance on its use, while at the same time, the lack of standardisation severely hampers the definition of uniform guidelines. Recent international efforts to standardise image acquisition in glioma[5,202] are instrumental to break this vicious circle and to facilitate studies for obtaining the much needed high-level evidence for providing clear guidance on the optimal choice and application of the various advanced imaging techniques.

At the same time, it seems that PWI and MRS, as well as AA-PET have found widespread application for diagnostic challenges, in particular for assessing tumour aggressiveness, extent, and differentiation from treatment-related effects, while DWI has its particular use for differential diagnosis and pre-surgical tractography. Novel tracers aimed at PSMA or FAP could mix up the landscape here as these tracers also seem to have specific diagnostic properties as well as the potential for radionuclide therapy. It remains to be seen if and which technique is superior to others,

and until such time individual institutions apply techniques according to local preferences and expertise. In the absence of a clearly superior technique, the local level of expertise is probably a more important factor than the choice of technique. This also means that the acquisition, post-processing, and interpretation need to be in the hands of experts who are not only technically but also clinically informed on the strengths *and* weaknesses of each applied technique.

The same could be said about AI-based tools, which have enormous potential to improve and enhance clinical practice, on the one hand automating tasks that are currently done manually (such as tumour segmentation) and on the other hand providing additional diagnostic information (such as prediction of tumour genotype). Again, levels of evidence are still low and the time is now ripe for studies with prospective, sufficiently powered cohorts and—crucially—external validation. Guidance for setting up and assessing the strength of AI studies is for instance provided by the radiomics quality score.[203]

The classification of diffuse glioma, including GBM, is a rapidly changing the landscape with an important role for diagnostic imaging at every step along the way from diagnosis to treatment decision-making and treatment monitoring. Advanced imaging acquisition and AI-based analyses provide powerful tools, both in their current form and in future developments, but need to be used with expert knowledge within the context of the currently available evidence.

REFERENCES

1. Dolecek TA, Propp JM, Stroup NE, Kruchko C. CBTRUS statistical report: primary brain and central nervous system tumors diagnosed in the united states in 2005-2009. *Neuro Oncol* 2012; **14 Suppl 5**: v1–49. https://doi.org/10.1093/neuonc/nos218
2. Lapointe S, Perry A, Butowski NA. Primary brain tumours in adults. *Lancet* 2018; **392**: 432–46. https://doi.org/10.1016/S0140-6736(18)30990-5
3. Louis DN, Perry A, Wesseling P, Brat DJ, Cree IA, Figarella-Branger D, et al. The 2021 WHO classification of tumors of the central nervous system: a summary. *Neuro Oncol* 2021; **23**: 1231–51. https://doi.org/10.1093/neuonc/noab106
4. Louis DN, Perry A, Reifenberger G, von Deimling A, Figarella-Branger D, Cavenee WK, et al. The 2016 world health organization classification of tumors of the central nervous system: a summary. *Acta Neuropathol* 2016; **131**: 803–20. https://doi.org/10.1007/s00401-016-1545-1
5. Ellingson BM, Bendszus M, Boxerman J, Barboriak D, Erickson BJ, Smits M, et al. Consensus recommendations for a standardized brain tumor imaging protocol in clinical trials. *Neuro Oncol* 2015; **17**: 1188–98. https://doi.org/10.1093/neuonc/nov095
6. Chang P, Grinband J, Weinberg BD, Bardis M, Khy M, Cadena G, et al. Deep-learning convolutional neural networks accurately classify genetic mutations in gliomas. *AJNR Am J Neuroradiol* 2018; **39**: 1201–7. https://doi.org/10.3174/ajnr.A5667
7. Carrillo JA, Lai A, Nghiemphu PL, Kim HJ, Phillips HS, Kharbanda S, et al. Relationship between tumor enhancement, edema, IDH1 mutational status, MGMT promoter methylation, and survival in glioblastoma. *AJNR Am J Neuroradiol* 2012; **33**: 1349–55. https://doi.org/10.3174/ajnr.A2950
8. Hong EK, Choi SH, Shin DJ, Jo SW, Yoo R-E, Kang KM, et al. Radiogenomics correlation between MR imaging features and major genetic profiles in glioblastoma. *Eur Radiol* 2018; **28**: 4350–61. https://doi.org/10.1007/s00330-018-5400-8
9. Altieri R, Zenga F, Ducati A, Melcarne A, Cofano F, Mammi M, et al. Tumor location and patient age predict biological signatures of high-grade gliomas. *Neurosurg Rev* 2018; **41**: 599–604. https://doi.org/10.1007/s10143-017-0899-8
10. Tejada Neyra MA, Neuberger U, Reinhardt A, Brugnara G, Bonekamp D, Sill M, et al. Voxel-wise radiogenomic mapping of tumor location with key molecular alterations in patients with glioma. *Neuro Oncol* 2018; **20**: 1517–24. https://doi.org/10.1093/neuonc/noy134
11. Thon N, Kreth S, Kreth FW. Personalized treatment strategies in glioblastoma: MGMT promoter methylation status. *Onco Targets Ther* 2013; **6**: 1363–72. https://doi.org/10.2147/OTT.S50208
12. Mulholland S, Pearson DM, Hamoudi RA, Malley DS, Smith CM, Weaver JMJ, et al. MGMT cpg island is invariably methylated in adult astrocytic and oligodendroglial tumors with IDH1 or IDH2 mutations. *Int J Cancer* 2012; **131**: 1104–13. https://doi.org/10.1002/ijc.26499
13. Yoon RG, Kim HS, Paik W, Shim WH, Kim SJ, Kim JH. Different diagnostic values of imaging parameters to predict pseudoprogression in glioblastoma subgroups stratified by MGMT promoter methylation. *Eur Radiol* 2017; **27**: 255–66. https://doi.org/10.1007/s00330-016-4346-y
14. Ellingson BM, Lai A, Harris RJ, Selfridge JM, Yong WH, Das K, et al. Probabilistic radiographic atlas of glioblastoma phenotypes. *AJNR Am J Neuroradiol* 2013; **34**: 533–40. https://doi.org/10.3174/ajnr.A3253
15. Patel SH, Poisson LM, Brat DJ, Zhou Y, Cooper L, Snuderl M, et al. T2-FLAIR mismatch, an imaging biomarker for IDH and 1p/19q status in lower-grade gliomas: A TCGA/TCIA project. *Clin Cancer Res* 2017; **23**: 6078–85. https://doi.org/10.1158/1078-0432.CCR-17-0560
16. Broen MPG, Smits M, Wijnenga MMJ, Dubbink HJ, Anten MHME, Schijns OEMG, et al. The T2-FLAIR mismatch sign as an imaging marker for non-enhancing IDH-mutant, 1p/19q-intact lower-grade glioma: a validation study. *Neuro Oncol* 2018; **20**: 1393–99. https://doi.org/10.1093/neuonc/noy048
17. Smits M. Imaging of oligodendroglioma. *Br J Radiol* 2016; **89**: 20150857: 1060: . https://doi.org/10.1259/bjr.20150857
18. van den Bent MJ, Smits M, Kros JM, Chang SM. Diffuse infiltrating oligodendroglioma and astrocytoma. *J Clin Oncol* 2017; **35**: 2394–2401. https://doi.org/10.1200/JCO.2017.72.6737
19. Jenkinson MD, du Plessis DG, Smith TS, Joyce KA, Warnke PC, Walker C. Histological growth patterns and genotype in oligodendroglial tumours: correlation with MRI features. *Brain* 2006; **129**: 1884–91. https://doi.org/10.1093/brain/awl108
20. Zikou A, Sioka C, Alexiou GA, Fotopoulos A, Voulgaris S, Argyropoulou MI. Radiation necrosis, pseudoprogression, pseudoresponse, and tumor recurrence: imaging challenges for the evaluation of treated gliomas. *Contrast Media Mol*

Imaging 2018; **2018**: 6828396. https://doi.org/10.1155/2018/6828396

21. Young RJ, Gupta A, Shah AD, Graber JJ, Zhang Z, Shi W, et al. Potential utility of conventional MRI signs in diagnosing pseudoprogression in glioblastoma. *Neurology* 2011; **76**: 1918–24. https://doi.org/10.1212/WNL.0b013e31821d74e7
22. Bammer R. Basic principles of diffusion-weighted imaging. *Eur J Radiol* 2003; **45**: 169–84. https://doi.org/10.1016/s0720-048x(02)00303-0
23. Sugahara T, Korogi Y, Kochi M, Ikushima I, Shigematu Y, Hirai T, et al. Usefulness of diffusion-weighted MRI with echo-planar technique in the evaluation of cellularity in gliomas. *J Magn Reson Imaging* 1999; **9**: 53–60. https://doi.org/10.1002/(sici)1522-2586(199901)9:1<53::aid-jmri7>3.0.co;2-2
24. Ellingson BM, Malkin MG, Rand SD, Connelly JM, Quinsey C, LaViolette PS, et al. Validation of functional diffusion maps (fdms) as a biomarker for human glioma cellularity. *J Magn Reson Imaging* 2010; **31**: 538–48. https://doi.org/10.1002/jmri.22068
25. Farace P, Amelio D, Ricciardi GK, Zoccatelli G, Magon S, Pizzini F, et al. Early MRI changes in glioblastoma in the period between surgery and adjuvant therapy. *J Neurooncol* 2013; **111**: 177–85. https://doi.org/10.1007/s11060-012-0997-y
26. Chang PD, Chow DS, Yang PH, Filippi CG, Lignelli A. Predicting glioblastoma recurrence by early changes in the apparent diffusion coefficient value and signal intensity on FLAIR images. *AJR Am J Roentgenol* 2017; **208**: 57–65. https://doi.org/10.2214/AJR.16.16234
27. Buemi F, Guzzardi G, Del Sette B, Sponghini AP, Matheoud R, Soligo E, et al. Apparent diffusion coefficient and tumor volume measurements help stratify progression-free survival of bevacizumab-treated patients with recurrent glioblastoma multiforme. *Neuroradiol J* 2019; **32**: 241–49. https://doi.org/10.1177/1971400919847184
28. Patel KS, Everson RG, Yao J, Raymond C, Goldman J, Schlossman J, et al. Diffusion magnetic resonance imaging phenotypes predict overall survival benefit from bevacizumab or surgery in recurrent glioblastoma with large tumor burden. *Neurosurgery* 2020; **87**: 931–38. https://doi.org/10.1093/neuros/nyaa135
29. Park JE, Kim HS, Park SY, Jung SC, Kim JH, Heo HY. Identification of early response to anti-angiogenic therapy in recurrent glioblastoma: amide proton transfer-weighted and perfusion-weighted MRI compared with diffusion-weighted MRI. *Radiology* 2020; **295**: 397–406. https://doi.org/10.1148/radiol.2020191376
30. Kim BS, Kim ST, Kim JH, Seol HJ, Nam D-H, Shin HJ, et al. Apparent diffusion coefficient as a predictive biomarker for survival in patients with treatment-naive glioblastoma using quantitative multiparametric magnetic resonance profiling. *World Neurosurg* 2019; **122**: e812–20. https://doi.org/10.1016/j.wneu.2018.10.151
31. Romano A, Calabria LF, Tavanti F, Minniti G, Rossi-Espagnet MC, Coppola V, et al. Apparent diffusion coefficient obtained by magnetic resonance imaging as a prognostic marker in glioblastomas: correlation with MGMT promoter methylation status. *Eur Radiol* 2013; **23**: 513–20. https://doi.org/10.1007/s00330-012-2601-4
32. Auer TA, Breit H-C, Marini F, Renovanz M, Ringel F, Sommer CJ, et al. Evaluation of the apparent diffusion coefficient in patients with recurrent glioblastoma under treatment with bevacizumab with radiographic pseudoresponse. *J Neuroradiol* 2019; **46**: 36–43. https://doi.org/10.1016/j.neurad.2018.04.002
33. Zeng QS, Li CF, Liu H, Zhen JH, Feng DC. Distinction between recurrent glioma and radiation injury using magnetic resonance spectroscopy in combination with diffusion-weighted imaging. *Int J Radiat Oncol Biol Phys* 2007; **68**: 151–58. https://doi.org/10.1016/j.ijrobp.2006.12.001
34. Xu J-L, Li Y-L, Lian J-M, Dou S, Yan F-S, Wu H, et al. Distinction between postoperative recurrent glioma and radiation injury using MR diffusion tensor imaging. *Neuroradiology* 2010; **52**: 1193–99. https://doi.org/10.1007/s00234-010-0731-4
35. Lee WJ, Choi SH, Park C-K, Yi KS, Kim TM, Lee S-H, et al. Diffusion-weighted MR imaging for the differentiation of true progression from pseudoprogression following concomitant radiotherapy with temozolomide in patients with newly diagnosed high-grade gliomas. *Acad Radiol* 2012; **19**: 1353–61. https://doi.org/10.1016/j.acra.2012.06.011
36. Song YS, Choi SH, Park C-K, Yi KS, Lee WJ, Yun TJ, et al. True progression versus pseudoprogression in the treatment of glioblastomas: A comparison study of normalized cerebral blood volume and apparent diffusion coefficient by histogram analysis. *Korean J Radiol* 2013; **14**: 662–72. https://doi.org/10.3348/kjr.2013.14.4.662
37. Chu HH, Choi SH, Ryoo I, Kim SC, Yeom JA, Shin H, et al. Differentiation of true progression from pseudoprogression in glioblastoma treated with radiation therapy and concomitant temozolomide: comparison study of standard and high-b-value diffusion-weighted imaging. *Radiology* 2013; **269**: 831–40. https://doi.org/10.1148/radiol.13122024
38. Prager AJ, Martinez N, Beal K, Omuro A, Zhang Z, Young RJ. Diffusion and perfusion MRI to differentiate treatment-related changes including pseudoprogression from recurrent tumors in high-grade gliomas with histopathologic evidence. *AJNR Am J Neuroradiol* 2015; **36**: 877–85. https://doi.org/10.3174/ajnr.A4218
39. Kazda T, Bulik M, Pospisil P, Lakomy R, Smrcka M, Slampa P, et al. Advanced MRI increases the diagnostic accuracy of recurrent glioblastoma: single institution thresholds and validation of MR spectroscopy and diffusion weighted MR imaging. *Neuroimage Clin* 2016; **11**: 316–21. https://doi.org/10.1016/j.nicl.2016.02.016
40. Zakhari N, Taccone MS, Torres C, Chakraborty S, Sinclair J, Woulfe J, et al. Diagnostic accuracy of centrally restricted diffusion in the differentiation of treatment-related necrosis from tumor recurrence in high-grade gliomas. *AJNR Am J Neuroradiol* 2018; **39**: 260–64. https://doi.org/10.3174/ajnr.A5485
41. Yang Y, Yang Y, Wu X, Pan Y, Zhou D, Zhang H, et al. Adding DSC PWI and DWI to BT-RADS can help identify postoperative recurrence in patients with high-grade gliomas. *J Neurooncol* 2020; **146**: 363–71. https://doi.org/10.1007/s11060-019-03387-6
42. Park YW, Ahn SS, Kim EH, Kang S-G, Chang JH, Kim SH, et al. Differentiation of recurrent diffuse glioma from treatment-induced change using amide proton transfer imaging: incremental value to diffusion and perfusion parameters. *Neuroradiology* 2021; **63**: 363–72. https://doi.org/10.1007/s00234-020-02542-5
43. Lee WJ, Choi SH, Park C-K, Yi KS, Kim TM, Lee S-H, et al. Diffusion-weighted MR imaging for the differentiation of true progression from pseudoprogression following concomitant radiotherapy with temozolomide in patients with newly diagnosed high-grade gliomas. *Acad Radiol* 2012; **19**: 1353–61. https://doi.org/10.1016/j.acra.2012.06.011
44. Kazda T, Bulik M, Pospisil P, Lakomy R, Smrcka M, Slampa P, et al. Advanced MRI increases the diagnostic accuracy of recurrent glioblastoma: single institution thresholds and validation of MR spectroscopy and diffusion weighted MR imaging. *Neuroimage Clin* 2016; **11**: 316–21. https://doi.org/10.1016/j.nicl.2016.02.016

45. Yang Y, Yang Y, Wu X, Pan Y, Zhou D, Zhang H, et al. Adding DSC PWI and DWI to BT-RADS can help identify postoperative recurrence in patients with high-grade gliomas. *J Neurooncol* 2020; **146**: 363–71. https://doi.org/10.1007/s11060-019-03387-6
46. Park YW, Ahn SS, Kim EH, Kang S-G, Chang JH, Kim SH, et al. Differentiation of recurrent diffuse glioma from treatment-induced change using amide proton transfer imaging: incremental value to diffusion and perfusion parameters. *Neuroradiology* 2021; **63**: 363–72. https://doi.org/10.1007/s00234-020-02542-5
47. O'Donnell LJ, Westin C-F. An introduction to diffusion tensor image analysis. *Neurosurg Clin N Am* 2011; **22**: 185–96. https://doi.org/10.1016/j.nec.2010.12.004
48. Jellison BJ, Field AS, Medow J, Lazar M, Salamat MS, Alexander AL. Diffusion tensor imaging of cerebral white matter: a pictorial review of physics, fiber tract anatomy, and tumor imaging patterns. *AJNR Am J Neuroradiol* 2004; **25**: 356–69.
49. Henderson F, Abdullah KG, Verma R, Brem S. Tractography and the connectome in neurosurgical treatment of gliomas: the premise, the progress, and the potential. *Neurosurg Focus* 2020; **48**: 2019.11.FOCUS19785. https://doi.org/10.3171/2019.11.FOCUS19785
50. Mohan S, Wang S, Coban G, Kural F, Chawla S, O'Rourke DM, et al. Detection of occult neoplastic infiltration in the corpus callosum and prediction of overall survival in patients with glioblastoma using diffusion tensor imaging. *Eur J Radiol* 2019; **112**: 106–11. https://doi.org/10.1016/j.ejrad.2019.01.015
51. Peeken JC, Molina-Romero M, Diehl C, Menze BH, Straube C, Meyer B, et al. Deep learning derived tumor infiltration maps for personalized target definition in glioblastoma radiotherapy. *Radiother Oncol* 2019; **138**: 166–72. https://doi.org/10.1016/j.radonc.2019.06.031
52. Esmaeili M, Stensjøen AL, Berntsen EM, Solheim O, Reinertsen I. The direction of tumour growth in glioblastoma patients. *Sci Rep* 2018; **8**(1): 1199. https://doi.org/10.1038/s41598-018-19420-z
53. Wang S, Martinez-Lage M, Sakai Y, Chawla S, Kim SG, Alonso-Basanta M, et al. Differentiating tumor progression from pseudoprogression in patients with glioblastomas using diffusion tensor imaging and dynamic susceptibility contrast MRI. *AJNR Am J Neuroradiol* 2016; **37**: 28–36. https://doi.org/10.3174/ajnr.A4474
54. Razek A, El-Serougy L, Abdelsalam M, Gaballa G, Talaat M. Differentiation of residual/recurrent gliomas from postradiation necrosis with arterial spin labeling and diffusion tensor magnetic resonance imaging-derived metrics. *Neuroradiology* 2018; **60**: 169–77. https://doi.org/10.1007/s00234-017-1955-3
55. Xu J-L, Li Y-L, Lian J-M, Dou S, Yan F-S, Wu H, et al. Distinction between postoperative recurrent glioma and radiation injury using MR diffusion tensor imaging. *Neuroradiology* 2010; **52**: 1193–99. https://doi.org/10.1007/s00234-010-0731-4
56. Wang S, Martinez-Lage M, Sakai Y, Chawla S, Kim SG, Alonso-Basanta M, et al. Differentiating tumor progression from pseudoprogression in patients with glioblastomas using diffusion tensor imaging and dynamic susceptibility contrast MRI. *AJNR Am J Neuroradiol* 2016; **37**: 28–36. https://doi.org/10.3174/ajnr.A4474
57. Wang N, Jain RK, Batchelor TT. New directions in anti-angiogenic therapy for glioblastoma. *Neurotherapeutics* 2017; **14**: 321–32. https://doi.org/10.1007/s13311-016-0510-y
58. Essig M, Shiroishi MS, Nguyen TB, Saake M, Provenzale JM, Enterline D, et al. Perfusion MRI: the five most frequently asked technical questions. *AJR Am J Roentgenol* 2013; **200**: 24–34. https://doi.org/10.2214/AJR.12.9543
59. Petrella JR, Provenzale JM. MR perfusion imaging of the brain: techniques and applications. *AJR Am J Roentgenol* 2000; **175**: 207–19. https://doi.org/10.2214/ajr.175.1.1750207
60. Boxerman JL, Quarles CC, Hu LS, Erickson BJ, Gerstner ER, Smits M, et al. Consensus recommendations for a dynamic susceptibility contrast MRI protocol for use in high-grade gliomas. *Neuro Oncol* 2020; **22**: 1262–75. https://doi.org/10.1093/neuonc/noaa141
61. Oei MTH, Meijer FJA, Mordang J-J, Smit EJ, Idema AJS, Goraj BM, et al. Observer variability of reference tissue selection for relativecerebral blood volume measurements in glioma patients. *Eur Radiol* 2018; **28**: 3902–11. https://doi.org/10.1007/s00330-018-5353-y
62. Cha S, Knopp EA, Johnson G, Wetzel SG, Litt AW, Zagzag D. Intracranial mass lesions: dynamic contrast-enhanced susceptibility-weighted echo-planar perfusion MR imaging. *Radiology* 2002; **223**: 11–29. https://doi.org/10.1148/radiol.2231010594
63. Amukotuwa SA, Yu C, Zaharchuk G. 3D pseudocontinuous arterial spin labeling in routine clinical practice: A review of clinically significant artifacts. *J Magn Reson Imaging* 2016; **43**: 11–27. https://doi.org/10.1002/jmri.24873
64. Grade M, Hernandez Tamames JA, Pizzini FB, Achten E, Golay X, Smits M. A neuroradiologist's guide to arterial spin labeling MRI in clinical practice. *Neuroradiology* 2015; **57**: 1181–1202. https://doi.org/10.1007/s00234-015-1571-z
65. Haller S, Zaharchuk G, Thomas DL, Lovblad KO, Barkhof F, Golay X. Arterial spin labeling perfusion of the brain: emerging clinical applications. *Radiology* 2016; **281**: 337–56. https://doi.org/10.1148/radiol.2016150789
66. van Santwijk L, Kouwenberg V, Meijer F, Smits M, Henssen D. A systematic review and meta-analysis on the differentiation of glioma grade and mutational status by use of perfusion-based magnetic resonance imaging. *Insights Imaging* 2022; **13**(1): 102. https://doi.org/10.1186/s13244-022-01230-7
67. Alsaedi A, Doniselli F, Jäger HR, Panovska-Griffiths J, Rojas-Garcia A, Golay X, et al. The value of arterial spin labelling in adults glioma grading: systematic review and meta-analysis. *Oncotarget* 2019; **10**: 1589–1601. https://doi.org/10.18632/oncotarget.26674
68. Çoban G, Mohan S, Kural F, Wang S, O'Rourke DM, Poptani H. Prognostic value of dynamic susceptibility contrast-enhanced and diffusion-weighted MR imaging in patients with glioblastomas. *AJNR Am J Neuroradiol* 2015; **36**: 1247–52. https://doi.org/10.3174/ajnr.A4284
69. Rau MK, Braun C, Skardelly M, Schittenhelm J, Paulsen F, Bender B, et al. Prognostic value of blood flow estimated by arterial spin labeling and dynamic susceptibility contrast-enhanced MR imaging in high-grade gliomas. *J Neurooncol* 2014; **120**: 557–66. https://doi.org/10.1007/s11060-014-1586-z
70. Kim SH, Cho KH, Choi SH, Kim TM, Park CK, Park SH, et al. Prognostic predictions for patients with glioblastoma after standard treatment: application of contrast leakage information from DSC-MRI within nonenhancing FLAIR high-signal-intensity lesions. *AJNR Am J Neuroradiol* 2019; **40**: 2052–58. https://doi.org/10.3174/ajnr.A6297
71. Romano A, Pasquini L, Di Napoli A, Tavanti F, Boellis A, Rossi Espagnet MC, et al. Prediction of survival in patients affected by glioblastoma: histogram analysis of perfusion MRI. *J Neurooncol* 2018; **139**: 455–60. https://doi.org/10.1007/s11060-018-2887-4
72. Patel P, Baradaran H, Delgado D, Askin G, Christos P, John Tsiouris A, et al. MR perfusion-weighted imaging in the

evaluation of high-grade gliomas after treatment: a systematic review and meta-analysis. *Neuro Oncol* 2017; **19**: 118–27. https://doi.org/10.1093/neuonc/now148

73. van Dijken BRJ, van Laar PJ, Holtman GA, van der Hoorn A. Diagnostic accuracy of magnetic resonance imaging techniques for treatment response evaluation in patients with high-grade glioma, a systematic review and meta-analysis. *Eur Radiol* 2017; **27**: 4129–44. https://doi.org/10.1007/s00330-017-4789-9
74. Kim HS, Goh MJ, Kim N, Choi CG, Kim SJ, Kim JH. Which combination of MR imaging modalities is best for predicting recurrent glioblastoma? study of diagnostic accuracy and reproducibility. *Radiology* 2014; **273**: 831–43. https://doi.org/10.1148/radiol.14132868
75. Young RJ, Gupta A, Shah AD, Graber JJ, Chan TA, Zhang Z, et al. MRI perfusion in determining pseudoprogression in patients with glioblastoma. *Clin Imaging* 2013; **37**: 41–49. https://doi.org/10.1016/j.clinimag.2012.02.016
76. Nael K, Bauer AH, Hormigo A, Lemole M, Germano IM, Puig J, et al. Multiparametric MRI for differentiation of radiation necrosis from recurrent tumor in patients with treated glioblastoma. *AJR Am J Roentgenol* 2018; **210**: 18–23. https://doi.org/10.2214/AJR.17.18003
77. Di Costanzo A, Scarabino T, Trojsi F, Popolizio T, Bonavita S, de Cristofaro M, et al. Recurrent glioblastoma multiforme versus radiation injury: a multiparametric 3-T MR approach. *Radiol Med* 2014; **119**: 616–24. https://doi.org/10.1007/s11547-013-0371-y
78. Welker K, Boxerman J, Kalnin A, Kaufmann T, Shiroishi M, Wintermark M, et al. ASFNR recommendations for clinical performance of MR dynamic susceptibility contrast perfusion imaging of the brain. *AJNR Am J Neuroradiol* 2015; **36**: E41–51. https://doi.org/10.3174/ajnr.A4341
79. Alsop DC, Detre JA, Golay X, Gunther M, Hendrikse J, Hernandez-Garcia L, et al. Recommended implementation of arterial spin-labeled perfusion MRI for clinical applications: A consensus of the ISMRM perfusion study group and the european consortium for ASL in dementia. *Magn Reson Med* 2015; **73**: 102–16. https://doi.org/10.1002/mrm.25197
80. Smits M, Bendszus M, Collette S, Postma LA, Dhermain F, Hagenbeek RE, et al. Repeatability and reproducibility of relative cerebral blood volume measurement of recurrent glioma in a multicentre trial setting. *Eur J Cancer* 2019; **114**: 89–96. https://doi.org/10.1016/j.ejca.2019.03.007
81. Castillo M, Kwock L, Mukherji SK. Clinical applications of proton MR spectroscopy. *AJNR Am J Neuroradiol* 1996; **17**: 1–15.
82. van der Graaf M. In vivo magnetic resonance spectroscopy: basic methodology and clinical applications. *Eur Biophys J* 2010; **39**: 527–40. https://doi.org/10.1007/s00249-009-0517-y
83. Chawla S, Oleaga L, Wang S, Krejza J, Wolf RL, Woo JH, et al. Role of proton magnetic resonance spectroscopy in differentiating oligodendrogliomas from astrocytomas. *J Neuroimaging* 2010; **20**: 3–8. https://doi.org/10.1111/j.1552-6569.2008.00307.x
84. Chawla S, Wang S, Wolf RL, Woo JH, Wang J, O'Rourke DM, et al. Arterial spin-labeling and MR spectroscopy in the differentiation of gliomas. *AJNR Am J Neuroradiol* 2007; **28**: 1683–89. https://doi.org/10.3174/ajnr.A0673
85. Bulik M, Jancalek R, Vanicek J, Skoch A, Mechl M. Potential of MR spectroscopy for assessment of glioma grading. *Clin Neurol Neurosurg* 2013; **115**: 146–53. https://doi.org/10.1016/j.clineuro.2012.11.002
86. Mohan S, Chawla S, Wang S, Verma G, Skolnik A, Brem S, et al. Assessment of early response to tumor-treating fields in newly diagnosed glioblastoma using physiologic and metabolic MRI: initial experience. *CNS Oncol* 2016; **5**: 137–44. https://doi.org/10.2217/cns-2016-0003
87. Verma G, Chawla S, Mohan S, Wang S, Nasrallah M, Sheriff S, et al. Three-dimensional echo planar spectroscopic imaging for differentiation of true progression from pseudoprogression in patients with glioblastoma. *NMR Biomed* 2019; **32**(2): e4042. https://doi.org/10.1002/nbm.4042
88. Mader I, Rauer S, Gall P, Klose U. (1)H MR spectroscopy of inflammation, infection and ischemia of the brain. *Eur J Radiol* 2008; **67**: 250–57. https://doi.org/10.1016/j.ejrad.2008.02.033
89. Aquino D, Gioppo A, Finocchiaro G, Bruzzone MG, Cuccarini V. MRI in glioma immunotherapy: evidence, pitfalls, and perspectives. *J Immunol Res* 2017; **2017**: 5813951. https://doi.org/10.1155/2017/5813951
90. D'Souza MM, Sharma R, Jaimini A, Panwar P, Saw S, Kaur P, et al. 11C-MET PET/CT and advanced MRI in the evaluation of tumor recurrence in high-grade gliomas. *Clin Nucl Med* 2014; **39**: 791–98. https://doi.org/10.1097/RLU.0000000000000532
91. Seeger A, Braun C, Skardelly M, Paulsen F, Schittenhelm J, Ernemann U, et al. Comparison of three different MR perfusion techniques and MR spectroscopy for multiparametric assessment in distinguishing recurrent high-grade gliomas from stable disease. *Acad Radiol* 2013; **20**: 1557–65. https://doi.org/10.1016/j.acra.2013.09.003
92. Zeng QS, Li CF, Zhang K, Liu H, Kang XS, Zhen JH. Multivoxel 3D proton MR spectroscopy in the distinction of recurrent glioma from radiation injury. *J Neurooncol* 2007; **84**: 63–69. https://doi.org/10.1007/s11060-007-9341-3
93. Cui Y, Zeng W, Jiang H, Ren X, Lin S, Fan Y, et al. Higher cho/NAA ratio in postoperative peritumoral edema zone is associated with earlier recurrence of glioblastoma. *Front Neurol* 2020; **11**: 592155. https://doi.org/10.3389/fneur.2020.592155
94. Di Ieva A, Magnussen JS, McIntosh J, Mulcahy MJ, Pardey M, Choi C. Magnetic resonance spectroscopic assessment of isocitrate dehydrogenase status in gliomas: the new frontiers of spectrobiopsy in neurodiagnostics. *World Neurosurg* 2020; **133**: e421–27. https://doi.org/10.1016/j.wneu.2019.09.040
95. Pope WB, Prins RM, Albert Thomas M, Nagarajan R, Yen KE, Bittinger MA, et al. Non-invasive detection of 2-hydroxyglutarate and other metabolites in IDH1 mutant glioma patients using magnetic resonance spectroscopy. *J Neurooncol* 2012; **107**: 197–205. https://doi.org/10.1007/s11060-011-0737-8
96. Choi C, Raisanen JM, Ganji SK, Zhang S, McNeil SS, An Z, et al. Prospective longitudinal analysis of 2-hydroxyglutarate magnetic resonance spectroscopy identifies broad clinical utility for the management of patients with IDH-mutant glioma. *J Clin Oncol* 2016; **34**: 4030–39. https://doi.org/10.1200/JCO.2016.67.1222
97. Bhandari A, Sharma C, Ibrahim M, Riggs M, Jones R, Lasocki A. The role of 2-hydroxyglutarate magnetic resonance spectroscopy for the determination of isocitrate dehydrogenase status in lower grade gliomas versus glioblastoma: a systematic review and meta-analysis of diagnostic test accuracy. *Neuroradiology* 2021; **63**: 1823–30. https://doi.org/10.1007/s00234-021-02702-1
98. [cited 2021 2nd November]; Available from. Available from: http://s-provencher.com/lcmodel.shtml
99. Albert NL, Weller M, Suchorska B, Galldiks N, Soffietti R, Kim MM, et al. Response assessment in neuro-oncology working group and european association for neuro-oncology recommendations for the clinical

use of PET imaging in gliomas. *Neuro Oncol* 2016; **18**: 1199–1208. https://doi.org/10.1093/neuonc/now058

100. Herholz K. Brain tumors: an update on clinical PET research in gliomas. *Semin Nucl Med* 2017; **47**: 5–17. https://doi.org/10.1053/j.semnuclmed.2016.09.004
101. Manabe O, Hattori N, Yamaguchi S, Hirata K, Kobayashi K, Terasaka S, et al. Oligodendroglial component complicates the prediction of tumour grading with metabolic imaging. *Eur J Nucl Med Mol Imaging* 2015; **42**: 896–904. https://doi.org/10.1007/s00259-015-2996-7
102. Valentini MC, Mellai M, Annovazzi L, Melcarne A, Denysenko T, Cassoni P, et al. Comparison among conventional and advanced MRI, ^{18}F-FDG PET/CT, phenotype and genotype in glioblastoma. *Oncotarget* 2017; **8**: 53: 91636–53: . https://doi.org/10.18632/oncotarget.21482
103. Makino K, Hirai T, Nakamura H, Murakami R, Kitajima M, Shigematsu Y, et al. Does adding FDG-PET to MRI improve the differentiation between primary cerebral lymphoma and glioblastoma? observer performance study. *Ann Nucl Med* 2011; **25**: 432–38. https://doi.org/10.1007/s12149-011-0483-1
104. Nakajima S, Okada T, Yamamoto A, Kanagaki M, Fushimi Y, Okada T, et al. Primary central nervous system lymphoma and glioblastoma: differentiation using dynamic susceptibility-contrast perfusion-weighted imaging, diffusion-weighted imaging, and (18)F-fluorodeoxyglucose positron emission tomography. *Clin Imaging* 2015; **39**: 390–95. https://doi.org/10.1016/j.clinimag.2014.12.002
105. Yamashita K, Hiwatashi A, Togao O, Kikuchi K, Kitamura Y, Mizoguchi M, et al. Diagnostic utility of intravoxel incoherent motion mr imaging in differentiating primary central nervous system lymphoma from glioblastoma multiforme. *J Magn Reson Imaging* 2016; **44**: 1256–61. https://doi.org/10.1002/jmri.25261
106. Zou Y, Tong J, Leng H, Jiang J, Pan M, Chen Z. Diagnostic value of using 18F-FDG PET and PET/CT in immunocompetent patients with primary central nervous system lymphoma: A systematic review and meta-analysis. *Oncotarget* 2017; **8**: 41518–28. https://doi.org/10.18632/oncotarget.17456
107. Kosaka N, Tsuchida T, Uematsu H, Kimura H, Okazawa H, Itoh H. 18F-FDG PET of common enhancing malignant brain tumors. *AJR Am J Roentgenol* 2008; **190**: W365–9. https://doi.org/10.2214/AJR.07.2660
108. Makino K, Hirai T, Nakamura H, Murakami R, Kitajima M, Shigematsu Y, et al. Does adding FDG-PET to MRI improve the differentiation between primary cerebral lymphoma and glioblastoma? observer performance study. *Ann Nucl Med* 2011; **25**: 432–38. https://doi.org/10.1007/s12149-011-0483-1
109. Nakajima S, Okada T, Yamamoto A, Kanagaki M, Fushimi Y, Okada T, et al. Primary central nervous system lymphoma and glioblastoma: differentiation using dynamic susceptibility-contrast perfusion-weighted imaging, diffusion-weighted imaging, and 18f-fluorodeoxyglucose positron emission tomography. *Clinical Imaging* 2015; **39**: 390–95. https://doi.org/10.1016/j.clinimag.2014.12.002
110. Iagaru A, Mosci C, Mittra E, Zaharchuk G, Fischbein N, Harsh G, et al. Glioblastoma multiforme recurrence: an exploratory study of (18)f FPPRGD2 PET/CT. *Radiology* 2015; **277**: 497–506. https://doi.org/10.1148/radiol.2015141550
111. Seligman L, Kovanlikaya I, Pisapia DJ, Naeger DM, Magge R, Fine HA, et al. Integrated PET-MRI for glioma surveillance: perfusion-metabolism discordance rate and association with molecular profiling. *AJR Am J Roentgenol* 2019; **212**: 883–91. https://doi.org/10.2214/AJR.18.20531
112. Hatzoglou V, Yang TJ, Omuro A, Gavrilovic I, Ulaner G, Rubel J, et al. A prospective trial of dynamic contrast-enhanced MRI perfusion and fluorine-18 FDG PET-CT in differentiating brain tumor progression from radiation injury after cranial irradiation. *Neuro Oncol* 2016; **18**: 873–80. https://doi.org/10.1093/neuonc/nov301
113. Kim YH, Oh SW, Lim YJ, Park C-K, Lee S-H, Kang KW, et al. Differentiating radiation necrosis from tumor recurrence in high-grade gliomas: assessing the efficacy of 18f-FDG PET, 11c-methionine PET and perfusion MRI. *Clin Neurol Neurosurg* 2010; **112**: 758–65. https://doi.org/10.1016/j.clineuro.2010.06.005
114. Prat R, Galeano I, Lucas A, Martínez JC, Martín M, Amador R, et al. Relative value of magnetic resonance spectroscopy, magnetic resonance perfusion, and 2-(18f) fluoro-2-deoxy-D-glucose positron emission tomography for detection of recurrence or grade increase in gliomas. *J Clin Neurosci* 2010; **17**: 50–53. https://doi.org/10.1016/j.jocn.2009.02.035
115. Hojjati M, Badve C, Garg V, Tatsuoka C, Rogers L, Sloan A, et al. Role of FDG-PET/MRI, FDG-PET/CT, and dynamic susceptibility contrast perfusion MRI in differentiating radiation necrosis from tumor recurrence in glioblastomas. *J Neuroimaging* 2018; **28**: 118–25. https://doi.org/10.1111/jon.12460
116. Jena A, Taneja S, Jha A, Damesha NK, Negi P, Jadhav GK, et al. Multiparametric evaluation in differentiating glioma recurrence from treatment-induced necrosis using simultaneous ^{18}F-FDG-PET/MRI: A single-institution retrospective study. *AJNR Am J Neuroradiol* 2017; **38**: 899–907. https://doi.org/10.3174/ajnr.A5124
117. Lundemann M, Munck Af Rosenschöld P, Muhic A, Larsen VA, Poulsen HS, Engelholm S-A, et al. Feasibility of multi-parametric PET and MRI for prediction of tumour recurrence in patients with glioblastoma. *Eur J Nucl Med Mol Imaging* 2019; **46**: 603–13. https://doi.org/10.1007/s00259-018-4180-3
118. Ozsunar Y, Mullins ME, Kwong K, Hochberg FH, Ament C, Schaefer PW, et al. Glioma recurrence versus radiation necrosis? A pilot comparison of arterial spin-labeled, dynamic susceptibility contrast enhanced MRI, and FDG-PET imaging. *Acad Radiol* 2010; **17**: 282–90. https://doi.org/10.1016/j.acra.2009.10.024
119. Cui M, Zorrilla-Veloz RI, Hu J, Guan B, Ma X. Diagnostic accuracy of PET for differentiating true glioma progression from post treatment-related changes: A systematic review and meta-analysis. *Front Neurol* 2021; **12**: 671867. https://doi.org/10.3389/fneur.2021.671867
120. Rapp M, Heinzel A, Galldiks N, Stoffels G, Felsberg J, Ewelt C, et al. diagnostic performance of ^{18} f-FET PET in newly diagnosed cerebral lesions suggestive of glioma . *J Nucl Med* 2013; **54**: 229–35. https://doi.org/10.2967/jnumed.112.109603
121. Hutterer M, Nowosielski M, Putzer D, Jansen NL, Seiz M, Schocke M, et al. [18F]-fluoro-ethyl-L-tyrosine PET: a valuable diagnostic tool in neuro-oncology, but not all that glitters is glioma. *Neuro-Oncology* 2013; **15**: 341–51. https://doi.org/10.1093/neuonc/nos300
122. Jansen NL, Suchorska B, Wenter V, Schmid-Tannwald C, Todica A, Eigenbrod S, et al. prognostic significance of dynamic ^{18} f-FET PET in newly diagnosed astrocytic high-grade glioma . *J Nucl Med* 2013; **56**: 9–15. https://doi.org/10.2967/jnumed.114.144675
123. Pöpperl G, Kreth FW, Mehrkens JH, Herms J, Seelos K, Koch W, et al. FET PET for the evaluation of untreated gliomas: correlation of FET uptake and uptake kinetics with tumour grading. *Eur J Nucl Med Mol Imaging* 2013; **34**: 1933–42. https://doi.org/10.1007/s00259-007-0534-y

124. Lohmann P, Herzog H, Rota Kops E, Stoffels G, Judov N, Filss C, et al. Dual-time-point O-(2-[18f]fluoroethyl)-L-tyrosine PET for grading of cerebral gliomas. *Eur Radiol* 2013; **25**: 3017–24. https://doi.org/10.1007/s00330-015-3691-6
125. Dunet V, Maeder P, Nicod-Lalonde M, Lhermitte B, Pollo C, Bloch J, et al. Combination of MRI and dynamic FET PET for initial glioma grading. *Nuklearmedizin* 2014; **53**: 155–61. https://doi.org/10.3413/Nukmed-0650-14-03
126. Moulin-Romsée G, D'Hondt E, de Groot T, Goffin J, Sciot R, Mortelmans L, et al. Non-invasive grading of brain tumours using dynamic amino acid PET imaging: does it work for 11C-methionine? *Eur J Nucl Med Mol Imaging* 2007; **34**: 2082–87. https://doi.org/10.1007/s00259-007-0557-4
127. Kratochwil C, Combs SE, Leotta K, Afshar-Oromieh A, Rieken S, Debus J, et al. Intra-individualcomparison of (1)(8)F-FET and (1)(8)F-DOPA in PET imaging of recurrent brain tumors. *Neuro Oncol* 2014; **16**: 434–40. https://doi.org/10.1093/neuonc/not199
128. Schiepers C, Chen W, Cloughesy T, Dahlbom M, Huang SC. 18F-FDOPA kinetics in brain tumors. *J Nucl Med* 2007; **48**: 1651–61. https://doi.org/10.2967/jnumed.106.039321
129. Pauleit D, Floeth F, Hamacher K, Riemenschneider MJ, Reifenberger G, Müller H-W, et al. O-(2-[18F]fluoroethyl)-L-tyrosine PET combined with MRI improves the diagnostic assessment of cerebral gliomas. *Brain* 2005; **128**: 678–87. https://doi.org/10.1093/brain/awh399
130. Lopez WOC, Cordeiro JG, Albicker U, Doostkam S, Nikkhah G, Kirch RD, et al. Correlation of (18)F-fluoroethyl tyrosine positron-emission tomography uptake values and histomorphological findings by stereotactic serial biopsy in newly diagnosed brain tumors using a refined software tool. *Onco Targets Ther* 2015; **8**: 3803–15. https://doi.org/10.2147/OTT.S87126
131. Filss CP, Galldiks N, Stoffels G, Sabel M, Wittsack HJ, Turowski B, et al. Comparison of 18F-FET PET and perfusion-weighted MR imaging: a PET/MR imaging hybrid study in patients with brain tumors. *J Nucl Med* 2014; **55**: 540–45. https://doi.org/10.2967/jnumed.113.129007
132. Cicone F, Filss CP, Minniti G, Rossi-Espagnet C, Papa A, Scaringi C, et al. Volumetric assessment of recurrent or progressive gliomas: comparison between F-DOPA PET and perfusion-weighted MRI. *Eur J Nucl Med Mol Imaging* 2015; **42**: 905–15. https://doi.org/10.1007/s00259-015-3018-5
133. Pafundi DH, Laack NN, Youland RS, Parney IF, Lowe VJ, Giannini C, et al. Biopsy validation of 18F-DOPA PET and biodistribution in gliomas for neurosurgical planning and radiotherapy target delineation: results of a prospective pilot study. *Neuro Oncol* 2013; **15**: 1058–67. https://doi.org/10.1093/neuonc/not002
134. Kosztyla R, Chan EK, Hsu F, Wilson D, Ma R, Cheung A, et al. High-grade glioma radiation therapy target volumes and patterns of failure obtained from magnetic resonance imaging and 18F-FDOPA positron emission tomography delineations from multiple observers. *Int J Radiat Oncol Biol Phys* 2013; **87**: 1100–1106. https://doi.org/10.1016/j.ijrobp.2013.09.008
135. Galldiks N, Ullrich R, Schroeter M, Fink GR, Jacobs AH, Kracht LW. Volumetry of [(11)c]-methionine pet uptake and mri contrast enhancement in patients with recurrent glioblastoma multiforme. *Eur J Nucl Med Mol Imaging* 2010; **37**: 84–92. https://doi.org/10.1007/s00259-009-1219-5
136. Harris RJ, Cloughesy TF, Pope WB, Nghiemphu PL, Lai A, Zaw T, et al. 18F-FDOPA and 18F-FLT positron emission tomography parametric response maps predict response in recurrent malignant gliomas treated with bevacizumab. *Neuro Oncol* 2012; **14**: 1079–89. https://doi.org/10.1093/neuonc/nos141
137. Schwarzenberg J, Czernin J, Cloughesy TF, Ellingson BM, Pope WB, Grogan T, et al. Treatment response evaluation using 18F-FDOPA PET in patients with recurrent malignant glioma on bevacizumab therapy. *Clin Cancer Res* 2014; **20**: 3550–59. https://doi.org/10.1158/1078-0432.CCR-13-1440
138. Pirotte B, Goldman S, Brucher JM, Zomosa G, Baleriaux D, Brotchi J, et al. PET in stereotactic conditions increases the diagnostic yield of brain biopsy. *Stereotact Funct Neurosurg* 1994; **63**: 144–49. https://doi.org/10.1159/000100306
139. Lindberg OR, McKinney A, Engler JR, Koshkakaryan G, Gong H, Robinson AE, et al. GBM heterogeneity as a function of variable epidermal growth factor receptor variant III activity. *Oncotarget* 2016; **7**: 79101–16. https://doi.org/10.18632/oncotarget.12600
140. Pirotte B, Goldman S, Massager N, David P, Wikler D, Vandesteene A, et al. Comparison of 18F-FDG and 11C-methionine for PET-guided stereotactic brain biopsy of gliomas. *J Nucl Med* 2004; **45**: 1293–98.
141. Furtak J, Rakowska J, Szylberg T, Harat M, Małkowski B, Harat M. Glioma biopsy based on hybrid dual time-point FET-PET/MRI-A proof of concept study. *Front Neurol* 2021; **12**: 634609. https://doi.org/10.3389/fneur.2021.634609
142. Heinzel A, Stock S, Langen K-J, Müller D. Cost-effectiveness analysis of FET PET-guided target selection for the diagnosis of gliomas. *Eur J Nucl Med Mol Imaging* 2012; **39**: 1089–96. https://doi.org/10.1007/s00259-012-2093-0
143. Navarria P, Reggiori G, Pessina F, Ascolese AM, Tomatis S, Mancosu P, et al. Investigation on the role of integrated PET/MRI for target volume definition and radiotherapy planning in patients with high grade glioma. *Radiother Oncol* 2014; **112**: 425–29. https://doi.org/10.1016/j.radonc.2014.09.004
144. Lee IH, Piert M, Gomez-Hassan D, Junck L, Rogers L, Hayman J, et al. Association of 11C-methionine PET uptake with site of failure after concurrent temozolomide and radiation for primary glioblastoma multiforme. *Int J Radiat Oncol Biol Phys* 2009; **73**: 479–85. https://doi.org/10.1016/j.ijrobp.2008.04.050
145. Grosu AL, Weber WA, Riedel E, Jeremic B, Nieder C, Franz M, et al. L-(methyl-11C) methionine positron emission tomography for target delineation in resected high-grade gliomas before radiotherapy. *Int J Radiat Oncol Biol Phys* 2005; **63**: 64–74.
146. Munck Af Rosenschold P, Costa J, Engelholm SA, Lundemann MJ, Law I, Ohlhues L, et al. Impact of [18f]-fluoro-ethyl-tyrosine PET imaging on target definition for radiation therapy of high-grade glioma. *Neuro Oncol* 2015; **17**: 757–63. https://doi.org/10.1093/neuonc/nou316
147. Rieken S, Habermehl D, Giesel FL, Hoffmann C, Burger U, Rief H, et al. Analysis of FET-PET imaging for target volume definition in patients with gliomas treated with conformal radiotherapy. *Radiother Oncol* 2013; **109**: 487–92. https://doi.org/10.1016/j.radonc.2013.06.043
148. Piroth MD, Galldiks N, Pinkawa M, Holy R, Stoffels G, Ermert J, et al. Relapse patterns after radiochemotherapy of glioblastoma with FET PET-guided boost irradiation and simulation to optimize radiation target volume. *Radiat Oncol* 2016; **11**. https://doi.org/10.1186/s13014-016-0665-z
149. Lundemann M, Costa JC, Law I, Engelholm SA, Muhic A, Poulsen HS, et al. Patterns of failure for patients with glioblastoma following 0-(2-[F-18] fluoroethyl)-L-tyrosine PET- and MRI-guided radiotherapy. *Radiother Oncol* 2017; **122**: 380–86.
150. Takenaka S, Asano Y, Shinoda J, Nomura Y, Yonezawa S, Miwa K, et al. Comparison

of (11)C-methionine, (11)C-choline, and (18)F-fluorodeoxyglucose-PET for distinguishing glioma recurrence from radiation necrosis. *Neurol Med Chir (Tokyo)* 2014; **54**: 280–89. https://doi.org/10.2176/nmc.oa2013-0117

151. Kim YH, Oh SW, Lim YJ, Park C-K, Lee S-H, Kang KW, et al. Differentiating radiation necrosis from tumor recurrence in high-grade gliomas: assessing the efficacy of 18F-FDG PET, 11C-methionine PET and perfusion MRI. *Clin Neurol Neurosurg* 2010; **112**: 758–65. https://doi.org/10.1016/j.clineuro.2010.06.005
152. Deuschl C, Kirchner J, Poeppel TD, Schaarschmidt B, Kebir S, El Hindy N, et al. 11C–MET PET/MRI for detection of recurrent glioma. *Eur J Nucl Med Mol Imaging* 2018; **45**: 593–601. https://doi.org/10.1007/s00259-017-3916-9
153. Minamimoto R, Saginoya T, Kondo C, Tomura N, Ito K, Matsuo Y, et al. Differentiation of brain tumor recurrence from post-radiotherapy necrosis with 11C-methionine PET: visual assessment versus quantitative assessment. *PLoS One* 2015; **10**(7): e0132515. https://doi.org/10.1371/journal.pone.0132515
154. Okamoto S, Shiga T, Hattori N, Kubo N, Takei T, Katoh N, et al. Semiquantitative analysis of C-11 methionine PET may distinguish brain tumor recurrence from radiation necrosis even in small lesions. *Ann Nucl Med* 2011; **25**: 213–20. https://doi.org/10.1007/s12149-010-0450-2
155. Tomura N, Kokubun M, Saginoya T, Mizuno Y, Kikuchi Y. Differentiation between treatment-induced necrosis and recurrent tumors in patients with metastatic brain tumors: comparison among ^{11}C-methionine-PET, FDG-PET, MR permeability imaging, and MRI-ADC-preliminary results. *AJNR Am J Neuroradiol* 2017; **38**: 1520–27. https://doi.org/10.3174/ajnr.A5252
156. Terakawa Y, Tsuyuguchi N, Iwai Y, Yamanaka K, Higashiyama S, Takami T, et al. Diagnostic accuracy of 11C-methionine PET for differentiation of recurrent brain tumors from radiation necrosis after radiotherapy. *J Nucl Med* 2008; **49**: 694–99. https://doi.org/10.2967/jnumed.107.048082
157. Dandois V, Rommel D, Renard L, Jamart J, Cosnard G. Substitution of 11C-methionine PET by perfusion MRI during the follow-up of treated high-grade gliomas: preliminary results in clinical practice. *J Neuroradiol* 2010; **37**: 89–97. https://doi.org/10.1016/j.neurad.2009.04.005
158. Qiao Z, Zhao X, Wang K, Zhang Y, Fan D, Yu T, et al. Utility of dynamic susceptibility contrast perfusion-weighted MR imaging and ^{11}C-methionine PET/CT for differentiation of tumor recurrence from radiation injury in patients with high-grade gliomas. *AJNR Am J Neuroradiol* 2019; **40**: 253–59. https://doi.org/10.3174/ajnr.A5952
159. Kim YH, Oh SW, Lim YJ, Park C-K, Lee S-H, Kang KW, et al. Differentiating radiation necrosis from tumor recurrence in high-grade gliomas: assessing the efficacy of 18F-FDG PET, 11C-methionine PET and perfusion MRI. *Clin Neurol Neurosurg* 2010; **112**: 758–65. https://doi.org/10.1016/j.clineuro.2010.06.005
160. Steidl E, Langen K-J, Hmeidan SA, Polomac N, Filss CP, Galldiks N, et al. Sequential implementation of dsc-mr perfusion and dynamic [^{18}f]fet pet allows efficient differentiation of glioma progression from treatment-related changes. *Eur J Nucl Med Mol Imaging* 2021; **48**: 1956–65. https://doi.org/10.1007/s00259-020-05114-0
161. Clement P, Smits M, van Osch MJP, Costa BM, Warnert EAH. Micro- to macroscale magnetic resonance imaging of glioma. *MAGMA* 2022; **35**: 1–2. https://doi.org/10.1007/s10334-021-00999-w
162. Galldiks N, Stoffels G, Filss C, Rapp M, Blau T, Tscherpel C, et al. The use of dynamic O-(2-18F-fluoroethyl)-l-tyrosine PET in the diagnosis of patients with progressive and recurrent glioma. *Neuro Oncol* 2015; **17**: 1293–1300. https://doi.org/10.1093/neuonc/nov088
163. Jena A, Taneja S, Gambhir A, Mishra AK, D'souza MM, Verma SM, et al. Glioma recurrence versus radiation necrosis: single-session multiparametric approach using simultaneous O-(2-18F-fluoroethyl)-L-tyrosine PET/MRI. *Clin Nucl Med* 2016; **41**: e228–36. https://doi.org/10.1097/RLU.0000000000001152
164. Pyka T, Hiob D, Preibisch C, Gempt J, Wiestler B, Schlegel J, et al. Diagnosis of glioma recurrence using multiparametric dynamic 18F-fluoroethyl-tyrosine PET-MRI. *Eur J Radiol* 2018; **103**: 32–37. https://doi.org/10.1016/j.ejrad.2018.04.003
165. Sogani SK, Jena A, Taneja S, Gambhir A, Mishra AK, D'Souza MM, et al. Potential for differentiation of glioma recurrence from radionecrosis using integrated ^{18}F-fluoroethyl-L-tyrosine (FET) positron emission tomography/magnetic resonance imaging: A prospective evaluation. *Neurol India* 2017; **65**: 293–301. https://doi.org/10.4103/neuroindia.NI_101_16
166. Verger A, Filss CP, Lohmann P, Stoffels G, Sabel M, Wittsack H-J, et al. Comparison of O-(2-^{18}f-fluoroethyl)-L-tyrosine positron emission tomography and perfusion-weighted magnetic resonance imaging in the diagnosis of patients with progressive and recurrent glioma: A hybrid positron emission tomography/magnetic resonance study. *World Neurosurg* 2018; **113**: e727–37. https://doi.org/10.1016/j.wneu.2018.02.139
167. Furuse M, Nonoguchi N, Yamada K, Shiga T, Combes J-D, Ikeda N, et al. Radiological diagnosis of brain radiation necrosis after cranial irradiation for brain tumor: a systematic review. *Radiat Oncol* 2019; **14**: 28. https://doi.org/10.1186/s13014-019-1228-x
168. Yu J, Zheng J, Xu W, Weng J, Gao L, Tao L, et al. Accuracy of ^{18}f-FDOPA positron emission tomography and ^{18}f-FET positron emission tomography for differentiating radiation necrosis from brain tumor recurrence. *World Neurosurg* 2018; **114**: e1211–24. https://doi.org/10.1016/j.wneu.2018.03.179
169. Fraioli F, Shankar A, Hyare H, Ferrazzoli V, Militano V, Samandouras G, et al. The use of multiparametric 18F-fluoro-L-3,4-dihydroxy-phenylalanine PET/MRI in post-therapy assessment of patients with gliomas. *Nucl Med Commun* 2020; **41**: 517–25. https://doi.org/10.1097/MNM.0000000000001184
170. Pellerin A, Khalifé M, Sanson M, Rozenblum-Beddok L, Bertaux M, Soret M, et al. Simultaneously acquired PET and ASL imaging biomarkers may be helpful in differentiating progression from pseudo-progression in treated gliomas. *Eur Radiol* 2021; **31**: 7395–7405. https://doi.org/10.1007/s00330-021-07732-0
171. Karunanithi S, Sharma P, Kumar A, Khangembam BC, Bandopadhyaya GP, Kumar R, et al. 18F-FDOPA PET/CT for detection of recurrence in patients with glioma: prospective comparison with 18F-FDG PET/CT. *Eur J Nucl Med Mol Imaging* 2013; **40**: 1025–35. https://doi.org/10.1007/s00259-013-2384-0
172. Clement P, Booth T, Borovečki F, Emblem KE, Figueiredo P, Hirschler L, et al. GliMR: cross-border collaborations to promote advanced MRI biomarkers for glioma. *J Med Biol Eng* 2021; **41**: 115–25. https://doi.org/10.1007/s40846-020-00582-z
173. Jensen JH, Helpern JA, Ramani A, Lu HZ, Kaczynski K. Diffusional kurtosis imaging: the quantification of non-gaussian water diffusion by means of magnetic resonance imaging. *Magn Reson Med* 2005; **53**: 1432–40. https://doi.org/10.1002/mrm.20508
174. Delgado AF, Fahlström M, Nilsson M, Berntsson SG, Zetterling M, Libard S, et al. Diffusion kurtosis imaging of gliomas

grades II and III - a study of perilesional tumor infiltration, tumor grades and subtypes at clinical presentation. *Radiol Oncol* 2017; **51**: 121–29. https://doi.org/10.1515/raon-2017-0010

175. Qiu J, Deng K, Wang P, Chen C, Luo Y, Yuan S, et al. Application of diffusion kurtosis imaging to the study of edema in solid and peritumoral areas of glioma. *Magn Reson Imaging* 2022; **86**: 10–16. https://doi.org/10.1016/j.mri.2021.11.001
176. Paech D, Windschuh J, Oberhollenzer J, Dreher C, Sahm F, Meissner J-E, et al. Assessing the predictability of IDH mutation and MGMT methylation status in glioma patients using relaxation-compensated multipool CEST MRI at 7.0 T. *Neuro Oncol* 2018; **20**: 1661–71. https://doi.org/10.1093/neuonc/noy073
177. Chan RW, Chen H, Myrehaug S, Atenafu EG, Stanisz GJ, Stewart J, et al. Quantitative CEST and MT at 1.5T for monitoring treatment response in glioblastoma: early and late tumor progression during chemoradiation. *J Neurooncol* 2021; **151**: 267–78. https://doi.org/10.1007/s11060-020-03661-y
178. Meissner J-E, Korzowski A, Regnery S, Goerke S, Breitling J, Floca RO, et al. Early response assessment of glioma patients to definitive chemoradiotherapy using chemical exchange saturation transfer imaging at 7 T. *J Magn Reson Imaging* 2019; **50**: 1268–77. https://doi.org/10.1002/jmri.26702
179. De Feyter HM, Behar KL, Corbin ZA, Fulbright RK, Brown PB, McIntyre S, et al. Deuterium metabolic imaging (DMI) for MRI-based 3D mapping of metabolism in vivo. *Sci Adv* 2018; **4**: eaat7314. https://doi.org/10.1126/sciadv.aat7314
180. Dennie J, Mandeville JB, Boxerman JL, Packard SD, Rosen BR, Weisskoff RM. NMR imaging of changes in vascular morphology due to tumor angiogenesis. *Magn Reson Med* 1998; **40**: 793–99. https://doi.org/10.1002/mrm.1910400602
181. Chakhoyan A, Yao J, Leu K, Pope WB, Salamon N, Yong W, et al. Validation of vessel size imaging (VSI) in high-grade human gliomas using magnetic resonance imaging, image-guided biopsies, and quantitative immunohistochemistry. *Sci Rep* 2019; **9**(1): 2846. https://doi.org/10.1038/s41598-018-37564-w
182. Kiselev VG, Strecker R, Ziyeh S, Speck O, Hennig J. Vessel size imaging in humans. *Magn Reson Med* 2005; **53**: 553–63. https://doi.org/10.1002/mrm.20383
183. Kim M, Park JE, Emblem K, Bjørnerud A, Kim HS. Vessel type determined by vessel architectural imaging improves differentiation between early tumor progression and pseudoprogression in glioblastoma. *AJNR Am J Neuroradiol* 2021; **42**: 663–70. https://doi.org/10.3174/ajnr.A6984
184. Emblem KE, Mouridsen K, Bjornerud A, Farrar CT, Jennings D, Borra RJH, et al. Vessel architectural imaging identifies cancer patient responders to anti-angiogenic therapy. *Nat Med* 2013; **19**: 1178–83. https://doi.org/10.1038/nm.3289
185. Traub-Weidinger T, Poetsch N, Woehrer A, Klebermass E-M, Bachnik T, Preusser M, et al. PSMA expression in 122 treatment naive glioma patients related to tumor metabolism in ^{11}C-methionine PET and survival. *J Pers Med* 2021; **11**(7): 624. https://doi.org/10.3390/jpm11070624
186. Holzgreve A, Biczok A, Ruf VC, Liesche-Starnecker F, Steiger K, Kirchner MA, et al. PSMA expression in glioblastoma as A basis for theranostic approaches: A retrospective, correlational panel study including immunohistochemistry, clinical parameters and PET imaging. *Front Oncol* 2021; **11**: 646387. https://doi.org/10.3389/fonc.2021.646387
187. Kumar A, ArunRaj ST, Bhullar K, Haresh KP, Gupta S, Ballal S, et al. Ga-68 PSMA PET/CT in recurrent high-grade gliomas: evaluating PSMA expression in vivo. *Neuroradiology* 2022; **64**: 969–79. https://doi.org/10.1007/s00234-021-02828-2
188. Kunikowska J, Kuliński R, Muylle K, Koziara H, Królicki L. 68Ga-prostate-specific membrane antigen-11 PET/CT: A new imaging option for recurrent glioblastoma multiforme? *Clin Nucl Med* 2020; **45**: 11–18.
189. Giesel FL, Kratochwil C, Lindner T, Marschalek MM, Loktev A, Lehnert W, et al. 68)ga-FAPI PET/CT: biodistribution and preliminary dosimetry estimate of 2 DOTA-containing FAP-targeting agents in patients with various cancers. *J Nucl Med* 2019; **60**: 386–92.
190. van Leeuwen KG, Schalekamp S, Rutten MJCM, van Ginneken B, de Rooij M. Artificial intelligence in radiology: 100 commercially available products and their scientific evidence. *Eur Radiol* 2021; **31**: 3797–3804. https://doi.org/10.1007/s00330-021-07892-z
191. van der Voort SR, Incekara F, Wijnenga MMJ, Kapas G, Gardeniers M, Schouten JW, et al. Predicting the 1p/19q codeletion status of presumed low-grade glioma with an externally validated machine learning algorithm. *Clin Cancer Res* 2019; **25**: 7455–62. https://doi.org/10.1158/1078-0432.CCR-19-1127
192. Abdel Razek AAK, Alksas A, Shehata M, AbdelKhalek A, Abdel Baky K, El-Baz A, et al. Clinical applications of artificial intelligence and radiomics in neuro-oncology imaging. *Insights Imaging* 2021; **12**(1): 152. https://doi.org/10.1186/s13244-021-01102-6
193. Menze BH, Jakab A, Bauer S, Kalpathy-Cramer J, Farahani K, Kirby J, et al. The multimodal brain tumor image segmentation benchmark (BRATS). *IEEE Trans Med Imaging* 2015; **34**: 1993–2024. https://doi.org/10.1109/TMI.2014.2377694
194. van der Voort SR, Incekara F, Wijnenga MMJ, Kapsas G, Gahrmann R, Schouten JW, et al. The erasmus glioma database (EGD): structural MRI scans, WHO 2016 subtypes, and segmentations of 774 patients with glioma. *Data Brief* 2021; **37**: 107191. https://doi.org/10.1016/j.dib.2021.107191
195. van der Voort SR, Smits M, Klein S, Alzheimer's Disease Neuroimaging Initiative. DeepDicomSort: an automatic sorting algorithm for brain magnetic resonance imaging data. *Neuroinformatics* 2021; **19**: 159–84. https://doi.org/10.1007/s12021-020-09475-7
196. van Kempen EJ, Post M, Mannil M, Witkam RL, Ter Laan M, Patel A, et al. Performance of machine learning algorithms for glioma segmentation of brain MRI: a systematic literature review and meta-analysis. *Eur Radiol* 2021; **31**: 9638–53. https://doi.org/10.1007/s00330-021-08035-0
197. van Garderen KA, van der Voort SR, Versteeg A, Koek M, Gutierrez A, van Straten M, et al. EASE: clinical implementation of automated tumor segmentation and volume quantification for adult low-grade glioma. *Front Med* 2021; **8**: 1791. https://doi.org/10.3389/fmed.2021.738425
198. De Looze C, Beausang A, Cryan J, Loftus T, Buckley PG, Farrell M, et al. Machine learning: a useful radiological adjunct in determination of a newly diagnosed glioma's grade and IDH status. *J Neurooncol* 2018; **139**: 491–99. https://doi.org/10.1007/s11060-018-2895-4
199. van Kempen EJ, Post M, Mannil M, Kusters B, ter Laan M, Meijer FJA, et al. (n.d.). Accuracy of machine learning algorithms for the classification of molecular features of gliomas on MRI: A systematic literature review and meta-analysis. *Cancers*; **13**: 2606. https://doi.org/10.3390/cancers13112606
200. Jian A, Jang K, Manuguerra M, Liu S, Magnussen J, Di Ieva A. Machine learning for the prediction of molecular markers in glioma on magnetic resonance imaging: A systematic review and meta-analysis.

Neurosurgery 2021; **89**: 31–44. https://doi.org/10.1093/neuros/nyab103

201. Manfrini E, Smits M, Thust S, Geiger S, Bendella Z, Petr J, et al. From research to clinical practice: a european neuroradiological survey on quantitative advanced MRI implementation. *Eur Radiol* 2021; **31**: 6334–41. https://doi.org/10.1007/s00330-020-07582-2
202. Boxerman JL, Quarles CC, Hu LS, Erickson BJ, Gerstner ER, Smits M, et al. Consensus recommendations for a dynamic susceptibility contrast MRI protocol for use in high-grade gliomas. *Neuro Oncol* 2020; **22**: 1262–75. https://doi.org/10.1093/neuonc/noaa141
203. Lambin P, Leijenaar RTH, Deist TM, Peerlings J, de Jong EEC, van Timmeren J, et al. Radiomics: the bridge between medical imaging and personalized medicine. *Nat Rev Clin Oncol* 2017; **14**: 749–62. https://doi.org/10.1038/nrclinonc.2017.141

BJR

https://doi.org/10.1259/bjr.20210927

Received: 10 August 2021 | Revised: 02 March 2022 | Accepted: 10 March 2022 | Published online: 27 April 2022

Cite this article as:
Bellini C, Bicchierai G, Amato F, Savi E, De Benedetto D, Di Naro F, et al. Comparison between second-look ultrasound and second-look digital breast tomosynthesis in the detection of additional lesions with presurgical CESM. *Br J Radiol* (2022) 10.1259/bjr.20210927.

FULL PAPER

Comparison between second-look ultrasound and second-look digital breast tomosynthesis in the detection of additional lesions with presurgical CESM

[1]CHIARA BELLINI, MD, [1]GIULIA BICCHIERAI, MD, [2]FRANCESCO AMATO, MD, [1]ELENA SAVI, MD, [1]DIEGO DE BENEDETTO, MD, [1]FEDERICA DI NARO, MD, [1]CECILIA BOERI, MD, [1]ERMANNO VANZI, MD, [3]VITTORIO MIELE, MD and [1]JACOPO NORI, MD

[1]Diagnostic Senology Unit, Azienda Ospedaliero-Universitaria Careggi, Florence, Italy
[2]Diagnostic Senology Unit – Radiology Dpt., "Ospedale San Giovanni di Dio", Agrigento, Italy
[3]Department of Radiology, Azienda Ospedaliero-Universitaria Careggi, Florence, Italy

Address correspondence to: Dr Chiara Bellini
E-mail: *1chiarabellini@gmail.com*

Objectives: To compare second-look ultrasound (SL-ultrasound) with second-look digital breast tomosynthesis (SL-DBT) in the detection of additional lesions (ALs) with presurgical contrast-enhanced spectral mammography (CESM).
Methods: We retrospectively included 121 women with 128 ALs from patients who underwent CESM for presurgical staging at our centre from September 2016 to December 2018. These ALs underwent SL-ultrasound and a retrospective review of DBT (SL-DBT) performed 1–3 weeks prior to CESM to evaluate the performance of each technique individually and in combination. ALs in CESM images were evaluated according to enhancement type (focus, mass, or non-mass), size (<10 mm or >10 mm) and level of suspicion (BI-RADS 2, 3, 4 or 5). Our gold-standard was post-biopsy histology, post-surgical specimen or >24 month negative follow-up. McNemar's test was used for the statistical analysis.
Results: Out of the 128 ALs, an imaging correlate was found for 71 (55.5 %) with ultrasound, 79 (61.7%) with DBT, 53 (41.4 %) with DBT and ultrasound, and 97 (75.8%) with ultrasound and/or DBT. SL-DBT demonstrated a higher detection rate *vs* SL-ultrasound in non-mass enhancement (NME) pattern (p: 0.0325) and ductal carcinoma in situ histological type (p: 0.0081). Adding SL-DBT improved the performance *vs* SL-ultrasound alone in the overall sample (p: <0.0001) and in every subcategory identified; adding SL-ultrasound to SL-DBT improved the detectability of ALs in the overall sample and in every category except for NME (p: 0.0833), foci (p: 0.0833) and B3 lesions (p: 0.3173).
Conclusion: Combined second-look imaging (SL-DBT+ SL-ultrasound) for CESM ALs is superior to SL-DBT alone and SL-ultrasound alone. In B3 lesions, NME, and foci, the analysis of a larger sample could determine whether adding SL-ultrasound to SL-DBT is necessary or not.
Advances in knowledge: Thanks to its high sensitivity, CESM is a useful tool in presurgical staging to detect the extent of the disease burden and identify ALs not detected with conventional imaging. Since CESM-guided biopsy systems are still scarcely available in clinical practice, it is necessary to look for other approaches to histologically characterize ALs detected with CESM. In our study, combined second-look imaging (SL-DBT + SL-ultrasound) showed better performance in terms of detectability of ALs, than either SL-DBT or SL-ultrasound alone, and allowed us to identify 91.2% of ALs that turned out to be malignant at final histology; for the remaining 8.8% it was still necessary to perform MRI or MRI-guided biopsy. However, this issue could be solved once CESM-guided biopsies spread in clinical practice. SL-DBT demonstrated a higher detection rate than SL-ultrasound in NME and ductal carcinoma in situ histology.

INTRODUCTION

Contrast-enhanced spectral mammography (CESM) is a new breast imaging diagnostic technique which highlights areas of tumoral neoangiogenesis via an injection of iodinated contrast media.[1] CESM demonstrated a high sensitivity in the detection of breast cancer (BC), up to 85–97% in two recent meta-analyses,[2,3] with a diagnostic performance similar to contrast-enhanced MRI (CE-MRI).[4] Thanks to its high sensitivity, it is a useful tool in presurgical staging to detect the extent of the disease burden and identify additional lesions (ALs) not detected with conventional imaging.[5] In a recent study, CESM performed as

pre-operative staging gave rise to additional biopsies in 17.5% and changed the type of surgery in 18.4% of patients, showing an overall sensitivity, specificity, positive predictive value, negative predictive value and accuracy of 93%, 98%, 90%, 98% and 97% respectively.[6] Previous studies have confirmed these results with similar detection percentages of ALs that led to necessary changes in surgical plans, confirmed by histologic post-surgical specimens.[7,8]

Since CESM-guided biopsy systems are still scarcely available in clinical practice, it is necessary to look for other approaches to histologically characterize ALs detected with CESM. Several studies have already demonstrated that CESM sensitivity is as high as CE-MRI,[4,5,9] so a choice could be to perform CE-MRI and MR-guided biopsy on ALs. However, this procedure is highly time-consuming and costly and not always feasible depending on the location of the ALs, as confirmed in literature.[10,11]

As with MRI,[12,13] second-look ultrasound (SL-ultrasound) targeting CESM findings is surely one of the most important alternatives, since ultrasound-guided core biopsies are widely available, and quick and easy to perform. To our knowledge, there are no studies on the detection rate of SL-ultrasound for ALs with CESM, but a previous study reported a lack of correlate for MRI additional findings of up to 53%.[14]

Since their introduction in clinical practice, digital breast tomosynthesis (DBT) and DBT-guided-biopsy systems have demonstrated an improvement in the detection rate of breast lesions, reducing false-positive recall rates in screening due to superimposition of normal glandular tissue.[15,16] Clauser et al, in their study evaluated the role of SL-DBT in ALs found with presurgical MRI and reported that when SL-DBT was combined with SL-ultrasound the detection rate for clinically relevant ALs increased from 52 to 75%, with MR-guided biopsy being necessary for the remaining 25%.[17]

The purpose of our study was to compare second-look ultrasound (SL-ultrasound) and second-look DBT (SL-DBT) in terms of performance in the overall sample and in every subcategory identified, and whether, and in which cases, the combination of both (SL-ultrasound + SL-DBT) could significantly improve the detectability of CESM ALs *vs* SL-ultrasound alone and SL-DBT alone.

Methods and materials

From the CESMs performed as presurgical staging from September 2016 to December 2018, we retrospectively screened those with evidence of ALs on recombined images not detected with conventional imaging [full-field digital mammography (FFDM) + whole-breast ultrasound] in the ipsilateral or contralateral breast. We reported and classified ALs according to the MRI BI-RADS reporting system[18] with distinct levels of suspicion: BI-RADS 2, BI-RADS 3, BI-RADS 4 and BI-RADS 5. Every AL underwent second-look ultrasound after CESM (SL-ultrasound) and review of DBT images that had been acquired 1–3 weeks prior to CESM (SL-DBT).

Among ALs with a correlate detected by SL-ultrasound and/or SL-DBT, those classified as BI-RADS 2 and/or 3 with CESM underwent a follow-up when the level of suspicion was confirmed with second-look imaging. Conversely, when SL-ultrasound and/or SL-DBT upgraded the level of suspicion to BI-RADS 4 or 5, we performed ultrasound-guided biopsy or tomo-guided biopsy, depending on the imaging technique showing the higher level of suspicion. In cases of ALs with the same level of suspicion in both SL-ultrasound and SL-DBT, we chose to perform ultrasound-guided biopsy.

Every AL reported as BI-RADS 4 and 5 with CESM with an imaging correlate detected by SL-ultrasound and/or SL-DBT underwent biopsy, regardless of the level of suspicion of the two SL techniques.

Every AL with a negative second-look underwent CE-MRI, whatever the level of suspicion identified in CESM. In this group, BI-RADS 3 CESM ALs without an imaging correlate in CE-MRI or with the same level of suspicion, underwent a follow-up. BI-RADS 4 and 5 CESM ALs with an imaging correlate in CE-MRI underwent MR-guided biopsy, regardless of the MRI level of suspicion, while those without an imaging correlate underwent short-term follow-up with CESM, since CESM-guided biopsy systems are not yet available in Italy. When ALs with negative CE-MRI were at a distance of <10 mm from the index lesion, we added the overall size of the enhancing area (index lesion + AL + intralesional distance) on our reports and recommended that the surgeon widen the surgical margin to include the ALs in the surgical excision (Figure 1).

All patients underwent whole-breast ultrasound, bilateral FFDM and DBT performed in the standard craniocaudal (CC) and mediolateral oblique (MLO) views using a full-field digital mammography unit with tomosynthesis (Selenia Dimensions, Hologic), between 1 and 3 weeks before CESM; in females of premenopausal age, CESM was performed during the second week of the menstrual cycle.

CESM was executed with a commercial mammography system (Selenia Dimensions, Hologic, Marlborough, MA), after an intravenous administration of 1.5 cc/kg of body weight of iodine-based contrast agent (Iopromide 370 mg ml^{-1}; Bayer HealthCare, Whippany, NJ or Iopamidol 370 mg ml^{-1}; Bracco Imaging S.p.A., Milan, Italy) at 3 cc/s followed by 20 ml of saline flush using an automated power injector. The first acquisition began 2 min after the injection. Standard mammographic views of each breast (CC and MLO images) were obtained in sequence within 5 min. After 8 min, a "delayed image" of each breast was acquired to permit a qualitative assessment of the enhancement kinetics. No issue was raised by our institutional ethics committee about radiation dose since our population was composed by females with a proven breast cancer and CESM was performed as pre-surgical staging and not as screening programme, so a minor increase in radiation dose was tolerated.

For each CESM view, a low-energy (LE) image and a high-energy image were performed serially, at 26–31 kVp with

Figure 1. Flowchart of diagnostic management of CESM ALs; * depending on the higher level of suspicion out of the two imaging techniques (SL-ultrasound and/or SL-DBT); ** follow-up or biopsy if level of suspicion is confirmed by the other SL imaging technique. LI: index lesion; SURGERY: explained in text. ALs; arterial lesion; CESM, contrast-enhanced spectral mammography; SL-DBT, second-look digital breast tomosynthesis.

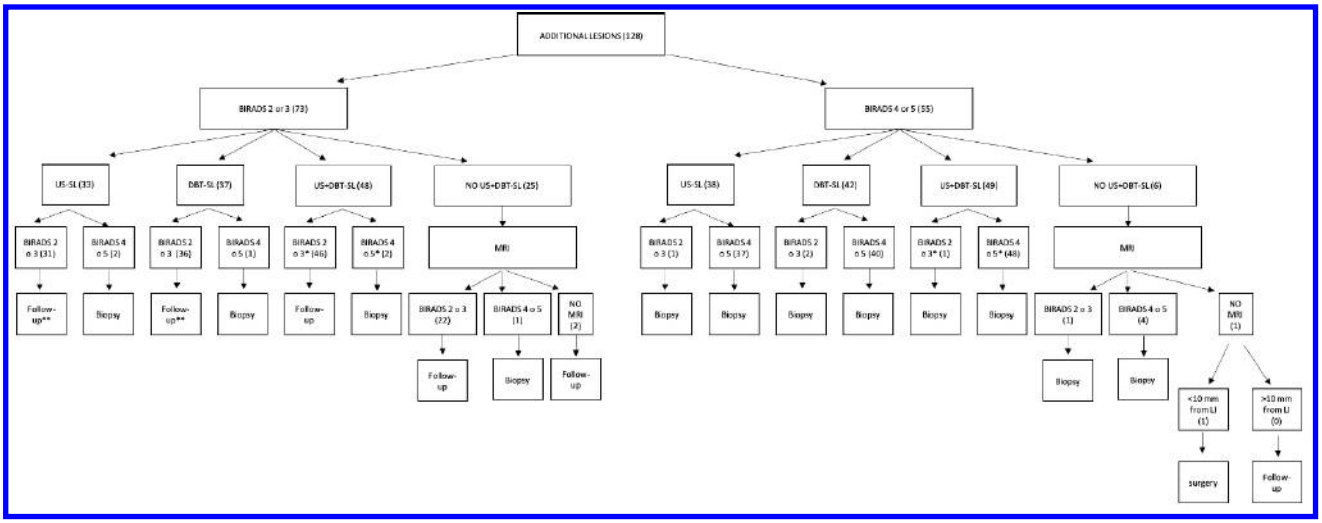

rhodium and silver (Rh and Ag) filters and at 45–49 kVp with a copper filter, respectively. A recombination algorithm was used to subtract the unenhanced breast tissue and provide a recombined image for highlighting the areas of relative contrast enhancement. All the mammographic views were used for our analysis.

CESM images were reviewed in consensus by three experienced breast radiologists with 4–27 years' experience in breast imaging.

The radiologists, not blinded to other imaging methods (ultrasound, FFDM and DBT), described the index lesions in terms of localization, size, and type of enhancement.

Every measurable enhancing finding at a distance >5 mm from the index lesion or on the contralateral breast was considered an AL. In order to distinguish ALs from background parenchymal enhancement (BPE) when present, the radiologists evaluated the symmetry, distribution and intensity of the enhancing findings, since BPE is more often symmetric and with a stronger intensity in the delayed recombined images acquired after 8 min than in the early recombined images acquired after 2 min. ALs were described and classified as mass, non-mass and focus according to the MRI BI-RADS lexicon, since a standardized lexicon for CESM does not yet exist.[18]

Both whole-breast bilateral ultrasound and targeted SL-ultrasound were performed using handheld ultrasound by a radiologist of our institution with a 10–13 MHz transducer and an ultrasound unit (ESAOTE, MyLab 70 XVG).

Target SL-ultrasound was performed after 3–7 days by a breast radiologist of our institution who retrospectively evaluated the CESM images, looking for the ALs' correlate, such as masses or distortions; when a correlate was found, we performed 14G CNB.

DBT images acquired 1–3 weeks prior to CESM were re-evaluated retrospectively in separate sessions by a breast radiologist of our institution; when a correlate with suspicious imaging characteristics (masses, architectural distortions, microcalcifications and asymmetries) and lesion size and localization correspondence with CESM ALs was found, we performed 8G tomo-VAB.

Lesions classified as benign (B2) were: B2 lesions confirmed by post-biopsy histology; lesions with at least a 2-year negative follow-up; lesions B1 or B2 after surgical excision in case of ALs with negative SL-ultrasound, SL-DBT and CE-MRI, and at a distance of <10 mm from the index lesion.

Lesions classified as having uncertain malignancy potential (B3) were: B3 lesions confirmed after surgical excision in case of ADH, papilloma, LN and phyllodes tumour, B3 lesions confirmed by post-biopsy histology for the remaining categories that did not undergo surgical excision.

Lesions were classified as malignant if confirmed by final histology after surgical excision.

We then divided the overall sample into subcategories according to histology (malignant, B3, benign lesion), and when malignant, also the cancer histological type [IDC, ILC, ductal carcinoma in situ (DCIS)], type of enhancement in CESM [focus, mass, non-mass enhancement (NME)], and maximum diameter (≤10 mm; >10 mm).

Following, we evaluated the performance of SL-ultrasound, SL-DBT and the combination of both in terms of detectability of ALs identified in CESM recombined images in the overall sample and in every subcategory identified.

Table 1. Side-distribution of 128 benign, high-risk (B3), and malignant additional lesions detected in patients who underwent pre-operative breast CESM

Additional lesions	n	Benign		High-risk lesions (B3)		Malignant	
Total	128	61	47.7%	10	7.8%	57	44.5%
Ipsilateral	68	26	38.2%	5	7.4%	37	54.4%
Contralateral	60	35	58.3%	5	8.3%	20	33.3%

CESM, contrast-enhanced spectral mammography.

Statistical analysis

Using McNemar's test, we compared SL-ultrasound and SL-DBT performances for the whole sample and the subcategories to discover which SL-technique was more effective and when. Then, we verified whether and when the combination of SL-ultrasound and SL-DBT was better than SL-ultrasound or SL-DBT alone. The analyses were performed using IBM SPSS Statistics 23.0 (IBM SPSS Inc., Chicago, IL) and Microsoft Excel (Microsoft Corporation, Redmond, WA).

RESULTS

In 304 CESMs carried out as pre-surgical staging, 128 ALs were found which were either ipsilateral or contralateral to the index lesion in 121 patients: among these, 57/128 (44.5%) were confirmed as malignant, 10/128 (7.8%) as B3 lesions, and 61/128 (47.7%) as benign (Table 1).

ALs found on SL-DBT were masses in 40 cases, microcalcifications in 22, distortions in 16, and 1 focal asymmetry.

Out of 57 malignant Als, 30 (52.6%) showed as mass enhancement in CESM, 18 (31.6%) as NME, and 9 (15.8%) as foci.

CESM NME ALs were observed in SL-DBT as 12 microcalcifications, 3 masses, 6 distortions and 1 focal asymmetry; mass-like ALs were observed in SL-DBT as 30 masses, 10 distortions and 4 microcalcifications; foci ALs were observed in SL-DBT as 7 masses and 6 microcalcifications.

SL-ultrasound detected an imaging correlate in 71/128 CESM ALs: 39/57 (68.4%) malignant lesions, with a significant decrease in performance in the DCIS histological type (3/11; 27.3%); 27/61 (44.2%) benign lesions, and 5/10 (50.0%) B3 lesions.

SL-DBT detected an imaging correlate in 79/128 CESM ALs: 41/57 (71.9%) malignant lesions; 29/61 (47.5%) benign lesions, and 9/10 (90.0%) B3 lesions.

The histologic characteristics of CESM ALs with and without a SL-detected correlate are reported in Table 2.

The combination of both techniques (SL-ultrasound + SL-DBT) detected 97/128 CESM Als: 52/57 (91.2%) malignant lesions, 35/61 (57.4%) benign lesions, and 10/10 (100%) B3 lesions.

Table 2. Histology of B5 and B3 lesions detected with SL-ultrasound, SL-DBT individually or combined, or with negative SL, in 121 women with 128 ALs found with presurgical CESM

B5 and B3 additional lesions	Detected at SL-ultrasound	Detected at SL-DBT	Detected at both SL-ultrasound and SL-DBT	Not detected at SL-DBT neither SL-ultrasound
B5 lesions (n = 57)	**39 (68.4%)**	**41 (71.9%)**	**28 (49.1%)**	**5 (8.8%)**
Invasive ductal carcinoma	31	27	22	4
Microinvasive ductal carcinoma	1	0	0	0
DCIS	3	10	3	1
Invasive lobular carcinoma	4	4	3	0
B3 lesions (n = 10)	**5 (50.0%)**	**8 (80.0%)**	**4 (40.0%)**	**0**
Atypical ductal hyperplasia	1	1	1	0
Lobular neoplasia	0	2	0	0
Flat epithelial atypia	0	2	0	0
Radial Scar	1	1	1	0
Papilloma	2	2	1	0
Atypical apocrine adenosis	1	1	1	0

CESM, contrast enhanced spectral mammography; DBT, digital breast tomosynthesis; DCIS, Ductal carcinoma in situ; SL, second-look.
Note: the three DCIS with an imaging correlate detected by SL-ultrasound, also had a correlate with SL-DBT; no DCIS positive with SL-ultrasound and negative with SL-DBT were observed.

In our study, 31/128 CESM ALs negative in both SL-ultrasound and SL-DBT underwent CE-MRI and 28/31 showed an imaging correlate. Of the 5/31 malignant ALs, 4 (all BI-RADS 4 in CESM and CE-MRI) underwent MR-guided biopsy and 1, negative with CE-MRI, was confirmed after surgical excision with wider margins, as it was <10 mm from the index lesion; the undetected malignant ALs were one DCIS, two G1 IDC, one G2 IDC and one G3 IDC. Of the 26/31 benign ALs, 24/31 were confirmed as benign after at least a 2-year negative follow-up with CESM, and 2/31 by histology after MR-guided biopsy.

The subcategories identified in our sample, in particular histology (malignant, B3, benign lesion), and when malignant, the cancer histological type (IDC, ILC, DCIS), type of enhancement in CESM (focus, mass, NME), maximum diameter (≤10 mm; >10 mm), level of suspicion (BI-RADS 2 or 3, BI-RADS 4, BI-RADS 5) are reported in Table 3.

SL-ultrasound alone *vs* SL-DBT alone showed no significant performance difference in terms of detectability of CESM ALs in the overall sample (SL-DBT 61.7% *vs* 55.5% SL-ultrasound), while the combination of DBT and ultrasound (SL-DBT + SL-ultrasound) showed a significantly higher performance *vs* SL-ultrasound alone (75.8% *vs* 55.5%; *p*: <0.001) and *vs* SL-DBT alone (75.8% *vs* 61.7% *p*: <0.001).

SL-DBT alone proved significantly better in terms of detectability *vs* SL-ultrasound alone in DCIS histological type (90.9% *vs* 27.3%; *p*: 0.008) and in the NME category (64.7% *vs* 41.2%; *p*: 0.032). In the remaining subcategories identified, no significant difference was found in the performance of SL-DBT alone *vs* SL-ultrasound alone.

When considering histology, the combination of both techniques (SL-DBT + SL-ultrasound), showed a significantly improved performance *vs* SL-ultrasound alone and SL-DBT alone in malignant lesions (91.2% *vs* 71.9% SL-DBT. $p < 0.001$; *vs* 68.4% SL-ultrasound. $p < 0.001$), especially in IDC histological type (90.2% *vs* 65.8% SL-DBT. *p*: 0.002; *vs* 78.0% SL-ultrasound. 0.025), and benign lesions (57.4% *vs* 47.5% SL-DBT. *p*: 0.014; *vs* 44.3% SL-ultrasound. *p*: 0.005); SL-DBT + SL-ultrasound also showed better performance *vs* SL-ultrasound alone in DCIS histological type (90.9% *vs* 27.3%; *p*: 0.008) and in B3 lesions (100.0% *vs* 50.0%; *p*: 0.025).

When considering the type of enhancement of CESM ALs, SL-DBT + SL-ultrasound improved the detectability *vs* both SL-ultrasound and SL-DBT alone in the mass category (81.2% *vs* 63.8% SL-DBT. *p*: 0.008; *vs* 71.0% SL-ultrasound. *p*: 0.001), and it also proved better *vs* SL-ultrasound alone in the NME (73.5% *vs* 41.2%; *p*: 0.001) and focus (64.0% *vs* 32.0%; *p*: 0.005) categories.

In relation to the AL size, the combination of SL-DBT + SL-ultrasound improved the performance *vs* SL-ultrasound alone and SL-DBT alone in both the ≤10 mm (75.6% *vs* 59.8% SL-DBT, $p < 0.001$; *vs* 57.3% SL-ultrasound. $p < 0.001$) and >10 mm categories (76.1% *vs* 65.2% SL-DBT, *p*: 0.025; 52.2% SL-ultrasound. $p < 0.001$).

As regards the level of suspicion. combined SL-DBT + SL-ultrasound improved the detectability of ALs *vs* both SL-ultrasound and SL-DBT alone in the BI-RADS 3 (65.7% *vs* 50.7% SL-DBT. $p < 0.001$; 45.2%. SL-ultrasound. $p < 0.001$) and BI-RADS 4 categories (88.7% *vs* 75.5% SL-DBT. *p*: 0.008; *vs* 67.9% SL-ultrasound. $p < 0.001$).

The other evaluations were not statistically significant.

Examples of malignant CESM ALs with only a correlate detected by SL-ultrasound and only a correlate by SL-DBT, are shown in Figures 2 and 3.

DISCUSSION

To our knowledge, this is the first study to report the role of SL-DBT and combined SL-DBT and/or SL-ultrasound in detecting ALs observed in CESM exams performed for pre-surgical staging.

In our study, we found 128 ALs in 304 presurgical CESMs, with a rate of 39.80%, higher than the few studies published in literature on this topic,[6,7] namely, 23.6% in the study of Bicchierai et al, and 16% in Ali-Mucheru et al, but similar to some studies of presurgical MRI,[17,19,20] such as that of Clauser et al which reports 39% of additional findings.

The overall malignancy rate for ALs was 44.5%, in agreement with several studies in literature,[6,21] including 54.3% that of Houben et al, and with other studies on MRI[17,22,23] ; similar values were also found in the study of Åhsberg et al. (48%).[24] This result confirms the already demonstrated accuracy of CESM in assessing multifocal, multicentric and bilateral lesions.[25,26]

Out of the 128 ALs, 68 were ipsilateral while 60 contralateral, with a significantly higher malignancy rate for the ipsilateral group, similar to previous studies in literature.[27] In our study, we included females with histologically proven breast cancer which underwent pre-surgical CESM with at least one additional lesion reported on recombined images, including females with high-risk females and those who had undergone previous surgery, as in clinical practice. This sample bias may have affected the high rate of contralateral synchronous lesions.

Our SL-ultrasound performance (55.5%) was in line with literature data,[13,17] while for SL-DBT it was 61.7%, higher than that of MRI,[17] 52 and 50% respectively in the study of Clauser et al. In our opinion, this may be due to the similar spatial representation of the recombined CESM image and of the DBT image, performed both in the same CC and MLO projections, allowing for easy detection of AL correlates; previous studies have already confirmed the equivalence between imaged LE and 2DFFDM.[28,29]

SL-DBT alone showed a higher detection rate *vs* SL-ultrasound in the NME pattern on CESM (p:0.0325) and in the DCIS histologic subtype (*p*: 0.0081). These results could be explained by the fact that microcalcifications are often the imaging correlate of NME and DCIS, and subtle microcalcifications can be exceedingly difficult to detect with ultrasound.[30] The 22 ALs corresponding to microcalcifications detected on SL-DBT in our study were visible also on the previously performed FFDM and on the LE CESM images; they

Table 3. Detectability of 128 CESM additional lesions at SL-DBT and SL-ultrasound overall and according to CESM characteristics and malignant, high-risk, or benign outcome

	n	Ultrasound	DBT	Ultrasound and DBT	Ultrasound and/or DBT
Overall	128	71 (55.5%)	79 (61.7%)	53 (41.4%)	97 (75.8%)
p-value Ultrasound *vs* DBT		0.227800			*vs* Ultrasound **0.000001**
					vs DBT **0.000022**
MALIGNANT	57	39 (68.4%)	41 (71.9%)	28 (49.1%)	52 (91.2%)
p-value Ultrasound *vs* DBT		0.683091			*vs* Ultrasound **0.000311**
					vs DBT **0.000911**
Invasive ductal carcinoma	41	32 (78.0%)	27 (65.8%)	22 (53.7%)	37 (90.2%)
p-value Ultrasound *vs* DBT		0.196706			*vs* Ultrasound **0.025347**
					vs DBT **0.001565**
Invasive lobular carcinoma	5	4 (80.0%)	4 (80.0%)	3 (60.0%)	5 (100.0%)
p-value Ultrasound *vs* DBT		1.000.000			*vs* Ultrasound 0.317311
					vs DBT 0.317311
Ductal carcinoma *in situ*	11	3 (27.3%)	10 (90.9%)	3 (27.3%)	10 (90.9%)
p-value Ultrasound *vs* DBT		**0.008151**			*vs* Ultrasound **0.008151**
					vs DBT N/A
High-risk lesions (B3)	10	5 (50.0%)	9 (90.0%)	4 (40.0%)	10 (100.0%)
p-value Ultrasound *vs* DBT		0.102470			*vs* Ultrasound **0.025347**
					vs DBT 0.317311
BENIGN	61	27 (44.3%)	29 (47.5%)	21 (34.4%)	35 (57.4%)
p-value Ultrasound *vs* DBT		0.592980			*vs* Ultrasound **0.004678**
					vs DBT **0.014306**
FOCUS	25	8 (32.0%)	13 (52.0%)	5 (20.0%)	16 (64.0%)
p-value Ultrasound *vs* DBT		0.131668			*vs* Ultrasound **0.004678**
					vs DBT 0.083265
MASSES	69	49 (71.0%)	44 (63.8%)	37 (53.6%)	56 (81.2%)
p-value Ultrasound *vs* DBT		0.251349			*vs* Ultrasound **0.008151**
					vs DBT **0.000532**
Non-mass enhancement	34	14 (41.2%)	22 (64.7%)	11 (32.3%)	25 (73.5%)
p-value Ultrasound *vs* DBT		**0.032509**			*vs* Ultrasound **0.000911**
					vs DBT 0.083265
≤10 mm	82	47 (57.3%)	49 (59.8%)	34 (41.5%)	62 (75.6%)
p-value Ultrasound *vs* DBT		0.705457			*vs* Ultrasound **0.000108**
					vs DBT **0.000311**
>10 mm	46	24 (52.2%)	30 (65.2%)	19 (41.3%)	35 (76.1%)
p-value Ultrasound *vs* DBT		0.133614			*vs* Ultrasound **0.000911**
					vs DBT **0.025347**
BI-RADS 3	73	33 (45.2%)	37 (50.7%)	22 (30.1%)	48 (65.7%)
p-value Ultrasound *vs* DBT		0.432768			*vs* Ultrasound **0.000108**
					vs DBT **0.000911**

(Continued)

Table 3. (Continued)

	n	Ultrasound	DBT	Ultrasound and DBT	Ultrasound and/or DBT
BI-RADS 4	53	36 (67.9%)	40 (75.5%)	29 (54.7%)	47 (88.7%)
p-value Ultrasound *vs* DBT		0.345779			*vs* Ultrasound **0.000911**
					vs DBT **0.008151**
BI-RADS 5	2	2 (100.0%)	2 (100.0%)	2 (100.0%)	2 (100.0%)
p-value Ultrasound *vs* DBT		N/A			*vs* Ultrasound N/A
					vs DBT N/A

CESM, contrast-enhanced spectral mammography; DBT, digital breast tomosynthesis; SL, second-look.

were classified as low-risk findings but since the corresponding contrast enhancement on the recombined images upgraded their level of suspicion, we decided to perform tomo-VAB.

We think that in comparison to FFDM or LE image, DBT could have played a role in more effectively assessing the spatial distribution and morphology of microcalcifications, thus increasing specificity, in a pre-surgical setting, as stated by Kuwabara et al in their study,[31] even though further studies will be necessary to confirm this hypothesis.

In terms of detectability, the addition of SL-DBT to SL-ultrasound improved the performance of SL-ultrasound alone, 75.8% *vs* 55.5% (*p*: 0.000001) in every subcategory identified, except for ILC (*p*: 0.317311); said improvement can be attributed to the presence of microcalcifications, architectural distortions and focal asymmetries in AL correlates, which can be more easily identified with DBT than with ultrasound.

The addition of SL-ultrasound to SL-DBT improved the detectability of ALs in the overall sample and in every category except for NME (*p*: 0.0833), foci (*p*: 0.0833) and B3 lesions (*p*: 0.3173). We have explained above what we believe to be the reasons for this result for NME. As regards B3 lesions, in our study, we had a histologic sample with uncertain malignant potential lesions, except for papilloma, which often manifests as microcalcifications (ADH, FEA) or architectural distortions (RS),[32] more easily detected with DBT.

Foci have always been a challenge for MRI, due to their difficult detectability with SL-ultrasound and the lack of data for their management [33]; we believe this improved performance of SL-DBT in foci management is due to the spatial overlap of CESM recombined image projection with DBT images, allowing for easier detection of imaging correlates. Moreover, the CE-MRI prone position for image acquisition is completely different from the position of the SL imaging methods, while CESM recombined images, paired with the low-energy image, are acquired in the same projections of FFDM and DBT. Furthermore, FFDM, DBT and CESM recombined images share a better spatial resolution than CE-MRI images. In the study of Clauser et al.,[17] SL-DBT performance is inferior to SL-ultrasound in the foci category in pre-surgical MRI, thus corroborating our opinion.

According to our results, combined second-look imaging (SL-DBT + SL-ultrasound) for CESM ALs in comparison to SL-DBT alone and SL-ultrasound alone allowed us to identify 91.2% of ALs that resulted malignant at final histology (+22.8% vs. SL-ultrasound alone); for the remaining 8.8% it was still necessary to perform MRI and MRI-guided biopsy.

In our study, 31 (24.2%) of the 128 ALs did not have an imaging correlate with SL-ultrasound or SL-DBT. In these cases, we chose to perform CE-MRI to look for a corresponding MRI AL and when present, we performed MRI-guided biopsy. Our results showed that 57 (44.5%) ALs detected in presurgical CESM were malignant: 52 were visible with SL-ultrasound and/or SL-DBT and 5 (8.8%) not visible. The undetected malignant ALs were one DCIS, two G1 IDC, one G2 IDC, and one G3 IDC.

In 4 out of these 5 cases we performed MRI-guided biopsy and in the other case, CESM AL was ipsilateral to the index lesion with an intralesional distance of <10 mm, which was subjected to surgical excision with histologic confirmation of malignancy. As confirmed for these five ALs, it seems evident that a CESM-guided biopsy approach could be extremely helpful in cases of ALs with negative SL. CESM-guided biopsies, still awaiting FDA approval, share the same approach as the stereotactic/tomo-guided biopsy with the additional injection of intravenous iodinated contrast medium 2 min before starting the procedure. Compared with the MRI-guided biopsy, the CESM-guided approach could be faster and more feasible.

This study has several limitations. Firstly, the readers knew the site and the histology of the index lesion before evaluating the CESM images, but this is usual in clinical practice. Secondly, CESM image evaluation was performed in consensus, so it was not possible to evaluate inter-reader reliability with Cohen's κ test. Other limitations included the retrospective nature of the study, its limited sample and the inclusion of high-risk females and those who had undergone previous surgery.

In conclusion, our study has shown that combined second-look imaging (SL-DBT + SL-ultrasound) for CESM ALs is superior to both SL-DBT and SL-ultrasound alone, since it allowed us to identify more than 90% of additional malignant lesions. In B3 lesions, NME, and foci, the analysis of a larger sample could determine whether adding SL-ultrasound to SL-DBT is necessary

Figure 2. An irregular mass with spiculated margins in the upper-central quadrant of the left breast (A, white circle) was found in a 67-year-old female with mammography screening (A: right CC FFDM; B: left CC FFDM). An ultrasound-guided core biopsy of this lesion was performed, and the pathological diagnosis was ILC. The patient underwent both bilateral DBT and presurgical CESM (C: right RC CC image; d: left RC CC image). CESM confirmed the index lesion (D, white circle), and identified an AL in the outer quadrants of the right breast (C, arrow). On SL-DBT no correlate for the contralateral AL was found (images not shown); with SL-ultrasound (E) an irregular hypoechoic, ill-defined nodule was found and subjected to ultrasound-guided biopsy and the result was another ILC. At surgery, the diagnosis was bilateral invasive lobular carcinoma. AL, arterial lesion; CC, craniocaudal; CESM, contrast-enhanced spectral mammography; DBT, digital breast tomosynthesis; FFDM, full-field digital mammography; ILC, invasive lobular carcinoma; SL-second-look.

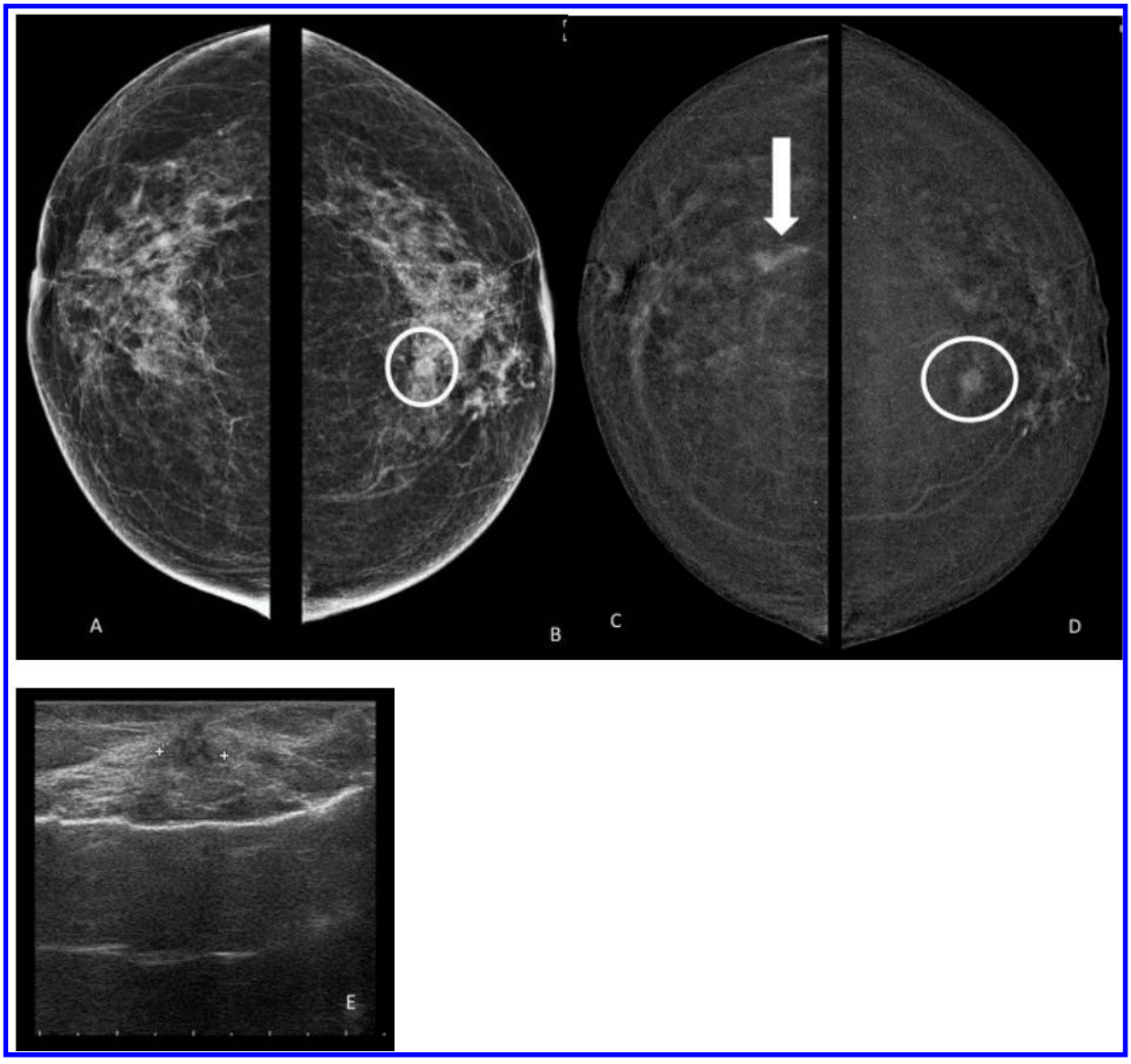

or not. CESM-guided biopsy systems might be a useful tool in cases where the second look is negative.

KEY RESULTS

(1) Combined second-look imaging (SL-DBT + SL-ultrasound) for CESM ALs is superior in terms of detectability to SL-DBT alone and SL-ultrasound alone.

(2) SL-DBT alone proved to be significantly better in terms of detectability *vs* SL-ultrasound alone in the DCIS histological type and NME category.

(3) When considering the type of enhancement of CESM ALs, SL-DBT + SL-ultrasound improved the detectability *vs* SL-ultrasound alone and SL-DBT alone in the mass category, while it also proved more effective than SL-ultrasound alone in the NME and focus categories.

Figure 3. 62-year-old female under annual surveillance (A: right MLO FFDM; B: left MLO FFDM), after a previous QUART, was diagnosed with an IDC in the upper-outer quadrant of the right breast (A, white circle) and underwent CESM as presurgical staging (C: right MLO RC image; D: left MLO RC image). The index lesion was confirmed (C, white circle), but an AL with strong enhancement was found in the upper-outer quadrant of the left breast (D, arrow). SL-ultrasound was negative (images not shown). With SL-DBT (E), an architectural distortion was found in the site of the AL (E, arrow), more visible under magnification (F), subjected to tomo-guided biopsy, the result was another IDC. At surgery, the diagnosis was bilateral IDC. AL, arterial lesion; CESM, contrast-enhanced spectral mammography; DBT, digital breast tomosynthesis; FFDM, full-field digital mammography; IDC, invasive ductal carcinoma; MLO, mediolateral oblique; SL-second-look.IDC.

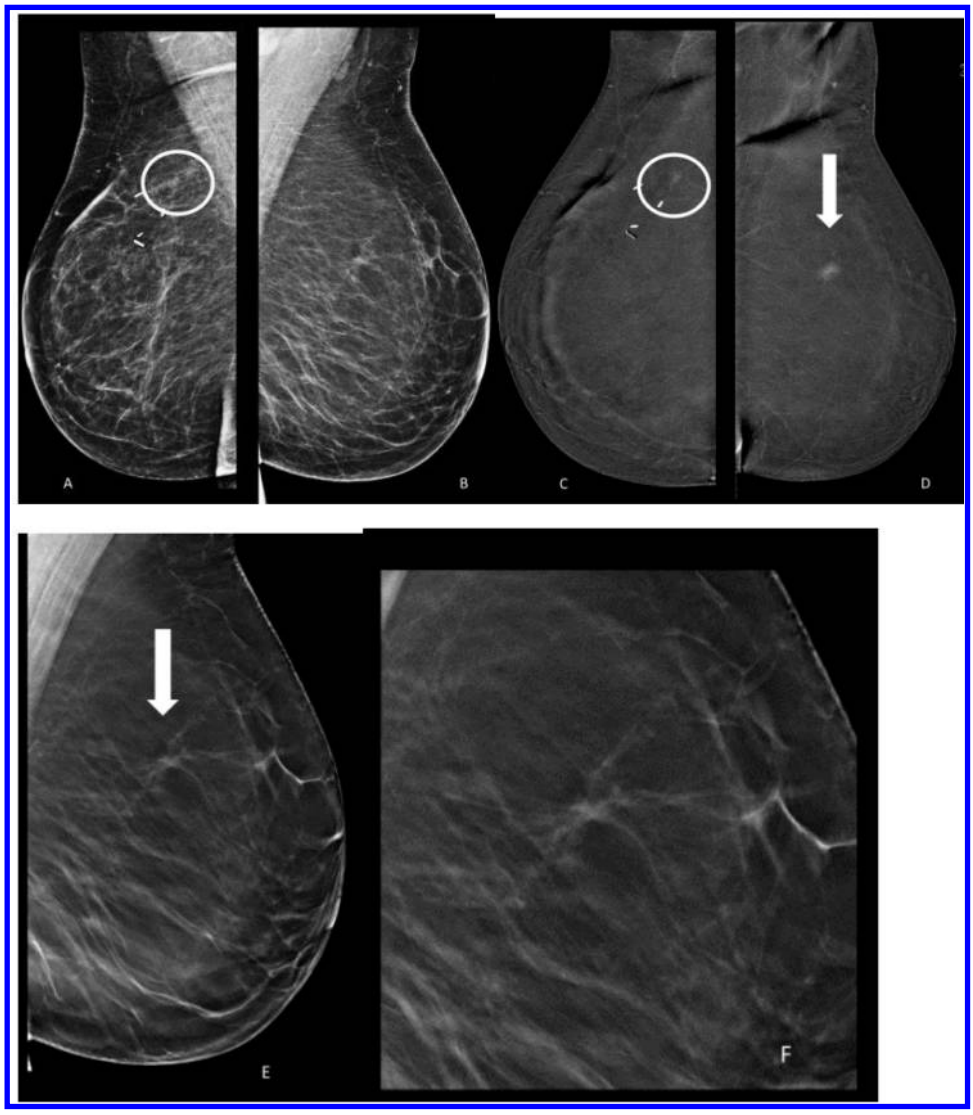

REFERENCES

1. James JJ, Tennant SL. Contrast-enhanced spectral mammography (CESM). *Clin Radiol* 2018; **73**: 715–23. https://doi.org/10.1016/j.crad.2018.05.005
2. Xiang W, Rao H, Zhou L. A meta-analysis of contrast-enhanced spectral mammography versus MRI in the diagnosis of breast cancer. *Thorac Cancer* 2020; **11**: 1423–32. https://doi.org/10.1111/1759-7714.13400
3. Suter MB, Pesapane F, Agazzi GM, Gagliardi T, Nigro O, Bozzini A, et al. Diagnostic accuracy of contrast-enhanced spectral mammography for breast lesions: A systematic review and meta-analysis. *Breast* 2020; **53**: 8–17. https://doi.org/10.1016/j.breast.2020.06.005
4. Fallenberg EM, Schmitzberger FF, Amer H, Ingold-Heppner B, Balleyguier C, Diekmann F, et al. Contrast-enhanced spectral mammography vs. mammography and MRI - clinical performance in a multi-reader evaluation. *Eur Radiol* 2017; **27**: 2752–64. https://doi.org/10.1007/s00330-016-4650-6
5. Patel BK, Lobbes MBI, Lewin J. Contrast enhanced spectral mammography: A review. *Semin Ultrasound CT MR* 2018; **39**: 70–79. https://doi.org/10.1053/j.sult.2017.08.005
6. Bicchierai G, Tonelli P, Piacenti A, De Benedetto D, Boeri C, Vanzi E, et al. Evaluation of contrast-enhanced digital mammography (CEDM) in the preoperative staging of breast cancer: large-scale single-center experience. *Breast J* 2020; **26**: 1276–83. https://doi.org/10.1111/tbj.13766

7. Ali-Mucheru M, Pockaj B, Patel B, Pizzitola V, Wasif N, Stucky C-C, et al. Contrast-enhanced digital mammography in the surgical management of breast cancer. *Ann Surg Oncol* 2016; **23**: 649–55. https://doi.org/10.1245/s10434-016-5567-7
8. Mariscotti G, Durando M, Tagliafico A, Campanino PP, Bosco D, Casella C, et al. Preoperative breast cancer staging with multi-modality imaging and surgical outcomes. *Eur J Radiol* 2020; **122**: 108766. https://doi.org/10.1016/j.ejrad.2019.108766
9. Patel BK, Gray RJ, Pockaj BA. Potential cost savings of contrast-enhanced digital mammography. *AJR Am J Roentgenol* 2017; **208**: W231–37. https://doi.org/10.2214/AJR.16.17239
10. Brennan SB, Sung JS, Dershaw DD, Liberman L, Morris EA. Cancellation of MR imaging-guided breast biopsy due to lesion nonvisualization: frequency and follow-up. *Radiology* 2011; **261**: 92–99. https://doi.org/10.1148/radiol.11100720
11. Johnson KS, Baker JA, Lee SS, Soo MS. Cancelation of MRI guided breast biopsies for suspicious breast lesions identified at 3.0 T MRI: reasons, rates, and outcomes. *Acad Radiol* 2013; **20**: 569–75. https://doi.org/10.1016/j.acra.2013.01.005
12. Leung JWT. Utility of second-look ultrasound in the evaluation of MRI-detected breast lesions. *Semin Roentgenol* 2011; **46**: 260–74. https://doi.org/10.1053/j.ro.2011.08.002
13. Spick C, Baltzer PAT. Diagnostic utility of second-look US for breast lesions identified at MR imaging: systematic review and meta-analysis. *Radiology* 2014; **273**: 401–9. https://doi.org/10.1148/radiol.14140474
14. Luciani ML, Pediconi F, Telesca M, Vasselli F, Casali V, Miglio E, et al. Incidental enhancing lesions found on preoperative breast MRI: management and role of second-look ultrasound. *Radiol Med* 2011; **116**: 886–904. https://doi.org/10.1007/s11547-011-0630-8
15. Powell JL, Hawley JR, Lipari AM, Yildiz VO, Erdal BS, Carkaci S. Impact of the addition of digital breast tomosynthesis (DBT) to standard 2D digital screening mammography on the rates of patient recall, cancer detection, and recommendations for short-term follow-up. *Acad Radiol* 2017; **24**: 302–7. https://doi.org/10.1016/j.acra.2016.10.001
16. Houssami N, Skaane P. Overview of the evidence on digital breast tomosynthesis in breast cancer detection. *Breast* 2013; **22**: 101–8. https://doi.org/10.1016/j.breast.2013.01.017
17. Clauser P, Carbonaro LA, Pancot M, Girometti R, Bazzocchi M, Zuiani C, et al. Additional findings at preoperative breast MRI: the value of second-look digital breast tomosynthesis. *Eur Radiol* 2015; **25**: 2830–39. https://doi.org/10.1007/s00330-015-3720-5
18. Edwards SD, Lipson JA, Ikeda DM, Lee JM. Updates and revisions to the BI-RADS magnetic resonance imaging lexicon. *Magn Reson Imaging Clin N Am* 2013; **21**: 483–93. https://doi.org/10.1016/j.mric.2013.02.005
19. Liberman L, Morris EA, Kim CM, Kaplan JB, Abramson AF, Menell JH, et al. MR imaging findings in the contralateral breast of women with recently diagnosed breast cancer. *AJR Am J Roentgenol* 2003; **180**: 333–41. https://doi.org/10.2214/ajr.180.2.1800333
20. Liberman L, Morris EA, Dershaw DD, Abramson AF, Tan LK. MR imaging of the ipsilateral breast in women with percutaneously proven breast cancer. *AJR Am J Roentgenol* 2003; **180**: 901–10. https://doi.org/10.2214/ajr.180.4.1800901
21. Houben IPL, Van de Voorde P, Jeukens C, Wildberger JE, Kooreman LF, Smidt ML, et al. Contrast-enhanced spectral mammography as work-up tool in patients recalled from breast cancer screening has low risks and might hold clinical benefits. *Eur J Radiol* 2017; **94**: 31–37. https://doi.org/10.1016/j.ejrad.2017.07.004
22. Meissnitzer M, Dershaw DD, Lee CH, Morris EA. Targeted ultrasound of the breast in women with abnormal MRI findings for whom biopsy has been recommended. *AJR Am J Roentgenol* 2009; **193**: 1025–29. https://doi.org/10.2214/AJR.09.2480
23. Beran L, Liang W, Nims T, Paquelet J, Sickle-Santanello B. Correlation of targeted ultrasound with magnetic resonance imaging abnormalities of the breast. *Am J Surg* 2005; **190**: 592–94. https://doi.org/10.1016/j.amjsurg.2005.06.019
24. Åhsberg K, Gardfjell A, Nimeus E, Rasmussen R, Behmer C, Zackrisson S, et al. Added value of contrast-enhanced mammography (CEM) in staging of malignant breast lesions-a feasibility study. *World J Surg Oncol* 2020; **18**(1): 100. https://doi.org/10.1186/s12957-020-01865-0
25. Dromain C, Vietti-Violi N, Meuwly JY. Angiomammography: A review of current evidences. *Diagn Interv Imaging* 2019; **100**: 593–605. https://doi.org/10.1016/j.diii.2019.01.011
26. Helal MH, Mansour SM, Salaleldin LA, Alkalaawy BM, Salem DS, Mokhtar NM. The impact of contrast-enhanced spectral mammogram (CESM) and three-dimensional breast ultrasound (3DUS) on the characterization of the disease extend in cancer patients. *Br J Radiol* 2018; **91**(1087): 20170977. https://doi.org/10.1259/bjr.20170977
27. Sardanelli F, Boetes C, Borisch B, Decker T, Federico M, Gilbert FJ, et al. Magnetic resonance imaging of the breast: recommendations from the EUSOMA working group. *Eur J Cancer* 2010; **46**: 1296–1316. https://doi.org/10.1016/j.ejca.2010.02.015
28. Lalji UC, Jeukens CRLPN, Houben I, Nelemans PJ, van Engen RE, van Wylick E, et al. Evaluation of low-energy contrast-enhanced spectral mammography images by comparing them to full-field digital mammography using EUREF image quality criteria. *Eur Radiol* 2015; **25**: 2813–20. https://doi.org/10.1007/s00330-015-3695-2
29. James JR, Pavlicek W, Hanson JA, Boltz TF, Patel BK. Breast radiation dose with CESM compared with 2D FFDM and 3D tomosynthesis mammography. *AJR Am J Roentgenol* 2017; **208**: 362–72. https://doi.org/10.2214/AJR.16.16743
30. Trop I, Labelle M, David J, Mayrand M-H, Lalonde L. Second-look targeted studies after breast magnetic resonance imaging: practical tips to improve lesion identification. *Curr Probl Diagn Radiol* 2010; **39**: 200–211. https://doi.org/10.1067/j.cpradiol.2009.07.006
31. Rageth CJ, O'Flynn EAM, Pinker K, Kubik-Huch RA, Mundinger A, Decker T, et al. Second international consensus conference on lesions of uncertain malignant potential in the breast (B3 lesions). *Breast Cancer Res Treat* 2019; **174**: 279–96. https://doi.org/10.1007/s10549-018-05071-1
32. Myers KS, Oluyemi ET, Mullen LA, Ambinder EB, Kamel IR, Harvey SC. Outcomes of foci on breast MRI: features associated with malignancy. *AJR Am J Roentgenol* 2020; **215**: 1012–19. https://doi.org/10.2214/AJR.19.22423

BJR

https://doi.org/10.1259/bjr.20220186

Received: 14 February 2022 | Revised: 10 August 2022 | Accepted: 16 August 2022 | Published online: 21 September 2022

Cite this article as:
Li Q, Huang Y, Xiao Q, Duan S, Wang S, Li J, et al. Value of radiomics based on CE-MRI for predicting the efficacy of neoadjuvant chemotherapy in invasive breast cancer. *Br J Radiol* (2022) 10.1259/bjr.20220186.

FULL PAPER

Value of radiomics based on CE-MRI for predicting the efficacy of neoadjuvant chemotherapy in invasive breast cancer

[1,2,3]QIN LI, Ph D, [1,2]YAN HUANG, MD, [1,2]QIN XIAO, MD, [4]SHAOFENG DUAN, MD, [1,2]SIMIN WANG, MD, [2,5]JIANWEI LI, MD, [3]QINGLIANG NIU and [1,2]YAJIA GU, Ph D

[1]Department of Radiology, Fudan University Shanghai Cancer Center, Shanghai, China
[2]Department of Oncology, Shanghai Medical College, Fudan University, Shanghai, China
[3]Department of Radiology, Weifang Traditional Chinese Hospital, Weifang, China
[4]GE Healthcare, Beijing, China
[5]Department of Breast Surgery, Fudan University Shanghai Cancer Center, Shanghai, China

Address correspondence to:
Dr Yajia Gu
E-mail: *guyajia@126.com*
Qingliang Niu
E-mail: *qingliangniu@126.com*

Qin Li and Yan Huang have contributed equally to this study and should be considered as co-first authors.

Objective: To establish and validate a radiomics nomogram based on contrast-enhanced (CE)-MRI for predicting the efficacy of neoadjuvant chemotherapy (NAC) in human epidermal growth factor receptor 2 (HER2)-positive breast cancer with non-mass enhancement (NME).

Methods: A cohort comprising 117 HER2-positive breast cancer patients showing NME on CE-MRI between January 2012 and December 2019 were retrospectively analysed in our study. Patients were classified as pathological complete respone (pCR) according to surgical specimens and axillary lymph nodes without invasive tumour cells. Clinicopathological data were recorded, and images were assessed by two radiologists. A total of 1130 radiomics features were extracted from the primary tumour and six radiomics features were selected by the maximal relevance and minimal redundancy and least absolute shrinkage and selection operator algorithms. Univariate logistic regression was used to screen meaningful clinical and imaging features. The rad-score and independent risk factors were incorporated to build a nomogram model. Calibration and receiver operator characteristic curves were used to confirm the performance of the nomogram in the training and testing cohorts. The clinical usefulness of the nomogram was evaluated by decision curve analysis.

Results: The difference in the rad-score between the pCR and non-pCR groups was significant in the training and testing cohorts ($p < 0.01$). The nomogram model showed good calibration and discrimination, with AUCs of 0.900 and 0.810 in the training and testing cohorts. Decision curve analysis indicated that the radiomics-based model was superior in terms of patient clinical benefit.

Conclusion: The MRI-based radiomics nomogram model could be used to pre-operatively predict the efficacy of NAC in HER2-positive breast cancer patients showing NME.

Advances in knowledge: HER2-positive breast cancer showing segmental enhancement on CE-MRI was more likely to achieve pCR after NAC than regional enhancement and diffuse enhancement.

The MRI-based radiomics nomogram model could be used to pre-operatively predict the efficacy of NAC in HER2-positive breast cancer that showed NME.

INTRODUCTION

Human epidermal growth factor receptor 2 (HER2)-positive breast cancer is highly invasive, with increased recurrence and metastasis rates and poor prognosis.[1] Preoperative neoadjuvant chemotherapy (NAC) could reduce the tumour burden and provide unresectable patients with an opportunity to undergo surgery. The rate of pathological complete response (pCR) after NAC based on anti-HER2 therapy can be significantly improved. However, not all patients can benefit from NAC. Several studies[2,3] have reported that less than 35% of HER2-positive breast cancers

are sensitive to NAC with trastuzumab. If patients with HER2-positive invasive breast cancer who are unsensitive to NAC could be identified earlier, unnecessary treatment could be prevented, and the change in treatment plan could be completed in a timely manner.

Radiomics is an image post-processing technology that obtains high-dimensional data from medical images, which are difficult to recognise by the naked eye.[4,5] Many researchers[6–9] reported that the effect of NAC in breast cancer could be predicted by radiomics, but all studies concentrated on breast cancer that showed masses on contrast-enhanced MRI (CE-MRI). To the best of our knowledge, few researchers have reported the role of radiomics in predicting the efficacy of NAC in breast cancers with non-mass enhancement (NME). Chen[10] et al reported that the oestrogen receptor (ER)/progesterone receptor (PR)-negative HER2-positive subtype was more frequent in the non-mass type than in the mass type. Gweon[11] et al concluded that HER2-positive invasive ductal carcinoma (IDC) was more frequently associated with NME. Therefore, the purpose of the current study was to investigate the value of the distribution of non-mass enhancement on CE-MRI images and radiomics in predicting the effect of NAC in HER2-positive breast cancer and to establish a nomogram to guide clinical treatment plans.

METHODS AND MATERIALS

Patients

This study was approved by the ethics committee of our hospital (Fudan University Shanghai Cancer Center), and the requirement

Table 1. Patient characteristics between the training and testing cohorts

Characteristics	Training cohort (n = 83)	Testing cohort (n = 34)	p value
Age	47.5 ± 9.4	48.7 ±8.5	0.506
Menopausal status			0.469
Pre-menopausal	51 (61.44%)	24 (70.58%)	
Post-menopausal	32 (38.56%)	10 (29.42%)	
FGT			0.411
Almost entirely fat	28 (33.73%)	9 (26.47%)	
Scattered	19 (22.89%)	8 (23.52%)	
Heterogeneous	15 (18.07%)	7 (20.58%)	
Extreme	21 (25.30%)	10 (29.43%)	
BPE			0.591
Minimal	14 (16.87%)	5 (14.70%)	
Mild	47 (56.62%)	18 (52.94%)	
Moderate	14 (16.87%)	7 (20.58%)	
Marked	8 (9.64%)	4 (11.78%)	
Pre-NAC T stage			0.292
T2	41 (49.39)	13 (38.23%)	
T3	42 (51.61%)	21 (61.76%)	
Pre-NAC N stage			0.083
N0	19 (22.89%)	5 (14.7%)	
N1	46 (55.42%)	17 (50.0%)	
N2	7 (8.44%)	1 (2.9%)	
N3	11 (13.25%)	11 (32.4%)	
Ki-67			0.293
>30%	65 (78.3%)	23 (67.6%)	
≤30%	17 (21.7%)	11 (32.4%)	
Distribution of NME			0.770
Segmental	26 (31.32%)	11 (32.35%)	
Regional	44 (53.01%)	16 (47.05%)	
Diffuse	13 (15.67%)	7 (20.60%)	
Rad-score	−0.200 (-0.500, 0.100)	−0.200 (-0.400, 0.100)	0.741

NAC, neoadjuvant chemotherapy; NME, non-mass enhancement.

Table 2. Univariate analysis of the pCR and non-pCR groups in the training cohort

Characteristic	pCR (n = 38)	Non-pCR (n = 45)	p value
Age	48.1 ± 8.7	46.9 ± 9.9	0.556
Menopausal status			0.700
Pre-menopausal	22 (57.9%)	29 (64.4%)	
Post-menopausal	16 (42.1%)	16 (36.6%)	
FGT			0.411
Almost entirely fat or scattered	17 (63.2%)	25 (55.6%)	
Heterogeneous or extreme	14 (36.8%)	20 (44.4%)	
BPE			0.632
Minimal or mild	24 (63.2%)	25 (55.6%)	
Moderate or marked	14 (36.8%)	20 (44.4%)	
Pre-NAC T stage			0.087
T2	18 (47.4%)	23 (51.1%)	
T3	12 (31.6%)	19 (42.2%)	
T4	8 (21.0%)	3 (6.7%)	
Pre-NAC N stage			0.083
N0	9 (23.7%)	10 (22.2%)	
N1	22 (57.9%)	24 (53.3%)	
N2	3 (7.9%)	4 (8.9%)	
N3	4 (10.5%)	7 (15.6%)	
Ki-67			0.293
>30%	24 (63.2%)	29 (64.4%)	
≤30%	14 (36.8%)	16 (35.6%)	
Distribution of NME			<0.001
Segmental	22 (57.9%)	4 (8.9%)	
Regional	15 (39.5%)	29 (64.4%)	
Diffuse	1 (2.6%)	12 (26.7%)	
Rad-score	0 (-0.200, 0.300)	−0.4 (-0.700,−0.100)	<0.001

NAC, neoadjuvant chemotherapy; NME, non-mass enhancement.

for informed consent was waived. 377 HER2-positive breast cancer patients receiving NAC in our hospital between January 2012 and December 2019 were retrospectively analysed in our study. The inclusion criteria included the following: (i) patients had invasive HER2-positive breast cancer confirmed by pathology (≥T2); (ii) tumours showed NME on CE-MRI; (iii) patients underwent complete standard treatment (4–6 cycles of paclitaxel+carboplatin+herceptin (PCH), paclitaxel: 80 mg/

Figure 1. (a) A 51-year-old female showing segmental enhancement in the right breast; biopsy pathology: invasive breast cancer. (b) A 49-year-old female showing regional enhancement in the left breast; biopsy pathology: invasive breast cancer. (c) A 31-year-old female showing diffuse enhancement in the right breast; biopsy pathology: invasive breast cancer IHC: ER negative, PR negative, HER2 positive; surgical pathology: non-pCR. IHC, immunohistochemistry; pCR, pathological complete response; HER2, human epidermal growth factor receptor 2.

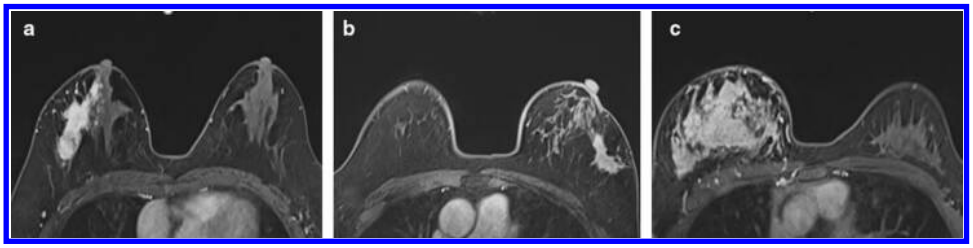

Figure 2. Radiomics feature selection by using mRMR and LASSO. (a) Tuning parameter (λ) selection in the LASSO model used tenfold cross-validation via minimum criteria. The LASSO coefficient profiles of the 30 radiomics features. (b) A coefficient profile plot was produced against the log (l) sequence, and six features were chosen. LASSO, least absolute shrinkage and selection operator; mRMR, maximal relevance and minimal redundancy.

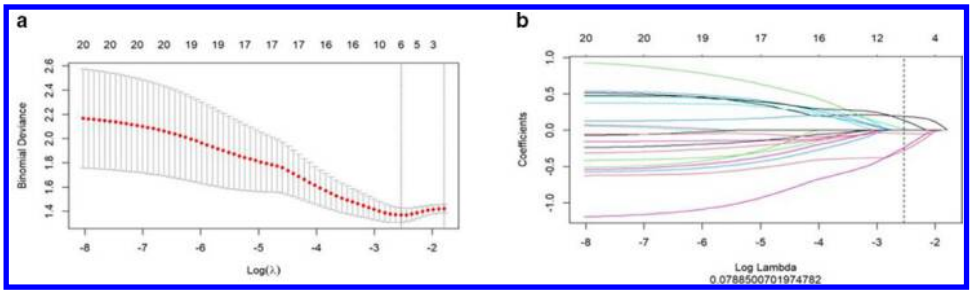

m^2, carboplatin: AUC = 2, herceptin was initially measured at 4 mg/kg ant maintained at 2 mg/kg; once a week, three times is a cycle of treatment and then patients underwent surgical treatment); (iv) patients did not undergo prior treatment before NAC; (v) patients underwent modified radical mastectomy or breast conservation within 1 month after NAC; and (vi) patients had available clinicopathological data. The exclusion criteria were as follows: (i) tumours showing a mass on CE-MRI (n = 235); (ii) patients with incomplete NAC (n = 15); (iii) patients who underwent surgery in another hospital or who did not undergo surgery (n = 4); and (iv) patients with poor MRI quality (n = 6). A total of 117 HER2-positive breast cancer patients who showed NME were enrolled in our study and were randomly divided into a training set and testing set at a ratio of 7:3.

Clinicopathological evaluations

The histopathological results of core needle biopsies or surgical specimens were determined according to the World Health Organisation guidelines and immunochemistry (IHC). The ER, PR, HER2, and Ki-67 expression statuses were assessed by a pathologist with 10 years of experience in breast pathology.

Figure 3. The developed imaging-radiomics nomogram for predicting the efficacy of NAC in HER2-positive breast cancer that showed non-mass enhancement. For distribution, 1 represents segmental enhancement, 2 represents regional enhancement, and 3 represents diffuse enhancement. By calculating the scores of each point and locating it on the total score scale, the estimated probability of pCR can be assessed. HER2, human epidermal growth factor receptor 2; NAC, neoadjuvant chemotherapy; pCR, pathological complete response.

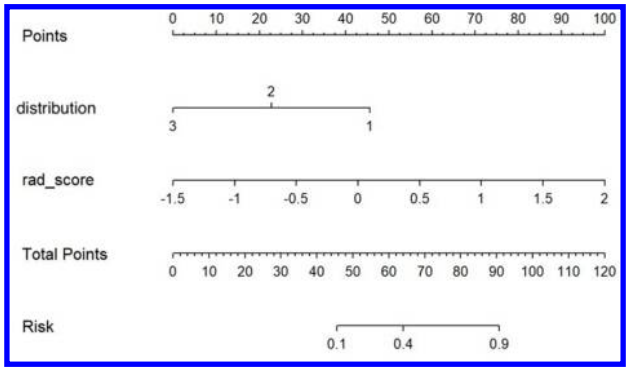

The ER and PR statuses were evaluated as positive only when at least 1% of tumour cells showed nuclear staining. Tumours with HER2 scores of 3+ based on IHC were considered positive. In the cases of 2+ scores, HER2 gene amplification was determined by fluorescent *in situ* hybridisation. Ki-67 ≥30% was assessed as positive. Surgical specimens and axillary lymph nodes without invasive tumour cells after NAC were defined as pCR.

MRI and imaging analysis

Breast CE-MRI was performed before NAC on a MAGNETOM Skyra 3.0 T MRI system (Siemens Healthineers, Erlangen, Germany) using a dedicated 16-channel surface breast coil and a 1.5 T MRI scanner (Aurora Dedicated Breast MRI System; USA) using a dedicated 8-channel surface breast coil in the prone position. The 3.0 T CE-MRI protocol included: (a) a T_1 weighted fat-saturated pre-contrast sequence and (b) multiple (five phases) T_1 weighted fat-saturated post-contrast sequences. The scan parameters were as follows: repetition time/echo time (TR/TE) = 4.5/1.6 ms; matrix = 384×384; field of view (FOV) = 340 cm×340 cm; slice thickness = 1.5 mm; and 80 slices. The 1.5 T CE-MRI protocol included: (a) a T_1 weighted fat-saturated precontrast sequence and (b) multiple (three phases) T_1 weighted fat-saturated post-contrast sequences. The scan parameters were as follows: TR/TE = 29.0/4.8 ms; FOV = 36 cm×36 cm; matrix = 360×360; slice thickness = 1.5 mm; and 108 slices. All post-contrast sequences were obtained after intravenous administration of a 0.1 mmol/kg dose of Gd-DTPA (Magnevist; Bayer-Schering Pharma, Berlin, Germany). On a pixel-by-pixel basis, subtraction images were obtained by subtracting the pre-contrast images from the first post-contrast CE-MRI images.

All images were assessed by two radiologists with 9–16 years of experience in the diagnosis of breast tumours. Both radiologists reviewed a standard training set of 50 non-study cases demonstrating the distribution of NME at the beginning of our study. In the processing of evaluating imaging, they were blinded to the effect of NAC. The distribution of NME included focal enhancement, linear enhancement, regional enhancement, segmental enhancement, multiregional enhancement, and diffuse enhancement, which were evaluated on CE-MRI according to coronal and sagittal images. Variables (Kappa values > 0.75) were further analysed by univariable analysis. For categorial data, the radiologists reached a consensus after discussion when there was inconsistency.

Table 3. Performance of the three models in predicting the efficacy of NAC in HER2-positive breast cancer

Model	AUC	95% CI	Accuracy	Sensitivity	Specificity	PPV	NPV
Imaging model[a]	0.750	0.700–0.870	0.750	0.570	0.910	0.840	0.710
Imaging model[b]	0.730	0.580–0.890	0.700	0.530	0.840	0.720	0.690
Radiomics model[a]	0.800	0.710–0.890	0.750	0.840	0.670	0.680	0.830
Radiomics model[b]	0.780	0.620–0.930	0.710	0.860	0.580	0.610	0.840
Imaging-radiomics model[a]	0.900	0.830–0.970	0.840	0.760	0.910	0.880	0.820
Imaging-radiomics model[b]	0.810	0.770–0.960	0.780	0.700	0.920	0.930	0.830

AUC, area under the curve; HER2, human epidermal growth factor receptor 2; NAC, neoadjuvant chemotherapy; NPV, negative-predictive vale; PPV, positive-predictive vale; pCR, pathological complete response.
[a]Training cohort.
[b]Testing cohort.

ROI segmentation and radiomics feature extraction

First, all CE-MRI images were normalised by the $u \pm 3\sigma$. Then, tumour regions of interest (ROIs) were manually drawn on each slice along the contour of the tumour on the subtraction image of the first post-contrast CE-MRI scan by two radiologists at the same time. A total of 1130 radiomics features were extracted in Python software (v. 3.7, https://www.python.org/), which included one shape-based feature, 18 histogram-based features, 22 grey-level co-occurrence matrix (GLCM)-based features, 16 run length matrix (RLM)-based features, 14 grey-level size zone matrix (GLSZM)-based features, 14 grey-level dependent matrix (GLDM)-based features and 1032 wavelet transform-based features. The interobserver reproducibility of ROI detection and radiomic feature extraction was measured by the interclass correlation coefficient (ICC). The ICC was defined as high (ICC ≥ 0.8), medium (0.8 > ICC ≥ 0.5), or low (ICC< 0.5). The ICC score for radiomics features was 0.848 ~ 0.998, which could indicate that those features reached satisfactory agreement.

Radiomics feature selection and rad-score calculation

Radiomics features were excluded by maximal relevance and minimal redundancy (mRMR) and least absolute shrinkage and selection operator (LASSO). First, redundant features were excluded by mRMR, and a total of 30 radiomics features remained. Second, the LASSO algorithm was used to select the optimal features, and six features were included finally. Last, the rad-score was calculated for each patient via optimal radiomics features weighted by their coefficients. Univariable analysis was used to compare the rad-score between the pCR and non-pCR groups in the training cohort, and it was validated in the testing cohort.

Nomogram development and evaluation

In the training cohort, clinical and MRI characteristics were analysed by univariable analysis. Then, the significant variables and rad-score were further analysed in multivariable analysis. Multiple stepwise reverse logistic regression was used to build an imaging-radiomics model, and the sensitivity, specificity, accuracy, area under the curve (AUC), positive-predictive value (PPV), and negative-predictive value (NPV) were calculated. Internal testing of the imaging-radiomics model was performed in the testing cohort. Finally, a nomogram based on the imaging-radiomics model was built. Calibration curves in the training and testing cohorts were created to evaluate the calibration of the nomogram using the Hosmer–Lemeshow goodness-of-fit test.

To evaluate the added value of the radiomics signature and the distribution of NME in predicting the effect of NAC in HER2-positive breast cancer, decision curves analysis was generated to evaluate the clinical utility by calculating the net benefits for a range of threshold probabilities.

Statistical analysis

Categorical variables are presented as the number and percentage, and continuous variables are presented as the mean ± SD or quartile. Categorical variables between the training set and testing set were compared with the χ^2 test or Fisher's test, and quantitative variables with the t test or Mann–Whitney U test. All statistical analyses were performed with R software (v. 3.60; http://www.r-project.org). $p < 0.05$ was considered statistically significant.

RESULTS

Clinical characteristics and MRI characteristics

There were no differences in age, menopausal status, FGT, BPE, T stage, N stage, distribution of NME, Ki-67 index or rad-score between the training and testing cohorts (Table 1).

The distribution of NME included the following: segmental enhancement (Figure 1a), regional enhancement (Figure 1b), and diffuse enhancement (Figure 1c). The distribution of NME was significantly different between the pCR and non-pCR groups in the training and testing cohorts (Table 2).

Radiomics signature

After the LASSO regression model (Figure 2a), 6 potential predictors were selected from 1130 radiomics features (Figure 2b). The rad-score was calculated by using the following formula:

Rad-score = −0.175+0.194*wavelet LHH first-order Mean + −0.277*wavelet HHH GLSZM Size Zone Non-Uniformity Normalised + 0.016*wavelet HHH GLCM MCC+−0.234*wavelet HLL GLDM Large Dependence High Grey Level Emphasis+0.138*wavelet HLH GLCM Correlation+−0.046*wavelet HLL first order Kurtosis

Figure 4. Calibration curves of the prediction nomogram in the training (a) and testing (b) sets. Calibration curves depict the calibration of the nomogram according to the agreement between the probability of the incidence of pCR and the actual observation. The black line represents the ideal estimation, and the red line represents the apparent prediction of the nomogram. The closer the red line is to the ideal black line, the better the prediction ability of the nomogram. pCR, pathological complete response

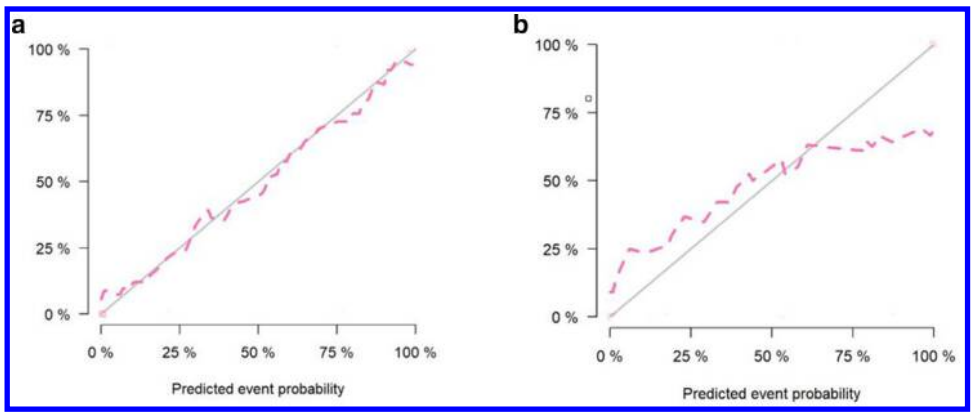

The rad-score between the pCR and non-pCR groups was significantly different in the training cohort ($p < 0.001$). The rad-score of the pCR group was higher than that of the non-pCR group in the training cohort, and this was validated in the testing cohort.

Development of the imaging model, radiomics-based model and imaging-radiomics model

The imaging model was built according to the distribution of NME. The AUCs of the distribution of NME in predicting pCR in HER2-positive invasive breast cancer after NAC were 0.750 [95% confidence interval (CI): 0.700–0.870] and 0.730 (95% CI: 0.580–0.890) in the training and testing cohorts, respectively (Table 3).

The radiomics-based model was built based on the rad-score. The AUCs of the rad-score in predicting pCR in HER2-positive breast cancer with NAC were 0.800 (95% CI: 0.710–0.890) in the training cohort and 0.780 (95% CI: 0.620–0.930) in the testing cohort (Table 3).

The distribution of NME and rad-score were independent predictors in predicting pCR in HER2-positive invasive breast cancer after NAC and were used to build an imaging-radiomics model. The AUCs of the imaging-radiomics model in predicting pCR in HER2-positive breast cancer with NAC were 0.900 (95% CI: 0.830–0.970) and 0.810 (95% CI: 0.770–0.960) in the training and testing cohorts, respectively.

Nomogram based on the imaging-radiomics model

The nomogram and calibration curves based on the imaging-radiomics model are shown in Figures 3 and 4. The decision curve analyses (DCAs) based on the models, including the imaging and imaging-radiomics models, are depicted in Figure 5. The imaging-radiomics model gained the most clinical utility for all of the threshold probabilities.

DISCUSSION

The prognosis of HER2-positive breast cancer can be improved by anti-HER2 treatment, but some patients could not achieve pCR after NAC.[2] In our study, the nomogram based on the imaging-radiomics model could preoperatively predict the efficacy of NAC in HER2-positive breast cancer patients who showed NME, which was validated in the testing cohort.

The distribution patterns of non-mass breast cancer may be closely related to its aggressiveness.[12,13] In our study, NME showed three types: segmental enhancement, regional enhancement and diffuse enhancement. It is difficult to perform surgery and/or breast-conserving surgery in breast cancer patients with the above three types of NME because of poorly defined boundaries. Therefore, patients with these lesions are more likely to be treated with NAC, which can potentially convert inoperable breast cancer to resectable breast cancer or convert mastectomy to breast-conserving surgery.[14] In our study, we confirmed that HER2-positive breast cancers that showed segmental enhancement on CE-MRI were more likely to achieve pCR after NAC than breast cancers with regional enhancement and diffuse enhancement [odds ratio (OR) = 48.56, 95% CI: 3.74–63.05]. Our result may be supported by the following research. Some literatures[10,15–17] reported that NME was more likely to be associated with ductal carcinoma *in situ* (DCIS), and NME in DCIS accounted for 60–81%. In addition, linear or segmental enhancement are the most common types in DCIS.[16] Hence, segmental enhancement is more likely to be DCIS than regional and diffuse enhancement. In our study, specimens and axillary lymph nodes without invasive tumour cells after NAC were defined as pCR. In summary, these could be considered as the reason why segmental enhancement was more likely to be related to pCR than regional and diffuse enhancement.

Some studies[8,18] have demonstrated that radiomics based on CE-MRI is a powerful tool to predict the efficacy of NAC in breast cancer. In our study, six features associated with pCR were chosen, including two first-order feature, two GLCM features, one GLDM feature and one GLSZM feature. The selected features were all wavelet features that reflect tumour heterogeneity that could not be recognised by the naked eye. The rad-score based on those features in the pCR group was higher than that in the non-pCR group, which was confirmed in the testing cohort. This result indicated that HER2-positive breast cancer patients with

Figure 5. DCAs for the imaging and combined imaging-radiomics models. The grey line represents the assumption that all patients have breast cancer. The black line represents the assumption that none of the patients have breast cancer. The blue line represents the imaging model. The red line represents the imaging-radiomics model. Across the various threshold probabilities, the imaging-radiomics curve shows a maximised net benefit compared with the imaging model for the individual performance. DCA, decision-curve analysis.

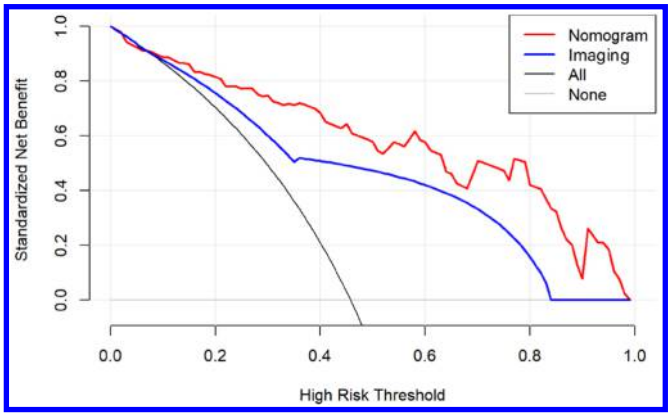

higher rad-scores more easily achieved pCR after NAC. In our study, the AUC values of the rad-score were 0.800 in the training cohort and 0.780 in the testing cohort.

The performance of the imaging-radiomics model that combined the distribution of NME and the rad-score improved the predictive efficacy of NAC in HER2-positive breast cancer, with AUC values of 0.900 and 0.810 in the training and testing cohorts, respectively. In addition, the distribution of NME and the rad-score could be obtained by a non-invasive method and could be easily acceptable in the clinic. Moreover, a nomogram based on the imaging-radiomics model was developed and validated. Logistic models can be visualised by nomograms, which have been used widely in clinics.[19–21] According to the nomogram, there was a positive correlation between the rad-score and the efficacy of NAC. Finally, the imaging-radiomics model had more net benefits than the rad-score only in the DCA. Therefore, it may have great potential to guide clinical treatment. We recommend that patients who are described as having a segmental distribution of NME and a higher rad-score should undergo NAC because these patients could attain better treatment efficacy. We believe that the clinical use of this nomogram can not only prevent unnecessary treatment for patients who are not sensitive to NAC but could also be helpful to guide the adjustment of the treatment plan.

The current study had several limitations. First, our study was single-centre and retrospective in design, and prospective and multicentre studies are needed to verify our results. Second, ROIs were drawn manually, which may limit the promotion of the research results. ROIs could be segmented using artificial intelligence with the cooperation of the engineering team to reduce the influence of subjective factors.

CONCLUSIONS

The nomogram based on the imaging-radiomics model could be used to pre-operatively predict the efficacy of NAC and may guide clinicians in making personal treatment decisions for HER2-positive breast cancer patients who show NME.

ACKNOWLEDGEMENTS

The authors of this manuscript declare no relationships with any companies, whose products or services may be related to the subject matter of the article.

FUNDING

This study has received funding by Sky imaging research fund of China international medical foundation (Z-2014-07-2003-06), Clinical Research Plan of SHDC (SHDC2020CR2008A), National Natural Science Foundation of China (NSFC 82071878), Shanghai Anticancer Association FLIGHT PROJECT (SACA-AX-201903), Shanghai Science and Technology Foundation (19DZ1930502), Shanghai Science and Technology Innovation Action Plan Medical Innovation Research Project(21Y11910200).

REFERENCES

1. Perez EA, Suman VJ, Davidson NE, Martino S, Kaufman PA, Lingle WL, et al. HER2 testing by local, central, and reference laboratories in specimens from the north central cancer treatment group N9831 intergroup adjuvant trial. *J Clin Oncol* 2006; **24**: 3032–38. https://doi.org/10.1200/JCO.2005.03.4744
2. Vu T, Claret FX. Trastuzumab: updated mechanisms of action and resistance in breast cancer. *Front Oncol* 2012; **2**: 62. https://doi.org/10.3389/fonc.2012.00062
3. Nahta R, Yu D, Hung MC, Hortobagyi GN, Esteva FJ. Mechanisms of disease: understanding resistance to HER2-targeted therapy in human breast cancer. *Nat Clin Pract Oncol* 2006; **3**: 269–80. https://doi.org/10.1038/ncponc0509
4. Gillies RJ, Kinahan PE, Hricak H. Radiomics: images are more than pictures, they are data. *Radiology* 2016; **278**: 563–77. https://doi.org/10.1148/radiol.2015151169
5. Liu Z, Li Z, Qu J, Zhang R, Zhou X, Li L, et al. Radiomics of multiparametric MRI for pretreatment prediction of pathologic complete response to neoadjuvant chemotherapy in breast cancer: A multicenter study. *Clin Cancer Res* 2019; **25**: 3538–347. https://doi.org/10.1158/1078-0432.CCR-18-3190
6. Parikh J, Selmi M, Charles-Edwards G, Glendenning J, Ganeshan B, Verma H, et al. Changes in primary breast cancer heterogeneity may augment midtreatment MR imaging assessment of response to neoadjuvant chemotherapy. *Radiology* 2014; **272**: 100–112. https://doi.org/10.1148/radiol.14130569
7. Braman NM, Etesami M, Prasanna P, Dubchuk C, Gilmore H, Tiwari P, et al. Intratumoral and peritumoral radiomics for the pretreatment prediction of pathological complete response to neoadjuvant chemotherapy based on breast DCE-MRI. *Breast Cancer Res* 2017; **19**: 57. https://doi.org/10.1186/s13058-017-0846-1

8. Fan M, Wu G, Cheng H, Zhang J, Shao G, Li L. Radiomic analysis of DCE-MRI for prediction of response to neoadjuvant chemotherapy in breast cancer patients. *Eur J Radiol* 2017; **94**: 140–47. https://doi.org/10.1016/j.ejrad.2017.06.019
9. Cain EH, Saha A, Harowicz MR, Marks JR, Marcom PK, Mazurowski MA. Multivariate machine learning models for prediction of pathologic response to neoadjuvant therapy in breast cancer using MRI features: a study using an independent validation set. *Breast Cancer Res Treat* 2019; **173**: 455–63. https://doi.org/10.1007/s10549-018-4990-9
10. Jeon-Hor C, Hyeon-Man B. Estrogen receptor and breast MR imaging features: a correlation study. *J Magn Reson Imaging* 2008; 27(4): 825–33. https://doi.org/10.1002/jmri.21330
11. Gweon HM, Jeong J, Son EJ, Youk JH, Kim JA. The clinical significance of accompanying NME on preoperative MR imaging in breast cancer patients. *PLoS One* 2017; **12(5)**. https://doi.org/10.1371/journal.pone.0178445
12. Lee SM, Nam KJ, Choo KS, Kim JY, Jeong DW, Kim HY, et al. Patterns of malignant non-mass enhancement on 3-T breast MRI help predict invasiveness: using the BI-RADS lexicon fifth edition. *Acta Radiol* 2018; **59**: 1292–99. https://doi.org/10.1177/0284185118759139
13. Machida Y, Shimauchi A, Tozaki M, Kuroki Y, Yoshida T, Fukuma E. Descriptors of malignant non-mass enhancement of breast MRI: their correlation to the presence of invasion. *Acad Radiol* 2016; **23**: 687–95. https://doi.org/10.1016/j.acra.2016.01.014
14. Jansen SA, Shimauchi A, Zak L, Fan X, Karczmar GS, Newstead GM. The diverse pathology and kinetics of mass, nonmass, and focus enhancement on MR imaging of the breast. *J Magn Reson Imaging* 2011; **33**: 1382–89. https://doi.org/10.1002/jmri.22567
15. Jansen SA, Newstead GM, Abe H, Shimauchi A, Schmidt RA, Karczmar GS. Pure ductal carcinoma in situ: kinetic and morphologic MR characteristics compared with mammographic appearance and nuclear grade. *Radiology* 2007; **245**: 684–91. https://doi.org/10.1148/radiol.2453062061
16. Rosen EL, Smith-Foley SA, DeMartini WB, Eby PR, Peacock S, Lehman CD. BI-RADS MRI enhancement characteristics of ductal carcinoma in situ. *Breast J* 2007; **13**: 545–50. https://doi.org/10.1111/j.1524-4741.2007.00513.x
17. Chan S, Chen J-H, Agrawal G, Lin M, Mehta RS, Carpenter PM, et al. Characterization of pure ductal carcinoma in situ on dynamic contrast-enhanced MR imaging: do nonhigh grade and high grade show different imaging features? *J Oncol* 2010; **2010**. https://doi.org/10.1155/2010/431341
18. Chamming's F, Ueno Y, Ferré R, Kao E, Jannot A-S, Chong J, et al. Features from computerized texture analysis of breast cancers at pretreatment MR imaging are associated with response to neoadjuvant chemotherapy. *Radiology* 2018; **286**: 412–20. https://doi.org/10.1148/radiol.2017170143
19. Balachandran VP, Gonen M, Smith JJ, DeMatteo RP. Nomograms in oncology: more than meets the eye. *Lancet Oncol* 2015; **16**: e173–80. https://doi.org/10.1016/S1470-2045(14)71116-7
20. van den Bergh RCN, Roobol MJ, Wolters T, van Leeuwen PJ, Schröder FH. The prostate cancer prevention trial and european randomized study of screening for prostate cancer risk calculators indicating a positive prostate biopsy: a comparison. *BJU Int* 2008; **102**: 1068–73. https://doi.org/10.1111/j.1464-410X.2008.07940.x
21. Han L, Zhu Y, Liu Z, Yu T, He C, Jiang W, et al. Radiomic nomogram for prediction of axillary lymph node metastasis in breast cancer. *Eur Radiol* 2019; **29**: 3820–29. https://doi.org/10.1007/s00330-018-5981-2

BJR

https://doi.org/10.1259/bjr.20220466

Received: 30 April 2022 | Revised: 30 September 2022 | Accepted: 08 November 2022 | Published online: 12 January 2023

Cite this article as:
Sartoretti T, McDermott M, Mergen V, Euler A, Schmidt B, Jost G, et al. Photon-counting detector coronary CT angiography: impact of virtual monoenergetic imaging and iterative reconstruction on image quality. *Br J Radiol* (2023) 10.1259/bjr.20220466.

FULL PAPER

Photon-counting detector coronary CT angiography: impact of virtual monoenergetic imaging and iterative reconstruction on image quality

[1,2,3]THOMAS SARTORETTI, BMed, [2,3,4]MICHAEL MCDERMOTT, BSc, [1]VICTOR MERGEN, MD, [1]ANDRÉ EULER, MD, [5]BERNHARD SCHMIDT, PhD, [4]GREGOR JOST, PhD, [2,3]JOACHIM E WILDBERGER, MD, PhD and [1]HATEM ALKADHI, MD, MPH, EBCR, FESER

[1]Diagnostic and Interventional Radiology, University Hospital Zurich, University of Zurich, Zurich, Switzerland
[2]Department of Radiology and Nuclear Medicine, Maastricht University Medical Center, Maastricht, the Netherlands
[3]Cardio-Vascular Research Institute Maastricht (CARIM), Maastricht, The Netherlands
[4]Bayer AG, Berlin, Germany
[5]Siemens Healthineers, Forchheim, Germany

Address correspondence to: Dr Hatem Alkadhi
E-mail: *hatem.alkadhi@usz.ch*

Objectives: To assess the impact of low kilo-electronvolt (keV) virtual monoenergetic image (VMI) energies and iterative reconstruction on image quality of clinical photon-counting detector coronary CT angiography (CCTA).

Methods: CCTA with PCD-CT (prospective ECG-triggering, 120 kVp, automatic tube current modulation) was performed in a high-end cardiovascular phantom with dynamic flow, pulsatile heart motion, and including different calcified plaques with various stenosis grades and in 10 consecutive patients. VMI at 40,50,60 and 70 keV were reconstructed without (QIR-off) and with all quantum iterative reconstruction (QIR) levels (QIR-1 to 4). In the phantom, noise power spectrum, vessel attenuation, contrast-to-noise-ratio (CNR), and vessel sharpness were measured. Two readers graded stenoses in the phantom and graded overall image quality, subjective noise, vessel sharpness, vascular contrast, and coronary artery plaque delineation on 5-point Likert scales in patients.

Results: In the phantom, noise texture was only slightly affected by keV and QIR while noise increased by 69% from 70 keV QIR-4 to 40 keV QIR-off. Reconstructions at 40 keV QIR-4 exhibited the highest CNR (46.1 ± 1.8), vessel sharpness (425 ± 42 ΔHU/mm), and vessel attenuation (1098 ± 14 HU). Stenosis measurements were not affected by keV or QIR level ($p > 0.12$) with an average error of 3%/6% for reader 1/reader 2, respectively. In patients, across all subjective categories and both readers, 40 keV QIR-3 and QIR-4 images received the best scores ($p < 0.001$).

Conclusion: Forty keV VMI with QIR-4 significantly improved image quality of CCTA with PCD-CT.

Advances in knowledge: PCD-CT at 40 keV and QIR-4 improves image quality of CCTA.

Computed Tomography Angiography; Coronary Vessels; Photons; Phantoms, Imaging

INTRODUCTION

In patients with a low-to-intermediate cardiovascular risk, coronary computed tomography angiography (CCTA) has emerged as the preferred non-invasive imaging modality for the initial diagnostic workup of coronary artery disease (CAD).[1] CCTA image data are usually acquired on an energy-integrating detector CT (EID-CT) system in the single-energy (SE) mode. More recently, dual-energy (DE) cardiac CT enabling the reconstruction of virtual monoenergetic images (VMI) has been introduced.[2–4] Reconstruction of VMI using high kilo-electronvolt (keV) levels may help reduce blooming artifacts from calcified coronary plaques.[5] On the other hand, reconstructions at low keV levels are of interest in CT angiography because of the energy dependent attenuation of iodine. Specifically, attenuation and contrast-to-noise-ratio in the arteries are increased due to the proximity of low monoenergetic energy levels to the k-edge of iodine.[2,6–8] Thus, DE-based cardiac CT with VMI reconstructions can be used to improve image quality and/or to reduce the amount of required contrast media.[3,9]

Recently, a whole-body full field-of-view dual-source photon-counting detector CT (PCD-CT) system has been

approved for clinical use.[10] In contrast to previous EID-CT systems, PCD-CT enables a direct conversion of photons to electrical signal. PCD-CT has shown potential to improve spatial resolution, contrast-to-noise ratio (CNR), and to lower image noise as compared to EID-CT systems.[10–15] Furthermore, PCD-CT has intrinsic spectral capabilities as PCD-generated signals include the energy information of every individual photon. With this scanner, VMI reconstructions represent the new reference standard for image evaluation, thereby substituting conventional polychromatic EID-CT images.[11,16] In regard to cardiac CT imaging, the inherent spectral capabilities of the PCD-CT system enable DE imaging at the unrestricted highest temporal resolution of the scanner.[17]

Along with the introduction of the new PCD-CT system, a novel iterative reconstruction (IR) algorithm called quantum iterative reconstruction (QIR) has been introduced. With this novel PCD-CT system, images can be reconstructed either without QIR (QIR-off) or with QIR at four different strength levels (QIR 1–4).[10,18]

To the best of our knowledge, no study so far has systematically assessed the impact of keV levels and QIR on CCTA on this novel clinical PCD-CT system. Previous studies on EID-CT systems suggested a trade-off between contrast enhancement and noise levels on low keV VMI reconstructions generated with various DECT technologies,[19–21] and between noise reduction and changes in noise texture at higher strength levels of various IR algorithms.[22–25]

In a dedicated phantom and in patients, we sought to systematically analyze the impact of low keV virtual monoenergetic images and quantum iterative reconstruction levels on objective and subjective image quality on CCTA on a clinical PCD-CT.

METHODS AND MATERIALS

CT imaging protocol

For all phantom and patient scans the same CT protocol was used. All scans were acquired on a first-generation, whole-body, dual-source PCD-CT system (NAEOTOM α; Siemens Healthineers, Forchheim, Germany, Version VA40) equipped with two photon-counting detectors (cadmium telluride), each with a 144 × 0.4 mm collimation. ECG-triggered sequential acquisitions were performed with ECG-pulsing depending on the heart rate. Importantly image acquisition was performed in the Quantum-Plus (*i.e.,* spectral) mode (and not in the ultra-high resolution (UHR) mode as shown elsewhere[26,27]). Tube voltage was set at 120kVp and the image quality (IQ) level was 44, representing the default CCTA protocol for clinical routine. The IQ level represents the effective mAs applied for the protocol-specific reference water-equivalent diameter with a CT geometry correction hereby representing a system- and reconstruction-independent image quality definition. The $CTDI_{vol}$ was 12.8 mGy (water-filled container) and 9.4 mGy in the phantom experiments, and 14.5 ± 10.2 mGy in patients, respectively. Gantry rotation time was 0.25 s. In patients, CCTA was performed after the intravenous injection of 40–70 ml contrast media (Iopromide, Ultravist, Bayer Healthcare, Berlin, Germany) at an iodine delivery rate of 1.85–2.22 gI/s depending on the body mass index (Table 1 for details) of the individual patient, followed by a second isovolumetric phase consisting of 20% contrast agent and 80% saline solution (NaCl 0.9%), followed by a saline flush.

Table 1. Patient demographics

Age	**59 ± 13 years**	
Sex	five female, five male	
Body mass index	27.8 ± 4.6 kg/m^2	
Body height	168 ± 10 cm	
Body weight	79 ± 14 kg	
Indications for coronary CT angiography	rule-out coronary artery disease at a low-to-intermediate pretest probability (8 patients, 80%). rule-out coronary artery disease prior to aortic valve surgery (2 patients, 20%)	
Cardiovascular risk factors	Positive family history	7 (70%)
	Smoking	3 (30%)
	Diabetes	2 (20%)
	Arterial hypertension	6 (60%)
	Dyslipidemia	8 (80%)
	Obesity	1 (10%)

CT image reconstruction

For both phantom and patient data, VMI at 40-70keV were reconstructed in 10keV increments with QIR-off and with all strength levels of QIR (QIR 1–4). A medium soft convolution kernel (Siemens Bv40), a section thickness of 0.6 mm, an increment of 0.3 mm, a field of view (FOV) of 200 mm, and a matrix size of 512 × 512 pixels were used.

For PCD-CT, a pure FBP-type reconstruction algorithm for spectral results is not available However, "QIR-off" is offered in which minimally possible statistical optimization is achieved compared to standard-weighted FBP. QIR strength levels 1–4 trigger an additional statistical optimization in terms of a globally reduced target noise level. Specifically, higher strength levels lead to stronger optimization, i.e., greater noise reduction.[28]

Phantom study

Phantom experiments were performed using a physiological, high-end generation III cardiovascular phantom (Figure 1) as described elsewhere in detail.[29] The phantom includes interconnected cerebral, thoracic, abdominal, and peripheral vasculature with hemodynamically accurate flows however, the focal region of this evaluation was the cardiac frame. The phantom includes a highly physiological heart model with four chambers and embedded tricuspid, pulmonary, mitral, and aortic valves. Modular connection points at the base of the aortic root lead to left and right coronary branching models overlaid on the exterior of the heart model. The coronary models are capable of being exchanged between healthy and diseased versions, including with soft (*i.e.,* non-calcified) or densely calcified plaques of varying occlusion percentages. In this investigation, the left

Figure 1. Overview of the cardiovascular phantom. The phantom setup on the CT scanner table is shown on the left. A close-up picture of the heart is shown in the middle together with a volume rendered CT image in the lower left part. A representative CT image of the heart is shown on the top right, whereby calcified plaques in the coronary artery wall are marked with small orange arrows. Close-up short- and long-axis images of a coronary plaque are shown in the lower right part of the figure.

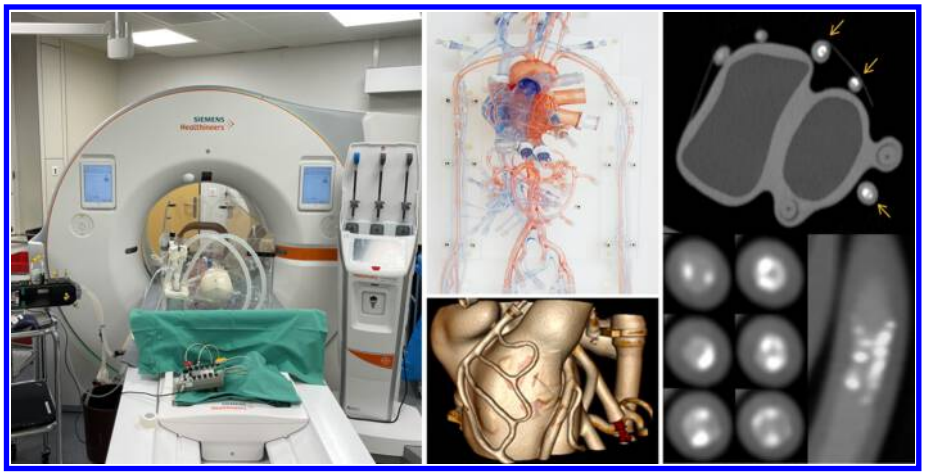

coronary model (Figure 2) included three plaques composed of deposited calcium carbonate with occlusion percentages of 50% in diagonal branch of the left anterior descending artery (D/LAD), 70% in the main branch of the LAD, and 90% in the circumflex artery (CX) as defined by the vendor. Specifically, the plaques with 50%, 70%, and 90% occlusion percentages had measurements of 1 mm lumen from 2-mm vessel inner diameter, 1.2-mm lumen from 4-mm vessel inner diameter, and 0.50 mm lumen from 5 mm inner diameter, respectively. All plaques were blow-deposited into the vessels. The length of the calcified sections was between 8 and 12 mm in length. The attenuation of the plaque material, in this case calcium carbonate crystals, measured between 200 and 600HU (120kV) across the three plaques depending on ROI and location along the plaque. The lower values than expected in some areas were explained by the manufacturer as likely micro-pores in the calcified plaque that absorbed water when the vessel was filled. Additionally, an electromechanical pump (SuperPump, ViVitro Labs, Victoria, BC, Canada) was connected to the phantom allowing for control over heart rate, stroke volume, and blood pressure, which together facilitate cardiac motion of the model.

For image acquisition the phantom was positioned in an acrylic container. The heart was mounted on top of two plastic 500-ml saline bottles to simulate attenuation of surrounding anatomical structures as encountered *in vivo*. Subsequently, the coronaries were manually filled with iodinated contrast media (Iopromide) titrated with water to a concentration of 15 mgI ml^{-1} as recommended elsewhere.[30] Although connected to the phantom, the coronaries were isolated from the dynamic flow through

Figure 2. Overview of the left coronary model. The model included three plaques composed of deposited calcium carbonate with occlusion percentages of 50% in diagonal branch of the left anterior descending artery (D/LAD), 70% in the main branch of the LAD, and 90% in the circumflex artery (CX) as defined by the vendor.

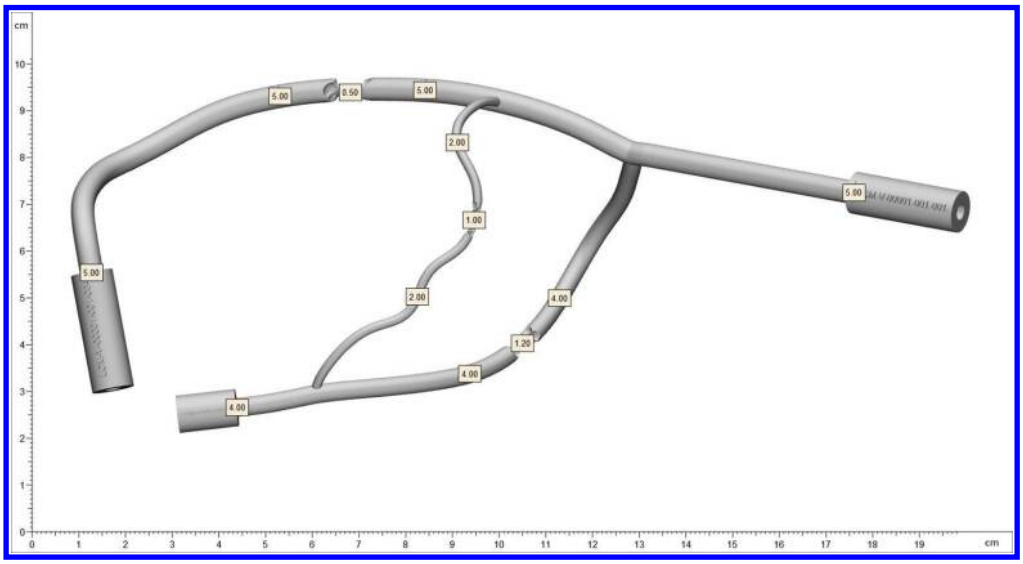

the rest of the vasculature to ensure precise concentration of contrast media in the target vessels throughout the various trials and to protect the geometry of the coronary plaques. The dynamic flow in the remaining vasculature and the heart chambers, resulting in a pulsatile movement of the heart and coronaries, was achieved by circulating room temperature water at a heart rate of 60 beats per minute (BPM) and a stroke volume of 80 ml. Internal blood pressure of the phantom was maintained at 120/80 mm Hg.

Objective image analysis - Noise Power Spectrum

A water-filled cylindrical container mimicking an intermediate-sized patient (diameter 30 cm) was scanned with the same CT protocol as used for the vascular phantom and patient scans. Noise power spectrum (NPS) analysis was performed with an open-source software (ImQuest Version 7, Duke University) in an effort to quantify image noise texture. Specifically, quadratic ROIs with an area of 15 cm^2 were placed in the center of the phantom across 200 consecutive slices. 1D-NPS profiles depicting the radial average of the 2D-NPS profile were generated. The average (f_{av}) and peak spatial frequencies (f_{peak}) and the area under the curve representing the noise level of the NPS curves were extracted for further analyses.

Objective image analysis – Further Metrics

First, one reader measured coronary attenuation and the CNR by manually placing regions of interests (ROI) into the coronaries and into the water filled left ventricle. CNR was calculated as follows:

$$CNR = \frac{HU_{Vessel} - HU_{Water}}{SD_{Water}}$$

Furthermore, the mean HU value (*i.e.,* HU_{Vessel}) within the ROI was taken as the coronary attenuation. The copy-paste function of our institutions image viewer (DeepUnity Viewer, Dedalus HealthCare) was used to copy ROIs from image to image. ROI placement was performed three times and the average values were taken for further analyses.

Second, vessel sharpness defined as the change in HU values per mm (ΔHU/mm) was measured. A line profile perpendicular to a vessel (in our case the CX artery) was generated using ImageJ's "Line Profile" function as shown elsewhere in detail[31] (ImageJ 1.53a, National Institutes of Health, USA). Then, the maximum slopes of the regression lines for the anterior and posterior vessel border were calculated and averaged by computing the derivative of the line profiles function in R using the package "pspline".

Third, two readers (board-certified radiologists with 5 and 10 years of experience in cardiovascular imaging, respectively) independently and blindly measured and recorded the maximum luminal diameter of all stenoses and calculated the percentage stenosis on all reconstructions. Specifically, the readers performed diameter stenosis measurements as routinely done in coronary CT angiography examinations using the electronic caliper tools of our institutions image viewer (DeepUnity Viewer, Dedalus HealthCare).

Patient study

Patients undergoing clinically indicated CCTA on the PCD-CT system between November and December 2021 were retrospectively screened. Consecutive patients for whom raw data were available for image reconstruction were reviewed ($n = 14$). Exclusion criteria were degraded image quality due to foreign materials ($n = 2$), previous coronary stent implantation ($n = 1$) and foregoing coronary artery bypass graft surgery ($n = 1$). Thus, a total of 10 patients were included in this study (Table 1).

Two board-certified radiologists (with 5 and 10 years of experience in cardiovascular imaging, respectively) performed subjective image analyses independently in a blinded and randomized manner. This study part was approved by our local ethics committee. All patients provided the written general informed consent statement of our hospital.

Readers used 5-point Likert scales (5: excellent, 4: good, 3: moderate, 2: poor, 1: non-diagnostic) to grade images qualitatively for the following categories: overall image quality, subjective image noise, vessel sharpness and, if applicable, coronary plaque visualization.

Statistical analysis

Quantitative data from the phantom scans were presented visually and by means of descriptive statistics. Generalized linear models (GLM) were fitted with keV and QIR as predictors and image quality metrics (*i.e.,* coronary attenuation, CNR, vessel sharpness, stenosis measurements) as response variables. Bland-Altman analysis was performed on the data from stenosis measurements in the phantom using the verified lumen and occlusion dimensions provided by the vendor as the reference standard.

To check for differences in qualitative scores between the various image reconstructions of patient scans, Friedman tests with post-hoc sign tests were used. Additionally, interreader agreement of qualitative scores was quantified with Krippendorff's α coefficients (0.0–0.20 = poor agreement, 0.21–0.40 = fair agreement, 0.41–0.60 = moderate agreement, 0.61–0.80 = substantial agreement, and 0.81–1.00 = almost perfect agreement).[11] Two-tailed p-values < 0.05 were considered to indicate statistical significance. All analyses were performed using R statistical software (version 4.1.1; R Core Team, R Foundation for Statistical Computing).

RESULTS

Phantom study

Noise Power Spectrum

Average (f_{av}) and peak (f_{peak}) spatial frequencies were similar for almost all reconstructions indicating similar image texture (Table 2, Figure 3). Specifically, for all reconstructions except for 40 keV QIR-4, f_{peak} ranged from 0.28 to 0.3 and f_{av} ranged from 0.28 to 0.32. For the 40keV QIR-4 reconstruction, f_{peak} was 0.05 and f_{av} was 0.26. Thus, for the 40keV QIR-4 images, low frequency noise indicated a slightly blotchier image texture. Noise magnitude decreased both from QIR-off to QIR-4 and

Table 2. Overview of quantitative image quality metrics as assessed in the phantom. keV: kilo electron volt; QIR: quantum iterative reconstruction

keV level	QIR	Contrast-to-Noise Ratio	Coronary Attenuation [HU]	Noise Magnitude [HU]	Peak Spatial Frequency (f_{peak})	Average Spatial Frequency (f_{av})	Vessel Sharpness (ΔHU/mm)
40	**QIR-off**	26 ± 1.8	1107 ± 26	35	0.28	0.3	409 ± 98
50	**QIR-off**	21.8 ± 1.5	747 ± 17	29	0.28	0.31	269 ± 78
60	**QIR-off**	19.9 ± 1.1	528 ± 12	24	0.28	0.32	184 ± 62
70	**QIR-off**	18.5 ± 0.7	395 ± 8	21	0.30	0.32	153 ± 37
40	**QIR-1**	29.3 ± 1.9	1107 ± 26	31	0.28	0.29	415 ± 91
50	**QIR-1**	24.6 ± 1.7	747 ± 17	26	0.28	0.31	273 ± 74
60	**QIR-1**	22.4 ± 1.2	528 ± 12	21	0.28	0.32	187 ± 60
70	**QIR-1**	20.8 ± 0.7	395 ± 8	18	0.30	0.32	159 ± 36
40	**QIR-2**	33.5 ± 2.0	1107 ± 26	27	0.28	0.29	419 ± 87
50	**QIR-2**	28.2 ± 1.9	747 ± 17	22	0.28	0.31	278 ± 70
60	**QIR-2**	25.6 ± 1.3	528 ± 11	19	0.28	0.32	194 ± 56
70	**QIR-2**	23.7 ± 0.7	395 ± 7	16	0.30	0.32	165 ± 34
40	**QIR-3**	39.1 ± 2.2	1109 ± 29	22	0.28	0.28	424 ± 82
50	**QIR-3**	32.9 ± 2.1	749 ± 19	19	0.28	0.3	283 ± 66
60	**QIR-3**	29.8 ± 1.5	529 ± 12	16	0.28	0.31	195 ± 55
70	**QIR-3**	27.7 ± 0.8	395 ± 7	13	0.30	0.31	175 ± 33
40	**QIR-4**	46.1 ± 1.8	1098 ± 14	18	0.05	0.26	425 ± 42
50	**QIR-4**	39.3 ± 2.2	746 ± 19	15	0.28	0.29	283 ± 31
60	**QIR-4**	35.4 ± 1.8	527 ± 12	13	0.28	0.31	196 ± 22
70	**QIR-4**	32.9 ± 1.3	393 ± 7	11	0.30	0.31	158 ± 11

Figure 3. Overview of objective image quality analysis in the phantom. (A) shows CNR and coronary attenuation (*i.e.,* mean HU values from ROI measurements) at different keV and QIR levels. (B) indicates data from noise power spectrum analysis. CNR increases at lower keV levels and at higher QIR strength levels. Coronary attenuation increases at lower keV levels but remains virtually unaffected by the QIR strength level. NPS analysis shows comparable image texture among all reconstructions yet decreasing noise levels for higher keV levels and QIR strength levels (graph in the bottom right corner).

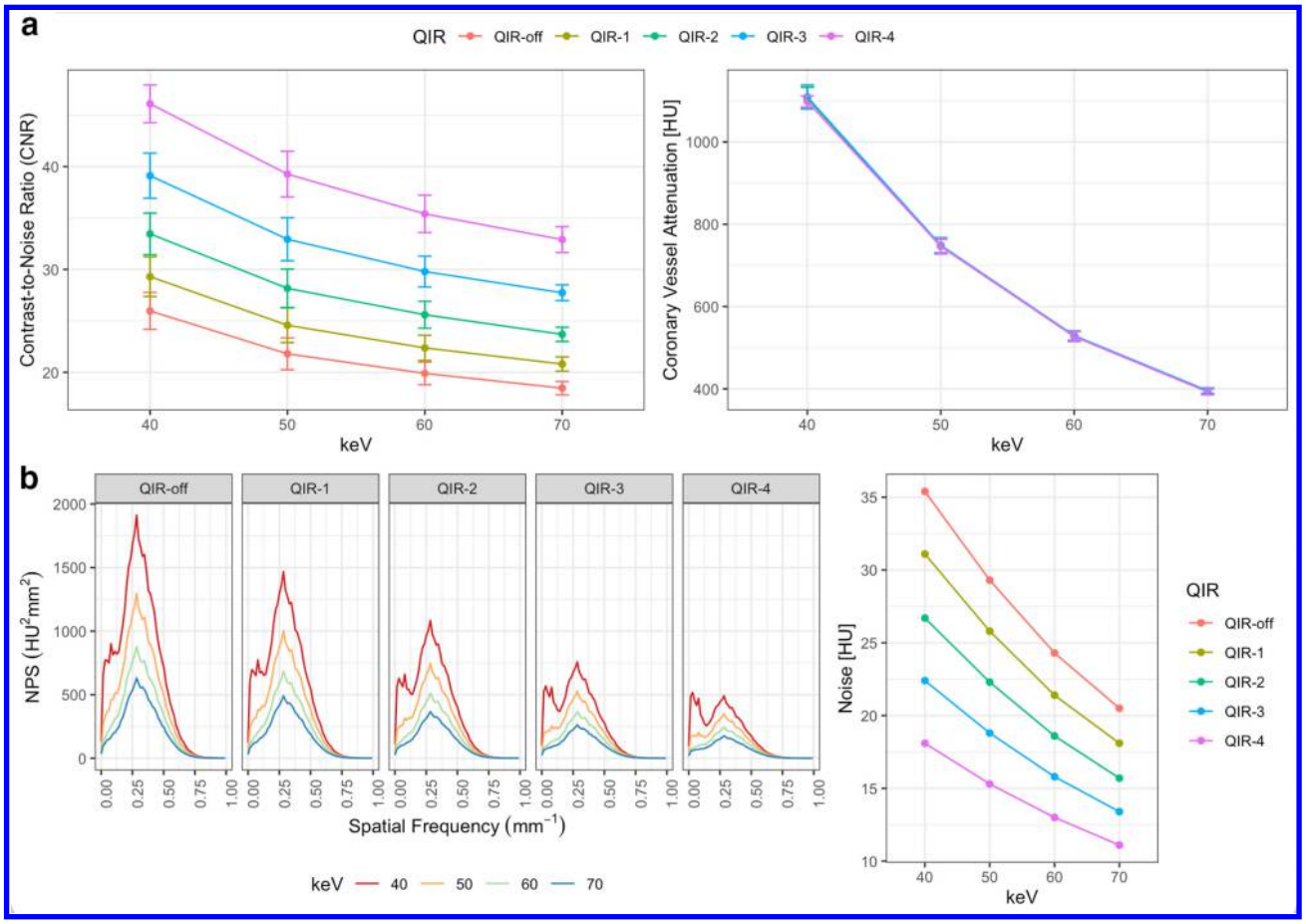

from 40-70keV with a maximum reduction of 68.6% (35HU *vs* 11HU) between 40keV QIR-off and 70keV QIR-4.

Coronary artery attenuation

The lowest coronary artery attenuation was found on 70keV QIR-4 images (397 ± 8 HU) and the highest attenuation on 40keV QIR-3 images (1109 ± 29 HU), corresponding to a 183% difference (Table 2 and Figure 3). keV level ($p < 0.001$) but not QIR strength level ($p = 0.97$) was a significant predictor of coronary attenuation. The effect of QIR on attenuation was negligible while decreasing the keV level considerably increased the vessel attenuation.

Contrast-to-Noise ratio

The smallest CNR was found on 70keV QIR-off images (18.5 ± 0.7) and the highest CNR was found on 40keV QIR-4 images (46.1 ± 1.8), corresponding to a 149% difference (Table 2, Figure 3). Both keV level and QIR strength level (both, $p < 0.001$) were significant predictors of CNR. Specifically, CNR increased at decreasing keV levels and at increasing QIR strength levels.

Vessel sharpness

The lowest vessel sharpness was measured on 70keV QIR-off images (153 ± 37 ΔHU/mm), while the highest vessel sharpness was found on 40keV QIR-4 images (425 ± 42 ΔHU/mm), corresponding to a 177% difference (Table 2, Figure 4). keV level ($p < 0.001$) but not QIR strength level ($p = 0.8$) was a significant predictor of vessel sharpness. Thus, the effect of QIR on vessel sharpness was negligible while decreasing the keV level increased the vessel sharpness.

Stenosis measurements

For readers 1 and 2, the average absolute percentage difference in stenosis quantification was 4%/3%/3 and 7%/4%/8% for vessel 1 (D/LAD, 50% stenosis)/vessel 2 (LAD, 70% stenosis) / vessel 3 (CX, 90% stenosis), respectively. Overall, Bland-Altman analysis revealed average errors of 1%/2%, an upper limit of agreement of 6%/12% and a lower limit of agreement of −3%/0% for stenosis grading by readers 1 and 2, respectively. For both readers, there was no impact of keV level ($p = 0.23–0.89$) and QIR strength level ($p = 0.12–0.98$) on quantification accuracy (Figure 4).

Figure 4. Overview of the vessel sharpness analysis and stenosis grading in the phantom. (A) shows the line profile and corresponding vessel sharpness as defined by the maximum slopes of the line profile at the vessel edges. (B) shows the stenosis measurements by both readers for all plaques stratified for keV and QIR strength levels. The black-dotted line indicates the true percentage stenosis as provided by the phantom vendor. Vessel sharpness increased at lower keV levels but remained virtually unchanged across the various QIR strength levels. Stenosis measurements were not affected by keV or QIR strength level.

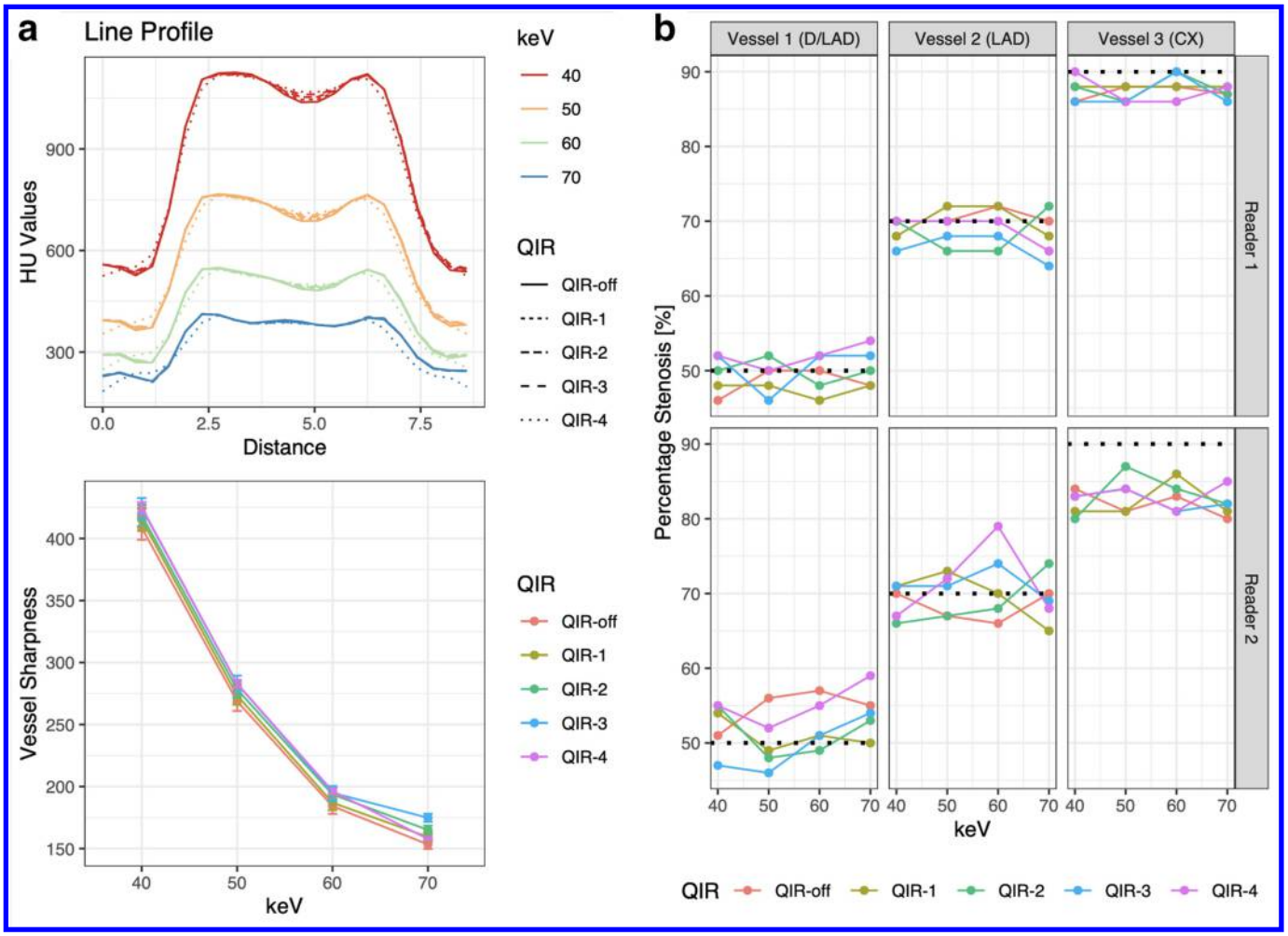

Patient study

Image examples are shown in Figure 5 and Figure 6. Inter-reader agreement of scores from subjective image analyses was moderate (α = 0.592). For all categories and for both readers, there were significant differences between reconstructions (all, $p < 0.001$).

Subjective image analysis revealed highest scores for 40 keV with QIR-3 and QIR-4 and for 50 keV with QIR-3 and QIR-4. For overall image quality, reader one found higher scores for 40 keV QIR-3 and QIR-4 as well as 50 keV QIR-4 relative to 50 keV QIR-3 (all, $p = 0.006$), while there were no differences between these four reconstructions for reader 2 ($p = 0.4$). For image noise, vessel sharpness, and plaque delineation, there were no significant differences between the four reconstructions both for reader 1 and 2 ($p = 0.08$–1). For vascular contrast, reader 1 deemed 40 keV images better than 50 keV images ($p = 0.008$), while reader two found no significant differences among reconstructions ($p > 0.99$). Thus, when considering all categories and both readers, 40 keV QIR-3 and QIR-4 reconstructions (overall image quality: 5[5,5];) received the best subjective scores.

DISCUSSION

This study summarizes an initial experience with CCTA on a novel clinical PCD-CT system as performed with a standard imaging and image reconstruction protocol (*i.e.*, 120 kV tube voltage and medium soft convolution kernel) including a systematic analysis of the impact of various low keV VMI reconstructions and QIR levels on subjective and objective image quality in a phantom and in patients. The phantom data indicate that low keV VMI reconstructions and high strengths levels of QIR may improve objective image quality with only minor changes in image noise texture and with no effect on quantification accuracy of coronary stenosis grading of calcified coronary plaques. Our subjective analysis of patient data suggests that 40keV QIR-3 and QIR-4 reconstructions may significantly improve image quality. Thus, when considering all data, 40keV QIR-4 reconstructions

Figure 5. Representative images of a 70-year-old female patient with an Agatston score of 475 and a calcified plaque in the left anterior descending (LAD) artery. 40 to 70 keV VMI reconstructions at QIR-4 are shown (upper row: standard field-of-view reconstruction, lower row: magnified view of the LAD). Note the high vascular contrast on 40 keV images along with the better delineation of the vessel lumen and plaque.

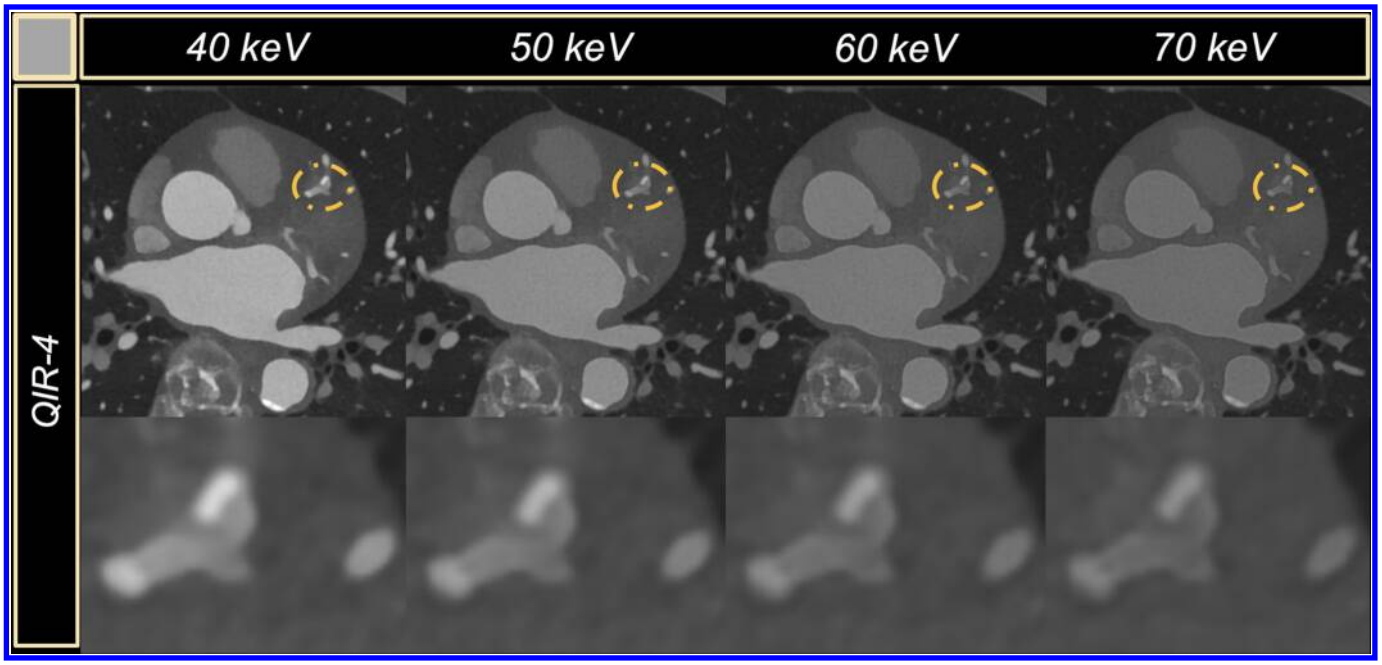

for CCTA with PCD-CT appear to be promising reconstructions that offer optimal objective and subjective image quality.

In a phantom study, Rotzinger et al investigated the performance of a prototype PCD-CT for CCTA relative to an EID-CT system.[32] These authors found that PCD-CT outperformed EID-CT for the detection of coronary atherosclerosis while providing images with a lower noise magnitude, higher spatial resolution, and superior lipid core detectability.[32] Boccalini et al investigated the performance of a prototype PCD-CT for imaging of coronary stents in eight patients and found improved objective and subjective image quality at a lower radiation dose than EID-CT.[15] Importantly, both these authors used a different PCD-CT system and no VMI reconstructions were used.

Rajendran et al provided a representative image example of a CCTA examination as performed on the same clinical PCD-CT system used in our study, but did not perform further

Figure 6. Representative images of a 46-year-old male patient with an Agatston score of 61 and a mixed plaque in the proximal left anterior descending (LAD) artery. 40 keV VMI reconstructions at QIR-off to QIR-4 are shown (upper row: standard field-of-view reconstruction, lower row: magnified view of the proximal LAD). Note the lower noise levels at higher levels of QIR.

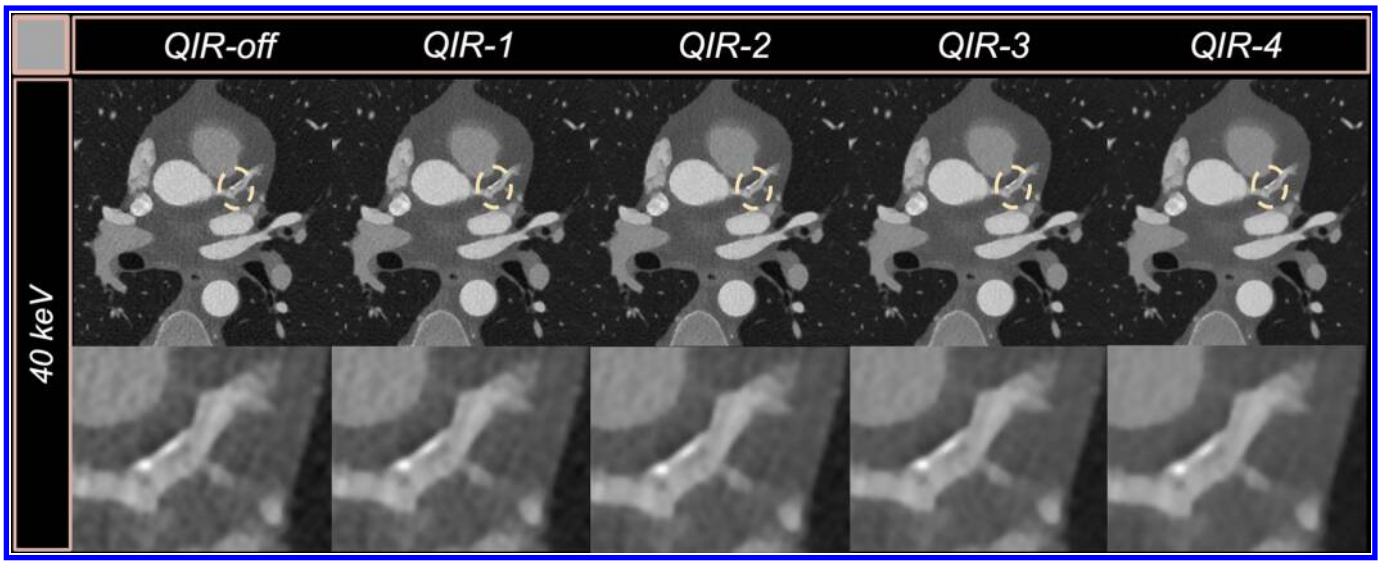

CCTA-specific analyses.[10] Here, we provide evidence that PCD-CT enables high quality CCTA imaging and that image quality can be further optimized by choosing appropriate keV levels and QIR strength levels.

Some previous studies assessed the impact of keV level on objective and subjective image quality of dual-energy EID-CT based CCTA. Arendt et al acquired DE CCTA datasets on a third-generation dual-source EID-CT system at 70/Sn150 kV tube voltage setting and automated tube current modulation in 51 patients.[2] They compared 40 to 100 keV and standard linear-blended CCTA images reconstructed with an IR algorithm at strength level three and found that 40keV images were superior to the other reconstructions in terms of image quality.[2]

Our study also indicated that 40keV images enabled significant improvements in terms of image quality, showing an improved vessel attenuation, a higher CNR, and a higher quantitative vessel sharpness. It is important to note that the improvements in vessel sharpness at low keV levels may be also partially related to improvements in vascular contrast at low energies. The differences in attenuation between the adjacent tissue and the iodinated contrast media in the vessel lumen increases at low keV levels thus leading to a steeper increase in the attenuation curve across the vessel wall.

Interestingly, a previous study assessing the impact of IR on vessel sharpness of CCTA on an EID-CT system found a higher vessel sharpness at higher strength levels of IR.[33] This is in contrast to the results of our study using a different CT scanner system, where the QIR strength level did not significantly impact on vessel sharpness. While it remains to be determined whether our findings can be reproduced across different kernels, it should be noted that one of the main aims of QIR (as intended by the vendor) was to reduce image noise without affecting noise texture and sharpness of structures.

We found no effect of keV and QIR level on stenosis grading of calcified coronary plaques. However, it should be considered that only three stenoses were graded and further studies are needed to validate our initial results. Such studies should include invasive coronary angiography as the reference standard to validate the accuracy of various reconstruction settings for the grading of coronary stenoses. Furthermore, the 90% stenosis was underestimated by both readers. After discussion with the vendor, it is expected that this was caused by breaking away of the innermost points of the calcium carbonate deposition for the 90% occlusion during the vessel filling process, resulting in a true diameter slightly less than the manufacturer's specification.

On the majority of previous EID-CT systems, VMI reconstructions are only available when dual-energy CT protocols are selected prior to the examination. This, however, precludes making use of the highest possible temporal resolution of the scanner.[10,17] With the intrinsic spectral capabilities of the novel PCD-CT, VMI and other dual-/multi-energy-based reconstructions (such as virtual non-contrast images or iodine maps) are available from every scan at full temporal resolution of 66 ms, and VMI were established as the new standard for routine image interpretation.[11,16]

We found that vessel contrast in VMI at 40 keV was very high, with attenuation values exceeding 1'000 HU. Interestingly, a previous study using a dual-energy CCTA protocol with EID-CT showed also attenuation values in coronary arteries > 1'000 HU in 40 keV VMI.[27] It is obvious that such high vessel attenuation is too high, potentially negatively affecting image interpretation, for which attenuation of around 300 HU is considered sufficient.[34,35] Specifically, very high coronary vessel attenuation may obscure the difference between normal arterial wall and calcium depositions in terms of CT values, which may compromise the detection of calcifications and the grading of stenoses. Furthermore, the detection of non-calcified plaques and stenoses may also be negatively impacted due to high-density artifacts.[36] Thus, this very high vascular contrast at low keV images in PCD-CT can be leveraged for reductions in the contrast media dose and/or for lowering of the radiation dose. While this issue was not examined in the current study, it should definitely be addressed in future studies.

Another important aspect of image reconstruction that defines objective and subjective image quality is the reconstruction algorithm. For PCD-CT a novel IR algorithm named QIR has been introduced. In contrast to previous EID-CT systems, the PCD-CT does not offer a standard FBP algorithm because of the complexity of the multi-energy data used for VMI reconstruction. Specifically, the retrieval of monoenergetic information from the threshold data directly without proper noise reduction techniques may result in the amplification of image noise – compromising the diagnosis quality. Our results indicate that QIR, a new iterative reconstruction algorithm specifically designed for PCD-CT, improves quality substantially at all VMI-energies by reducing noise. Therein, important metrics such as vascular enhancement, vessel sharpness or image noise texture remain almost unaffected. The latter may represent an advantage over previous IR for EID-CT, which were shown to alter the noise frequency distribution thus leading to a suboptimal image impression particularly at higher strength levels.[22,24,25,37]

The ultimate question remains, which reconstructions should be used for clinical interpretation of CCTA with PCD-CT. Using the current imaging parameters and reconstruction settings (*i.e.,* 120 kV tube voltage and a medium soft convolution kernel) the 40 keV QIR-4 reconstructions enable significant improvements in image quality without compromising the accuracy of stenosis grading of calcified plaques or image noise texture. Thus, our initial results suggest that these reconstructions can be recommended for clinical image interpretation. Nevertheless, particular attention should be given to high keV reconstructions, since these have shown potential to reduce blooming artifacts.[5]

Our study has the following limitations. First, we only included a limited number of patients who were scanned on one CT scanner type at a single-center with a single imaging protocol. This prohibited us from performing subgroup analyses of patient data. Still, we performed a relatively extensive phantom study to

obtain solid objective and subjective image quality metrics for CCTA with PCD-CT. Importantly, we used the most advanced vascular, anthropomorphic phantom currently available exceeding the capabilities of previous phantoms.[38] Nonetheless we have to acknowledge that the results of our phantom experiments may not be fully transferable to an *in vivo* clinical setting in patients. In this regard it should be noted that our study was further limited by including only calcified plaques into the analyses. Second, we evaluated the performance of CCTA using only one (*i.e.,* the only currently clinically available) PCD-CT system. Finally, we limited our analysis to certain low keV levels, and other settings might have also impacted image quality.

In conclusion, this study provides initial experience of CCTA on a clinical PCD-CT system as performed with a standard imaging and image reconstruction protocol (*i.e.,* 120 kV tube voltage and medium soft convolution kernel), suggesting that 40keV VMI reconstructions at QIR-4 may enable significant improvements in terms of objective and subjective image quality.

AUTHOR CONTRIBUTIONS

TS, MMD, VM, GJ, BS, JEW and HA designed the study and interpreted the results. TS, MMD, VM and GJ performed the experiments. TS, AE and HA analyzed the data. TS, JEW and HA wrote the paper. BS provided technical advice. All coauthors contributed constructively to the manuscript.

FUNDING

No funding was received for this study.

DISCLOSURE

J.W.: Institutional grants via Clinical Trial Center Maastricht: Bard, Bayer, Boston, Brainlab, GE, Philips, Siemens. Speaker's bureau via Maastricht UMC+: Bayer, Siemens. H.A.: Institutional grants: Bayer, Guerbet, Canon, Siemens. Speaker's bureau: Siemens. G.J. is employee of Bayer. B.S. is employee of Siemens.

REFERENCES

1. Knuuti J, Wijns W, Saraste A, Capodanno D, Barbato E, Funck-Brentano C, et al. 2019 ESC guidelines for the diagnosis and management of chronic coronary syndromes. *Eur Heart J* 2020; **41**: 407–77. https://doi.org/10.1093/eurheartj/ehz425
2. Arendt CT, Czwikla R, Lenga L, Wichmann JL, Albrecht MH, Booz C, et al. Improved coronary artery contrast enhancement using noise-optimised virtual monoenergetic imaging from dual-source dual-energy computed tomography. *Eur J Radiol* 2020; **122**: S0720-048X(19)30316-X: 108666: . https://doi.org/10.1016/j.ejrad.2019.108666
3. Huang X, Gao S, Ma Y, Lu X, Jia Z, Hou Y. The optimal monoenergetic spectral image level of coronary computed tomography (CT) angiography on a dual-layer spectral detector CT with half-dose contrast media. *Quant Imaging Med Surg* 2020; **10**: 592–603. https://doi.org/10.21037/qims.2020.02.17
4. Ruzsics B, Lee H, Zwerner PL, Gebregziabher M, Costello P, Schoepf UJ. Dual-Energy CT of the heart for diagnosing coronary artery stenosis and myocardial ischemia-initial experience. *Eur Radiol* 2008; **18**: 2414–24. https://doi.org/10.1007/s00330-008-1022-x
5. Van Hedent S, Große Hokamp N, Kessner R, Gilkeson R, Ros PR, Gupta A. Effect of virtual monoenergetic images from spectral detector computed tomography on coronary calcium blooming. *J Comput Assist Tomogr* 2018; **42**: 912–18. https://doi.org/10.1097/RCT.0000000000000811
6. Kok M, Mihl C, Hendriks BMF, Altintas S, Kietselaer BLJH, Wildberger JE, et al. Optimizing contrast media application in coronary CT angiography at lower tube voltage: evaluation in a circulation phantom and sixty patients. *Eur J Radiol* 2016; **85**: S0720-048X(16)30097-3: 1068–74: . https://doi.org/10.1016/j.ejrad.2016.03.022
7. Noda Y, Nakamura F, Yasuda N, Miyoshi T, Kawai N, Kawada H, et al. Advantages and disadvantages of single-source dual-energy whole-body CT angiography with 50 % reduced iodine dose at 40 keV reconstruction. *Br J Radiol* 2021; **94**: 20201276: 20201276: . https://doi.org/10.1259/bjr.20201276
8. Noda Y, Kawai N, Kawamura T, Kobori A, Miyase R, Iwashima K, et al. Radiation and iodine dose reduced thoraco-abdomino-pelvic dual-energy CT at 40 kev reconstructed with deep learning image reconstruction. [BJR 20211163]. *Br J Radiol* 2022; **95**(1134): 20211163. https://doi.org/10.1259/bjr.20211163
9. Raju R, Thompson AG, Lee K, Precious B, Yang T-H, Berger A, et al. Reduced iodine load with CT coronary angiography using dual-energy imaging: a prospective randomized trial compared with standard coronary CT angiography. *J Cardiovasc Comput Tomogr* 2014; **8**: S1934-5925(14)00153-1: 282–88: . https://doi.org/10.1016/j.jcct.2014.06.003
10. Rajendran K, Petersilka M, Henning A, Shanblatt ER, Schmidt B, Flohr TG, et al. First clinical photon-counting detector CT system: technical evaluation. *Radiology* 2022; **303**: 130–38. https://doi.org/10.1148/radiol.212579
11. Euler A, Higashigaito K, Mergen V, Sartoretti T, Zanini B, Schmidt B, et al. High-pitch photon-counting detector computed tomography angiography of the aorta: intraindividual comparison to energy-integrating detector computed tomography at equal radiation dose. *Invest Radiol* 2022; **57**: 115–21. https://doi.org/10.1097/RLI.0000000000000816
12. Decker JA, Bette S, Lubina N, Rippel K, Braun F, Risch F, et al. Low-Dose CT of the abdomen: initial experience on a novel photon-counting detector CT and comparison with energy-integrating detector CT. *Eur J Radiol* 2022; **148**: S0720-048X(22)00031-6: 110181: . https://doi.org/10.1016/j.ejrad.2022.110181
13. Bette SJ, Braun FM, Haerting M, Decker JA, Luitjens JH, Scheurig-Muenkler C, et al. Visualization of bone details in a novel photon-counting dual-source CT scanner-comparison with energy-integrating CT. *Eur Radiol* 2022; **32**: 2930–36. https://doi.org/10.1007/s00330-021-08441-4
14. Rajendran K, Petersilka M, Henning A, Shanblatt E, Marsh J Jr, Thorne J, et al. Full field-of-view, high-resolution, photon-counting detector CT: technical assessment and initial patient experience. *Phys Med Biol* 2021; **66**: 205019. https://doi.org/10.1088/1361-6560/ac155e
15. Boccalini S, Si-Mohamed SA, Lacombe H, Diaw A, Varasteh M, Rodesch P-A, et al. First in-human results of computed tomography angiography for coronary stent assessment with a spectral photon counting

computed tomography. *Invest Radiol* 2022; **57**: 212–21. https://doi.org/10.1097/RLI.0000000000000835

16. Mergen V, Ried E, Allmendinger T, Sartoretti T, Higashigaito K, Manka R, et al. Epicardial adipose tissue attenuation and fat attenuation index: phantom study and in vivo measurements with photon-counting detector CT. *AJR Am J Roentgenol* 2022; **218**: 822–29. https://doi.org/10.2214/AJR.21.26930
17. Mergen V, Sartoretti T, Klotz E, Schmidt B, Jungblut L, Higashigaito K, et al. Extracellular volume quantification with cardiac late enhancement scanning using dual-source photon-counting detector CT. *Invest Radiol* 2022; **57**: 406–11. https://doi.org/10.1097/RLI.0000000000000851
18. Mergen V, Higashigaito K, Allmendinger T, Manka R, Euler A, Alkadhi H, et al. Tube voltage-independent coronary calcium scoring on a first-generation dual-source photon-counting CT-a proof-of-principle phantom study. *Int J Cardiovasc Imaging* 2021. https://doi.org/10.1007/s10554-021-02466-y
19. Grant KL, Flohr TG, Krauss B, Sedlmair M, Thomas C, Schmidt B. Assessment of an advanced image-based technique to calculate virtual monoenergetic computed tomographic images from a dual-energy examination to improve contrast-to-noise ratio in examinations using iodinated contrast media. *Invest Radiol* 2014; **49**: 586–92. https://doi.org/10.1097/RLI.0000000000000060
20. Albrecht MH, Trommer J, Wichmann JL, Scholtz J-E, Martin SS, Lehnert T, et al. Comprehensive comparison of virtual monoenergetic and linearly blended reconstruction techniques in third-generation dual-source dual-energy computed tomography angiography of the thorax and abdomen. *Invest Radiol* 2016; **51**: 582–90. https://doi.org/10.1097/RLI.0000000000000272
21. Greffier J, Si-Mohamed S, Guiu B, Frandon J, Loisy M, de Oliveira F, et al. Comparison of virtual monoenergetic imaging between a rapid kilovoltage switching dual-energy computed tomography with deep-learning and four dual-energy CTs with iterative reconstruction. *Quant Imaging Med Surg* 2022; **12**: 1149–62. https://doi.org/10.21037/qims-21-708
22. Laurent G, Villani N, Hossu G, Rauch A, Noël A, Blum A, et al. Full model-based iterative reconstruction (MBIR) in abdominal CT increases objective image quality, but decreases subjective acceptance. *Eur Radiol* 2019; **29**: 4016–25. https://doi.org/10.1007/s00330-018-5988-8
23. McCollough CH, Yu L, Kofler JM, Leng S, Zhang Y, Li Z, et al. Degradation of CT low-contrast spatial resolution due to the use of iterative reconstruction and reduced dose levels. *Radiology* 2015; **276**: 499–506. https://doi.org/10.1148/radiol.15142047
24. Racine D, Becce F, Viry A, Monnin P, Thomsen B, Verdun FR, et al. Task-based characterization of a deep learning image reconstruction and comparison with filtered back-projection and a partial model-based iterative reconstruction in abdominal CT: a phantom study. *Phys Med* 2020; **76**: S1120-1797(20)30137-X: 28–37: . https://doi.org/10.1016/j.ejmp.2020.06.004
25. Morsbach F, Desbiolles L, Raupach R, Leschka S, Schmidt B, Alkadhi H. Noise texture deviation: a measure for quantifying artifacts in computed tomography images with iterative reconstructions. *Invest Radiol* 2017; **52**: 87–94. https://doi.org/10.1097/RLI.0000000000000312
26. Mergen V, Sartoretti T, Baer-Beck M, Schmidt B, Petersilka M, Wildberger JE, et al. Ultra-high-resolution coronary CT angiography with photon-counting detector CT: feasibility and image characterization. *Invest Radiol* 2022; **57**: 780–88. https://doi.org/10.1097/RLI.0000000000000897
27. Mergen V, Eberhard M, Manka R, Euler A, Alkadhi H. First in-human quantitative plaque characterization with ultra-high resolution coronary photon-counting CT angiography. *Front Cardiovasc Med* 2022; **9**: 981012: 981012: . https://doi.org/10.3389/fcvm.2022.981012
28. Sartoretti T, Landsmann A, Nakhostin D, Eberhard M, Roeren C, Mergen V, et al. Quantum iterative reconstruction for abdominal photon-counting detector CT improves image quality. *Radiology* 2022; **303**: 339–48. https://doi.org/10.1148/radiol.211931
29. McDermott MC, Sartoretti T, Mihl C, Pietsch H, Alkadhi H, Wildberger JE. Third-Generation cardiovascular phantom: the next generation of preclinical research in diagnostic imaging. *Invest Radiol* 2022; **57**: 834–40. https://doi.org/10.1097/RLI.0000000000000894
30. Sartoretti T, Eberhard M, Nowak T, Gutjahr R, Jost G, Pietsch H, et al. Photon-Counting multienergy computed tomography with spectrally optimized contrast media for plaque removal and stenosis assessment. *Invest Radiol* 2021; **56**: 563–70. https://doi.org/10.1097/RLI.0000000000000773
31. Sartoretti T, van Smoorenburg L, Sartoretti E, Schwenk Á, Binkert CA, Kulcsár Z, et al. Ultrafast intracranial vessel imaging with non-cartesian spiral 3-dimensional time-of-flight magnetic resonance angiography at 1.5 T: an in vitro and clinical study in healthy volunteers. *Invest Radiol* 2020; **55**: 293–303. https://doi.org/10.1097/RLI.0000000000000641
32. Rotzinger DC, Racine D, Becce F, Lahoud E, Erhard K, Si-Mohamed SA, et al. Performance of spectral photon-counting coronary CT angiography and comparison with energy-integrating-detector CT: objective assessment with model observer. *Diagnostics (Basel)* 2021; **11**(12): 2376. https://doi.org/10.3390/diagnostics11122376
33. Gordic S, Desbiolles L, Sedlmair M, Manka R, Plass A, Schmidt B, et al. Optimizing radiation dose by using advanced modelled iterative reconstruction in high-pitch coronary CT angiography. *Eur Radiol* 2016; **26**: 459–68. https://doi.org/10.1007/s00330-015-3862-5
34. De Santis D, Caruso D, Schoepf UJ, Eid M, Albrecht MH, Duguay TM, et al. Contrast media injection protocol optimization for dual-energy coronary CT angiography: results from a circulation phantom. *Eur Radiol* 2018; **28**: 3473–81. https://doi.org/10.1007/s00330-018-5308-3
35. Cademartiri F, Mollet NR, van der Lugt A, McFadden EP, Stijnen T, de Feyter PJ, et al. Intravenous contrast material administration at helical 16-detector row CT coronary angiography: effect of iodine concentration on vascular attenuation. *Radiology* 2005; **236**: 661–65. https://doi.org/10.1148/radiol.2362040468
36. Luan X, Gao Z, Sun J, Chen G, Song H, Yao J, et al. Feasibility of an ultra-low dose contrast media protocol for coronary CT angiography. *Clin Radiol* 2022; **77**: S0009-9260(22)00283-5: e705–10: . https://doi.org/10.1016/j.crad.2022.05.029
37. Steuwe A, Weber M, Bethge OT, Rademacher C, Boschheidgen M, Sawicki LM, et al. Influence of a novel deep-learning based reconstruction software on the objective and subjective image quality in low-dose abdominal computed tomography. *Br J Radiol* 2021; **94**: 20200677: 20200677: . https://doi.org/10.1259/bjr.20200677
38. Mihl C, Wildberger JE, Jurencak T, Yanniello MJ, Nijssen EC, Kalafut JF, et al. Intravascular enhancement with identical iodine delivery rate using different iodine contrast media in a circulation phantom. *Invest Radiol* 2013; **48**: 813–18. https://doi.org/10.1097/RLI.0b013e31829979e8

BJR

https://doi.org/10.1259/bjr.20201456

Received: 18 December 2020 | Revised: 23 November 2021 | Accepted: 12 January 2022 | Published online: 04 February 2022

Cite this article as:
Fischer AM, Decker JA, Schoepf J, Varga-Szemes A, Flohr T, Schmidt B, et al. Optimization of contrast material administration for coronary CT angiography using a software-based test-bolus evaluation algorithm. *Br J Radiol* (2022) 10.1259/bjr.20201456.

FULL PAPER

Optimization of contrast material administration for coronary CT angiography using a software-based test-bolus evaluation algorithm

[1,2]ANDREAS M FISCHER, MD, [1,3]JOSUA A. DECKER, [1]JOSEPH SCHOEPF, MD, [1]AKOS VARGA-SZEMES, MD, PhD, [4]THOMAS FLOHR, PhD, [4]BERNHARD SCHMIDT, PhD, [4]RALF GUTJAHR, PhD, [5]POOYAN SAHBAEE, PhD, [1]DANTE A GIOVAGNOLI, MS, [1,6,7]TILMAN EMRICH, MD, [1]JOHN D MARTINEZ, MS, [8]KIA B LARI, BS, [1,9]ROBERT R BAYER II, MD and [1,10]SIMON S MARTIN, MD

[1]Division of Cardiovascular Imaging, Department of Radiology and Radiological Science, Medical University of South Carolina, Charleston, South Carolina, USA
[2]University Department of Geriatric Medicine FELIX PLATTER and University of Basel, Basel, Switzerland
[3]Department of Diagnostic and Interventional Radiology, University Hospital Augsburg, Augsburg, Germany
[4]Siemens Healthcare, Forchheim, Germany
[5]Siemens Medical Solutions, Ann Arbor, Michigan, USA
[6]Department of Diagnostic and Interventional Radiology, University Medical Center, Mainz, Germany
[7]German Center for Cardiovascular Research (DZHK), Partner Site Rhine Main, Mainz, Germany
[8]University of South Carolina School of Medicine Greenville, Greenville, South Carolina, USA
[9]Division of Cardiology, Department of Medicine, Medical University of South Carolina, Charleston, South Carolina, USA
[10]Department of Diagnostic and Interventional Radiology, University Hospital Frankfurt, Frankfurt, Germany

Address correspondence to: Professor Joseph Schoepf
E-mail: *schoepf@musc.edu;grayhu@musc.edu*

The authors Andreas M Fischer and Josua A. Decker contributed equally to the work.

Objectives: To evaluate the benefit of a prototype circulation time-based test bolus evaluation algorithm for the individualized optimal timing of contrast media (CM) delivery in patients undergoing coronary CT angiography (CCTA).
Methods: Thirty-two patients (62 ± 16 years) underwent CCTA using a prototype bolus evaluation tool to determine the optimal time-delay for CM administration. Contrast attenuation, signal-to-noise ratio (SNR), objective, and subjective image quality were evaluated by two independent radiologists. Results were compared to a control cohort (matched for age, sex, body mass index, and tube voltage) of patients who underwent CCTA using the generic test bolus peak attenuation +4 s protocol as scan delay.
Results: In the study group, the mean time delay to CCTA acquisition was significantly longer (26.0 ± 2.9 s) compared to the control group (23.1 ± 3.5 s; $p < 0.01$). In the study group, SNR improvement was seen in the right coronary artery (17.5 *vs* 13; $p = 0.028$), the left main (15.3 *vs* 12.3; $p = 0.027$), and the left anterior descending artery (18.5 *vs* 14.1; $p = 0.048$). Subjective image quality was rated higher in the study group (4.75 ± 0.7 vs 3.64 ± 0.5; $p < 0.001$).
Conclusions: The prototype test bolus evaluation algorithm provided a reliable patient-specific scan delay for CCTA that ensured homogenous vascular attenuation, improvement in objective and subjective image quality, and avoidance of beam hardening artifacts.
Advances in knowledge: The prototype contrast bolus evaluation and optimization tool estimated circulation time-based time-delay improves the overall quality of CCTA.

INTRODUCTION

Coronary computed tomography angiography (CCTA) has become the examination of choice for non-invasive imaging of the coronary arteries.[1–3] The assessment of the coronary arteries for atherosclerotic disease relies heavily on image quality and contrast conditions. Optimal timing of contrast media (CM) administration is crucial to fully utilize the advantages of CCTA. With increasing scan speed achieved by advanced CT scanners, this task is becoming more complex.[4–6]

In clinical routine, bolus tracking and test bolus are the most frequently used techniques for the determination of the timing of CCTA acquisition post CM administration.

The bolus tracking technique based on a single contrast injection for patient-specific timing adjustment is utilized in the majority of clinical scenarios. Conversely, the test bolus technique allows for prospectively planning the shape of the time-attenuation curve to improve signal homogeneity.[5] Usually, contrast timing is derived based upon a standard 20-ml test bolus injection. However, the time-to-peak enhancement of the test bolus and the diagnostic scan may differ significantly due to the amount of CM administered. In many clinical institutions, the time-to-peak enhancement derived from the test bolus scan leads to the selection of a generic +4 s time delay.[5,7,8] To date, there is however no gold standard for a specific time delay in CCTA and recent SCCT guidelines suggest a range of +2 to+4 s.[9] Previous simulation studies performed on a physiological compartment model were able to simulate the patient- and organ-specific enhancement curves for a given CM injection,[10,11] and predict the required injection protocol to achieve optimized contrast enhancement.[12] However, those studies have not been tested in a clinical setting.

A prototype bolus evaluation tool has been developed to optimize CM delivery using simulated contrast dynamics for given test bolus information. The purpose of this study was to prospectively evaluate the utility of this novel test bolus evaluation tool for the individualized optimal timing of CM delivery in patients undergoing CCTA.

METHODS AND MATERIALS

Study design

This prospective, single-center, HIPAA-compliant study was approved by the local Institutional Review Board and all patients provided written informed consent. Consecutive patients referred for clinically indicated CCTA for evaluation of suspected coronary artery disease were enrolled between February 2019 and August 2019. Exclusion criteria included: glomerular filtration rate below 45 mL/min, respiratory impairment, and unstable clinical status. A matched control cohort was retrospectively assembled to evaluate image quality parameters of CCTA using time to test bolus peak attenuation +4 s as scan delay. Patients were matched based upon patient age, sex, body weight, and tube voltage.

Coronary CT angiography

CCTA examinations were performed on a third-generation dual-source CT system (SOMATOM Force, Siemens Healthineers, Forchheim, Germany). Prospective electrocardiography (ECG)-triggering was used for all CCTA acquisitions. Beta-blockers were typically administered before scanning with a target heart rate as close to 60 beats per minute (bpm) as possible. Sublingual nitroglycerin (0.4 mg) was administered before CCTA to patients with no contraindication.

A topogram of the chest was obtained to determine z-coverage for the CCTA scan. CM volume and injection rate for the test bolus were 20 ml and 4 ml s^{-1}, respectively. A biphasic contrast injection protocol was used for the main CCTA scan to administer 1.0 ml per kg body weight (maximum 120 ml) of CM (iopromide, Ultravist, 370 mg of iodine per mL, Bayer, Indianola, PA) at 4–6 ml s^{-1}, followed by 25 ml of CM diluted with 25 ml of saline chaser at the same rate. All images were acquired during inspiratory breath-hold.

Figure 1. Representative time-attenuation plot showing the calculation of scan delay using the conventional test bolus technique (green dashed curve) and the test bolus evaluation algorithm (yellow dashed curve). In this subject, peak enhancement was measured at 24 s (orange arrow) after contrast bolus administration. Using the generic +4 s time delay (blue arrow), the total time delay before the start the CCTA would be 28 s. On the other hand, the simulated peak enhancement was achieved at 33 s after contrast administration using the test bolus algorithm (purple arrow), with a 5 s time difference (red arrow) between the conventional technique and the test bolus algorithm. CCTA, coronary computed tomography angiography.

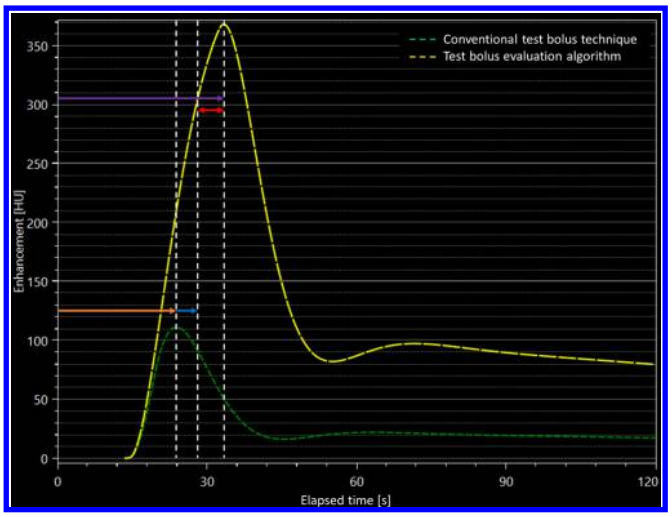

The main scanning parameters were as follows: tube potential automatically selected using an automated tube voltage selection algorithm (CARE kV, Siemens Healthineers), 70–130 kV, tube current–time product, 200–650 mAs; gantry rotation time, 0.25 s; detector collimation, 2 × 192 × 0.6 mm. The CT dose index (CTDI) and dose length product (DLP) were obtained from patients' records.

Test bolus technique

The test bolus technique was based on the i.v. injection of 20-mL CM during the acquisition of a series of dynamic low-dose (120 kV, 20 mAs) monitoring scans at the level of the ascending aorta. Monitoring scans were stared 10 s after the beginning of the injection of i.v. CM with a 1 s delay between each monitoring scan acquisition. In the control group, the time to peak enhancement was calculated and a + 4 s delay was applied prior to the start of the CCTA scan. In the study group, a dedicated prototype software (Bolus Evaluation, Siemens) was used to analyze the test bolus enhancement curve and calculate the time to peak enhancement for the CCTA acquisition depending on individual circulation time. Figure 1 shows a representative example for the difference between the standard and the prototype-based CCTA timing.

In order to optimize the scan delay for each patient, the software first predicts the expected contrast enhancement in the ascending aorta before the CCTA scan. In general, the algorithm considers a patient as a linear time-invariant (LTI) system so that the contrast enhancement over time, $CE(t)$, can be described as a convolution of the injection protocol, IP(t), with the arterial impulse response (AIR) of the patient $AIR_{patient}(t)$:

$$CE(t) = IP(t) \otimes AIR_{patient}(t)$$

with $CE(t)$ in Hounsfield Units (HU), $IP(t)$ in mL/s, and $AIR_{patient}(t)$ in HU/mL. For a given $AIR_{patient}(t)$, a patient-specific contrast enhancement $CE(t)$ can be predicted for any desirable injection protocol $IP(t)$. First, the algorithm extracts the right $AIR_{patient}(t)$ function from the test bolus injection protocol and the test bolus signal ($CE(t)$) in the descending aorta. Then, the algorithm predicts the contrast enhancement of the CCTA scan in the descending aorta on the basis of the previously derived $AIR_{patient}(t)$ and the injection protocol used for the CCTA scan. Finally, the software simply estimates the scan delay as the time to peak of the $CE(t)$ curve. In both the control and the study cohort, the protocol ensured that there was enough time for table adjustments and breath-hold instructions prior to image acquisition to ensure scanning at the optimal enhancement.

Objective image quality analysis

The CCTA data were analyzed on a dedicated workstation (syngo.via MM Reading, v. VB20A, Siemens) by a radiologist with 4 years of CCTA experience. Measurements included mean attenuation (HU) of the major coronary arteries (right, left main, left anterior descending, and left circumflex), the left and right ventricles, the ascending aorta, and the superior vena cava. Additional measurements were performed in the interventricular septum and mediastinal fat to assess image contrast and noise. Measurements were performed twice and averaged to ensure data consistency and high measurement accuracy. The following formulas were used for calculating signal-to-noise (SNR) and contrast-to-noise ratios (CNR):

$$SNR = HU_{artery}/SD_{fat}$$

$$CNR = (HU_{artery} - HU_{septum}) / SD_{fat}$$

Subjective image quality analysis

All CCTA scans were interpreted by two board certified cardiovascular radiologists. All images were independently reviewed, and the reviewers were blinded to the test bolus technique. To reduce recall bias, all image series were evaluated in random order. Subjective image quality of the coronary arteries was evaluated using a 5-point Likert scale ranging from 1 = poor image quality to 5 = excellent image quality.

Statistical analysis

Statistical analyses were performed using MedCalc v. 19.2 (MedCalc Software bvba, Ostend, Belgium) and R v. 4.1.0 (https://www.r-project.org/). Categorical variables were reported as frequency with percentage. Normal distribution was assessed using the Shapiro-Wilk test. Data are presented as mean ± standard deviation (SD) or as median with interquartile range (IQR). Group comparison was performed using the Mann-Whitney U-test and Fisher's exact test/chi-square tests for continuous and categorical variables, respectively. To assess interobserver agreement, intraclass correlation coefficients (ICC) were calculated and interpreted as:<0.50, poor agreement; 0.50–0.75, moderate agreement; 0.75–0.90, good agreement; and >0.90, excellent agreement. Statistical significance was assumed at a p-value of <0.05.

RESULTS

Study population

From a total of 36 patients, two were excluded due to renal dysfunction, one due to respiratory impairment and one due to unstable clinical status. Thus, the final study population comprised a total of 32 patients. The study population included 16 men (50%) and 16 women (50%) with a mean age of 59.4 ± 17.4 years. Patients in the control group were matched based on age, sex, body mass index (BMI) and tube voltage with a mean age of 59.4 ± 14 years. The two study cohorts did not significantly differ regarding age ($p = 0.56$), sex ($p = 1$)and BMI ($p = 0.66$). In addition, cardiac risk factors did not significantly differ between the cohorts. The mean $CTDI_{vol}$ and DLP in the study and control groups were 40.9 ± 30.7 mGy *vs* 42.9 ± 31.9 mGy, and 660.8 ± 575.6 mGy*cm *vs* 705.2 ± 373.2 mGy*cm, respectively. Patient characteristics are summarized in Table 1.

Time delay for CCTA

The time to peak measured during test bolus administration was not different between the study group (19.2 ± 2.9 s) and the control group (19.1 ± 3.5 s; $p = 0.95$). In the study group, the mean time delay for CCTA determined by the prototype algorithm was significantly longer (26.0 ± 2.9 s; range 18.9–31.2 s) than that of the control group using the standard +4 s delay adjustment (23.1 ± 3.5 s; range 16.0–28.1 s; $p < 0.01$).

Objective image quality analysis

Mean attenuation, SNR and CNR values are reported in Table 2 and Figure 2. Attenuation values in the superior vena cava (128.7 HU *vs* 657.7 HU, $p < 0.001$), the right ventricle (142.8 HU *vs* 360 HU, $p < 0.001$), and the pulmonary artery (200.9 HU *vs* 334.8 HU, $p < 0.001$) and were significantly lower in the study group. The study cohort showed higher SNR in the RCA (17.5 *vs* 13.0; $p = 0.028$), the LM (15.3 *vs* 12.3; $p = 0.027$), and the LAD (18.5 *vs* 14.1; $p = 0.048$). The LCX showed no significant difference regarding SNR (19.6 *vs* 17.8; $p = 0.525$). In the study group, CNR was lower in the superior vena cava, the right ventricle and the pulmonary artery but not significantly different in the coronary arteries.

Subjective image quality analysis

Subjective image quality ratings were significantly higher in the study group compared to the control group (4.75 ± 0.7 vs 3.64 ± 0.5; $p < 0.001$). In Figure 3, corresponding images of both the study group and the control group are represented. Interobserver

Table 1. Patient characteristics

Variables	Study group	Control group	*p*-value
N	32	32	
Age (years)	59.4 ± 17.4	59.4 ± 14	0.563
Gender (male)	16 (50.0%)	16 (50.0%)	1
BMI (kg/m^2)	29.2 ± 5.9	29.8 ± 5.6	0.656
BMI ≥ 30 kg/m^2	12 (37.5%)	14 (43.8%)	0.248
Heart rate (bpm)	68.5 ± 12.2	66.1 ± 10.7	0.318
CTDI (mGy)	40.9 ± 30.7	42.9 ± 31.9	0.783
DLP (mGy*cm)	660.8 ± 575.6	705.2 ± 373.2	0.763
Tube voltage (kV)	105.3 ± 21.9	106.9 ± 18.4	0.995
Contrast media (ml)	55.6 ± 13.3	55.8 ± 11.5	0.952

BMI, body mass index; CAD, coronary artery disease; CTDI, computed tomography dose index; DLP, dose length product.

agreement was good for both the study group (ICC 0.86) and the control group (ICC 0.79).

DISCUSSION

In this study, we prospectively investigated a test bolus evaluation prototype algorithm in patients undergoing CCTA with the aim of optimizing individual acquisition timing after CM administration to ensure homogeneous contrast attenuation in the coronary arteries. Our data suggest that circulation time-based patient-specific timing adjustment provides additional value by optimizing CM administration and scan delay for CCTA examinations, thus improving image quality. None of the patients who underwent CCTA with an individualized trigger delay showed non-diagnostic image quality.

An optimal contrast protocol should guarantee uniform, prolonged contrast attenuation during the CCTA scan. Using these techniques, we were able to show stable contrast enhancement between 300 and 400 HU in the coronary arteries. This is of particular importance for CCTA because optimal contrast attenuation in the coronary arteries has a considerable influence on image quality and the ability to evaluate images for stenosis and arteriosclerotic changes.[5,13] In addition to sufficient contrast attenuation above 200 HU, which allows adequate evaluation of smaller vessels, it should also be noted that attenuation beyond 400 HU may limit the evaluation of coronary calcifications.[5,14] In contrast to the control group, the individually timed and uniform CM application avoids the presence of beam hardening artifacts caused by iodinated CM *e.g.* in the superior vena cava, which otherwise would have negative impact on image interpretation.[15–17]

The mean and peak level of arterial contrast enhancement show substantial interindividual differences, even when CM is administered at the same volume and flow rate. These differences are confirmed by the wide range of time delay to peak attenuation observed in our study cohort. Several physiologic parameters including body weight, body surface area, central blood volume and circulation time all influence arterial peak enhancement. In fact, circulation time proves to be the physiologic factor with the greatest impact on the magnitude and timing of contrast enhancement.[14,18–21] Therefore, patients with pre-existing cardiac conditions or impaired cardiac function stand to benefit the most from individualized contrast media delay timing which factors in the individuals' circulation time.

One of the most important methods currently used is test bolus injection.[22] Sandfort et al examined a total of 151 patients using three different test bolus protocols.[23] The authors investigated the enhancement of the ascending aorta and showed that a protocol, which included a lower flow rate but a higher concentration of contrast agent, demonstrated a lower and more stable range of attenuation values compared to the other two protocols. The remaining protocols tested were a standard test bolus protocol and a body weight adapted protocol which showed the highest standard deviation of aortic enhancement.[23,24] However, all protocols tested considered the maximum arterial enhancement as the delay, which factors in each individual's CO. Seifarth et al also investigated three different test bolus protocols in 120 patients using different amounts of contrast agent and flow rates. In addition to the previous study these three protocols were based on the peak enhancement curve of the ascending aorta +4 s. However, this calculation is only an approximation to the individual circulation time. Exact measurement methods of cardiac output and circulation time include echocardiography, angiocardiography, thermo-dilution by Swan-Ganz catheter and advanced imaging methods of cardiac magnetic resonance imaging and CCTA.[25,26] These cardiac output measurements are rarely used in everyday clinical practice to determine the time delay to maximum enhancement in the ascending aorta before CCTA. Whereas CCTA-based estimation of circulation time would only be available after the completion of the imaging study.

In order to take into account, the myriad of influences on circulation time and the associated variability of individual flow velocity, we tested a test-bolus algorithm, which calculated the interindividual delay based on the patient-specific flow curve of the test-bolus injection protocol by taking into account a substantial, extensive database of archived improvement curves for its precise calculations. Embedding this approach into a routine workflow

Table 2. Objective image quality including attenuation (HU), SNR and CNR values

Location	Attenuation (HU)			SNR			CNR		
	Study group	Control group	*p*-value	Study group	Control group	*p*-value	Study group	Control group	*p*-value
Superior vena cava	128.7 ± 38.1	657.7 ± 290	<0.001	4.4 ± 1.5	6.6 ± 5.6	0.036	1 ± 1.4	18.3 ± 9.4	<0.001
Right ventricle	142.8 ± 128.7	360 ± 162.4	<0.001	4.7 ± 1.8	11.4 ± 5.2	<0.001	1.8 ± 3.0	8.8 ± 6.5	<0.001
Pulmonary artery	200.9 ± 72.4	334.8 ± 102.7	<0.001	7.8 ± 3	12.3 ± 5	<0.001	3.7 ± 2.6	7.7 ± 3.9	<0.001
Left ventricle	345.4 ± 89.9	362.2 ± 116.6	0.707	10.7 ± 3.2	10.9 ± 4.9	0.758	9.8 ± 4.8	9.4 ± 5.3	0.728
Ascending aorta	397.8 ± 67.2	410.3 ± 108.3	0.799	15.0 ± 5.3	15.0 ± 5.2	0.931	12.1 ± 5.1	10.8 ± 4.9	0.289
Right coronary artery	348.4 ± 67.9	348.9 ± 87.1	0.804	17.5 ± 10.3	13 ± 5.3	0.028	10.1 ± 4.7	8.4 ± 3.7	0.119
Left main	382.2 ± 76.1	361.6 ± 77.6	0.280	15.3 ± 5.3	12.3 ± 5.1	0.027	11.4 ± 4.9	9.3 ± 5.5	0.127
Left anterior descending	350.7 ± 49.8	356.7 ± 93.1	0.867	18.5 ± 9.9	14.1 ± 7	0.048	10.1 ± 4.2	8.6 ± 3.6	0.137
Left circumflex	365 ± 79.3	319 ± 81.1	0.036	19.6 ± 12.3	17.8 ± 10	0.525	10.5 ± 4.4	7.7 ± 4.2	0.011

CNR, contrast to noise ratio; HU, Hounsfield unit; SNR, signal to noise ratio.

Figure 2. Box plot diagram shows opacification (HU) values at the different anatomic structures in the study group (blue) and the control group (orange). Significant differences can be observed in the SVC (superior vena cava), RV (right ventricle) and PA (pulmonary artery). LV, left ventricle; AA, ascending aorta; RCA, right coronary artery; LM, left main; LAD, left anterior descending; LCX, left circumflex artery.

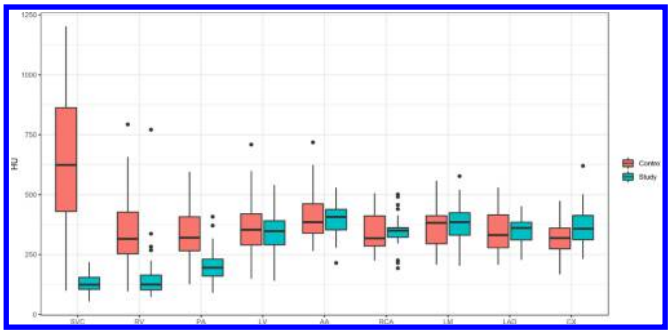

for a CT scan, we ensured that by determining the individual delay time, a sufficient and homogeneous contrast within the desired scan area could be provided in order to obtain noticeably better objective and subjective image quality compared to that of the control group.

To our knowledge, there are no comparable studies that have used a similar test-bolus algorithm for CCTA. In a prospective study, Hinzpeter et al examined 108 participants with CTA of the aorta by comparing a cohort with fixed trigger delay and a cohort with patient-specific, individualized trigger delay for contrast

Figure 3. 66 year-old female with chest pain underwent standard CCTA (Case 1, (A-C) and 65-year-old male with known coronary artery disease and recurrence of angina underwent CCTA using the test bolus evaluation algorithm (Case 2, (D-F). Axial CCTA sections are shown. Beam hardening artifact is shown in the superior vena cava in case one with standard CCTA (A, B; yellow arrows), while artifact is not present in Case two with test bolus algorithm based CCTA (D, E; blue arrows). Furthermore, panel (C) shows a contrast filled right ventricle with a density of 412 HU. In contrast, panel (F) demonstrates low attenuation in the right ventricle (81 HU). CCTA, coronary computed tomography angiography; HU = Hounsfield Units.

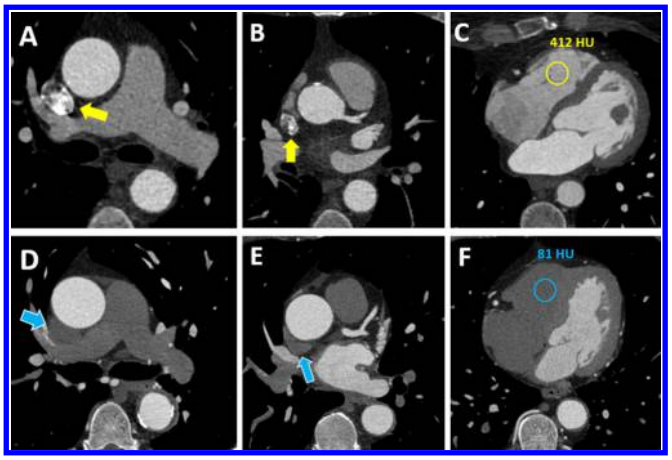

medium timing.[27] It was shown that patients with individualized trigger delay were accompanied by more uniform contrast attenuation and improved image quality. Instead of a test bolus algorithm, they used the bolus tracking method for patient-specific trigger delays.

There are several study limitations that need to be considered. First, this is a single-center study with a relatively small cohort size. Second, cohort assignment was not randomized. Our study focused solely on CCTA and its objective and subjective image quality. The extent to which other arterial or pulmonary arterial, patient-specific time delays would be proven by the test bolus evaluation was outside the scope of this study. Moreover, the variations of the patients' specific circulation time may have influenced our study results. The test-bolus evaluation was associated with a slightly longer time required to transfer data to an external computer for calculation, which should improve with evolving clinical integration. Additionally, in this study we only adjusted the time delay and did not alter other variables such as test bolus volume and flow. Further analyses on this patient specific approach are needed to provide an individually tailored CCTA protocol.

CONCLUSION

In conclusion, the patient-specific test bolus evaluation algorithm for CCTA reliably provided a patient specific scan delay to ensure constant vascular attenuation, which led to an improvement in objective and subjective image quality in addition to the avoidance of beam hardening artifacts. This technique has the potential to benefit patients with decreased circulation time who present for CCTA exams by individualizing scan parameters to the benefit of each patient.

FUNDING

This study was supported by Siemens Healthcare.

DISCLOSURE

Akos Varga-Szemes receives institutional research and travel support from Siemens Healthcare and is a consultant for Bayer and Elucid Bioimaging. U. Joseph Schoepf is a consultant for and / or receives research support from Bayer, Bracco, Elucid Bioimaging, Guerbet, HeartFlow, and Siemens Healthcare. Thomas Flohr, Bernhard Schmidt, Ralf Gutjahr, and Pooyan Sahbaee are employees of Siemens Healthcare. Tilman Emrich receives travel support and speaker fee from Siemens Healthcare.

REFERENCES

1. Schoepf UJ, Zwerner PL, Savino G, Herzog C, Kerl JM, et al. Coronary ct angiography. *Radiology* 2007; **244**: 48–63. https://doi.org/10.1148/radiol.2441052145
2. Budoff MJ, Dowe D, Jollis JG, Gitter M, Sutherland J, et al. Diagnostic performance of 64-multidetector row coronary computed tomographic angiography for evaluation of coronary artery stenosis in individuals without known coronary artery disease: results from the prospective multicenter accuracy (assessment by coronary computed tomographic angiography of individuals undergoing invasive coronary angiography) trial. *J Am Coll Cardiol* 2008; **52**: 1724–32. https://doi.org/10.1016/j.jacc.2008.07.031
3. Maroules CD, Rajiah P, Bhasin M, Abbara S. Current evidence in cardiothoracic imaging: growing evidence for coronary computed tomography angiography as a first-line test in stable chest pain. *J Thorac Imaging* 2019; **34**: 4–11. https://doi.org/10.1097/RTI.0000000000000357
4. Johnson TRC, Nikolaou K, Wintersperger BJ, Leber AW, von Ziegler F, et al. Dual-source ct cardiac imaging: initial experience. *Eur Radiol* 2006; **16**: 1409–15. https://doi.org/10.1007/s00330-006-0298-y
5. Mahnken AH, Rauscher A, Klotz E, Mühlenbruch G, Das M, et al. Quantitative prediction of contrast enhancement from test bolus data in cardiac msct. *Eur Radiol* 2007; **17**: 1310–19. https://doi.org/10.1007/s00330-006-0486-9
6. Eberhard M, Alkadhi H. Machine learning and deep neural networks: applications in patient and scan preparation, contrast medium, and radiation dose optimization. *J Thorac Imaging* 2020; **35 Suppl 1**: S17–20. https://doi.org/10.1097/RTI.0000000000000482
7. Konno M, Hosokai Y, Usui A, Abe M, Tateishi T, et al. Cardiac output obtained from test bolus injections as a factor in contrast injection rate revision of following coronary ct angiography. *Acta Radiol* 2012; **53**: 1107–11. https://doi.org/10.1258/ar.2012.120276
8. Ichikawa S, Yamamoto H, Ito O, Fukunaga M. Pulmonary artery/vein separation using single-phase computed tomography: feasibility and the influence of patient characteristics on vessel enhancement. *J Thorac Imaging* 2020; **35**: 173–78. https://doi.org/10.1097/RTI.0000000000000455
9. Abbara S, Blanke P, Maroules CD, Cheezum M, Choi AD, et al. SCCT guidelines for the performance and acquisition of coronary computed tomographic angiography: a report of the society of cardiovascular computed tomography guidelines committee: endorsed by the north american society for cardiovascular imaging (nasci). *J Cardiovasc Comput Tomogr* 2016; **10**: 435–49. https://doi.org/10.1016/j.jcct.2016.10.002
10. Sahbaee P, Segars WP, Marin D, Nelson RC, Samei E. The effect of contrast material on radiation dose at ct: part i. *Incorporation of Contrast Material Dynamics in Anthropomorphic Phantoms Radiology* 2017; **283**: 739–48.
11. Sahbaee P, Abadi E, Segars WP, Marin D, Nelson RC, et al. The effect of contrast material on radiation dose at ct: part ii. a systematic evaluation across 58 patient models. *Radiology* 2017; **283**: 749–57. https://doi.org/10.1148/radiol.2017152852
12. Sahbaee P, Segars PP, Marin D, Nelson R, Samei E. Determination of contrast media administration to achieve a targeted contrast enhancement in computed tomography. *J Med Imaging (Bellingham)* 2016; **3**: 013501. https://doi.org/10.1117/1.JMI.3.1.013501
13. Becker CR, Hong C, Knez A, Leber A, Bruening R, et al. Optimal contrast application for cardiac 4-detector-row computed tomography. *Invest Radiol* 2003; **38**: 690–94. https://doi.org/10.1097/01.rli.0000084886.44676.e4
14. Husmann L, Alkadhi H, Boehm T, Leschka S, Schepis T, et al. Influence of cardiac hemodynamic parameters on coronary artery opacification with 64-slice computed tomography. *Eur Radiol* 2006; **16**: 1111–16. https://doi.org/10.1007/s00330-005-0110-4
15. Bucher AM, Wichmann JL, Schoepf UJ, Wolla CD, Canstein C, et al. Quantitative evaluation

of beam-hardening artefact correction in dual-energy ct myocardial perfusion imaging. *Eur Radiol* 2016; **26**: 3215–22. https://doi.org/10.1007/s00330-015-4137-x

16. So A, Hsieh J, Li JY, Lee TY. Beam hardening correction in ct myocardial perfusion measurement. *Phys Med Biol* 2009; **54**: 3031–50. https://doi.org/10.1088/0031-9155/54/10/005
17. Henry TS, Hammer MM, Little BP, Jensen LE, Kligerman SJ, et al. Smoke: how to differentiate flow-related artifacts from pathology on thoracic computed tomographic angiography. *J Thorac Imaging* 2019; **34**: W109–20. https://doi.org/10.1097/RTI.0000000000000429
18. Yamaguchi T. Scanning techniques of ccta that uses 64-rows mdct. *Nihon Hoshasen Gijutsu Gakkai Zasshi* 2009; **65**: 104–11. https://doi.org/10.6009/jjrt.65.104
19. Sakai S, Yabuuchi H, Chishaki A, Okafuji T, Matsuo Y, et al. Effect of cardiac function on aortic peak time and peak enhancement during coronary ct angiography. *Eur J Radiol* 2010; **75**: 173–77. https://doi.org/10.1016/j.ejrad.2009.04.022
20. Bae KT. Intravenous contrast medium administration and scan timing at ct: considerations and approaches. *Radiology* 2010; **256**: 32–61. https://doi.org/10.1148/radiol.10090908
21. Mahnken AH, Klotz E, Hennemuth A, Jung B, Koos R, et al. Measurement of cardiac output from a test-bolus injection in multislice computed tomography. *Eur Radiol* 2003; **13**: 2498–2504. https://doi.org/10.1007/s00330-003-2054-x
22. Sun K, Liu G-R, Li Y-C, Han R-J, Cui L-F, et al. Intravenous contrast material administration at high-pitch dual-source ct coronary angiography: bolus-tracking technique with shortened time of respiratory instruction versus test bolus technique. *Chin Med Sci J* 2013; **27**: 225–31. https://doi.org/10.1016/s1001-9294(13)60006-1
23. Sandfort V, Choi Y, Symons R, Chen MY, Bluemke DA. An optimized test bolus contrast injection protocol for consistent coronary artery luminal enhancement for coronary ct angiography. *Acad Radiol* 2020; **27**: 371–80. https://doi.org/10.1016/j.acra.2019.05.003
24. Wang Y, Yu M, Wang M, Wang Y, Kong L, et al. Application of artificial intelligence-based image optimization for computed tomography angiography of the aorta with low tube voltage and reduced contrast medium volume. *J Thorac Imaging* 2019; **34**: 393–99. https://doi.org/10.1097/RTI.0000000000000438
25. Sangkum L, Liu GL, Yu L, Yan H, Kaye AD, et al. Minimally invasive or noninvasive cardiac output measurement: an update. *J Anesth* 2016; **30**: 461–80. https://doi.org/10.1007/s00540-016-2154-9
26. Hofer CK, Ganter MT, Zollinger A. What technique should i use to measure cardiac output? *Curr Opin Crit Care* 2007; **13**: 308–17. https://doi.org/10.1097/MCC.0b013e3280c56afb
27. Hinzpeter R, Eberhard M, Gutjahr R, Reeve K, Pfammatter T, et al. CT angiography of the aorta: contrast timing by using a fixed versus a patient-specific trigger delay. *Radiology* 2019; **291**: 531–38. https://doi.org/10.1148/radiol.2019182223

BJR https://doi.org/10.1259/bjr.20190868

Received: 10 October 2019 | Revised: 28 January 2020 | Accepted: 29 January 2020

Cite this article as:
McDermott M, Kemper C, Barone W, Jost G, Endrikat J. Impact of CT Injector Technology and Contrast Media Viscosity on Vascular Enhancement: Evaluation in a Circulation Phantom. *Br J Radiol* 2020; **93**: 20190868.

FULL PAPER

Impact of CT Injector Technology and Contrast Media Viscosity on Vascular Enhancement: Evaluation in a Circulation Phantom

[1]MICHAEL MCDERMOTT, [1]COREY KEMPER, PhD, [1]WILLIAM BARONE, PhD, [2]GREGOR JOST, PhD and [3,4]JAN ENDRIKAT, MD, PhD

[1]Bayer U.S. LLC, Bayer Pharmaceuticals, Radiology R&D, Indianola, PA 15051, USA
[2]Bayer AG, MR & CT Contrast Media Research, Berlin, Germany
[3]Bayer AG, Radiology R&D, 13353 Berlin, Germany
[4]Department of Gynecology, Obstetrics and Reproductive Medicine, University Medical School of Saarland, 66421 Homburg/Saar, Germany

Address correspondence to: Prof Dr Jan Endrikat
E-mail: *jan.endrikat@bayer.com*

Objective: To assess the impact of piston-based *vs* peristaltic injection system technology and contrast media viscosity on achievable iodine delivery rates (IDRs) and vascular enhancement in a pre-clinical study.
Methods: Four injectors were tested: MEDRAD® Centargo, MEDRAD® Stellant, CT Exprès®, and CT motion™ using five contrast media [iopromide (300 and 370 mgI ml^{-1}), iodixanol 320 mgI ml^{-1}, iohexol 350 mgI ml^{-1}, iomeprol 400 mgI ml^{-1}]. Three experiments were performed evaluating achievable IDR and corresponding enhancement in a circulation phantom.
Results: Experiment I: Centargo provided the highest achievable IDRs with all tested contrast media ($p < 0.05$). Iopromide 370 yielded the highest IDR with an 18G catheter (3.15 gI/s); iopromide 300 yielded the highest IDR with 20G (2.70 gI/s) and 22G (1.65 gI/s) catheters ($p < 0.05$).
Experiment II: with higher achievable IDRs, piston-based injectors provided significantly higher peak vascular enhancement (up to 48% increase) than the peristaltic injectors with programmed IDRs from 1.8 to 2.4 gI/s ($p < 0.05$).
Experiment III: with programmed IDRs (*e.g.* 1.5 gI/s) achievable by all injection systems, Centargo, with sharper measured bolus shape, provided significant increases in enhancement of 34–73 HU in the pulmonary artery with iopromide 370 ($p < 0.05$).
Conclusion: The tested piston-based injection systems combined with low viscosity contrast media provide higher achievable IDRs and higher peak vascular enhancement than the tested peristaltic-based injectors. With equivalent IDRs, Centargo provides higher peak vascular enhancement due to improved bolus shape.
Advances in knowledge: This paper introduces a new parameter to compare expected performance among contrast media: the concentration/viscosity ratio. Additionally, it demonstrates previously unexplored impacts of bolus shape on vascular enhancement.

INTRODUCTION

The practice of CT intravenous contrast media (CM) administration has been continuously debated and updated[1]; however, performance of power injection systems has largely gone unstudied. Previous publications have focused on workflow efficiency as the main differentiator between systems.[2,3] Further, patient-to-patient variability, as well as inconsistencies in scanner protocols and technology can mask differences in the technical capabilities of the injection systems.

When looking at differences between injection systems, there are two main fluid delivery technologies to analyze: piston-based systems and peristaltic-pump-based systems. Both are positive displacement pumps, which translate kinetic energy from the pump into displacement of a given quantity of fluid. However, piston-based systems act by using a piston/ram to displace a plunger down the barrel of a reservoir, operating in two directions to first fill the reservoir and then to displace the fluid from the reservoir to the patient, similar to a hand syringe. Peristaltic pumps act as rotary pumps, using rollers to pinch sections of flexible tubing which draws fluid directly from the supply source and displaces it out to the patient. These differences in fluid delivery technology can cause differences in performance.

In early 2019, Chaya et al[4] published results of a pre-clinical study in which a piston-based injection system demonstrated higher maximum achievable flow rates and more consistent steady-state flow when compared to the two tested peristaltic pump-based injection systems.[4] The authors, however, acknowledged several limitations of their study. Primarily, the study included only two CM types spanning a small range of viscosities, a critical element when determining the iodine delivery rates (IDRs) achievable for a given injection system. This is because increased contrast viscosity results in increasing injection pressures.[5] An additional limitation of Chaya et al was that no link was provided between measured performance and potential clinical outcomes.

Building upon the work of Chaya et al, this study aimed to evaluate the technical performance of contemporary power injection systems by applying a broader range of CM concentrations and viscosities, as well as more sophisticated measurement techniques to determine flow rates and injected concentrations. In addition, a circulation phantom was used to quantify vascular enhancement in CT while minimizing experimental variables. Similar phantoms have been used in previous experiments to study the impact on CT imaging of variables such as different catheter types,[6] CM viscosity/temperature,[5] saline use,[7] contrast injection protocols for low kVp imaging,[8] and iodine delivery rate.[9]

In the present study, four injection systems and five CM were compared across a range of catheter gauges. Three experiments were performed to determine: (I) contribution of injection system technology and CM viscosity to maximum achievable IDR; (II) impact of differences in achievable IDR on vascular enhancement in a circulation phantom; and (III) impact of injection system technology and bolus shape on peak enhancement with the same achievable IDRs.

METHODS

Injection Systems and Contrast Media

Four CT injection systems were used from three manufacturers: MEDRAD® Centargo CT Injection System and MEDRAD® Stellant CT Injection System with the Multi Patient Kit ('Centargo' and 'Stellant MP', Bayer AG, Berlin, Germany), Bracco CT Exprès® Contrast Injection System with Multi Patient Set ('CT Exprès', Bracco Injeneering, Lausanne, Switzerland) and ulrich CT motion™ Contrast Media Injector ('CT motion', ulrich Medical, Ulm, Germany). All injection systems were operated according to the manufacturers' instructions with disposable components designed for multiple injections/patients, with an exception for CT Exprès, which requires selection of the catheter gauge to restrict the programmable flow rate of the injection system. As the flow rate restrictions prevent programming of equivalent IDRs to the other tested injection systems, the catheter gauge was intentionally selected as a lower gauge than that which was used. The systems were connected to 18G, 20G, and 22G intravenous catheters (Becton Dickinson, Franklin Lakes, NJ) to generate a range of expected clinical injection pressures.[10] Details on the tested CM are shown in Table 1. All CM tested were at room temperature, which was monitored during the study to be at 21.5°C.

Real-time Density and Volumetric Flow Rate Measurement

Real-time density and volumetric flow rate were measured using a MicroMotion 5700 Coriolis Transmitter (Emerson Electric Co., St. Louis, MO). The transmitter was positioned at the outlet of the catheter to record the bolus shape as measured by the concentration and flow rate of the fluid exiting the catheter over time. The signal from the transmitter was recorded using a LabVIEW virtual instrument (2012 SPI, National Instruments). This measurement method allows for actual IDRs to be calculated, irrespective of the programmed IDR for that injection.

Table 1. Contrast media used for this study, with properties reported by the manufacturer, measured viscosity, and the derived concentration/viscosity ratio

Generic (Brand Name)	Concentration (mgI/mL)	Published Viscosity (cP)([a])	Measured Viscosity (cP)([b])	Concentration / Viscosity Ratio (mgI/mL/cP)([c])	Concentration / Viscosity Ratio (mgI/mL/cP) at 37 °C([d])	Manufacturer
Iopromide (Ultravist)[11]	300	9.2	7.64	39.3	61.2	Bayer AG Berlin, Germany
Iodixanol (Visipaque)[12]	320	26.6	21.1	15.2	27.1	GE Healthcare New Jersey, USA
Iohexol (Omnipaque)[13]	350	20.4	18.7	18.7	33.7	GE Healthcare New Jersey, USA
Iopromide (Ultravist)[14]	370	22	17.1	21.6	37	Bayer AG Berlin, Germany
Iomeprol (Iomeron)[15]	400	27.5	23	17.4	31.7	Bracco Imaging Milan, Italy

[a]Official data from manufacturers at 20°C.
[b]Measured data using Brookfield DV-II+ Pro Viscometer at tested temperature of 21.5°C.
[c]Determined using measured contrast media viscosity.
[d]Calculated from manufacturer reported viscosities at 37°C.

Figure 1. Circulation phantom A: Circulation phantom; B: Aortic arch + pulmonary artery with dyed fluid to enhance visibility of vasculature. Dye was not used for experimental trials; C: Cross-section through B (dotted line) showing regions of interest: 1 = ascending aorta, 2 = pulmonary artery, 3 = descending aorta, D: Graphical monitor of blood pressure and heart rate of the phantom.

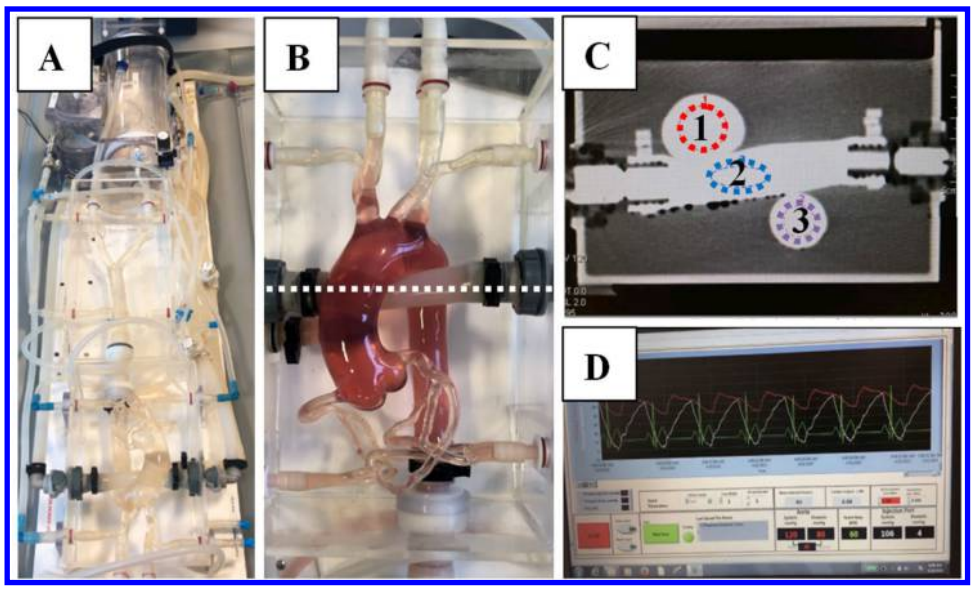

Circulation Phantom

A circulation phantom was used to assess the effects of maximum achievable IDR and bolus shape on vascular enhancement in CT. The phantom mimics the transport and distribution dynamics of iodinated contrast material in a mammalian circulatory system. The design of the phantom is equivalent to those used in previously published experiments.[6–8] For all acquisitions, the phantom was configured to have a heart rate of 60 beats per minute and a blood pressure of 120/80 mmHg (Figure 1). The phantom was drained and re-filled with laboratory water between each injection to prevent the effects of residual contrast material contamination across injections.

CT Scanner Settings & Image Evaluation

All CT acquisitions were performed on a dual-source CT scanner (SOMATOM Force; Siemens Healthineers, Erlangen, Germany) with a tube voltage of 120 kV and tube current of 100 mAs. A dynamic CT of the aortic arch was acquired without table feed utilizing the following parameters: 200 mm field of view, 2.0 mm slice thickness, 40 s scan duration, and 0.5 s rotation time. Image reconstruction was performed with a temporal resolution of 0.3 s enabling the monitoring of the bolus curve. Regions of interest (ROIs) were drawn at the level of the ascending aorta (AA), descending aorta (DA), as well as within the pulmonary artery (PA), as shown in Figure 1c. Equivalent enhancement trends and magnitudes were observed in the AA and DA; therefore, only the results for the AA are included for simplicity. The peak signal enhancement was derived from the resulting time-enhancement curve. All CT scans were repeated three times and measurements taken within the same slice plane to ensure accuracy, determine repeatability, and allow for statistical analysis across groups. Methods to obtain enhancement values are consistent with previously published results.[8]

Statistical Analysis

Independent non-parametric Kruskal–Wallis tests using $\alpha = 5\%$ as a significance level were conducted for comparison of peak enhancement, IDR, contrast media, and injection system. Each analysis was conducted independently across each ROI and catheter gauge. As an exploratory analysis, p-values ≤ 0.05 were interpreted to be statistically significant. Minitab statistical software (v. 17, Minitab, LLC, State College, PA) was used for all analyses.

Experiment I—Maximum Achievable IDR

Maximum achievable IDRs were determined for all four injection systems delivering five CM through 18G, 20G, and 22G catheters. Each of these three variables was varied to generate a testing matrix of 60 combinations. Injections were programmed at 1 $ml\,s^{-1}$ and increased in 0.5 $ml\,s^{-1}$ increments until the injection systems were unable to deliver the flow rate without exceeding the maximum programmable pressure limit as selected on or defined by the system. Injection volumes of 100 ml were chosen to ensure steady state flow was achieved.

Experiment II—Relationship Between IDR and Peak Enhancement

In order to relate the differences in achievable IDR to potential clinical results, dynamic CT acquisitions were obtained using the phantom. The impact of achievable IDR on peak vascular enhancement was assessed with specific focus on the contribution of the injection systems. This was achieved by varying the programmed IDR from 1.8 to 2.4 gI/s in 0.2 gI/s increments. Iopromide 300 and 370 were used in this experiment, as they achieved the highest IDRs in Experiment I for all injection systems. This allowed for comparison of all injection systems at the higher end of clinically relevant IDRs. Volumes were varied to maintain constant duration across the programmed injections.

Experiment III—Impact of Bolus Geometry on CT Peak Vascular Enhancement

Experiment III was designed to compare differences in peak vascular enhancement with common injection protocols. Specifically, IDRs of 1.5 and 2.0 gI/s were utilized in this study, consistent with literature for adequate vascular enhancement in CT angiography procedures.[16–18] By comparing vascular enhancement at IDRs that are achievable by all systems, differences can be attributed to injection system performance characteristics such as bolus shape.

To maintain consistency with Experiment II, iopromide 300 and 370 were used. In order to achieve an IDR of 1.5 gI/s, all injectors were programmed to deliver at 5 and 4.1 $ml\,s^{-1}$ for iopromide 300 and iopromide 370, respectively. Similarly, to achieve an IDR of 2.0 gI/s, all injectors were programmed to deliver at 6.7 and 5.4 $ml\,s^{-1}$ for iopromide 300 and iopromide 370, respectively. The volumes (40 and 54 ml) were appropriate relative to the central blood volume of the phantom and ensured the injection reached steady state, while avoiding recirculation effects.

RESULTS

Experiment I—Maximum Achievable IDR (Figure 2, Table 2)

Centargo provided the highest achievable IDRs among the tested injection systems with all five CM and all catheter gauges ($p < 0.05$) (Table 2). Iopromide 370 yielded the highest IDR among the tested CM with an 18G catheter (3.15 gI/s) ($p < 0.05$), while iopromide 300 yielded the highest IDR with both a 20G (2.70 gI/s) and 22G (1.65 gI/s) catheter ($p < 0.05$). Following iopromide across all catheter gauges were iohexol 350, iomeprol 400, and then iodixanol 320. With a 20G catheter, Centargo with

Figure 2. Maximum achievable IDR vs injection system with different contrast media through a 20G catheter: This figure represents the maximum achievable IDR for each combination of injection system and contrast media through a 20G catheter. The measured concentration/viscosity ratio is shown below each contrast media in mgI/mL/cP. Error bars represent standard deviation across the three trials performed for each programmed injection. Graph A represents the data ordered from left to right by concentration, while graph B represents the data ordered from left to right by measured concentration/viscosity ratio. IDR,iodine delivery rate.

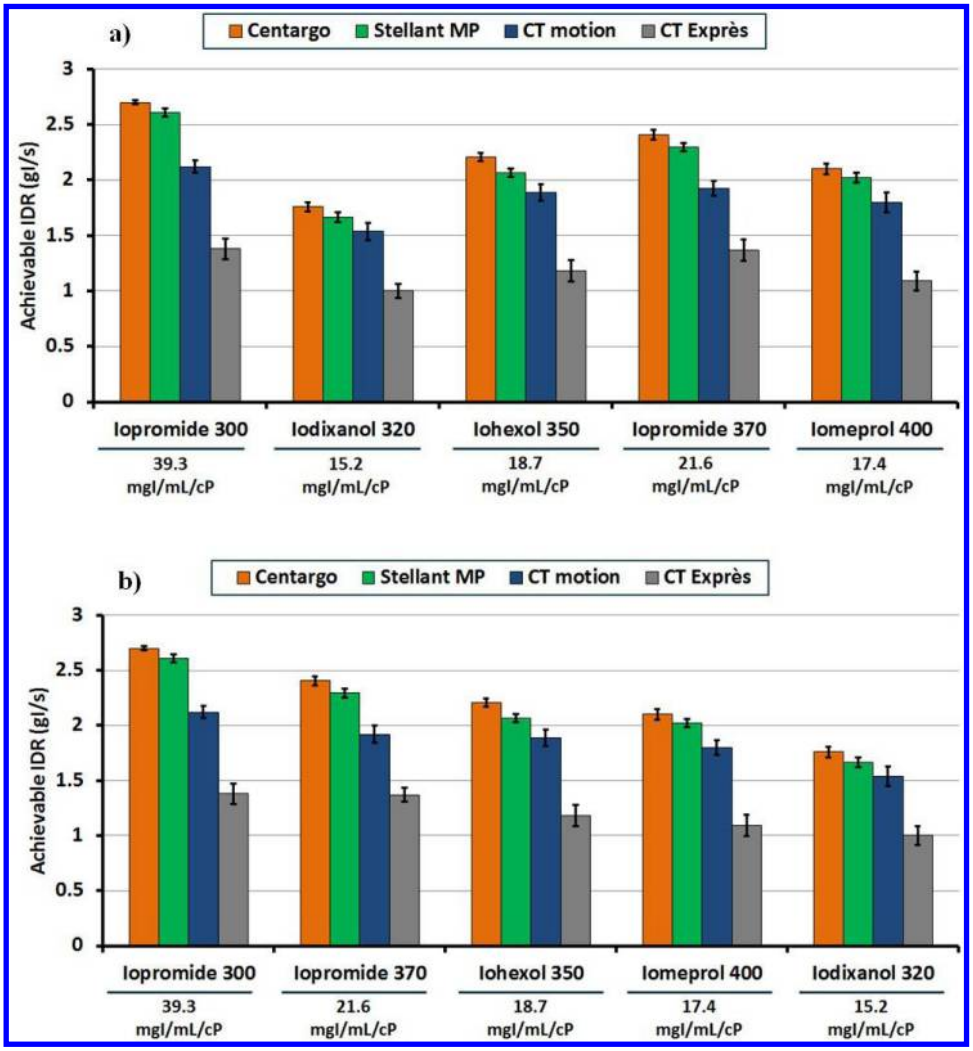

Table 2. Complete results for maximum achievable IDR vs injection system vs contrast media vs catheter gauge: values represent the average of three trials for each combination of contrast media, injection system, and catheter gauge

Catheter gauge	Contrast media	Concentration (mgI/mL)	Maximum iodine delivery rate (gI/s)			
			Centargo	Stellant MP	CT motion	CT Exprès
18G	Iopromide	300	3.00	3.00	2.70	1.59
	Iodixanol	320	2.27	2.18	2.02	1.18
	Iohexol	350	2.91	2.77	2.49	1.40
	Iopromide	370	3.15	3.07	2.70	1.63
	Iomeprol	400	2.48	2.40	2.14	1.32
20G	Iopromide	300	2.70	2.61	2.12	1.38
	Iodixanol	320	1.76	1.66	1.54	1.00
	Iohexol	350	2.21	2.07	1.89	1.18
	Iopromide	370	2.41	2.29	1.92	1.37
	Iomeprol	400	2.10	2.02	1.80	1.09
22G	Iopromide	300	1.65	1.56	1.26	0.99
	Iodixanol	320	1.12	1.02	0.78	0.66
	Iohexol	350	1.37	1.16	0.98	0.81
	Iopromide	370	1.48	1.41	1.13	0.83
	Iomeprol	400	1.28	1.16	0.88	0.74

IDR, iodine delivery rate.

iopromide 300 achieved the highest IDR (2.7 gI/s), while CT Exprès with iodixanol 320 achieved the lowest IDR (1.0 gI/s) (Figure 2).

Experiment II—Relationship Between IDR and Peak Vascular Enhancement (Figure 3)

In all measured ROIs, Centargo provided the highest peak vascular enhancement of the tested injection systems across all programmed IDRs ranging from 1.8 to 2.4gI/s. Statistically significant results ($p < 0.05$) were recorded for all tested IDRs, except for the pulmonary artery at 1.8 gI/s (Figure 3). With a programmed IDR of 2.0 gI/s, Centargo achieved an average peak enhancement increase of 104–195 Hounsfield units (HUs) in the pulmonary artery, and 50–116 HU in the ascending aorta compared to both peristaltic injection systems. Enhancement results across all programmed IDRs are shown in Table 3.

Figure 3. Achievable vascular enhancement *vs* injection system with varied IDRs through a 22G catheter: The left graph (a) provides peak enhancement results from all injection systems in the pulmonary artery, while the right graph (b) was acquired from the ascending aorta. Error bars represent standard deviation across the three trials performed for each programmed injection. * denotes statistical difference between injection systems ($p < 0.05$).

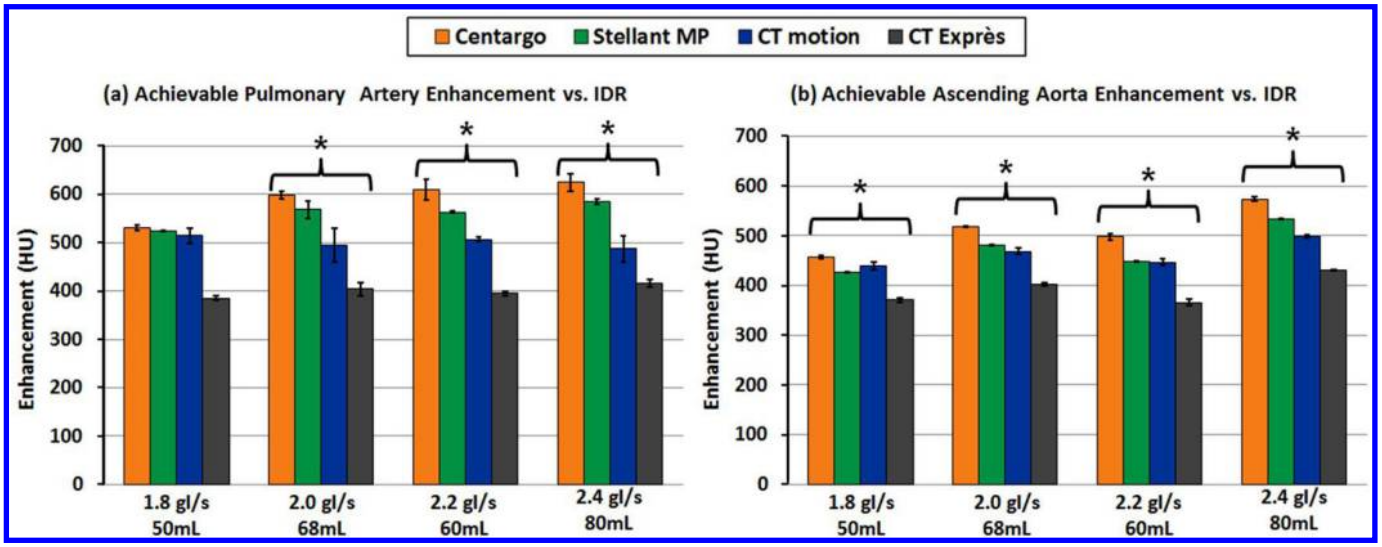

Table 3. Mean increase in vascular enhancement across all tests of Figure 3 of Centargo vs other injectors: the table represents the mean increase in vascular enhancement across all injections with programmed IDRs from 1.8 to 2.4 gI/s

		Enhancement in pulmonary artery			Enhancement in ascending aorta		
Programmed IDR (gI/s)	Injection system	Mean (HU)	Variation (HU)	% Difference of means (relative to Centargo)	Mean (HU)	Range (HU)	% Difference of means (relative to Centargo)
1.8–2.4 gI/s	Centargo	591	531–624	-	512	457–574	-
	Stellant MP	560	524–584	−6%	473	427–534	−8%
	CT motion	500	494–514	−18%	463	440–499	−11%
	CT Exprès	400	385–416	−48%	392	366–430	−31%

HU, Hounsfield unit; IDR, iodine delivery rate.
Iopromide 300 and iopromide 370 were used with a 22G catheter. Differences in HU are represented as a percentage relative to Centargo as the top performing injection system.

Figure 4. Achievable vascular enhancement vs injection system with varied IDRs through a 20G catheter: the top two graphs (a, b) provide results using iopromide 300, while the bottom graphs (c, d) utilized iopromide 370. In addition, (a, c) are measurements from the pulmonary artery while (b, d) are measurements from the ascending aorta. Error bars represent standard deviation across the three trials performed for each programmed injection. ♦ denotes data obtained using the CT Exprès injection system where iodine was over delivered. Due to the additional contrast media, comparisons with CT Exprès were not considered, though the data are provided for completeness. * denotes statistical difference between injection systems ($p < 0.05$).

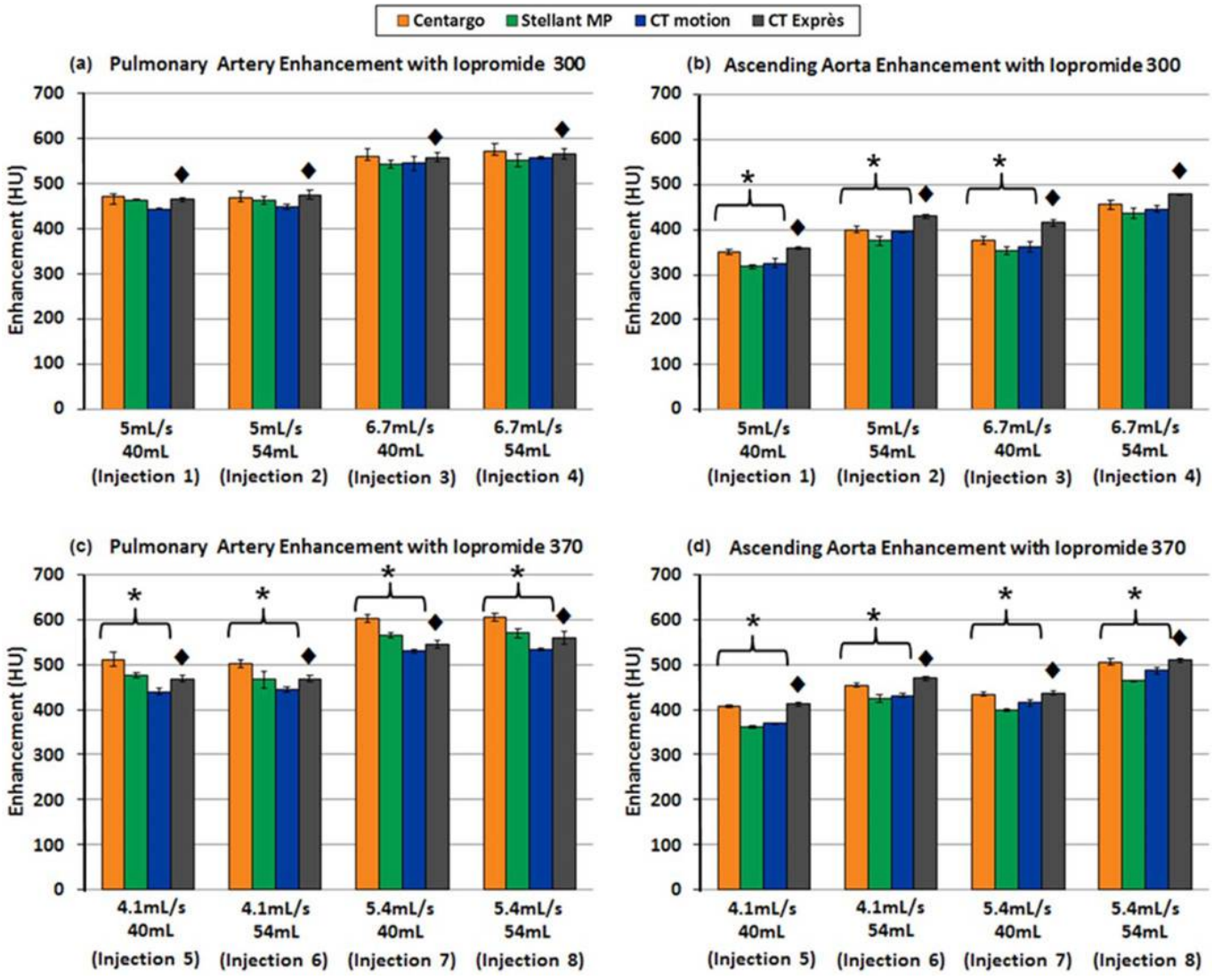

Experiment III—Bolus Geometry Impacts Peak Vascular Enhancement (Figure 4)

In general, Centargo and CT Exprès provided greater enhancement, however CT Exprès was excluded from statistical analysis due to observed over delivery of contrast (see "Discussion"). With iopromide 300, Centargo provided an average increase of ~14–26 HU and ~5–32 HU in the PA and AA respectively. Centargo demonstrated significantly increased enhancement in the PA with iopromide 370, with a 34–73 HU increase relative to the other tested injection systems (Figure 4c). Similar differences in peak enhancement were observed in the AA with iopromide 370 ($p < 0.05$).

DISCUSSION

This study assessed the impact of injection system technologies and CM viscosity on achievable iodine delivery rates and vascular enhancement. In order to translate IDR to vascular enhancement, a circulation phantom was used in combination with dynamic CT. This provided a stable model that, unlike patients in a clinical setting, could be injected into and scanned many times under standardized conditions.

Experiment I—Maximum Achievable IDR

Consistent with Chaya et al,[4] piston-based systems, Centargo and Stellant MP, had higher achievable flow rates than peristaltic-based systems, CT motion and CT Exprès across all CM tested. The combination of the fluid delivery technology and differences in maximum programmable pressure limits were the key contributors to observed differences in achievable flow rates and corresponding IDRs.

Across CM types, the higher viscosity agents (iodixanol 320 and iomeprol 400) had the lowest achievable IDRs for all injection systems. This is not necessarily an intuitive result, as theoretical maximum IDR increases with increasing concentration.[18,19] This study has found the impact of increasing viscosity is greater than the effect of increasing concentration. Still, a balance of both properties is important for determining achievable IDR and achievable vascular enhancement. We propose a new parameter for CM performance by calculating the ratio of concentration to viscosity (Table 1). Figure 2b demonstrates a strong correlation of decreased achievable IDR with decreasing concentration/viscosity ratio (R^2 >0.92 for all combinations of catheter gauge and injection system). While not tested in this study, Table 1 includes the calculated concentration/viscosity ratios for all tested CM if warmed to 37°C. It is expected that achievable IDRs increase for all contrast media at higher temperatures, however, differences in viscosity with heated CM are still expected to lead to differences in performance.

Yet, based on manufacturer reported viscosity, the concentration/viscosity ratio was not able to explain the improved maximum achievable IDR of iopromide 370 relative to iohexol 350. Upon review of the manufacturer's data, published CM viscosities were obtained at a temperature of 20°C. However, using a calibrated viscometer (Brookfield DV-II +Pro, AMETEK Inc.) the viscosity of iohexol 350 at the ambient testing laboratory temperature of 21.5°C was measured to be higher than that of iopromide 370 (18.70 and 17.10 cP respectively). Correcting the concentration/viscosity ratio for the temperature of the testing environment explains the improved performance for iopromide 370 (Table 1). This result aligns with previous observations relating achievable IDR and concentration/viscosity ratio while highlighting the dependence of CM viscosity on temperature.

Figure 5. Sample aortic enhancement comparison of injection systems with 2.0 gI/s programmed injection (time shifted based on contrast media arrival time): This figure represents the enhancement profile in the ascending aorta of the phantom when the same 2.0 gI/s injection is executed on each of the four injection systems. The impact of reduced achievable IDRs as the systems reduce flow to limit pressure is seen in the enhancement profiles and resulting peak enhancement values.

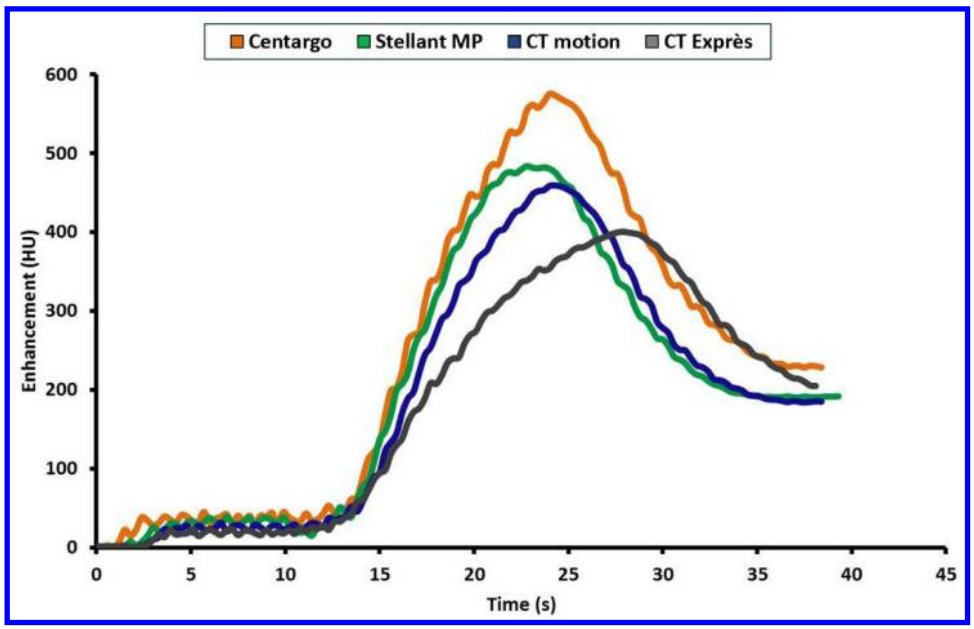

Iopromide 300, with the highest measured concentration/viscosity ratio of 39.3 mgI ml^{-1}/cP, produced the highest achievable IDRs using a 20G and 22G catheter by a significant margin ($p < 0.05$). With an 18G catheter, iopromide 370 produced the highest achievable IDR (3.15 gI/s), representing the only result where the highest measured concentration/viscosity ratio CM did not achieve the highest IDR. This is explained as iopromide 300 was restricted to 3.0 gI/s due to a maximum programmable flow rate of 10 ml s^{-1} on the tested injection systems, a limitation of the systems and not the CM. Conversely, iodixanol 320 has the lowest measured concentration/viscosity ratio of 15.2 mgI ml^{-1}/cP. As expected, this resulted in the lowest achievable IDRs among the tested CM for all catheter gauges.

Experiment II—Relationship Between IDR and Peak Enhancement

While the data from Experiment I established differences between injection systems and CM for achievable IDR, Experiment II provided potential clinical relevance for these results.

Before analyzing the results, it is important to note the difference between programmed IDRs and achievable IDRs. While programmed IDR is theoretical, based on the programmed rate and concentration used, achievable IDR is the measured flow rate and concentration exiting the catheter. Differences between programmed and achieved IDR arise from injection system performance. For example, when the pressure limit of the injection system is reached, the systems reduce the flow rate to prevent the pressure from exceeding the maximum limit. This reduction in flow rate decreases the achieved IDR, which is shown to decrease peak vascular enhancement (Figure 5).

In the PA and AA of the phantom, Centargo provided the highest peak vascular enhancement of all four injection systems across the programmed IDRs (Table 3). These results can be explained by the inability of the peristaltic injection systems to reach the programmed IDR, as the achieved IDR for CT motion and CT Exprès were markedly lower. This is attributed to a reduction in flow rate by both systems to prevent pressure from exceeding the maximum limit, as previously discussed. Review of the data from Experiment II (Figure 5) shows the clinical impact of this flow reduction, which is seen as broadening of the CM bolus and subsequent enhancement profile. The resulting enhancement is reduced and the peak is shifted later in time. This analysis further illustrates the relationship between achievable IDR and peak vascular enhancement.

Experiment III—Bolus Shape Impacts Peak Vascular enhancement

While the previous experiment established the performance differences between the injection systems with IDRs at the higher end of the clinically relevant range, Experiment III compared the injection systems using nominal protocols for CT angiography with the most common catheter gauge. As the experiment was designed to ensure all injection systems were able to achieve the programmed IDRs without reaching their maximum pressure limit, the resulting vascular enhancement should be dependent only on bolus shape. Concentration curves generated using the Coriolis Transmitter allow for comparison of bolus shapes across injection systems (Figure 6).

Theoretically, optimal bolus shape (not enhancement profile) is recognized as a square wave, with concentration of the fluid entering the patient rising instantaneously to the desired level at the start of the injection and falling instantaneously with the onset of the saline flush. As seen in Figure 6, Centargo was found to provide sharper leading and trailing edges of the bolus. This improved bolus shape provides more efficient use of CM, with more iodine entering the patient at the desired IDR for a longer duration. These differences in bolus shape largely explain the general increase in enhancement provided by Centargo in Experiment III.

Figure 6. Sample of contrast bolus shape comparison between injection systems: this figure represents the concentration plots as measured at the 20G catheter for Injection 8 of Experiment III. Differences in leading and trailing edge of the bolus can be seen between injection systems.

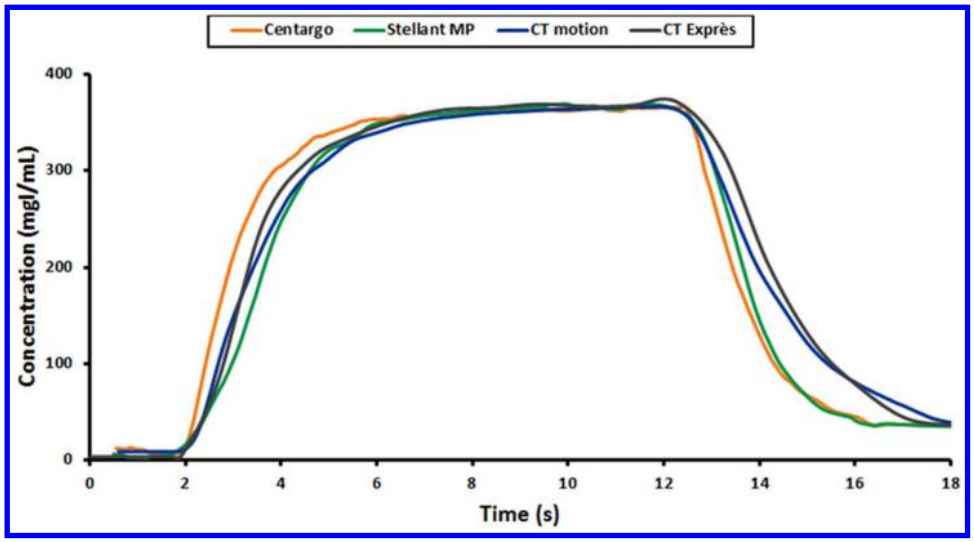

Figure 7. Contrast dose volume error with Ultravist 370 vs injection system: this graph represents the results of the volume accuracy assessment for all injection systems considered. Results were obtained using a 20G catheter, and demonstrate a substantial over delivery of contrast media by CT Exprès compared to the other injection systems.

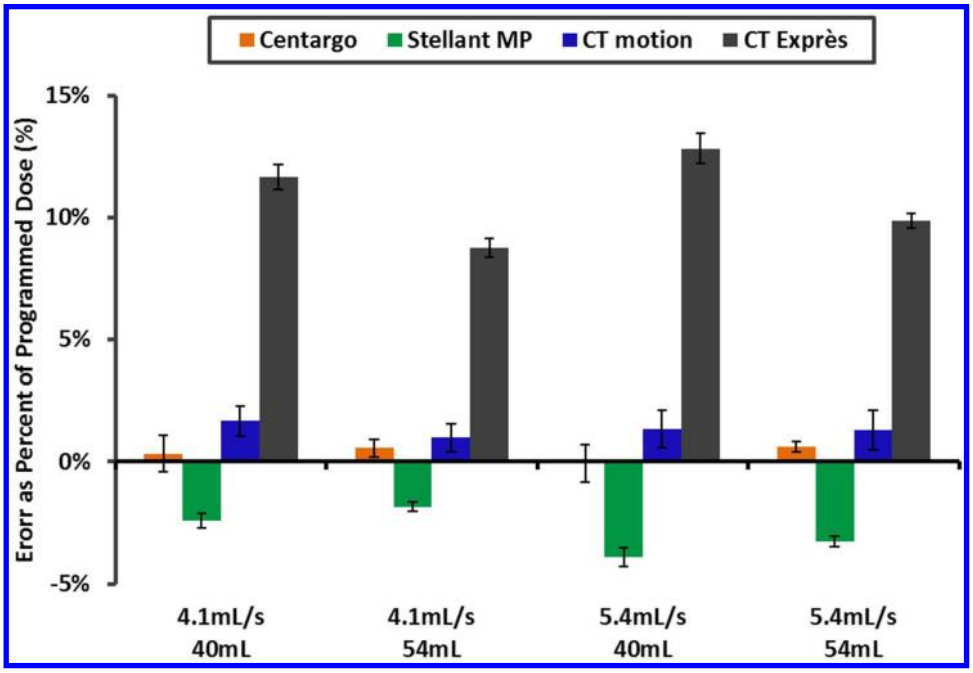

When reviewing the enhancement data, it was noted that trends in injection system performance were consistent from the PA to the AA. The exception was CT Exprès, which exhibited improved performance in the AA. To investigate this observation, volume accuracy performance was conducted on all systems. As shown in Figure 7, CT Exprès delivered 8–14% more contrast than the programmed volume. The operations manual for CT Exprès acknowledges the risk for inaccurate dosing when the catheter gauge as selected on the system is incorrect, which was required in this study to program equivalent IDRs on all systems. Conversely, all other injection systems did not exceed the programmed volume by more than 2.5%. The unintended increase in delivered iodine load explains improved performance of CT Exprès in the AA (Figure 4b and d) relative to the trends observed in the PA (Figure 4a and c).

LIMITATIONS

With the use of the phantom instead of animal or human studies, only first-pass imaging can be performed. Therefore, these results cannot be directly translated to steady-state or parenchymal imaging. An additional limitation of the phantom is the relative size and internal blood volume, which roughly correspond to a 40 kg human. As such, the enhancement levels are artificially higher than one would expect for an average-sized patient. Finally, all CM were tested at room temperature, though warming may be performed clinically. This effect of temperature on CM viscosity is well established.[5] Although testing was not completed at 37°C, the range of official viscosities in this study (9.2–27.5 cP) includes that of higher concentration CM heated to body temperature (*e.g.* iomeprol 400 at 37°C is 12.6 cP).[15]

CONCLUSION

Piston-based injection systems, Centargo and Stellant MP, in combination with low viscosity CM provide higher achievable IDRs. This translates to higher peak vascular enhancement than the tested peristaltic injection systems, CT motion and CT Exprès. With IDRs achievable on all tested injection systems, Centargo provides higher peak vascular enhancement due to improved bolus shape.

ACKNOWLEDGEMENTS

Timothy Syciarz (Bayer U.S. LLC, Bayer Pharmaceuticals, Radiology R&D, USA) and Lisa Bengs (Bayer AG, MR & CT CM Research, Berlin) for testing support.

CONFLICT OF INTEREST AND FINANCIAL DISCLOSURE

All authors are employees of Bayer

REFERENCES

1. Bae KT. Intravenous contrast medium administration and scan timing at CT: considerations and approaches. *Radiology* 2010; **256**: 32–61. doi: https://doi.org/10.1148/radiol.10090908
2. Colombo GL, Bergamo Andreis IA, Di Matteo S, Bruno G, Mondellini C. Syringeless power injector versus dual-

syringe power injector: economic evaluation of user performance, the impact on contrast enhanced computed tomography (CECT) workflow exams, and hospital costs. *MDER* 2013; **6**: 169–74. doi: https://doi.org/10.2147/MDER.S51757

3. Ma X, Singh A, Fay J, Boland G, Sahani DV. Comparison of dual-syringe and syringeless power injectors in outpatient MDCT practice: impact on the operator's performance, CT workflow, and operation cost. *J Am Coll Radiol* 2012; **9**: 578–82. doi: https://doi.org/10.1016/j.jacr.2012.04.007
4. Chaya A, Jost G, Endrikat J. Piston-Based vs peristaltic Pump-Based CT injector systems. *Radiol Technol* 2019; **90**: 344–52.
5. Kok M, Mihl C, Mingels AA, Kietselaer BL, Mühlenbruch G, Seehofnerova A, et al. Influence of contrast media viscosity and temperature on injection pressure in computed tomographic angiography: a phantom study. *Invest Radiol* 2014; **49**: 217–23. doi: https://doi.org/10.1097/RLI.0000000000000019
6. Behrendt FF, Bruners P, Keil S, Plumhans C, Mahnken AH, Stanzel S, et al. Impact of different vein catheter sizes for mechanical power injection in CT: in vitro evaluation with use of a circulation phantom. *Cardiovasc Intervent Radiol* 2009; **32**: 25–31. doi: https://doi.org/10.1007/s00270-008-9359-8
7. Behrendt FF, Bruners P, Keil S, Plumhans C, Mahnken AH, Das M, et al. Effect of different saline chaser volumes and flow rates on intravascular contrast enhancement in CT using a circulation phantom. *Eur J Radiol* 2010; **73**: 688–93. doi: https://doi.org/10.1016/j.ejrad.2009.01.008
8. Caruso D, Eid M, Schoepf UJ, De Santis D, Varga-Szemes A, Mangold S, et al. Optimizing contrast media injection protocols in computed tomography angiography at different tube voltages: evaluation in a circulation phantom. *J Comput Assist Tomogr* 2017; **41**: 804–10. doi: https://doi.org/10.1097/RCT.0000000000000613
9. Mihl C, Wildberger JE, Jurencak T, Yanniello MJ, Nijssen EC, Kalafut JF, et al. Intravascular enhancement with identical iodine delivery rate using different iodine contrast media in a circulation phantom. *Invest Radiol* 2013; **48**: 813–8. doi: https://doi.org/10.1097/RLI.0b013e31829979e8
10. Murphy DJ, Aghayev A, Steigner ML, Vascular CT. Vascular CT and MRI: a practical guide to imaging protocols. *Insights Imaging* 2018; **9**: 215–36. doi: https://doi.org/10.1007/s13244-018-0597-2
11. Iopromide 300. Available from: https://dailymednlmnihgov/dailymed/drugInfocfm?setid=65647318-27e4-4f37-bd68-50eea52d6c5b.
12. Iodixanol 320. Available from: https://dailymednlmnihgov/dailymed/drugInfocfm?setid=952d0aa5-6dfd-49cc-8476-b781e5c7b86c.
13. Iohexol 350. Available from: https://dailymednlmnihgov/dailymed/fda/fdaDrugXslcfm?setid=442aed6e-6242-4a96-90aa-d988b62d55e8&type=display.
14. Iopromide 370. Available from: https://dailymednlmnihgov/dailymed/drugInfocfm?setid=65647318-27e4-4f37-bd68-50eea52d6c5b.
15. Iomeprol 400. Available from: https://wwwoldhealthgovil/units/pharmacy/trufot/alonim/Iomeron_300_350_400_solution_for_injection_7-2015_1437900644612pdf.
16. Mihl C, Kok M, Wildberger JE, Turek J, Muehlenbruch G, Das M. Computed tomography angiography with high flow rates: an in vitro and in vivo feasibility study. *Invest Radiol* 2015; **50**: 464–9. doi: https://doi.org/10.1097/RLI.0000000000000153
17. Lell MM, Fleischmann U, Pietsch H, Korporaal JG, Haberland U, Mahnken AH, et al. Relationship between low tube voltage (70 kV) and the iodine delivery rate (IDR) in CT angiography: an experimental in-vivo study. *PLoS One* 2017; **12**: e0173592. doi: https://doi.org/10.1371/journal.pone.0173592
18. Guerrisi A, Marin D, Nelson RC, De Filippis G, Di Martino M, Barnhart H, et al. Effect of varying contrast material iodine concentration and injection technique on the conspicuity of hepatocellular carcinoma during 64-section MDCT of patients with cirrhosis. *Br J Radiol* 2011; **84**: 698–708. doi: https://doi.org/10.1259/bjr/21539234
19. Aschoff AJ, Catalano C, Kirchin MA, Krix M, Albrecht T. Low radiation dose in computed tomography: the role of iodine. *Br J Radiol* 2017; **90**: 20170079.. doi: https://doi.org/10.1259/bjr.20170079

BJR https://doi.org/10.1259/bjr.20211172

Received: 19 October 2021 | Accepted: 05 January 2023 | Published online: 03 March 2023

Cite this article as:
Taylor DB, Burrows S, Dessauvagie BF, Saunders CM, Ives A. Accuracy and precision of contrast enhanced mammography versus MRI for predicting breast cancer size: how "good" are they really?. *Br J Radiol* (2023) 10.1259/bjr.20211172.

FULL PAPER

Accuracy and precision of contrast enhanced mammography versus MRI for predicting breast cancer size: how "good" are they really?

[1,2]DONNA BLANCHE TAYLOR, MBBS, FRANZCR, FRCP(C), [3,4]SALLY BURROWS, BMath, Grad Dip Med Stat, [5,6]BENJAMIN FREDERIK DESSAUVAGIE, BMedSci (Hons) MBBS (Hons) FRCPA, [7]CHRISTOBEL MARY SAUNDERS, FRCS, FRACS and [8]ANGELA IVES, Dip App Sc (Diag Rad), MSc (Public Health), PhD

[1]Division of Surgery, Medical School, University of Western Australia, Crawley, Perth, Western Australia, Australia
[2]Department of Diagnostic and Interventional Radiology, Royal Perth Hospital, Wellington Street, Perth, Western Australia
[3]Royal Perth Hospital Research Foundation, Perth, Western Australia, Australia
[4]Medical School, Crawley, Perth, Western Australia, Australia
[5]Division of Pathology and Laboratory Medicine, Medical School, UWA, Crawley, WA, Australia
[6]Anatomical Pathology, PathWest Laboratory Medicine WA, Perth, WA, Australia
[7]Division of Surgery, Medical School, University of Western Australia, Crawley, Perth, Western Australia, Australia
[8]Medical School, University of Western Australia, Crawley, Perth, Western Australia, Australia

Address correspondence to: Dr Donna Blanche Taylor
E-mail: *donna.taylor@health.wa.gov.au; 00064392@uwa.edu.au*

Objective: To evaluate and compare the accuracy and precision of contrast-enhanced mammography (CEM) *vs* MRI to predict the size of biopsy-proven invasive breast cancer.

Methods: Prospective study, 59 women with invasive breast cancer on needle biopsy underwent CEM and breast MRI. Two breast radiologists read each patient's study, with access limited to one modality. CEM lesion size was measured using low-energy and recombined images and on MRI, the first post-contrast series. Extent of abnormality per quadrant was measured for multifocal lesions. Reference standards were size of largest invasive malignant lesion, invasive (PathInvasive) and whole (PathTotal). Pre-defined clinical concordance ±10 mm.

Results: Mean patient age 56 years, 42 (71%) asymptomatic. Lesions were invasive ductal carcinoma 40 (68%) with ductal carcinoma *in situ* (31/40) in 78%, multifocal in 12 (20%). Median lesion size was 17 mm (invasive) and 27 mm (total), range (5–125 mm). Lin's concordance correlation coefficients for PathTotal 0.75 (95% CI 0.6, 0.84) and 0.71 (95% CI 0.56, 0.82) for MRI and contrast-enhanced spectral mammography (CESM) respectively. Mean difference for total size, 3% underestimated and 4% overestimated, and for invasive 41% and 50% overestimate on MRI and CESM respectively. LOAs for PathTotal varied from 60% under to a 2.4 or almost threefold over estimation. MRI was concordant with PathTotal in 36 (64%) cases compared with 32 (57%) for CESM. Both modalities concordant in 26 (46%) cases respectively.

Conclusion Neither CEM nor MRI have sufficient accuracy to direct changes in planned treatment without needle biopsy confirmation.

Advances in knowledge: Despite small mean differences in lesion size estimates using CEM or MRI, the 95% limits of agreement do not meet clinically acceptable levels.

INTRODUCTION

Breast cancer is a heterogeneous disease that is frequently multifocal and/or multicentric.[1–4] The American Joint Committee on Cancer (AJCC) TNM staging system is used to classify breast cancer extent and predict prognosis. Tumour size for TNM stage is defined as maximum size of the invasive lesion on surgical pathology, and for multifocality, tumour size is determined by the size of the largest invasive component alone.[5]

For the surgeon, an accurate estimate of the local extent of disease is crucial for counselling patients regarding the type of surgery required, and whether breast conservation is possible. Estimates of lesion size on imaging should reflect total size, including surrounding *in-situ* disease, and multifocality ± interconnecting *in-situ* disease.

Standard breast imaging (full-field digital mammography (FFDM), tomosynthesis and ultrasound) has limitations in

estimating lesion size; ultrasound and FFDM tending to underestimate,[6] and tomosynthesis to overestimate, particularly in females with dense breasts.[7]

Functional imaging techniques that are able to demonstrate neo-angiogenesis in addition to anatomical morphology, such as contrast-enhanced breast MRI (MRI), not only improve the detection of breast cancer but are more accurate in estimating lesion size and extent.[8] However, MRI does have disadvantages, including high cost, relatively low specificity,[9] inability to visualise microcalcifications, suboptimal accessibility and limited patient tolerance.[10] An association with significant delays in treatment have also been reported with MRI.[11,12]

Contrast-enhanced mammography (CEM) is a quick and easy to perform, inexpensive new technique able to demonstrate both neovascularity and lesion morphology, including microcalcification.

CEM is performed by obtaining two view mammograms using high and low energy X-ray exposures approximately 2 min after the injection of intravenous contrast. Two images per view are available for reporting, a " low energy" image that displays morphology (equivalent to a standard mammogram[13]) and a recombined image that shows areas of iodine uptake.[14] Although lacking many of the disadvantages of MRI, a CEM examination does require breast compression and exposure to ionising radiation, whereas MRI does not. Both techniques involve intravenous contrast media injection, with renal failure or known contrast allergy contraindications for both.

The aim of this study was to evaluate the comparative and independent accuracy and precision of CEM and MRI in estimating malignant lesion size in females with core biopsy-proven invasive breast cancer, using final histopathology as the reference standard.

METHODS AND MATERIALS

This prospective study (Australian and New Zealand Clinical Trials Registry: ACTRN 12613000684729) was conducted at two tertiary referral hospitals, approved by our institutional Human Research and Ethics Committee, and compliant with the National Health and Medical Research Council Statement on Ethical Conduct in Human Research. Written informed consent was obtained from all participants. Aspects of this cohort have been reported in two prior publications, addressing background parenchymal enhancement[15] and patient preference.[10]

Females aged over 21 years attending the Breast Clinic at two tertiary institutions in Perth, Western Australia between June 2013 and October 2015, with an invasive breast cancer (of any type) on needle biopsy and fit to undergo surgery, were invited to participate.

Exclusion criteria were: inability to give written informed consent, allergy to iodinated or gadolinium-based contrast, renal insufficiency, diabetes mellitus treated with metformin, pregnancy or lactation, breast implants, and contraindications to MRI.

Standard breast imaging included FFDM with or without further views and high resolution ultrasound performed at outside practices or in our clinic.

Each participant underwent both CEM and breast MRI according to appointment availability and not timed to menstrual cycle. The examinations were performed at one centre using previously described standardised protocols,[15] by experienced breast imaging technologists.

A Breast Imaging Fellow assessed lesion type (using the National Breast Cancer Center synoptic reporting system[16] as mandated by the national screening program) and maximum size on standard breast imaging. Breast density was independently assessed by two readers (breast imaging fellow and consultant breast radiologist), with third reader arbitration in case of disagreement, and dichotomised into non-dense (BI-RADS 1 or 2) and dense (BI-RADS 3 or 4).[17]

MRI findings were reported according to the BI-RADS fifth Edition lexicon.[18] For CEM studies, low energy and recombined images were reviewed, and reported using modified MRI BI-RADS descriptors.[19] Background parenchymal enhancement (BPE) on CEM and MRI was dichotomised into minimal—mild and moderate—marked.

CEM and MRIs were independently read by pairs of subspecialist breast radiologists. A consensus report was issued, with third reader arbitration in the event of disagreement. Readers were able to view the initial standard breast imaging but were only permitted to view and report one of the two study modalities per patient. Radiologists who read the MRI and CEM studies were subspecialty trained with between 5 and 25 years of experience in breast imaging. Our centre was one of the early adopters of CEM; readers completed a series of nine training cases supplied by the CEM vendor prior to study commencement.

Reference lesions were defined as those detected on standard imaging and confirmed to be malignant on needle biopsy. The largest invasive malignant lesion per patient on surgical histopathology formed the reference lesion. Multifocal disease was defined as the presence of more than one ipsilateral malignant lesion situated more than 5 mm from but within ≤4 cm of the reference lesion, usually within the same quadrant.[20] Multicentric disease was defined as presence of more than one ipsilateral malignant lesion separated >4 cm, usually within a different quadrant.[20]

Lesions were viewed on Agfa picture archive and communication workstations (Agfa-Gevaert NV Mortsel, Belgium) with 5MPixel Barco (NYSE Euronext Brussels, Belgium:BAR) monitors measured to the nearest millimetre in three orthogonal dimensions using electronic callipers. For MRI, measurements were made on the first post-contrast series. For CEM, low energy (LE) and recombined images were considered together: suspicious

Figure 1. Breast imaging studies of one of the study participants. CEM: LE and RC craniocaudal (a, e) and mediolateral oblique views (b, f). Left lateral magnification view (c). Breast MRI: sagittal image (d) and axial first post-contrast MIP (g). A 71-year-old patient with a calcified left breast mass on screening mammography. Clinical examination revealed a 30 mm palpable mass. LE CEM images demonstrate an irregularly shaped spiculated mass (solid arrow) with associated microcalcifications (dotted arrow) in the left UOQ. On the RC images, the left UOQ lesion shows marked heterogeneous internal enhancement measuring 16 mm. Total lesion size on CEM including the associated calcification was 28 mm. Maximum lesion size on MRI was 23 mm. Final histopathology revealed an invasive duct carcinoma not otherwise specified (25 mm), with intermediate grade micropapillary DCIS measuring 45 mm. The total tumour size was 50 mm. Lesion size was significantly underestimated by both CEM and MRI and re-excision for close margins was needed. CEM, contrast-enhanced mammography; DCIS, ductal carcinoma *in situ*; LE, low energy; MIP, maximum intensity projection; RC, recombined; UOQ, upper outer quadrant.

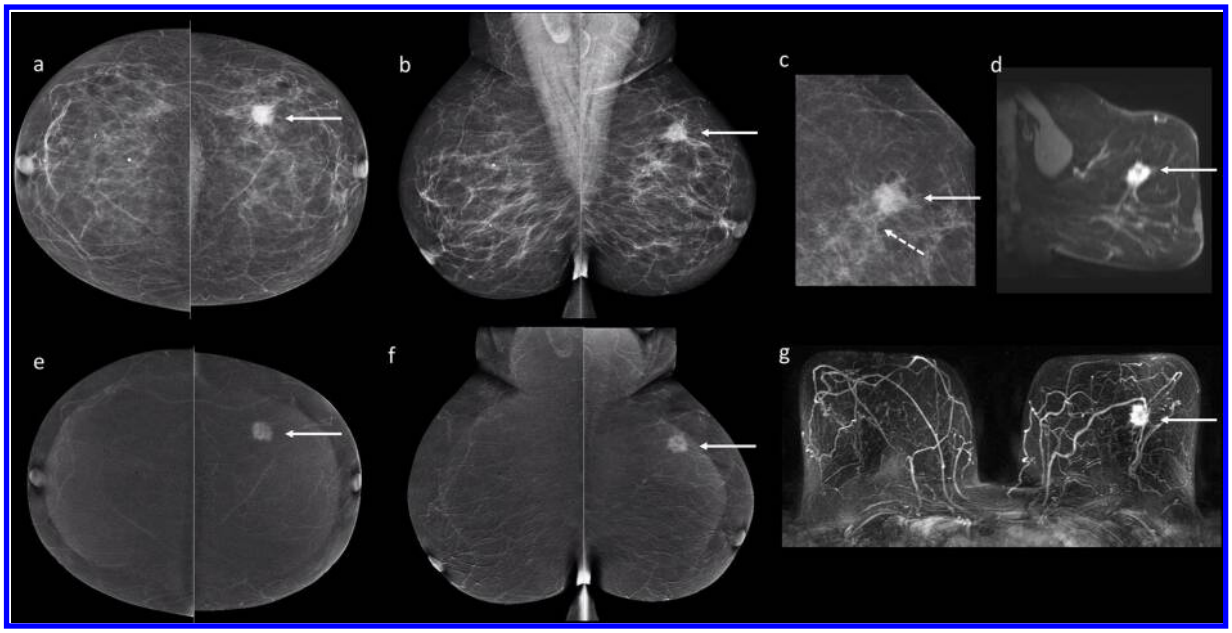

microcalcifications were included in the estimated lesion size and the size of any non-enhancing malignant lesion was recorded from the LE images (Figure 1). In cases of suspected multifocal disease, the extent of suspicious mass and/or non-mass enhancement in that quadrant was measured.

To optimise radiological–pathological correlation, the pathologist was given a diagram showing the location of lesions detected on imaging (Figure 2) prior to tissue processing. Wide local excision specimens were received fresh and following overnight fixation in 10% neutral buffered formalin, the specimens were weighed, placed in a grid and radiographed. Coordinates of imaging lesions were identified from review of the diagram and specimen radiograph and pins inserted into the specimen through the holes in the grid based on the given coordinates (Figure 3). The specimens were measured and margins inked using the surgeon's orientation sutures.

The entire specimen was serially sectioned in 3–5 mm parallel slices in the sagittal plane and consecutively laid out, maintaining orientation. The lesion and margins were blocked (Figure 4) and processed using standard processing techniques. One 4 µm section was cut from each block and stained with haematoxylin and eosin (H & E).

Following formalin fixation, mastectomies were serially sectioned in 5–10 mm parallel slices in the sagittal plane, with slices either held together by overlying skin (akin to a book-end) or consecutively laid out, maintaining orientation. If a lesion was not apparent, or the pre-operative imaging/core biopsy suggested a predominantly *in-situ* process, slices were radiographed prior to blocking. Region(s) of interest (including marker clips) and margins were blocked then processed using standard techniques. One 4 µm section was cut from each block and stained with H & E.

The first author and a study pathologist reviewed each case to ensure lesion concordance. The pathologist measured[1] size of the largest invasive component (Path Invasive) and[2] total lesion size including surrounding ductal carcinoma *in situ* (DCIS) and/or satellite malignant lesions within the same quadrant (Path Total).

Statistical analysis

An *a priori* power calculation determined a sample size of 60 would have 95% power to detect a difference of ± 5 mm between CEM and MRI, and a conclusion of equivalence to be drawn if the 90% CI around the difference between the two methods was above 5 mm or below 5 mm. This *a priori* 10 mm margin for concordance was selected as being likely to result in clear pathological margins while avoiding excess tissue removal.

Demographics and imaging findings were reported using descriptive statistics. Lesion size on imaging and pathology (Path Invasive and Path Total) were illustrated using scatter plots of raw

Figure 2. Imaging-pathology case report form for the case shown in Figure 1. The location of the lesion detected on imaging and the imaging findings are listed for the pathologist.

This form was reviewed prior to tissue processing to ensure the blocks taken were focused on the lesion site.

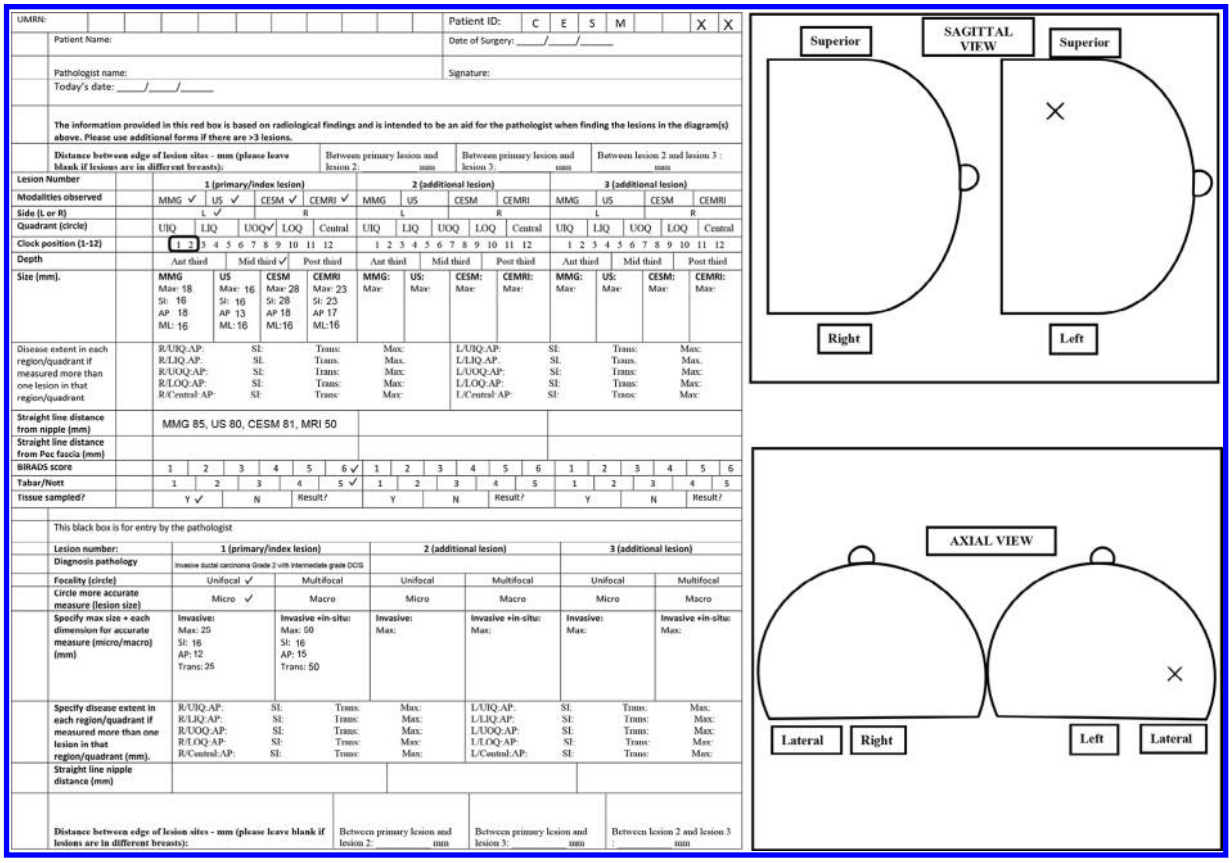

data around the line of perfect agreement. Outliers for lesion size estimation (defined using Tukey's rule as those values 1.5 times the InterQuartile Range above the 75th percentile or below the 25th percentile), were evaluated for underlying common factors.

Agreement between imaging and pathology was assessed initially by generating a Bland–Altman plot of the difference between imaging and pathology *vs* the mean of the two measures using raw data. Clinically acceptable limits of agreement (LOAs) were set *a priori* to be ± 10 mm. However, these graphs demonstrated an increasing spread or fanning-out of differences with increasing size, illustrating the common association between difference and magnitude which can lead to LOA too wide for smaller sizes and too narrow for larger sizes. As per Bland and Altman,[21] a log transformation was applied to remove this association and the graph regenerated. The mean difference and LOAs derived from the log transformed data were exponentiated to obtain values on the original scale. Once back transformed, these values represented relative (proportional) rather than absolute differences.

To quantify the degree of agreement between imaging and pathology, Lin's concordance correlation coefficient (CCC) and 95% CI were calculated on log transformed lesion sizes. Pearson correlation is often inappropriately reported in agreement studies, however, this test only evaluates whether points lie on any straight line, not whether data conform to the line of equality (or the 45° line). Lin's concordance correlation coefficient corrects Pearson correlation for how far the line of best fit sits from the line of equality. A CCC of >0.75 was considered good agreement.

A paired sample *t*-test was used to assess the mean difference between tests. A 90% CI around the mean difference between imaging methods was calculated to determine equivalence (within ± 5 mm). The absolute value of the differences between imaging tests and pathology were dichotomised using a cut point of 10 mm (*a priori* acceptable margin of error) to calculate the proportion of lesions where imaging was concordant with pathology for descriptive purposes.

All tests of significance were two-sided and the level of significance used was $p < 0.05$. Analyses were undertaken using SAS v. 9.4 and Stata 16 (StataCorp. 2019. *Stata Statistical Software: Release 16*. College Station, TX: StataCorp LL).

RESULTS

Of the 75 women who underwent CEM, MRI or both, data were available for review in 59. The mean time interval between the two contrast-enhanced studies was 4.6 days, sd = 3.2 days, range 1–15 days. The mean patient age was 56 years, range 35–77, sd = 11. Most females (42, 71%) were asymptomatic, with lesions detected on screening mammography, 13 (22%) had palpable

Figure 3. X-ray of the fixed surgical specimen taken in a perspex grid. The ill-defined calcified lesion (dotted arrow) is seen towards the centre of the specimen at co-ordinates G-I, 8–12. A localising iodine 125 seed is present within (solid arrow). Scattered microcalcifications are seen in the tissue surrounding the lesion. Pins are inserted through the holes in the grid to mark the coordinates of the lesion so that pathology sampling can be focused on this area.

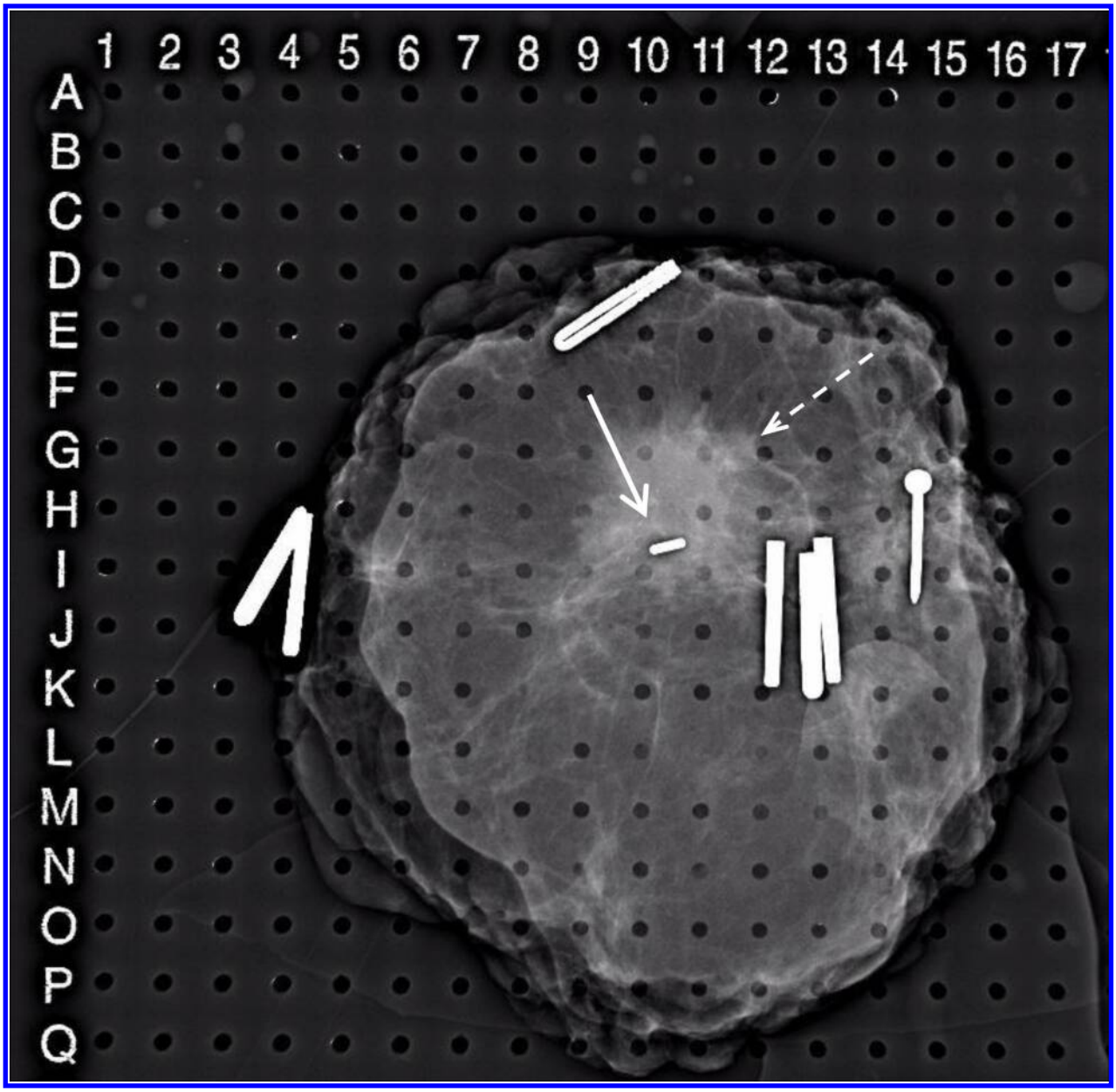

masses and 4 other symptoms (nipple retraction, mastitis, rash, tenderness). Two (3%) had a previous breast cancer (ipsilateral in one and contralateral in the other), four (7%) had a family history of breast and one of ovarian cancer. None had a known gene mutation.

One-third of patients had mammographically dense breasts. Minimal-mild background parenchymal enhancement was noted on CEM and MRI in 44 (75%) and 41 (69%) patients respectively, and on both modalities in 38 (64%) patients.

The commonest morphology of the reference lesion on CEM and MRI was a mass (Table 1). A measurement was available for MRI in 57 patients and CEM in 58 patients. In two cases where the reference lesion did not enhance on CEM, estimated lesion size was based on the extent of residual suspicious microcalcification. The single reference lesion not visible on CEM was a 6 mm cluster of calcifications prior to diagnostic core biopsy and no residual calcifications were visible on the LE image. This lesion was visible on MRI (5 mm mass) and final pathology revealed a 9 mm Grade 1 invasive ductal carcinoma (IDC) with low grade DCIS. The two lesions not visible on MRI were a 12 mm stellate mass and a 6 mm mass prior to core biopsy. Both were visible on CEM as masses and shown to be a 7 mm Grade 2 IDC and a 6 mm Grade 2 IDC respectively, on final pathology.

Figure 4. Pathologist's block diagram. This provides a key for the sites where blocks were taken from the surgical specimen of the case shown in Figure 1. Invasive tumour is present in blocks 8, 9, 10, 11, 12, 16, 17, 18, 19, 20 (SLICES 6–10 inclusive).The greatest dimension of invasive tumour is measured medial to lateral as five slices (with each slice 5 mm in thickness) = 25 mm. DCIS is present in blocks 1, 2, 3, 4, 5, 6, 7, 8, 9, 10, 11, 12, 16, 17, 18, 19 (SLICES 1–9 inclusive).The greatest dimension of DCIS is measured medial to lateral as nine slices (with each slice 5 mm in thickness) = 45 mm. The whole tumour size (invasive+DCIS) is 50 mm (SLICES 1–10 inclusive). DCIS, ductal carcinoma *in situ*.

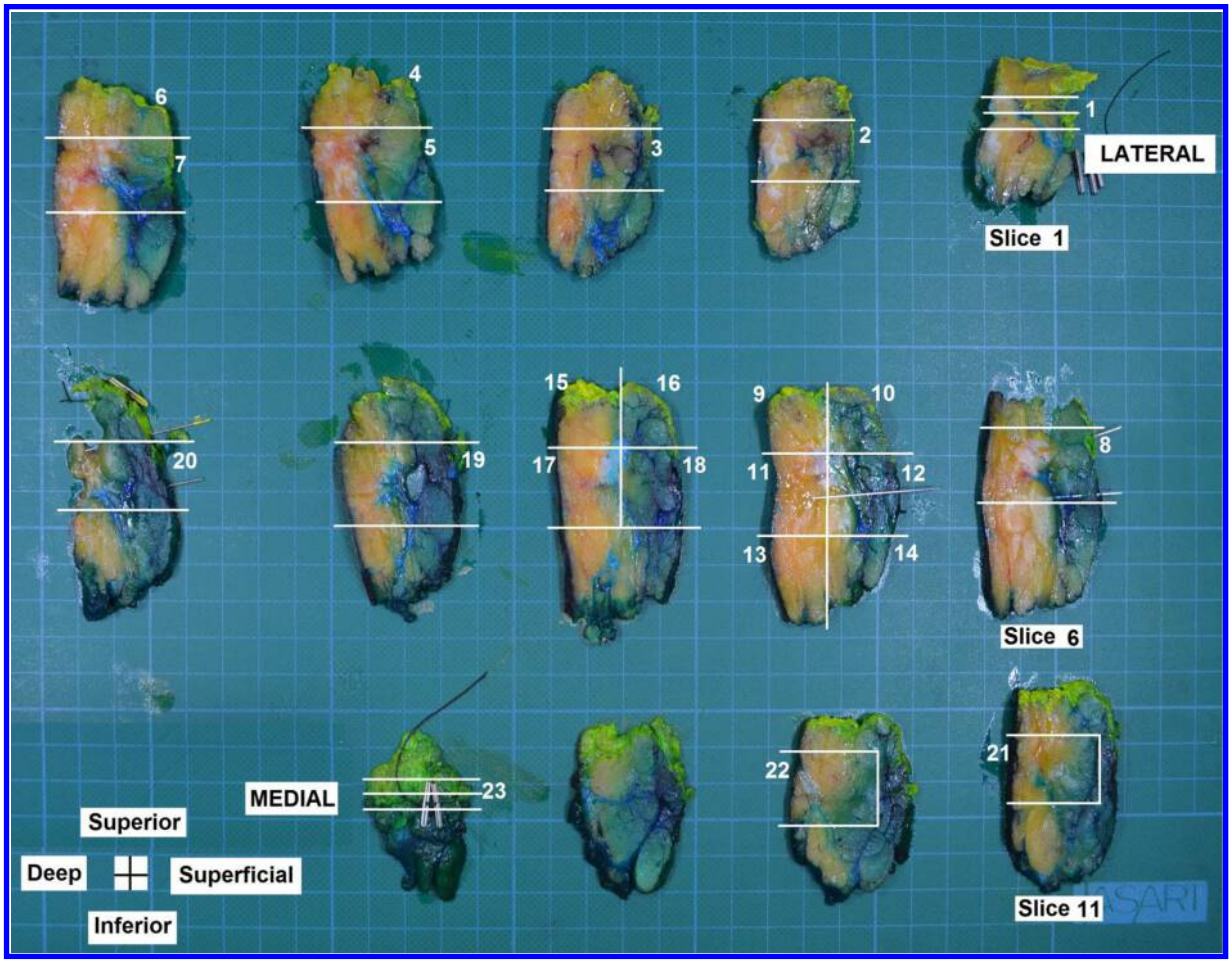

Most of the reference lesions (Table 2) were invasive ductal carcinoma 40/59 (68%), associated with DCIS (31/40) in 78%. DCIS in adjacent tissue was noted in 25 (42%) cases and extensive intraduct component in 14 (24%). Multifocality was noted in 12 (20%) cases.

The median size of the reference lesions on pathology was 17 mm (invasive) and 27 mm (Path Total), (range 5–125 mm) (Table 3). MRI and CEM lesion size outliers failed to reveal any predominant features. Scatter plots for total and invasive pathology size *vs* MRI and CEM (Figure 5 and Figure 6), show observations further from the line of perfect agreement as their magnitude increases, and illustrate the leftward shift of observations when only the invasive component was measured on pathology. Multifocal cases (denoted by triangles) tended to produce substantial discrepancies when only the (largest) invasive component of the lesion was measured. Lin's CCCs were comparable between modalities but not within modality (between total and invasive) with total lesion size producing better results (CCC = 0.75, 95% CI 0.6, 0.84 and CCC = 0.71, 95% CI 0.56, 0.82 for MRI and CEM respectively, Table 4). When the lower bound of the 95% CI is considered, none of these indices of agreement reflect an acceptable level of agreement.

The Bland–Altman LOAs for each of the modalities *vs* pathology are illustrated in Figure 7 and Figure 8 and detailed with back transformations in Table 4. The mean differences for total lesion size are small (3% underestimated and 4% overestimated for MRI and CEM respectively) but bigger for invasive lesion size (41 and 50% overestimated for MRI and CEM respectively). However, the graphs show undesirably wide LOA for both modalities, neither demonstrating superior performance, given the similar widths of the LOA for both total and invasive lesion size. Back transformed limits indicate differences in total lesion size vary between a 60% underestimation to almost threefold overestimation (exponentiated LOA MRI: 0.38, 2.4, CEM: 0.37, 2.9). For invasive lesion size, the error margin ranges from a 60% under to sixfold over estimation (exponentiated LOA MRI:0.4, 5, CEM:0.37, 6).

Table 1. Imaging findings (*N* = 59)

Characteristics of reference lesion used for size comparison	N (%)
Side	
Right	34 (58)
Left	25
Mammographic breast density	
Non-dense	40 (68)
Dense	19
Background parenchymal enhancement	
CEM	
Minimal-mild	44 (75)
Moderate-marked	15
MRI	
Minimal-mild	41 (69)
Moderate-marked	18
Mammographic findings	
Not visible	4 (7)
Mass	24 (41)
Mass with calcification	10 (1)
Architectural distorsion	11 (19)
Focal asymmetry	5 (8)
Calcification[a]	5 (1)
Ultrasound findings	
Not performed	1 (2)
Not visible	2 (3)
Hypoechoic mass	55 (93)
Multiple masses	1 (2)
CEM findings	N (%)
Mass	46 (78)
Non-mass	6 (10)
Calcification	2 (3)
Mass and non-mass	4 (7)
Clip only	1 (2)
MRI findings	
Mass	48 (82)
Non-mass	6 (10)
Mass and non-mass	3 (5)
Clip only	2 (3)

CEM, contrast-enhanced mammography.
The sum of column % differ from column totals due to rounding.
[a]Includes one case of asymmetrical density with calcifications.

No significant difference was detected between mean estimated lesion size using MRI and CEM (mean difference −2.48 mm (p = 0.26)). The 90% CI extends outside the interval that would demonstrate equivalence (±5 mm).

Table 2. Histopathological features of the reference lesions

Histopathology variables	N (%)
Invasive tumour size	
≤20 mm	36 (61)
>20 and <50 mm	16 (27)
≥50 mm	7(12)
Histopathological type	
IDC with DCIS	31 (52)
ILC	14 (24)
IDC	9 (15)
Other invasive (mucinous, tubular)	3 (5)
Mixed IDC and ILC	2 (3)
Focality	
Unifocal	47 (80)
Multifocal	12 (20)
DCIS with largest invasive lesion	
EIC	14 (24)
DCIS in adjacent tissue	25 (42)
Grade of invasive tumour	
Grade 1	9 (15.3)
Grade 2	34 (57.6)
Grade 3	16 (27.1)
Subtype of largest invasive lesion	
Luminal A	4 (7)
Luminal B	47 (80)
Her2 positive	1 (2)
Triple negative	7
Total	59

EIC, extensive intraduct component; IDC, invasive ductal carcinoma; ILC, invasive lobular carcinoma.
The sum of column % differ from column totals due to rounding.

Based on a ±10 mm acceptable margin of error, total size estimation by MRI was concordant with pathology in 36 (64%) cases compared to 32 (57%) for CEM, with both modalities concordant for 26 (46%) cases (Table 5). For 14 (25%) cases, neither modality was within acceptable error limits.

DISCUSSION

While the differences between mean estimated total lesion size using CEM or MRI are small, not statistically different, nor equivalent, the wide LOA observed in this study indicate that neither could be considered accurate for estimating lesion size. Small differences in mean estimated lesion size between CEM and MRI, and between either modality and Path Total have been reported, with variability as to whether this represents under- or overestimation.[22–25] In our study, CEM slightly overestimated and MRI slightly underestimated total lesion size. Youn et al[24] found CEM and MRI both underestimated lesion size by

Table 3. Measurements of reference lesion on pathology, CEM and MRI

Lesion variables	Mean (sd)	Median [Q1,Q3]	Min,Max
Maximum lesion size pathology (total) *n* = 59	33.8 (23.2)	27 [16,50]	5,125
Maximum lesion size pathology (invasive) *n* = 59	25.2 (22.9)	17 [12,30]	6,125
Maximum lesion size CEM (*n* = 58)	33.3 (23.2)	29.5 [26.9,52]	6.5,100
Maximum lesion size MRI (*n* = 57)	35.3 (20.3)	29.0 [19,45]	5,80
Differences: CEM *vs* Pathology size (total)	1.2 (20.9)	0.75 [-7,7]	−79,50
CEM *vs* pathology size (invasive)	9.9 (25.8)	6.5 [0,22]	−79,91
MRI *vs* pathology (total)	−1.5 (16.4)	0 [-6,4]	−50,40
MRI *vs* pathology size (invasive)	7.4 (20.5)	2 [-2,14]	−50,71

CEM, contrast-enhanced mammography.
All measurements are in mm. N=59 pathology, N=58 CEM & N=57 MRI.

−0.97 mm (95% CI −3.7 to 1.76 mm) and −3.53 (95% CI −6.19 to −0.87 mm) respectively, whereas Luczynska et al[25] reported CEM and MRI both overestimated lesion size by 1.7 mm, and 1.8 mm, respectively.

The 95% CI for Lin's concordance coefficients found in our study, all failed to exclude the benchmark of 0.75 for good agreement between lesion size estimated with either CEM or MRI and pathology. Youn et al[24] reported ICCs of 0.863 (95%CI 0.752–0.924) for CEM and 0.884 (95%CI 0.791–0.935) for MRI, indicating higher agreement with pathology than in our study, however, their lesion sizes were smaller, and had less variability.

The log transformation of sizes for the Bland–Altman plot created some difficulty for comparing the calculated LOA to the pre-specified acceptable margin of error. However, the range of relative errors (of between 3 and 6 fold in estimates of lesion size using CEM or MRI compared with pathology) suggested neither CEM nor MRI perform well. Other studies have reported 95% LOAs that exceed the same pre-specified 10 mm margin of error: Patel et et al[26] −15.6 to 21.4 mm, Travieso-Aja et al[27] −10.3 to 16.2 mm, Blum et al[28] −18.8 to 19.48, Lobbes et al[22] −18.44 to 18.4 mm (CEM), and −11.46 to 15.71 (MRI). However, despite this, half of these authors concluded that the quality of tumour size measurement with CEM is "good." These wide LOA

Figure 5. Scatter diagram: lesion size on pathology (a) total (invasive plus *in situ*) and (b) invasive *vs* size on CEM. CEM, contrast-enhanced mammography. Lin's concordance correlation coefficient is based on the log transformed data.

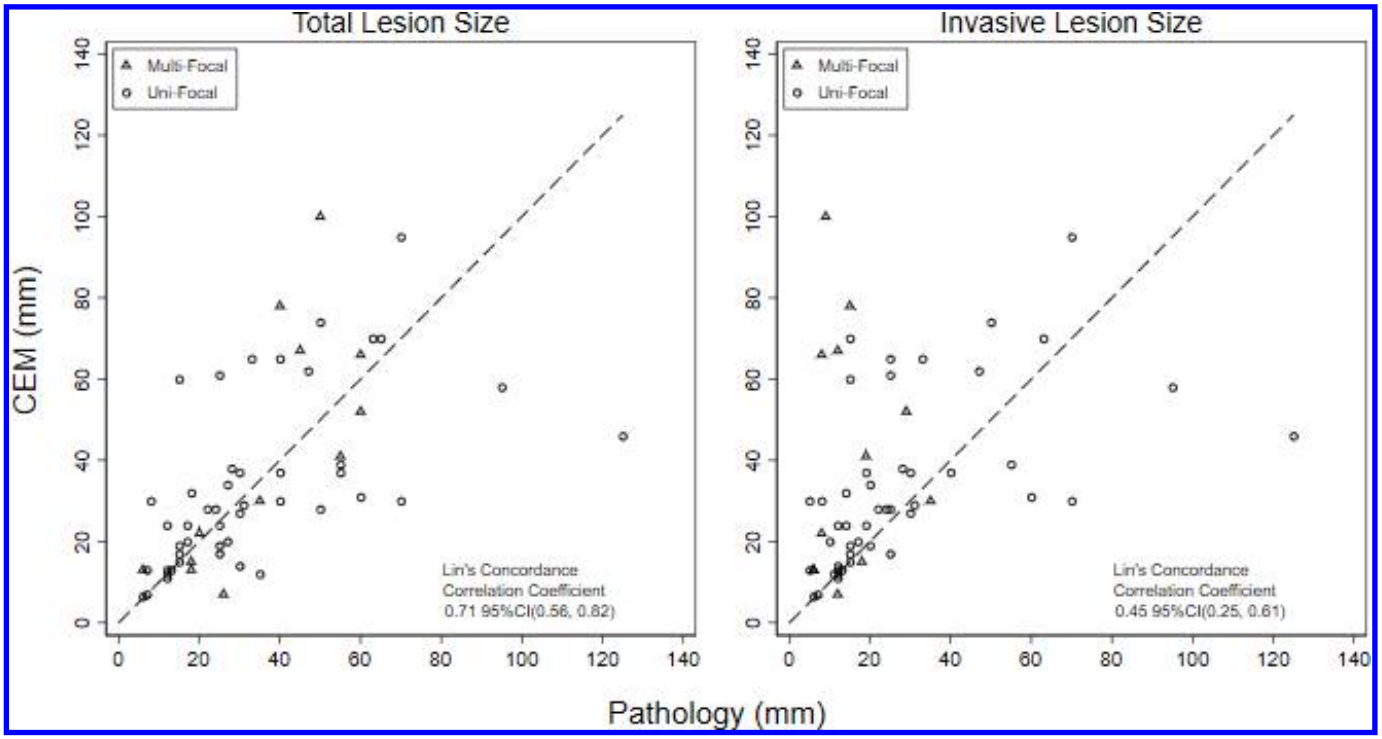

Figure 6. Scatter diagram: lesion size on pathology (a) total (invasive plus *in situ*) and (b) invasive *vs* size on MRI.

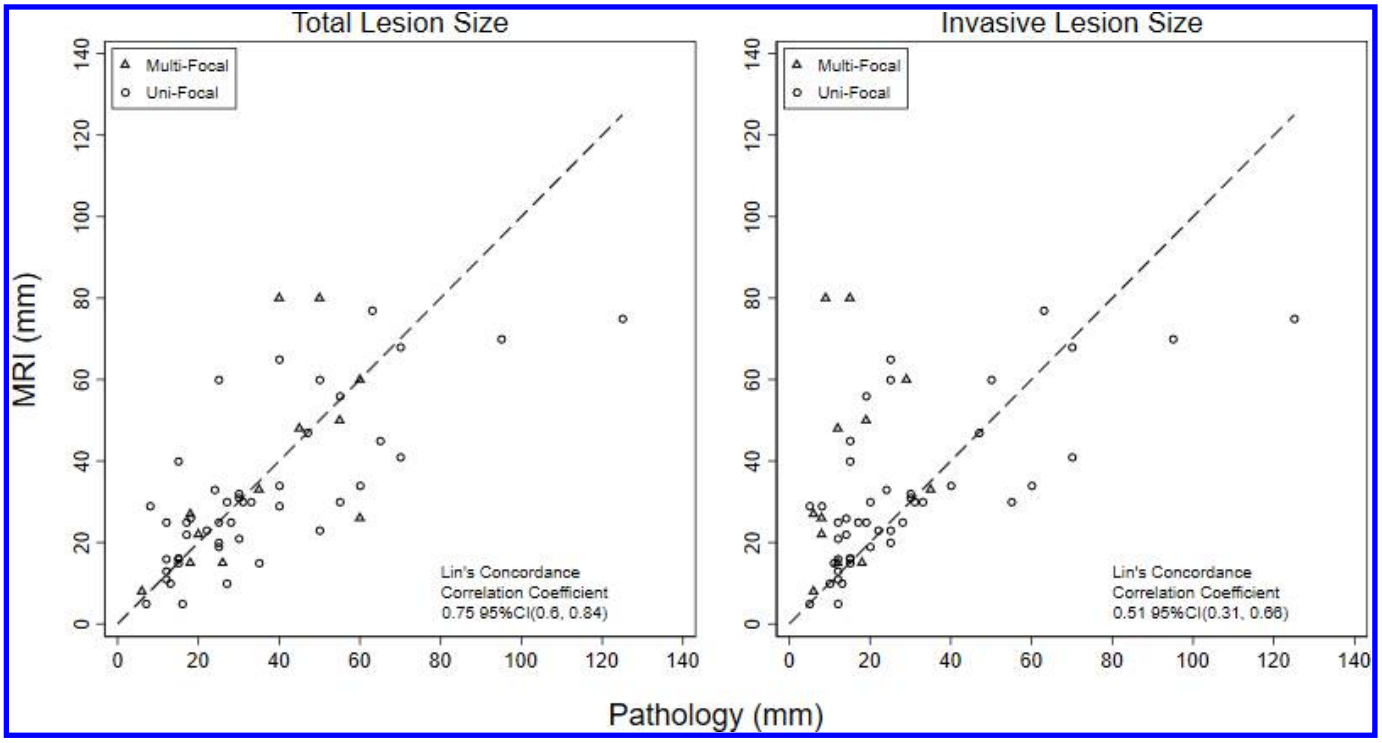

emphasize the need for additional needle biopsies to confirm lesion size where significant changes in treatment planning could result.

Variability exists as to the error margins used to define "concordance" between lesion size estimated with imaging *vs* pathology, ranging from 5 mm,[24,27,29–31]10 mm[32,33] and 15 mm.[34] Our results lie in between those reported in prior studies that have used a 10 mm error margin. McGuire et al[33] compared lesion size measured on CEM with pathology and found a 47.1% concordance rate. Lobbes et al[22] found both CEM and MRI to be concordant with pathology in 84.5% of cases and concluded that the addition of MRI to CEM did not improve the accuracy of size prediction. Our findings differ: the addition of MRI to CEM would have resulted in acceptable lesion size estimates in a further 10 patients (18%).

The small number of patients in our study precluded analysis of patient and lesion related variables that could influence the ability of CEM and/or MRI to predict tumour size such as: breast and lesion size,[24] lesion type on imaging (mass *vs* non-mass)[34–36] and pathology (lobular subtype, multifocality, extensive intraduct component).[27,29,36] Technical considerations include the mammographic view or MRI sequence on which the lesion is measured,[24] and pathology processing and measurement techniques.[37–39] Further studies are needed to identify patient/lesion subgroups most likely to benefit from use of one or other modality and the optimal measurement methods for each.

The strengths of this study include the in-depth prospectively guided imaging and pathology correlation, pragmatic measurement of whole tumour size and use of robust and appropriate statistical methods. Despite a plethora of literature[22,40–42] explaining why the

Table 4. Log transformed mean differences between lesion size as estimated with MRI and CEM and path total and invasive lesion sizes, with LOA

		Log scale		Exponentiated			
		Average difference	95% LOA	Average difference	95% LOA	CCC[1]	95% CI CCC
Path total	MRI	−0.03	−0.96, 0.89	0.97	0.38, 2.4	0.75	(0.6, 0.84)
	CEM	0.04	−1.0, 1.1	1.04	0.37, 2.9	0.71	(0.56, 0.82)
Path invasive	MRI	0.34	−0.93, 1.6	1.41	0.4, 5	0.51	(0.31, 0.66)
	CEM	0.41	−0.98, 1.8	1.5	0.37, 6	0.45	(0.25, 0.61)

CEM, contrast-enhanced mammography; LOA, limit of agreement.
Lin's correlation coefficient, with 95% confidence intervals.
[a]Concordance correlation coefficient.

Figure 7. Bland–Altman plots for tumour size total (invasive plus *in situ*) *vs* lesion size on MRI and CEM. CEM, contrast-enhanced mammography.

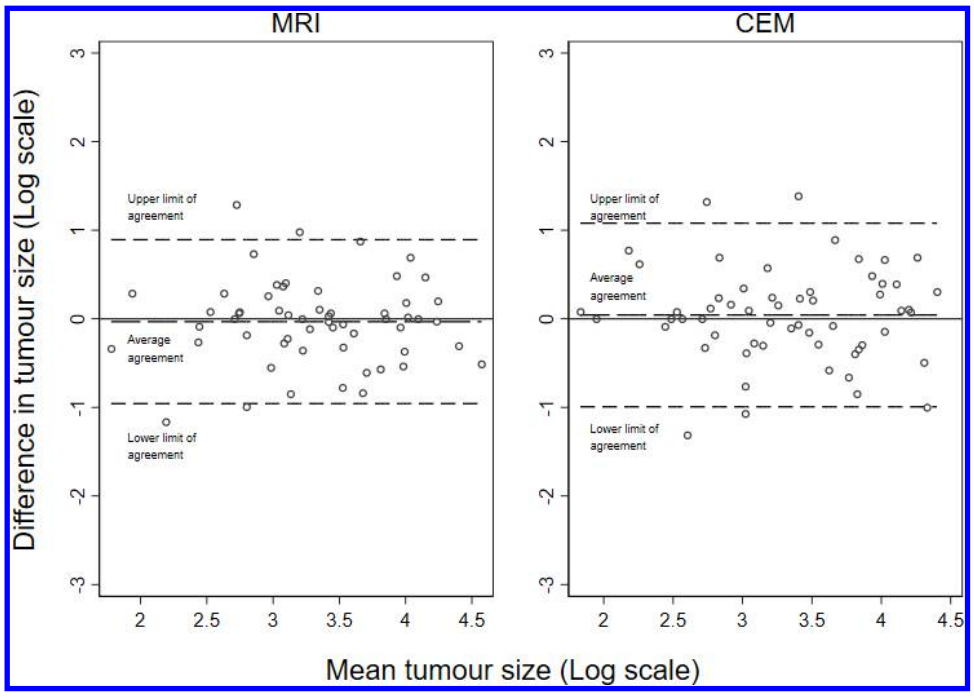

use of Pearson correlation in the assessment of agreement is inappropriate, use of correlation persists. The analysis adopted in this paper follows the guidelines of Bland and Altman,[21] including the use of log transformations to obtain more accurate LOA.

Our study has some limitations: we fell short of the sample size determined by our power analysis to address our primary aim (whether lesion size estimation with CEM was equivalent to MRI) and the planned sample size was insufficient for subgroup analyses.

While our inclusion criteria were wide, selection bias may have occurred during recruitment (*e.g.* tendency to offer the study to patients where it was thought contrast imaging may be beneficial based on knowledge of situations where MRI would be offered, *e.g.*

Figure 8. Bland–Altman plots for tumour size (invasive only) *vs* lesion size on MRI and CEM CEM, contrast-enhanced mammography.

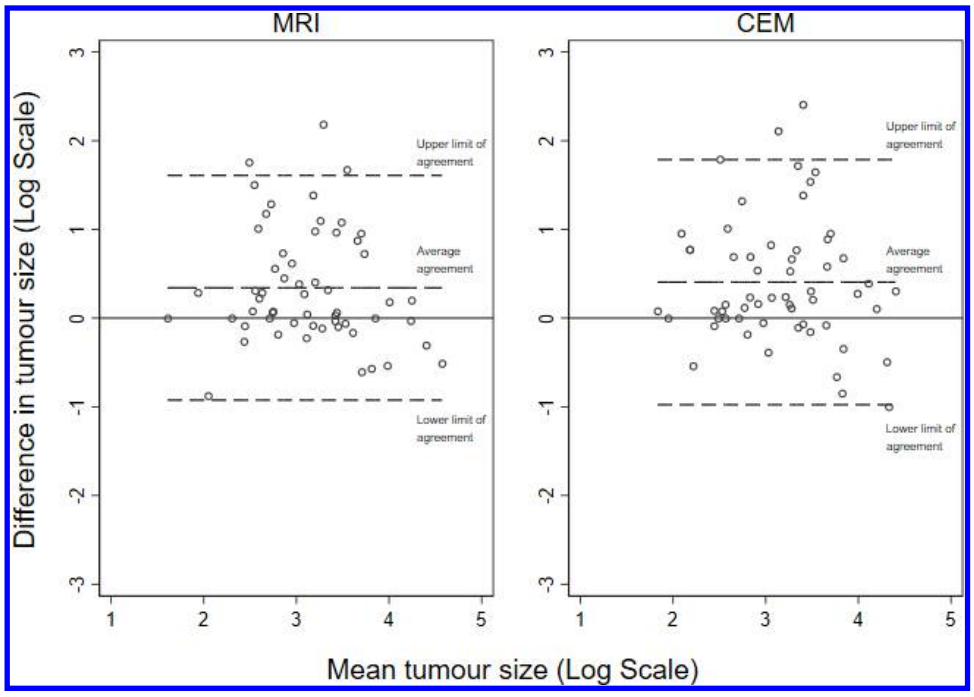

Table 5. Comparison of proportion of agreement with total and invasive tumour size on pathology (within ± 10 mm) between modalities

Total lesion size		CEM *vs* pathology		
		Difference >10 mm	Difference ≤10 mm	Total
MRI *vs* Pathology	Difference >10 mm	14 (25%)	6 (11%)	20 (36%)
	Difference ≤10 mm	10 (18%)	26 (46%)	36 (64%)
	Total	24 (43%)	32 (57%)	56 (100%)
Invasive lesion size		CEM *vs* pathology		
		Difference >10 mm	Difference ≤10 mm	Total
MRI *vs* Pathology	Difference >10 mm	20 (36%)	3 (5%)	23 (41%)
	Difference ≤10 mm	6 (11%)	27 (48%)	33 (59%)
	Total	26 (46%)	30 (54%)	56 (100%)

CEM, contrast-enhanced mammography.
The sum of column % differ from column totals due to rounding.

larger tumours, dense breasts, mammographically occult lesions). However, given the intraindividual nature of this study, this would have affected CEM and MRI equally, and in practice, these are the cases for which MRI and CEM would be considered beneficial.

CONCLUSION

Although the mean differences between estimated lesion size using CEM or MRI *vs* pathology are small, the wide LOAs observed suggest that neither CEM nor MRI has sufficient precision to direct changes in planned treatment without needle biopsy confirmation.

ACKNOWLEDGEMENTS

Radiologists: Drs Michelle Bennett, Deepika Gunawardena, Deepthi Dissanayake, James Anderson, James Seow, Tracey Muir, Clin. Assoc. Prof. Liz Wylie, Dr Sebastian Buzinski, Dr Matthew Brookes, Prof Paul Parizel. Pathologists: Drs Bruce Latham, Dr Jeremy Parry, Dr Dugald McCallum, Dr Mireille Hardie. Medical Imaging Technologists: Ms Leonie Maddren, Ms Lisa Towler, Ms Carolyn Madeley, Ms Meredith Kessell. Research assistants: Mr Max Hobbs, Ms Rachel Peake, Ms Sharon Rule. Thanks also to Mr Michael Phillips and Dr M Luke Marinovich.

COMPETING INTERESTS

GE Healthcare (Chicago, Ill) provided the equipment upgrade required for the first three months of this study at no charge. The authors had full control of the data and the information presented for publication.

FUNDING

Funding support for this study was received from the Department of Radiology, Royal Perth Hospital Special Purposes Trust Account. Open access publishing facilitated by The University of Western Australia, as part of the Wiley - The University of Western Australia agreement via the Council of Australian University Librarians.

PATIENT CONSENT

Written informed consent was obtained from all participants prior to any study procedures commencing.

ETHICS APPROVAL

Institutional Ethics Committee approval: EC 2012/048 Royal Perth Hospital Human Research Ethics Committee.

REFERENCES

1. Lagios MD. Multicentricity of breast carcinoma demonstrated by routine correlated serial subgross and radiographic examination. *Cancer* 1977; **40**: 1726–34. https://doi.org/10.1002/1097-0142(197710)40:4<1726::aid-cncr2820400449>3.0.co;2-o
2. Holland R, Veling SH, Mravunac M, Hendriks JH. Histologic multifocality of TIS, T1-2 breast carcinomas. Implications for clinical trials of breast-conserving surgery. *Cancer* 1985; **56**: 979–90. https://doi.org/10.1002/1097-0142(19850901)56:5<979::aid-cncr2820560502>3.0.co;2-n
3. Vaidya JS, Vyas JJ, Chinoy RF, Merchant N, Sharma OP, Mittra I. Multicentricity of breast cancer: whole-organ analysis and clinical implications. *Br J Cancer* 1996; **74**: 820–24. https://doi.org/10.1038/bjc.1996.442
4. Rosen PP, Fracchia AA, Urban JA, Schottenfeld D, Robbins GF. " residual " mammary carcinoma following simulated partial mastectomy. *Cancer* 1975; **35**: 739–47. https://doi.org/10.1002/1097-0142(197503)35:3<739::aid-cncr2820350329>3.0.co;2-5
5. Edition S, Edge S, Byrd D. AJCC cancer staging manual. AJCC cancer staging manual. 2017.
6. Gruber IV, Rueckert M, Kagan KO, Staebler A, Siegmann KC, Hartkopf A, et al. Measurement of tumour size with mammography, sonography and magnetic resonance imaging as compared to histological tumour size in primary breast

cancer. *BMC Cancer* 2013; **13**: 328. https://doi.org/10.1186/1471-2407-13-328
7. Marinovich ML, Bernardi D, Macaskill P, Ventriglia A, Sabatino V, Houssami N. Agreement between digital breast tomosynthesis and pathologic tumour size for staging breast cancer, and comparison with standard mammography. *Breast* 2019; **43**: 59–66. https://doi.org/10.1016/j.breast.2018.11.001
8. Mann RM, Cho N, Moy L. Breast MRI: state of the art. *Radiology* 2019; **292**: 520–36. https://doi.org/10.1148/radiol.2019182947
9. Saslow D, Boetes C, Burke W, Harms S, Leach MO, Lehman CD, et al. American cancer Society guidelines for breast screening with MRI as an adjunct to mammography. *CA Cancer J Clin* 2007; **57**: 75–89. https://doi.org/10.3322/canjclin.57.2.75
10. Hobbs MM, Taylor DB, Buzynski S, Peake RE. Contrast-Enhanced spectral mammography (CESM) and contrast enhanced MRI (CEMRI): patient preferences and tolerance. *J Med Imaging Radiat Oncol* 2015; **59**: 300–305. https://doi.org/10.1111/1754-9485.12296
11. Zhang M, Sun S, Mesurolle B. The impact of pre-operative breast MRI on surgical waiting time. *PLoS One* 2017; **12**(1): e0169756. https://doi.org/10.1371/journal.pone.0169756
12. Bleicher RJ, Ciocca RM, Egleston BL, Sesa L, Evers K, Sigurdson ER, et al. Association of routine pretreatment magnetic resonance imaging with time to surgery, mastectomy rate, and margin status. *J Am Coll Surg* 2009; **209**: 180–87; . https://doi.org/10.1016/j.jamcollsurg.2009.04.010
13. Francescone MA, Jochelson MS, Dershaw DD, Sung JS, Hughes MC, Zheng J, et al. Low energy mammogram obtained in contrast-enhanced digital mammography (CEDM) is comparable to routine full-field digital mammography (FFDM). *Eur J Radiol* 2014; **83**: 1350–55. https://doi.org/10.1016/j.ejrad.2014.05.015
14. Lewin JM, Isaacs PK, Vance V, Larke FJ. Dual-Energy contrast-enhanced digital subtraction mammography: feasibility. *Radiology* 2003; **229**: 261–68. https://doi.org/10.1148/radiol.2291021276
15. Savaridas SL, Taylor DB, Gunawardana D, Phillips M. Could parenchymal enhancement on contrast-enhanced spectral mammography (CESM) represent a new breast cancer risk factor? correlation with known radiology risk factors. *Clin Radiol* 2017; **72**: 1085. https://doi.org/10.1016/j.crad.2017.07.017
16. National Breast Cancer Centre (Australia). Synoptic breast imaging report: including imaging classification (1-5) [PDF]. Camperdown, NSW: National Breast Cancer Centre; 2007. Available from: https://www.canceraustralia.gov.au/publications-and-resources/cancer-australia-publications/synoptic-breast-imaging-report-update.
17. Ikeda D, Hylton N, Kuhl C. *Breast Imaging Reporting and Data System, ACR BI-RADS—breast imaging atlas*. Reston, VA: American College of Radiology; 2003.
18. Mendelson E, Atlas MEAAB-R. *ACR BI-RADS® Atlas, Breast Imaging Reporting and Data System. Reston, VA: American College of Radiology; 2013*. Reston, VA: American College of Radiology; 2013.
19. Kamal RM, Helal MH, Mansour SM, Haggag MA, Nada OM, Farahat IG, et al. Can we apply the MRI BI-RADS lexicon morphology descriptors on contrast-enhanced spectral mammography? *Br J Radiol* 2016; **89**: 20160157. https://doi.org/10.1259/bjr.20160157
20. Fisher ER, Gregorio R, Redmond C, Vellios F, Sommers SC, Fisher B. Pathologic findings from the National surgical adjuvant breast project (protocol No. 4). I. observations concerning the multicentricity of mammary cancer. *Cancer* 1975; **35**: 247–54. https://doi.org/10.1002/1097-0142(197501)35:1<247::aid-cncr2820350130>3.0.co;2-s
21. Bland JM, Altman DG. Measuring agreement in method comparison studies. *Stat Methods Med Res* 1999; **8**: 135–60. https://doi.org/10.1177/096228029900800204
22. Lobbes MBI, Lalji UC, Nelemans PJ, Houben I, Smidt ML, Heuts E, et al. The quality of tumor size assessment by contrast-enhanced spectral mammography and the benefit of additional breast MRI. *J Cancer* 2015; **6**: 144–50. https://doi.org/10.7150/jca.10705
23. Fallenberg EM, Schmitzberger FF, Amer H, Ingold-Heppner B, Balleyguier C, Diekmann F, et al. Contrast-Enhanced spectral mammography vs. mammography and MRI-clinical performance in a multi-reader evaluation. *Eur Radiol* 2017; **27**: 2752–64. https://doi.org/10.1007/s00330-016-4650-6
24. Youn I, Choi S, Choi YJ, Moon JH, Park HJ, Ham S-Y, et al. Contrast enhanced digital mammography versus magnetic resonance imaging for accurate measurement of the size of breast cancer. *Br J Radiol* 2019; **92**: 20180929. https://doi.org/10.1259/bjr.20180929
25. Łuczyńska E, Heinze-Paluchowska S, Hendrick E, Dyczek S, Ryś J, Herman K, et al. Comparison between breast MRI and contrast-enhanced spectral mammography. *Med Sci Monit* 2015; **21**: 1358–67. https://doi.org/10.12659/MSM.893018
26. Patel BK, Garza SA, Eversman S, Lopez-Alvarez Y, Kosiorek H, Pockaj BA. Assessing tumor extent on contrast-enhanced spectral mammography versus full-field digital mammography and ultrasound. *Clin Imaging* 2017; **46**: 78–84. https://doi.org/10.1016/j.clinimag.2017.07.001
27. Travieso-Aja MDM, Naranjo-Santana P, Fernández-Ruiz C, Severino-Rondón W, Maldonado-Saluzzi D, Rodríguez Rodríguez M, et al. Factors affecting the precision of lesion sizing with contrast-enhanced spectral mammography. *Clin Radiol* 2018; **73**: 296–303. https://doi.org/10.1016/j.crad.2017.10.017
28. Blum KS, Rubbert C, Mathys B, Antoch G, Mohrmann S, Obenauer S. Use of contrast-enhanced spectral mammography for intramammary cancer staging: preliminary results. *Acad Radiol* 2014; **21**: 1363–69. https://doi.org/10.1016/j.acra.2014.06.012
29. Bozzini A, Nicosia L, Pruneri G, Maisonneuve P, Meneghetti L, Renne G, et al. Clinical performance of contrast-enhanced spectral mammography in pre-surgical evaluation of breast malignant lesions in dense breasts: a single center study. *Breast Cancer Res Treat* 2020; **184**: 723–31. https://doi.org/10.1007/s10549-020-05881-2
30. Jochelson MS, Dershaw DD, Sung JS, Heerdt AS, Thornton C, Moskowitz CS, et al. Bilateral contrast-enhanced dual-energy digital mammography: feasibility and comparison with conventional digital mammography and MR imaging in women with known breast carcinoma. *Radiology* 2013; **266**: 743–51. https://doi.org/10.1148/radiol.12121084
31. Ali-Mucheru M, Pockaj B, Patel B, Pizzitola V, Wasif N, Stucky C-C, et al. Contrast-Enhanced digital mammography in the surgical management of breast cancer. *Ann Surg Oncol* 2016; **23**: 649–55. https://doi.org/10.1245/s10434-016-5567-7
32. Lobbes MBI, Lalji UC, Nelemans PJ, Houben I, Smidt ML, Heuts E, et al. The quality of tumor size assessment by contrast-enhanced spectral mammography and the benefit of additional breast MRI. *J Cancer* 2015; **6**: 144–50. https://doi.org/10.7150/jca.10705
33. McGuire A, O'Leary DP, Ryan M, Khan Z, Corrigan M, Redmond HP, et al. Contrast-enhanced spectrum mammography-A useful adjunct to digital mammography in predicting tumor size. *Breast J* 2017; **23**: 484–86. https://doi.org/10.1111/tbj.12774
34. Sumkin JH, Berg WA, Carter GJ, Bandos AI, Chough DM, Ganott MA, et al. Diagnostic performance of MRI, molecular breast imaging, and contrast-enhanced mammography in women with newly diagnosed breast cancer. *Radiology* 2019; **293**: 531–40. https://doi.org/10.1148/radiol.2019190887

35. Rominger M, Berg D, Frauenfelder T, Ramaswamy A, Timmesfeld N. Which factors influence MRI-pathology concordance of tumour size measurements in breast cancer? *Eur Radiol* 2016; **26**: 1457–65. https://doi.org/10.1007/s00330-015-3935-5
36. Choi WJ, Cha JH, Kim HH, Shin HJ, Chae EY. The accuracy of breast MR imaging for measuring the size of a breast cancer: analysis of the histopathologic factors. *Clin Breast Cancer* 2016; **16**: e145–52. https://doi.org/10.1016/j.clbc.2016.07.007
37. Pritt B, Weaver DL. Accurate determination of breast cancer size: the role of histopathology and imaging. *Current Diagnostic Pathology* 2005; **11**: 435–42. https://doi.org/10.1016/j.cdip.2005.08.008
38. Tabár L, Dean PB, Lindhe N, Ingvarsson M. The ongoing revolution in breast imaging calls for a similar revolution in breast pathology. *Int J Breast Cancer* 2012; **2012**: 489345. https://doi.org/10.1155/2012/489345
39. Tot T, Gere M. Radiological-pathological correlation in diagnosing breast carcinoma: the role of pathology in the multimodality era. *Pathol Oncol Res* 2008; **14**: 173–78. https://doi.org/10.1007/s12253-008-9061-9
40. Lobbes M, Nelemans P. Good correlation does not automatically imply good 407 agreement: the trouble with comparing tumour size by breast MRI versus 408 histopathology. *Eur J Radiol* 2013; **82**: e906–7.
41. Edwards C, Allen H, Chamunyonga C. Correlation does not imply agreement:A cautionary tale for researchers and reviewers. *Sonography* 2021.
42. Watson P, Petrie A. Method agreement analysis: a review of correct methodology. *Theriogenology* 2010; **73**: 1167–79. https://doi.org/10.1016/j.theriogenology.2010.01.003